

Materials Properties from Electron Density Distributions

Molecular Magnetism and Linear Optical Properties

Inauguraldissertation

der Philosophisch-naturwissenschaftlichen Fakultät

der Universität Bern

vorgelegt von

Leonardo Humberto Rezende Dos Santos

von Brasilien

Leiter der Arbeit:

PD Dr. P. Macchi

Departement für Chemie und Biochemie der Universität Bern

Original document saved on the web server of the University Library of Bern



This work is licensed under a

Creative Commons Attribution-Non-Commercial-No derivative works 2.5 Switzerland licence. To see the licence go to <http://creativecommons.org/licenses/by-nc-nd/2.5/ch/> or write to Creative Commons, 171 Second Street, Suite 300, San Francisco, California 94105, USA.

Copyright Notice

This document is licensed under the Creative Commons Attribution-Non-Commercial-No derivative works 2.5 Switzerland. <http://creativecommons.org/licenses/by-nc-nd/2.5/ch/>

You are free:



to copy, distribute, display, and perform the work

Under the following conditions:



Attribution. You must give the original author credit.



Non-Commercial. You may not use this work for commercial purposes.



No derivative works. You may not alter, transform, or build upon this work..

For any reuse or distribution, you must take clear to others the license terms of this work.

Any of these conditions can be waived if you get permission from the copyright holder.

Nothing in this license impairs or restricts the author's moral rights according to Swiss law.

The detailed license agreement can be found at:

<http://creativecommons.org/licenses/by-nc-nd/2.5/ch/legalcode.de>

Materials Properties from Electron Density Distributions

Molecular Magnetism and Linear Optical Properties

Inauguraldissertation

der Philosophisch-naturwissenschaftlichen Fakultät

der Universität Bern

vorgelegt von

Leonardo Humberto Rezende Dos Santos

von Brasilien

Leiter der Arbeit:

PD Dr. P. Macchi

Departement für Chemie und Biochemie der Universität Bern

Von der Philosophisch-naturwissenschaftlichen Fakultät angenommen.

Bern, 03. Februar 2016

Der Dekan:

Prof. Dr. G. Colangelo

Acknowledgments

First and foremost, I express my gratitude to Piero Macchi for giving me the opportunity and pleasure to work under his supervision, and to complete this doctorate in his research group. I am thankful for the enthusiastic scientific discussions, his careful listening and answering to my questions, his enormous patience, and invaluable advices on my professional concerns. I have learned a lot from his experience and will certainly carry his lessons for life.

I am grateful to my collaborators Dr. Alessandro Genoni (University of Lorraine, France), Dr. Anna Krawczuk (Jagiellonian University, Poland), and Prof. Jamie L. Manson (Eastern Washington University, United States), for their interest in my research and for kindly answering my questions. Their collaboration not only provided me insights into new techniques, but also essential information for this thesis.

A special thank you goes to everyone of the Chemical and Mineralogical Crystallographic Groups: to the colleagues Abita S. Chimpri and Rosa M. Danisi, for help putting me on the right track during my first weeks in Switzerland; to my closer co-workers in the last months, Michelle Ernst and Rebecca Scatena, from whom I had the opportunity to learn many things while assisting them; to Jürg Hauser, for his enormous tech support; to Arianna Lanza, always trying to make me more sociable; to Martin Fisch, Maria Clara R. Freitas, Luzia Germann, Fabio Montisci, Elena Marelli, Shaun Evans, Meigeng Gao, Frank Gfeller, Georgia Cametti, Vladimir Malogajski and Thomas Armbruster, for an stimulating and fruitful working atmosphere, and to my office mate Simon Gantenbein.

Last but not least, I thank my parents, sister and friends for supporting me during the studies, which would have certainly been less encouraging without their reinforcement.

Contents

Motivation and goal of the study

Background	7
Aim of this thesis	8

Chapter 1 Materials Properties from Electron Density Distributions

1.1. Charge, electron and spin-electron densities	11
1.2. Electron densities from ab initio quantum mechanics	14
1.2.1. Molecular electronic problem	14
1.2.2. Hartree-Fock approximation	16
1.2.3. Correlated methods	18
1.2.4. Density functional theory	21
1.2.5. Periodic boundary conditions	24
1.2.6. Calculations under electric fields	25
1.2.7. Open-shell determinants and spin Hamiltonians	27
1.3. Electron densities from high-resolution X-ray diffraction	29
1.3.1. Elastic X-ray scattering and the independent-atom formalism	29
1.3.2. Generalized scattering factors and the Hansen-Coppens formalism	32
1.3.3. Extended electron density models	36
1.3.4. X-ray constrained wavefunctions	37
1.3.5. X-ray diffraction under electric fields	40
1.4. Molecular and crystal properties from electron densities	42
1.4.1. Topological analysis of electron density distributions	42
1.4.2. Atomic and molecular electric properties	46
1.4.3. Crystalline electric properties	50
1.4.4. Magnetic properties of metal-organic materials	54
1.4.5. Other properties from electron densities	58

Chapter 2 Distributed Polarizabilities of Amino Acids and their Hydrogen-Bonded Aggregates

2.1. Introduction, motivation and specific goals	65
2.2. Theoretical methods	66
2.3. Results and discussion	68
2.3.1. Atomic and functional-group polarizabilities in amino acid molecules	68

2.3.2. Electron correlation and basis-set effects	73
2.3.3. Benchmarking of density functionals for distributed polarizabilities	75
2.3.4. Hydrogen bond effects on the distributed polarizability of amino acid aggregates	77
2.3.5. Polarizabilities and refractive indices of amino acid salts	80
2.4. Conclusions and perspectives	82

Chapter 3 Electron Density Distributions and Magnetic Properties in Copper Pyrazine Nitrate Quasi-Low-Dimensional Quantum Magnets

3.1. Introduction, motivation and specific goals	86
3.2. Experimental and computational techniques	87
3.2.1. X-ray data collection and structure refinement	87
3.2.2. Multipole refinement	89
3.2.3. Theoretical calculations	90
3.3. Results and discussion	91
3.3.1. Crystal structures	92
3.3.2. Electron density distributions and topological analyses	92
3.3.3. d-Orbital populations and magnetic moment	96
3.3.4. Magnetic exchange-coupling constants	97
3.3.5. Molecular orbital analysis and magnetic-exchange mechanism	98
3.3.6. Spin density distributions	99
3.4. Conclusions and perspectives	101

Chapter 4 Unconstrained and X-ray Constrained Extremely Localized Molecular Orbitals: Analysis of the Reconstructed Electron Density

4.1. Introduction, motivation and specific goals	105
4.2. Extremely localized molecular orbitals	107
4.3. Experimental and computational details	109
4.3.1. X-ray data collection and processing	109
4.3.2. Spherical, independent atom refinement	109
4.3.3. Multipole refinement	111
4.3.4. Ab initio periodic calculation and multipole refinement of theoretical structure factors	111
4.3.5. Unconstrained and X-ray constrained ELMO and Hartree-Fock calculations	112
4.3.6. Topological analyses	112
4.4. Fitting effects on the multipole model	113
4.5. Fitting effects on the ELMO wavefunctions	115
4.5.1. Agreement statistics and energy	115

4.5.2. Electron density distribution and its topology	118
4.5.3. QTAIM atomic charges and dipoles	121
4.6. Fitting effects on the multipole model-projected ELMO electron densities	123
4.6.1. Deformation density	123
4.6.2. Topological properties, charges and dipoles	124
4.7. Influence of fractional coordinates and ADPs on the X-ray constrained calculations	126
4.8. Conclusions and perspectives	127
General Conclusions and Outlook	132

Motivation and goal of the study

Background

Knowing the electron density is fundamental for all chemistry. Chemical reactions and molecular responses, supramolecular assemblies and materials properties all depend on the distribution and movement of the electrons.¹ The chemist frequently uses the quantum-mechanical understanding of the electronic structure in order to not only explain chemical bonding mechanisms or predict molecular geometries,² but also to efficiently synthesize a molecule or fabricate a functional material. The importance of the electron density is due to its relation to energy³ and to the fact that it is an observable, therefore it can be not only calculated from first-principles, but also measured, in particular using X-ray diffraction from crystals.⁴

Many progresses occurred since the first experimental observations of the so-called aspherical, deformation densities in crystals of small organic molecules.⁵ Nowadays, deformation densities are obtained for ever-larger molecules, perhaps containing heavy transition metals, so even when the more polarizable valence electrons are few compared to the almost spherical core electrons. Recently, it has become possible to observe core polarizations from X-ray diffraction.⁶

Analogous progresses took place on the theoretical side, especially due to Density Functional Theory (DFT), that provides accurate molecular properties at low computational costs. Calculations of larger molecules and extended structures, within periodic boundary conditions, are frequent nowadays. Moreover, the number of investigations combining theoretical and experimental modelling of electron density distributions is growing fast, for instance, opening the possibility to optimize X-ray constrained molecular orbitals.⁷

Apart from more accurate techniques, electron density analysis has become more informative thanks to the development and application of the Quantum Theory of Atoms in Molecules (QTAIM).⁸ Among the most relevant results, one can mention the comprehensive understanding of bonding involving transition metals, such as coordination of inorganic ligands,⁹ agostic interactions¹⁰ and metal-metal bounded clusters,¹¹ and the characterization of so-called weak interactions, which include hydrogen,¹² halogen¹³ and chalcogen bonds.¹⁴ These results confirm that qualitative and even quantitative insights in the interactions between atoms and molecules are now possible from the analysis of the electron density.

On the side of materials properties, a few research groups have pioneered the applications of electron density analysis.

Overgaard *et al.*¹⁵ adopted the analysis of the crystal electron density through QTAIM for magnetic metal-organic materials. The experimentally available d-orbital occupations for the metal centers, in conjunction with magnetic susceptibility measurements, allow insight on the actual magnetization and exchange mechanisms. The spin density is potentially available from polarized neutron diffraction on single crystals, and increasing interest was generated by the possibility to simultaneously refine the electron and the spin densities by combining X-ray and polarized neutron scattering.¹⁶

Macchi *et al.*¹⁷ have correlated the measured or DFT-calculated refractive indices of crystalline amino acid derivatives with the main features of their electron densities, focusing on the role of intermolecular interactions and the crystal packing on determining the optical linear properties of organic materials. Moreover, atomic polarizabilities have been calculated from QTAIM partition of the total electron density¹⁸ and eventually used to analyse the origin of the linear susceptibility in the crystals.

Scherer *et al.*¹⁹ have used QTAIM to characterize subtle features of the chemical bonds in inorganic low-dimensional superconductors. The topology of the electron density at the Valence Shell Charge Concentration (VSCC) region of transition metals have been used to correlate the changes of the electronic structure induced by structural phase transitions with the bulk behaviour of the materials. Additionally, organometallic systems presenting agostic or anagostic M...H-C interactions have been investigated,²⁰ and bonding models proposed that are based on electron localization/delocalization profiles along the relevant bond paths.

Spackman *et al.*²¹ have proposed a tool to understand crystal packing in organic molecular crystals based on so-called energy frameworks. The approach combines efficient calculation of meaningful intermolecular interaction energies with a graphical representation of their magnitude in such a way that structure-property correlations can be derived. In particular, mechanical properties such as shearing and brittleness have been rationalized in terms of the anisotropy of the topology of these pairwise intermolecular interaction energies.

Modern research in electron density analysis spans a broad range of experimental and theoretical investigations. Crystallization and crystal morphology, polymorphism, supramolecular ensembles, crystal structure determination and prediction and the measurement of crystal thermal, magnetic, linear and non-linear optical properties, all have the common focus on rationally design crystalline materials with desirable chemical or physical properties. Fundamental outcomes of these researches exploit the insight gained from an in-depth understanding of the ways crystalline materials are formed from their component atoms, chemical bonds, functional groups and molecules.

Additionally, as discussed by Spackman,²² engineering materials implies the selection of adequate molecular carriers of specific functionalities, and their optimal arrangement in a periodically homogeneous system. Some functions and indicators, readily available from the electron density analyses, can be used for the comprehension of the role played by a given functional group on determining specific properties.

Aim of this thesis

This puts the bases for the investigations carried out in this thesis. The general goal is correlating observable properties of organic and metal-organic materials with their ground-state electron density distribution. In a long-term view, we expect to develop empirical or semi-empirical approaches to predict materials properties from the electron density of their building blocks, thus allowing to rationally engineering molecular materials from their constituent subunits, such as their functional groups.^{17b}

In particular, this thesis has focused on linear optical properties of naturally occurring amino acids and their organic and metal-organic derivatives, and on magnetic properties of metal-organic frameworks.

This is mainly because of the well-defined formalism that connects the microscopic, atomic or molecular property to the macroscopic, crystalline behaviour of the materials. For optical materials, one defines (hyper)polarizabilities at atomic and molecular levels; summation of these quantities over the crystal lattice enables the calculation of the macroscopic electric susceptibilities. For magnetic materials, one defines exchange-coupling constants between two paramagnetic building blocks at the molecular level; lattice summation of these energy contributions enables estimation of the macroscopic magnetic susceptibility.

For analysing the optical properties and the magnetic behaviour of the molecular or sub-molecular building blocks in materials, we mostly used the more traditional QTAIM partitioning scheme of the molecular or crystalline electron densities, however, in Chapter 4, we have also investigated a new approach, namely, X-ray Constrained Extremely Localized Molecular Orbitals (XC-ELMO), that can be used in future to extract the electron densities of crystal subunits.

With the purpose of rationally engineering linear optical materials, we have calculated atomic and functional group polarizabilities of amino acid molecules, their hydrogen-bonded aggregates and their metal-organic frameworks. This has enabled the identification of the most efficient functional groups, able to build-up larger electric susceptibilities in crystals, as well as the quantification of the role played by intermolecular interactions and coordinative bonds on modifying the polarizability of the isolated building blocks. Furthermore, we analysed the dependence of the polarizabilities on the one-electron basis set and the many-electron Hamiltonian. This is useful for selecting the most efficient level of theory to estimate susceptibilities of molecular-based materials.

With the purpose of rationally design molecular magnetic materials, we have investigated the electron density distributions and the magnetism of two copper(II) pyrazine nitrate metal-organic polymers. High-resolution X-ray diffraction and DFT calculations were used to characterize the magnetic exchange pathways and to establish relationships between the electron densities and the exchange-coupling constants. Moreover, molecular orbital and spin-density analyses were employed to understand the role of different magnetic exchange mechanisms in determining the bulk magnetic behaviour of these materials.

As anticipated, we have finally investigated a modified version of the X-ray constrained wavefunction technique, XC-ELMOs, that is not only a useful tool for determination and analysis of experimental electron densities, but also enables one to derive transferable molecular orbitals strictly localized on atoms, bonds or functional groups. In future, we expect to use XC-ELMOs to predict materials properties of large systems, currently challenging to calculate from first-principles, such as macromolecules or polymers. In this thesis, we point out advantages, needs and pitfalls of the technique.

This work fulfils, at least partially, the prerequisites to understand materials properties of organic and metal-organic materials from the perspective of the electron density distribution of their building blocks. Empirical or semi-empirical evaluation of optical or magnetic properties from a preconceived assembling of building blocks could be extremely important for rationally design new materials, a field where accurate but expensive first-principles calculations are generally not used. This research could impact the community in the fields of crystal engineering, supramolecular chemistry and, of course, electron density analysis.

References

1. Schleyer, P. von R. *Encyclopedia of Computational Chemistry*; John Wiley and Sons: Chichester, **1998**.
2. (a) Pauling, L. *The Nature of the Chemical Bond and the Structure of Molecules and Crystals: An Introduction to Modern Structural Chemistry*; Cornell University Press: New York. **1960**. (b) Gillespie, R. J.; Hargittai, I. *The VSEPR Model of Molecular Geometry*; Allyn and Bacon: Boston. **1991**.
3. Hohenberg, P.; Kohn, W. *Phys. Rev. B*. **1964**, *136*, 864-871.
4. Gatti, C.; Macchi, P. (Eds.) *Modern Charge-Density Analysis*; Springer: Netherlands. **2012**.
5. Coppens, P. *Science*. **1967**, *158*, 1577-1579.
6. Fischer, A.; Tiana, D.; Scherer, W.; Batke, K.; Eickerling, G.; Svendsen, H.; Bindzus, N.; Iversen, B. B. *J. Phys. Chem. A*. **2011**, *115*, 13061-13071.
7. Jayatilaka, D.; Grimwood, D. J. *Acta Cryst. Sect. A*. **2001**, *57*, 76-86.
8. Bader, R. F. W. *Atoms in Molecules: A Quantum Theory*; Oxford University Press: Oxford. **1990**.
9. Macchi, P.; Sironi, A. *Coord. Chem. Rev.* **2003**, *238*, 383-412.
10. Scherer, W.; McGrady, G. S. *Angew. Chem. Int. Ed. Engl.* **2004**, *43*, 1782-1806.
11. Farrugia, L. J.; Macchi, P. *Struct. Bond.* **2012**, *146*, 127-158.
12. Gilli, G.; Gilli, P. *The Nature of the Hydrogen Bond*; Oxford University Press: Oxford. **2009**.
13. Bui, T. T. T.; Dahaoui, S.; Lecomte, C.; Desiraju, G. R.; Espinosa, E. *Angew. Chem. Int. Ed.* **2009**, *48*, 3838-3841.
14. Wang, W.; Ji, B.; Zhang, Y. *J. Phys. Chem. A*. **2009**, *113*, 8132-8135.
15. (a) Overgaard, J.; Hibbs, D. E.; Rentschler, E.; Timco, G. A.; Larsen, F. K. *Inorg. Chem.* **2003**, *42*, 7593-7601. (b) Overgaard, J.; Walsh, J. P. S.; Hathwar, V. R.; Jorgensen, M. R. V.; Hoffman, C.; Platts, J. A.; Piltz, R.; Winpenny, R. E. P. *Inorg. Chem.* **2014**, *53*, 11531-11539.
16. Deutsch, M.; Gillon, B.; Claiser, N.; Gillet, J.-M.; Lecomte, C.; Souhassou, M. *IUCrJ*. **2014**, *1*, 194-199.
17. (a) Chimpri, A. S.; Gryl, M.; Dos Santos, L. H. R.; Krawczuk, A.; Macchi, P. *Cryst. Growth Des.* **2013**, *13*, 2995-3010. (b) Macchi, P. *Chimia*. **2014**, *68*, 31-37.
18. Krawczuk, A.; Pérez, D.; Macchi, P. *J. Appl. Cryst.* **2014**, *47*, 1452-1458.
19. Eickerling, G.; Hauf, C.; Scheidt, E.-W.; Reichardt, L.; Schneider, C.; Muñoz, A.; Lopez-Moreno, S.; Romero, A. H.; Porcher, F.; André, G.; Pöttgen, R.; Scherer, W. *Z. Anorg. Allg. Chem.* **2013**, *639*, 1985-1995.
20. (a) Scherer, W.; Sirsch, P.; Shorokhov, D.; Tafipolsky, M.; McGrady, G. S.; Gullo, E. *Chem. Eur. J.* **2003**, *9*, 6057-6070. (b) Scherer, W.; Dunbar, A. C.; Barquera-Lozada, J. E.; Schmitz, D.; Eickerling, G.; Kratzert, D.; Stalke, D.; Lanza, A.; Macchi, P.; Casati, N. P. M.; Ebad-Allah, J.; Kuntscher, C. *Angew. Chem. Int. Ed.* **2015**, *54*, 2505-2509.
21. Turner, M. J.; Thomas, S. P.; Shi, M. W.; Jayatilaka, D.; Spackman, M. A. *Chem. Comm.* **2015**, *51*, 3735-3738.
22. Spackman, M. A. Charge Densities and Crystal Engineering. In *Modern Charge-Density Analysis*. Gatti, C.; Macchi, P. (Eds.); Springer: Netherlands, **2012**; p 553-572.

Chapter 1

Materials Properties from Electron Density Distributions

This chapter provides the fundamental definitions of charge, electron and spin-electron densities, as well as an introduction on the methodologies to obtain accurate electron density mapping in molecules and crystalline materials, from both theory and experiment. The concept of extracting materials properties from electron density distributions is examined and past efforts are reviewed. In particular, the deep connection between the coherent and elastic X-ray scattering and the first-principles quantum mechanics is highlighted. The entanglement of X-ray diffraction and quantum mechanics finds applications on a broad range of problems of interest to solid-state chemistry and physics and eventually it sheds light on the search for new materials and on how to modify their properties for desired applications.

1.1. Charge, electron and spin-electron densities

The quantum-mechanical nature of small particles travelling at high speed guarantees that one can only know a probabilistic distribution of electrons in molecules that is an averaged probability to find any electron at a given position in space. Considering a molecular system of N electrons and M nuclei, the probability of finding any of its electrons at a position \mathbf{r}_1 regardless of the position of the other electrons is $\rho_1(\mathbf{r}_1)d\mathbf{r}_1$, where the corresponding probability density, the *one-electron density*, is defined as¹

$$\rho_1(\mathbf{r}_1) = N \int \Psi_{el}^*(\mathbf{r}_1, \mathbf{r}_2, \dots, \mathbf{r}_N; \{\mathbf{R}\}) \cdot \Psi_{el}(\mathbf{r}_1, \mathbf{r}_2, \dots, \mathbf{r}_N; \{\mathbf{R}\}) d\mathbf{r}_2 \dots d\mathbf{r}_N \quad (1.1)$$

Within the Schrödinger formalism and following the Born-Oppenheimer approximation, Ψ_{el} is the stationary wavefunction describing the N electrons at fixed nuclear coordinates $\{\mathbf{R}\}$. The one-electron density may be obtained either from experiment, for example by means of coherent and elastic (Bragg) X-ray scattering, or from ab initio calculations.² The *charge density* is instead the sum of electronic and nuclear densities. Even though the terms “charge density” and “electron density” are often used interchangeably, the former emphasizes situations where both electronic and nuclear distributions are simultaneously determined, as it happens in ab initio molecular dynamics.³

The notation ρ_1 refers to one particle; but it is also possible to introduce probability densities for any number of particles. Thus, the *two-electron density*

$$\rho_2(\mathbf{r}_1, \mathbf{r}_2) = \frac{N(N-1)}{2} \int \Psi_{el}^*(\mathbf{r}_1, \mathbf{r}_2, \dots, \mathbf{r}_N; \{\mathbf{R}\}) \cdot \Psi_{el}(\mathbf{r}_1, \mathbf{r}_2, \dots, \mathbf{r}_N; \{\mathbf{R}\}) d\mathbf{r}_3 \dots d\mathbf{r}_N \quad (1.2)$$

defines the probability density of finding two electrons simultaneously at positions \mathbf{r}_1 and \mathbf{r}_2 . In general, the *p-order electron density* $\rho_p(\mathbf{r}_1, \mathbf{r}_2, \dots, \mathbf{r}_p)$ determines the probability of p electrons being found simultaneously at the positions from \mathbf{r}_1 to \mathbf{r}_p .

However, in order to describe completely the correlation among the electrons, more general functions than the p -order electron densities are necessary. These are called p -order density matrices. A density matrix of order p for an N -electron system is given by

$$\begin{aligned} \gamma_p(\mathbf{r}_1, \mathbf{r}_2, \dots, \mathbf{r}_p; \mathbf{r}'_1, \mathbf{r}'_2, \dots, \mathbf{r}'_p) \\ = \binom{N}{p} \int \Psi_{el}^*(\mathbf{r}_1, \mathbf{r}_2, \dots, \mathbf{r}_p, \mathbf{r}_{p+1}, \dots, \mathbf{r}_N) \cdot \Psi_{el}(\mathbf{r}'_1, \mathbf{r}'_2, \dots, \mathbf{r}'_p, \mathbf{r}'_{p+1}, \dots, \mathbf{r}'_N) d\mathbf{r}_{p+1} \dots d\mathbf{r}_N \end{aligned} \quad (1.3)$$

where $\{\mathbf{r}\}$ and $\{\mathbf{r}'\}$ are two sets of independent electron coordinates, $\binom{N}{p}$ is a binomial coefficient which ensures normalization, and the parametric dependence on the nuclear coordinates $\{\mathbf{R}\}$ have been omitted. A value is assigned to γ_p by two sets of indices. Therefore, $\gamma_p(\{\mathbf{r}\}; \{\mathbf{r}'\})$ is a matrix element. In particular, the first- and second-order density matrices are written as

$$\gamma_1(\mathbf{r}_1; \mathbf{r}'_1) = N \int \Psi_{el}^*(\mathbf{r}_1, \mathbf{r}_2, \dots, \mathbf{r}_N) \cdot \Psi_{el}(\mathbf{r}'_1, \mathbf{r}'_2, \dots, \mathbf{r}'_N) d\mathbf{r}_2 \dots d\mathbf{r}_N \quad (1.4)$$

$$\gamma_2(\mathbf{r}_1, \mathbf{r}_2; \mathbf{r}'_1, \mathbf{r}'_2) = \frac{N(N-1)}{2} \int \Psi_{el}^*(\mathbf{r}_1, \mathbf{r}_2, \dots, \mathbf{r}_N) \cdot \Psi_{el}(\mathbf{r}'_1, \mathbf{r}'_2, \dots, \mathbf{r}'_N) d\mathbf{r}_3 \dots d\mathbf{r}_N \quad (1.5)$$

The functions ρ_1 and ρ_2 are the traces of γ_1 and γ_2 , respectively.

Density matrices allow one to relate expectation values of operators directly to the electron distributions, providing a powerful tool for discussing the behaviour of many-electron systems.¹ Noteworthy, all one-electron properties can be evaluated using the first-order density matrix (1.4) and all two-electron properties using the second-order matrix (1.5). Eventually, a subset of one-electron properties may be obtained from the electron density ρ_1 alone. Those are, at least formally if not operationally, available from the elastic and coherent X-ray scattering.

On the one hand, higher p -order density matrices are in principle necessary for describing many-body effects. But because the second-order density matrix tell us how the motion of two different electrons are correlated due to their interaction, distribution functions of order $p > 2$ are certainly less relevant for the interpretation of the chemical bonding. On the other hand, the knowledge of the one-electron density ρ_1 alone is not able to reveal the whole nature of the chemical interactions.⁴

In recent years, more information concerning chemical bonding has become available from both experiment and theory.

The incoherent and inelastic (Compton) X-ray scattering, produced by the off-diagonal terms of γ_1 , have been combined with Bragg scattering in order to determine the full γ_1 matrix.⁵ Many papers also report on the possibility of recovering γ_1 from Bragg X-ray scattering only, either by jointly minimizing the energy or imposing mathematical constraints.⁶

From the theoretical side, two-electron density functions have been used to derive important descriptors for chemical bond analysis.² Among them, the localization and delocalization indices are certainly necessary towards a full comprehension of the chemical bonding. However, all of the so-called *pair-density functions* suffer from being not directly available from X-ray scattering. For this reason, Gatti proposed the use of the *source function*,⁷ an observable of the one-electron density. Although he has stressed the ability of source functions to represent the localization and delocalization of electrons, this view received some criticism.⁸

Finally, to describe an electron fully, the specification of its spin is necessary. In the context of a nonrelativistic treatment, we introduce two spin functions, $\alpha(\omega)$ and $\beta(\omega)$, and describe an electron not only by the three spatial coordinates \mathbf{r} , but also by one spin variable ω . We denote these four coordinates by $\mathbf{x} = \{\mathbf{r}, \omega\}$. Because electrons obey Fermi-Dirac statistics, two identical-spin electrons cannot occupy the same position in space whereas two opposite-spin electrons tend to pair in order to lower their energy. Additionally, some multi-electronic systems may be characterized by unpaired electrons, thus giving rise to an excess of electrons of a given spin. A formulation of density matrices in terms of \mathbf{x} is quite straightforward.^{1,2} The *spin-electron density*, i.e. the excess of electron density of a given spin, is

$$\begin{aligned} \rho_\alpha(\mathbf{r}_1) - \rho_\beta(\mathbf{r}_1) &= N \int \Psi_{el}^*(\mathbf{x}_1, \mathbf{x}_2, \dots, \mathbf{x}_N; \{\mathbf{R}\}) \cdot \Psi_{el}(\mathbf{x}_1, \mathbf{x}_2, \dots, \mathbf{x}_N; \{\mathbf{R}\}) d\omega_\alpha d\mathbf{r}_2 \dots d\mathbf{r}_N \\ &\quad - N \int \Psi_{el}^*(\mathbf{x}_1, \mathbf{x}_2, \dots, \mathbf{x}_N; \{\mathbf{R}\}) \cdot \Psi_{el}(\mathbf{x}_1, \mathbf{x}_2, \dots, \mathbf{x}_N; \{\mathbf{R}\}) d\omega_\beta d\mathbf{r}_2 \dots d\mathbf{r}_N \end{aligned} \quad (1.6)$$

The scattering of spin-active particles, such as polarized neutrons, can reveal the excess of electronic spin, and hence the spin density. Moreover, a method combining experimental information from Bragg X-ray diffraction and polarized neutron diffraction has been proposed for the determination of spin-dependent electron densities.⁹

In this work, we focus on the applications of the one-electron density in chemistry and materials science. Minor reference is made to theoretically predicted spin-electron densities. We start by considering how these functions can be predicted from first-principle quantum-mechanical calculations (section 1.2). We briefly discuss the familiar Hartree-Fock procedure that not only sets the stage for more accurate methods, but also finds relevance for the investigation of X-ray constrained and unconstrained molecular orbitals, considered in Chapter 4. Then, we describe the state-of-the-art approaches to include electronic correlation in wavefunctions and their related densities. This is of relevance because it allows accurate estimation of properties and provide benchmark densities that are explored in details in all forthcoming chapters. After mentioning the periodic boundary conditions that enables calculation of extended systems, we discuss how the theoretical methods can be used to yield the properties of interest in this thesis, magnetic, Chapter 3, and linear optical properties, Chapter 2.

Section 1.3 is devoted to modelling of electron densities from the coherent and elastic X-ray scattering. We begin by a description of X-ray diffraction in crystals and consider the approximations that enable one to write the electron density distribution within a unit cell as the Fourier transform of its structure factors. We discuss how to fit an electron density model against the set of measured intensities, initially considering the spherical, independent atom model that is the current paradigm for crystal structure determination and analysis. The inability to deal with electronic polarization due to chemical bonding makes this model quite limited for estimating the materials properties of interest in this thesis. Thus, we turn to more sophisticated, aspherical electron density models, and describe in some detail the multipolar formalism applied in the crystalline materials considered in Chapters 3 and 4. Then, we mention an alternative to the multipolar fitting, namely, wavefunctions constrained to X-ray intensities. This is further explored in Chapter 4. Of relevance for the electric properties treated in Chapter 2 are the advances and limitations in X-ray diffraction under electric fields, considered in the last part of the section.

In the final part of this chapter, section 1.4, we briefly mention the key aspects of topological analysis by means of Quantum Theory of Atoms in Molecules (QTAIM), used throughout all this research. Finally, we critically examine the recent advances in correlation between density functions and materials properties, focusing on electrical, optical, and magnetic properties, but also considering many other properties of relevance for materials science.

1.2. Electron densities from *ab initio* quantum mechanics

Eqn. 1.1 leads to different expressions for $\rho_1(\mathbf{r})$, depending on the functional form of Ψ_{el} . In this section, we describe the adopted theoretical methods to obtain Ψ_{el} with high accuracy. Most of these methods allow the derivation of an electron density matrix,² hence provide theoretical electron density distributions.

1.2.1. Molecular electronic problem

The electronic structure and properties of a molecular system in a stationary state is determined by its electronic wavefunction $\Psi_{el}(\{\mathbf{x}\}; \{\mathbf{R}\})$, a mathematical function that depends on the spatial and spin coordinates of each electron in the system. Ψ_{el} is the solution of the nonrelativistic time-independent Schrödinger equation that, for a system of N electrons moving in the potential field due to M nuclei, takes the form¹

$$\mathbf{H}\Psi_{el}(\mathbf{x}_1, \mathbf{x}_2, \dots, \mathbf{x}_N; \{\mathbf{R}\}) = E\Psi_{el}(\mathbf{x}_1, \mathbf{x}_2, \dots, \mathbf{x}_N; \{\mathbf{R}\}) \quad (1.7)$$

where E is the energy of the N electrons moving in the field provided by the nuclei and \mathbf{H} is the electronic Hamiltonian operator

$$\mathbf{H} = -\frac{1}{2} \sum_{i=1}^N \nabla_i^2 - \sum_{i=1}^N \sum_{k=1}^M \frac{Z_k}{|\mathbf{r}_i - \mathbf{R}_k|} + \sum_{i=1}^N \sum_{j>i}^N \frac{1}{|\mathbf{r}_i - \mathbf{r}_j|} \quad (1.8)$$

Here Z_k is the atomic number of nucleus k and the Laplacian operator ∇_i^2 involves second-differentiation with respect to the spatial coordinates of the i -th electron. The first term is the operator for the kinetic energy of the electrons; the second term represents the potential energy of the electrons in the field of the nuclei; the third term represent the repulsion between electrons. Eqn. 1.7 is an *eigenvalue equation* characterized by possessing valid Ψ_{el} solutions only for certain values of the *eigenvalue* E . The solutions Ψ_{el} are the *eigenfunctions* of the operator \mathbf{H} and the corresponding eigenvalues are the quantized electronic energies of the allowed stationary states of the molecular system. The ground-state wavefunction being associated with the lowest eigenvalue E .

The fact that electrons are fermions, indistinguishable particles with spin quantum number $1/2$, places an important restriction on Ψ_{el} : it must be antisymmetric with respect to the interchange of the coordinate \mathbf{x} of any two electrons¹⁰

$$\Psi_{el}(\mathbf{x}_1, \dots, \mathbf{x}_i, \dots, \mathbf{x}_j, \dots, \mathbf{x}_N) = -\Psi_{el}(\mathbf{x}_1, \dots, \mathbf{x}_j, \dots, \mathbf{x}_i, \dots, \mathbf{x}_N) \quad (1.9)$$

Therefore, the exact wavefunction not only has to satisfy (1.7), but also (1.9). However, owing to the presence of the electron-electron repulsion terms in the Hamiltonian, the solutions of the eigenvalue Eqn. 1.7 cannot be obtained in closed form. We make approximations in its solution, providing simplified descriptions that incorporate the most relevant features of the electronic system.^{11a}

We define a *molecular orbital* as a single-electron wavefunction in a molecular system. A *spatial orbital* $\varphi_i(\mathbf{r})$ describes the spatial distribution of an electron in such a way that $\varphi_i^*(\mathbf{r}) \cdot \varphi_i(\mathbf{r}) d\mathbf{r}$ is the probability of finding the electron in a volume element $d\mathbf{r}$ surrounding \mathbf{r} . The description of the electronic spin is made by two orthogonal functions, $\alpha(\omega)$ and $\beta(\omega)$. The one-electron wavefunction that describes both spatial and spin distributions is a *spin orbital* $\chi_i(\mathbf{x})$. From each spatial orbital, two different spin orbitals can be formed:

$$\chi(\mathbf{x}) = \begin{cases} \varphi_i(\mathbf{r}) \cdot \alpha(\omega) \\ \varphi_i(\mathbf{r}) \cdot \beta(\omega) \end{cases} \quad (1.10)$$

For a fictitious system of N non-interacting electrons (this means neglecting the electron-electron repulsion terms in Eqn. 1.8), the exact wavefunction takes the form of a *Slater determinant*, i.e. an antisymmetric product of N spin molecular orbitals

$$\Psi_{el}(\mathbf{x}_1, \mathbf{x}_2, \dots, \mathbf{x}_N) = \frac{1}{\sqrt{N!}} \begin{vmatrix} \chi_i(\mathbf{x}_1) & \chi_j(\mathbf{x}_1) & \dots & \chi_k(\mathbf{x}_1) \\ \chi_i(\mathbf{x}_2) & \chi_j(\mathbf{x}_2) & \dots & \chi_k(\mathbf{x}_2) \\ \vdots & \vdots & & \vdots \\ \chi_i(\mathbf{x}_N) & \chi_j(\mathbf{x}_N) & \dots & \chi_k(\mathbf{x}_N) \end{vmatrix} \quad (1.11)$$

The single-Slater determinant incorporates *exchange correlation*, which means that the motion of two electrons with parallel spins is correlated.¹⁰ However, since the motion of electrons with opposite spins remains uncorrelated, it is common to refer to a single-determinant wavefunction as uncorrelated.

For a system of interacting electrons, the exact wavefunction is not a single-Slater determinant. Nevertheless, we may take this particularly simple form as an *ansatz* for an approximate description of the electronic system. To generate the best possible ground-state single-determinant wavefunction, we use the *variation principle*¹⁰ and minimize the expectation value of the Hamiltonian with respect to the one-electron molecular orbitals,

$$E = \min_{\chi_i(\mathbf{x})} \int \Psi_{el}^* \mathbf{H} \Psi_{el} d\mathbf{x}_1 d\mathbf{x}_2, \dots, d\mathbf{x}_N \geq E_{exact} \quad (1.12)$$

subject to the constraint that the set of orbitals $\{\chi(\mathbf{x})\}$ remains orthonormal. E_{exact} denotes the exact ground-state electronic energy and the ground-state eigenfunction Ψ_{el} is normalized.

The variational flexibility in the wavefunction is in the choice of the spatial orbitals. Within the linear combination of atomic orbitals (LCAO) approach, the molecular orbital $\varphi_i(\mathbf{r})$ is expanded in a set of K basis functions

$$\varphi_i(\mathbf{r}) = \sum_{\mu=1}^K C_{\mu i} \phi_{\mu}(\mathbf{r}) \quad (1.13)$$

In particular, $\phi_{\mu}(\mathbf{r})$ is referred to as an *atomic orbital*, that has associated with it some coefficient $C_{\mu i}$, and it is usually taken to be a finite set of simple analytical functions centered on the atomic nuclei.¹²

For a closed-shell system in which the molecular orbitals are of type (1.13), the one-electron density ρ_1 assumes the form²

$$\rho_1(\mathbf{r}) = \sum_{\mu=1}^K \sum_{\delta=1}^K \mathbf{P}_{\mu\delta} \phi_{\mu}^*(\mathbf{r}) \cdot \phi_{\delta}(\mathbf{r}) \quad (1.14)$$

where the matrix $\mathbf{P}_{\mu\delta}$ is the representation of the one-electron density matrix γ_1 in the basis $\{\phi(\mathbf{r})\}$ and is composed of the following elements:

$$\mathbf{P}_{\mu\delta} = 2 \sum_{i=1}^{N/2} C_{\mu i}^* C_{\delta i} \quad (1.15)$$

1.2.2. Hartree-Fock approximation

The Hartree-Fock procedure is the cornerstone of molecular wavefunction theory because it constitutes the starting point for more accurate approximations. To derive the Hartree-Fock equations, we replace the exact electron-electron repulsion term in Eqn. 1.8 by a “mean field” that each electron experiences due to the presence of the other electrons, and use the variational principle to minimize

the electronic energy of the molecular system with respect to the spin orbitals that compose the single-determinant wavefunction. This leads to a set of N one-electron eigenvalue equations, in which a given spin orbital $\chi_i(\mathbf{x})$ is an eigenfunction of its own operator \mathbf{f}_i ,¹⁰

$$\mathbf{f}_i \chi_i(\mathbf{x}) = \varepsilon_i \chi_i(\mathbf{x}) \quad (1.16)$$

The one-electron operator \mathbf{f}_i takes the form

$$\mathbf{f}_i = -\frac{1}{2} \nabla_i^2 - \sum_{k=1}^M \frac{Z_k}{|\mathbf{r}_i - \mathbf{R}_k|} + \mathbf{V}_i\{j\} \quad (1.17)$$

where $\mathbf{V}_i\{j\}$ represents an averaged interaction potential for the i -th electron with all the other $N - 1$ electrons. In fact, the essence of the Hartree-Fock method is to replace the N -electron problem by a set of N one-electron problems in which the electron-electron repulsion is treated only in average. The expression for $\mathbf{V}_i\{j\}$ can be found in textbooks.¹⁰ We just point out that it involves two terms. The first is a *Coulomb operator* interpreted as the electrostatic potential acting on the electron in the orbital χ_i , that arises from the remaining electrons in the other spin orbitals; the second term is an *exchange operator* that arises from correlation effects unique to electrons of the same spin.

The Hartree-Fock equation (1.16) is an eigenvalue problem with the spin orbitals as eigenfunctions and the corresponding energies as eigenvalues. The operator $\mathbf{V}_i\{j\}$ has a functional dependence on the set of N occupied spin orbitals. However, once $\mathbf{V}_i\{j\}$ is known, \mathbf{f}_i becomes well defined and (1.16) leads to an infinite number of eigenfunctions. The N spin orbitals with the lowest energies are the *occupied spin orbitals*, used to construct the ground-state single-determinant wavefunction according to (1.11), which we denote by Ψ_{HF} . The remaining unoccupied orbitals are *virtual spin orbitals*. Noteworthy, the expectation value of the total electronic energy for Ψ_{HF} is not just the sum of the individual occupied-orbital energies ε_i .¹⁰

Because the Hartree-Fock potential $\mathbf{V}_i\{j\}$ depends on the spin orbitals, the operator \mathbf{f}_i depends on its eigenfunctions. Therefore, (1.16) must be solved iteratively. The procedure is the *self-consistent field* (SCF) method. It consists of calculating $\mathbf{V}_i\{j\}$ by making an initial guess at orbitals in the form of Eqn. 1.13. Then, the eigenvalue problem (1.16) can be solved for a new set of orbitals. By using these new trial spin orbitals, new fields can be obtained. The procedure is repeated until self-consistency is reached, i.e. $\mathbf{V}_i\{j\}$ no longer change and the spin orbitals used to construct \mathbf{f}_i are the same as its eigenfunctions.

However, the exact solutions to (1.16), which correspond to the exact Hartree-Fock spin orbitals, cannot be obtained by introducing an uncomplete set of basis functions for expansion of the orbitals. Only as the basis set approaches completeness, will the obtained spin orbitals approach the exact Hartree-Fock spin orbitals. Using a basis set of K functions $\phi_\mu(\mathbf{r})$ results in a set of $2K$ spin orbitals. This leads to N occupied spin orbitals and a complementary set of $2K - N$ virtual orbitals. The single-Slater determinant formed from the occupied spin orbitals is the variational Hartree-Fock wavefunction of the ground state and constitutes the best approximation to the ground state of the molecular system of the single-determinant form.

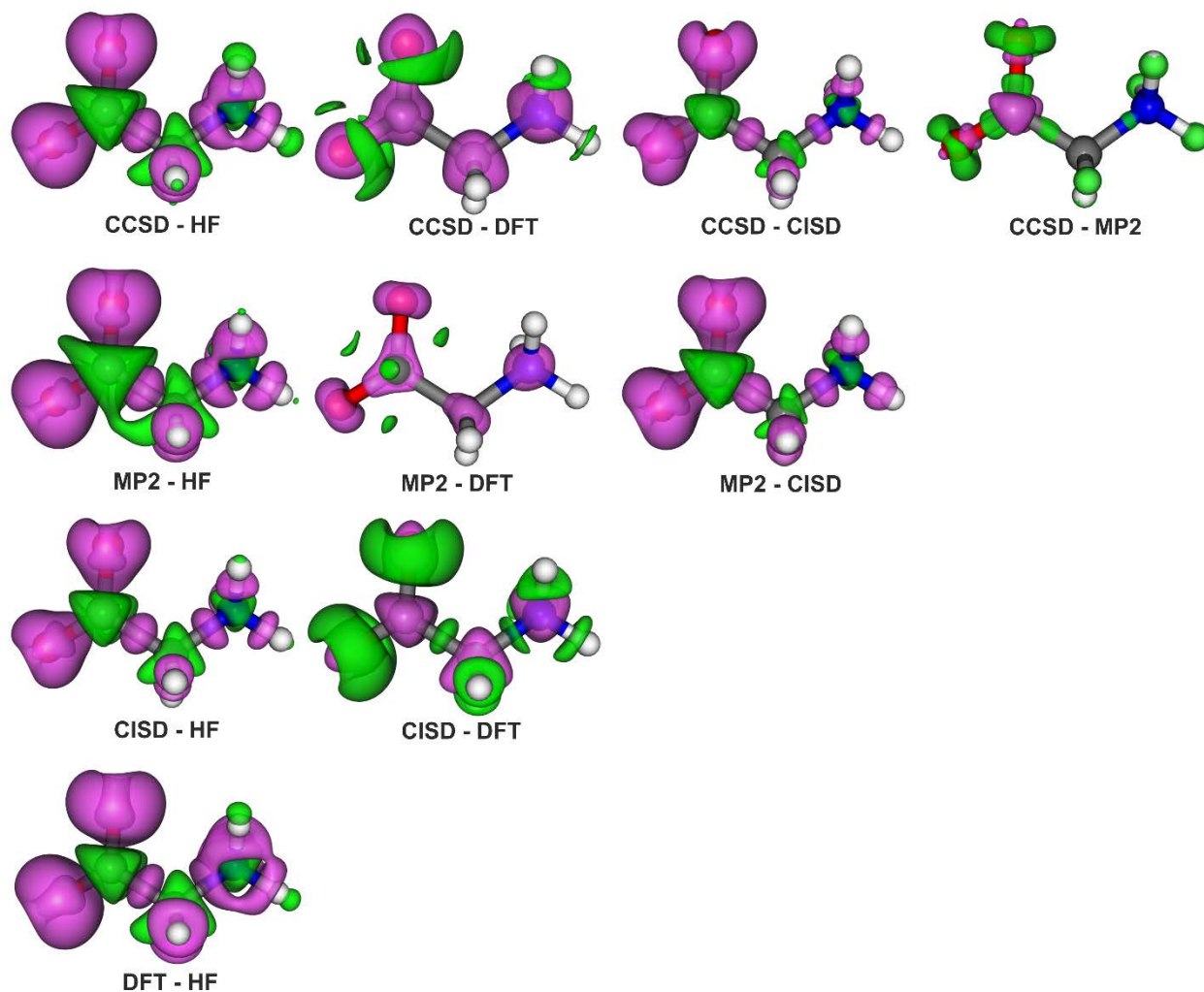


Figure 1.1. Electron density differences between some of the correlated and uncorrelated Hamiltonians considered in this work for the zwitterionic glycine molecule. Isodensity surfaces are shown at the values of ± 0.002 au, with the positive surface in green and the negative one in magenta. The d-aug-pVDZ basis set was used in all cases, and the DFT calculation was performed with the CAM-B3LYP hybrid functional.

Typical errors of the Hartree-Fock model are 0.5% in the total energy, 1% in bond distances and 5-10% in many other molecular properties such as dipole moments and force constants.^{11a} To improve upon this description, one must take into account the instantaneous correlation among the electrons. However, this is usually very computationally demanding and the Hartree-Fock procedure is still the choice for various larger molecular systems.

Nevertheless, electronic correlation is significant to accurate estimations of electron density distributions. As shown in Fig. 1.1 for the glycine molecule, the usual effect of correlation is to deplete electron density from the chemical bonds and the lone pairs, and to increase it around the atomic nuclei and at the periphery of the molecules.^{11b-d}

1.2.3. Correlated methods

Within the LCAO, the Hartree-Fock procedure leads to $2K$ spin orbitals, the ground state being constructed from the subset of the N occupied ones. However, this is only one of many determinants that can be formed from the $2K > N$ spin orbitals. To produce the other determinants, we consider

the Hartree-Fock ground state as a reference and describe the other determinants in terms of electronic excitations from the occupied to the virtual spin orbitals.¹⁰ These determinants can be used in linear combination with Ψ_{HF} for a more accurate description of the ground state of the electronic system.

If we denote the occupied orbitals by $\{\chi_a, \chi_b, \dots\}$ and the virtual spin orbitals as $\{\chi_r, \chi_s, \dots\}$, a singly excited determinant is one in which an electron occupying χ_a in the ground state is promoted to χ_r . This is denoted by Ψ_a^r . Analogously, a doubly excited determinant is Ψ_{ab}^{rs} . Therefore, all possible determinants can be classified as either the ground state or singly, doubly, triply, ..., excited states.

The *configuration interaction* (CI) method is based on excited determinants as basis functions for the expansion of the exact states of the N -electron system. Within the one-electron subspace spanned by the $2K$ spin orbitals, the exact wavefunction for any state of the system can be written as

$$\Psi_{CI} = c_0 \Psi_{HF} + \sum_{a=1}^N \sum_{r=1}^{2K} c_a^r \Psi_a^r + \sum_{a<b}^N \sum_{r<s}^{2K} c_{ab}^{rs} \Psi_{ab}^{rs} + \sum_{a<b<c}^N \sum_{r<s<t}^{2K} c_{abc}^{rst} \Psi_{abc}^{rst} + \dots \quad (1.18)$$

where $c_0, c_a^r, c_{ab}^{rs}, c_{abc}^{rst}, \dots$ are coefficients to be variationally determined, and the restrictions on the summation indices ensure that a given excited determinant is included only once.

The extremely large number of excited determinants to be included in (1.18) prevents the application of the so-called *full-CI* method for most systems, even for small molecules and minimal basis sets. Thus, in practice one truncates the full-CI expansion and uses only a small number of possible determinants. The importance of these determinants as approximate representations of the true states diminishes with the number of excitations. Therefore, the most important determinants are certainly the singly and doubly excited ones.^{10,11a} The corresponding approaches are called CI singles (only singly excited determinants, CIS), CI doubles (double excitations only, CID) and CI singles and doubles (both single and double excitations, CISD). Because the Hartree-Fock ground state is unaffected by the inclusion of single excitations alone*, CIS finds no application for ground states, although it can be useful for describing the excited states of a system. According to these definitions, the CISD expansion corresponds to

$$\Psi_{CISD} = c_0 \Psi_{HF} + \sum_{a=1}^N \sum_{r=1}^{2K} c_a^r \Psi_a^r + \sum_{a<b}^N \sum_{r<s}^{2K} c_{ab}^{rs} \Psi_{ab}^{rs} \quad (1.19)$$

The CID and CISD methods usually recover 80-90% of the correlation energy while errors for many molecular properties are usually around 5%.¹⁰ The next levels of improvement are inclusion of the triply and quadruply excited determinants, thus giving the CISDT and CISDTQ methods. The latter gives results quite close to the full-CI limit, but truncating the excitations at fourth order produces so many configurations that it can only be applied to small molecules.

*One might expect the singly excited determinants to give the leading corrections to the ground state. However, if one considers only the single excitations, then the variationally determined coefficients c_a^r are all zero. The Hartree-Fock ground state cannot be improved by mixing it with singly excited determinants only. Thus, the double excitations provide the leading corrections to Ψ_{HF} . This result is the Brillouin's theorem.

In truncated-CI descriptions, double or higher excitations are not allowed to occur as a result of applying lower excitations multiple times to the ground state. For example, in the CISD description, double excitations do not occur due to pairs of single excitations. These subtle features are included in a related series, called *coupled-cluster* (CC).^{10,11a} The CC approach leads to the following expansion up to doubly excited determinants :

$$\begin{aligned} \Psi_{CCSD} = & c_0 \Psi_{HF} + \sum_{a=1}^N \sum_{r=1}^{2K} c_a^r \Psi_a^r + \sum_{a<b}^N \sum_{r<s}^{2K} (c_a^r c_b^s + c_{ab}^{rs}) \Psi_{ab}^{rs} \\ & + \sum_{a<b<c}^N \sum_{r<s<t}^{2K} (c_a^r c_{ab}^{st} + c_a^r c_b^s c_c^t) \Psi_{abc}^{rst} \\ & + \sum_{a<b<c<d}^N \sum_{r<s<t<u}^{2K} (c_{ab}^{rs} c_{cd}^{tu} + c_a^r c_b^s c_{cd}^{tu} + c_a^r c_b^s c_c^t c_d^u) \Psi_{abcd}^{rstu} + \dots \end{aligned} \quad (1.20)$$

The CCS description, similarly to CIS, is not of interest to us. In Eqn. 1.20, $c_{ab}^{rs} \Psi_{ab}^{rs}$ is known as a *connected cluster*, while $c_a^r c_b^s \Psi_{ab}^{rs}$ is an *unconnected* one. In CCSD, all clusters involving three or more electrons are disconnected. The compact description of the disconnected processes as products renders to CC the key to its success compared to CI, where all excitations are either described as connected clusters, or not described at all. At the limit of no truncation, the CC and CI wavefunctions become equivalent, differing only in their parameterization. In this situation, the CI linear parameterization is usually preferable to the CC non-linear one.^{10d,11a}

The CCSD level of theory is able to describe the most important correlation effects in the electronic system. At this level, the errors in the correlation energy typically reduce to less than 10% and many molecular properties can be described within 3-5% of accuracy. At the next level, connected triple excitations are introduced, arriving at the CCSDT level of theory, often sufficient for full agreement with experiments. If needed, further improvements are in principle possible, although not always in practice. This includes connected quadruple or quintuple excitations at the CCSDTQ and CCSDTQ5 levels of theory.^{10d}

The coefficients of coupled-cluster wavefunctions are not determined variationally, but by application of a non-variational iterative projection technique.^{10d} To further reduce the computational costs and extend the applications of CC, they are sometimes determined by perturbation methods. Thus, at the CCSD(T) level of theory, the coefficients relative to the single and double excitations are generated iteratively in the usual projective manner, whereas the more expensive connected triple excitations are determined by perturbation theory. It has been demonstrated that this approach introduces an error of about 10% in the description of the triply excited determinants.^{11a} However, because triple excitations are a rather small correction to the CCSD description, this error is of little importance.

Independently, perturbative methods can be seen as alternatives to CI and CC. In particular, we consider the perturbation theory due to C. Møller and M. S. Plesset, called *MP perturbation theory*.¹⁰ It is referred to by the acronym MP_n , where n is the order at which the perturbation is truncated. The Hartree-Fock energy corresponds to the MP energy corrected through first-order. Therefore, MP1 does not advance beyond the Hartree-Fock level and MP2 provides the leading term for estimate the correlation energy.

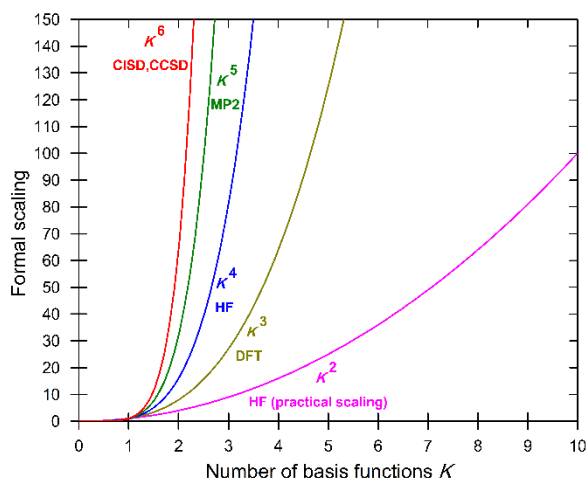


Figure 1.2. Scaling of the computational methods used in this work as a function of the number of basis functions. For Hartree-Fock, the formal scaling is also compared to the practical one, typically observed. Several of the post-Hartree-Fock methods become prohibitively costly as the basis-set rank increases.

The fundamental problem with MP theory is that only low-order perturbation can be carried out, because if taken to sufficiently high order, it usually diverges, i.e. it does not approach the full-CI limit as the description is refined. It is understood that, for sufficiently large basis sets, MP3 and MP4 are typically very accurate and that MP2 usually overestimates the correlation effects. However, in cases where moderate-sized basis sets are used, MP2 often gives better answers than MP3.

For accurate calculation of properties, it is necessary to carry out sequence of electronic calculations where the flexibility of the N -electron descriptions and the one-electron basis sets is systematically explored, and the convergence of the property is carefully monitored. In the N -electron description, improvements are obtained by including higher excitations in the wavefunction. In terms of computational cost, Fig. 1.2 shows the scaling for the post-Hartree-Fock methods discussed in this section.

The electron density accumulation observed in the bonds and lone pairs of molecules calculated at the Hartree-Fock level typically diminishes as the level of electronic correlation is increased.^{11b-d} In Fig. 1.1, having CC electron densities as benchmark, it is clear that CISD gives too small shifts of electronic charge to the nuclei. In fact, significant electron density is still accumulated at the oxygen lone pairs, see CCSD – CISD difference in that picture. Conversely, MP2 tends to exaggerates the shift of density from bond and lone-pair regions to nuclei, see CCSD – MP2 difference.

1.2.4. Density functional theory

A different route to the molecular electronic problem is provided by *density functional theory* (DFT). All information about the electronic system is extracted from the electron density distribution, rather than from the wavefunction. DFT is based on the Hohenberg-Kohn theorems, according to which the one-electron density uniquely defines the ground-state energy and the corresponding properties of an electronic system.^{13a} Therefore, the electronic energy is regarded as a functional of the one-electron density, $E[\rho_1(\mathbf{r})]$, in the sense that there is a one-to-one correspondence between $\rho_1(\mathbf{r})$ and E .

Current applications are based on the formalism developed by W. Kohn and L. J. Sham.^{13b} They provided a practical manner to solve the Hohenberg-Kohn theorems for a set of interacting electrons starting from a fictitious system of non-interacting electrons for which the ground-state electron density equals the density of some real system of interest where electrons do interact. Following the orbital formulation of the Kohn-Sham approach, the ground-state electronic energy is¹⁰

$$E[\rho_1(\mathbf{r}_1)] = -\frac{1}{2} \sum_{i=1}^N \int \varphi_i^*(\mathbf{r}_1) \nabla_i^2 \varphi_i(\mathbf{r}_1) d\mathbf{r}_1 - \sum_{k=1}^M \int \frac{Z_k}{|\mathbf{r}_1 - \mathbf{R}_k|} \rho_1(\mathbf{r}_1) d\mathbf{r}_1 + \frac{1}{2} \int \frac{\rho_1(\mathbf{r}_1) \rho_1(\mathbf{r}_2)}{|\mathbf{r}_1 - \mathbf{r}_2|} d\mathbf{r}_1 d\mathbf{r}_2 + E^{XC}[\rho_1(\mathbf{r}_1)] \quad (1.21)$$

The first term represents the kinetic energy of the non-interacting electrons, the second term accounts for the nucleus-electron interactions, and the third term corresponds to the electrostatic repulsions between the charge distributions at \mathbf{r}_1 and \mathbf{r}_2 . The fourth term, known as exchange-correlation term, accounts for the correlation arising from the interacting nature of the electrons and all non-classical corrections to the electron-electron repulsion energy. The challenge in DFT is the accurate description of $E^{XC}[\rho_1(\mathbf{r}_1)]$.¹⁴

The Kohn-Sham orbitals $\varphi_i(\mathbf{r})$ are determined by solving equations that assume the form of (1.16). Similar to the Hartree-Fock procedure, the Kohn-Sham equations are derived by applying the variational principle to $E[\rho_1(\mathbf{r})]$.^{14a} The Kohn-Sham Hamiltonian \mathbf{f}_i^{KS} can be written as

$$\mathbf{f}_i^{KS} = -\frac{1}{2} \nabla_i^2 - \sum_{k=1}^M \frac{Z_k}{|\mathbf{r}_i - \mathbf{R}_k|} + \int \frac{\rho_1(\mathbf{r}_2)}{|\mathbf{r}_i - \mathbf{r}_2|} d\mathbf{r}_2 + \mathbf{V}_i^{XC}\{j\} \quad (1.22)$$

where $\mathbf{V}_i^{XC}\{j\}$ is a so-called functional derivative.¹⁴ The solution of the Kohn-Sham equations proceeds in a self-consistent fashion, starting from a trial electron density. An approximate form of the functional describing the dependence of E^{XC} on the electron density is used to calculate \mathbf{V}_i^{XC} . Although exact DFT is variational, this is not true once approximations to E^{XC} are adopted. The exchange-correlation energy is typically divided into two separate terms, an exchange $E^X[\rho_1]$ and a correlation $E^C[\rho_1]$ contribution. Both are themselves functionals of the density and can be either local or gradient corrected.^{14b}

The *local density approximation* (LDA) is the simplest approach to represent the exchange-correlation energy. It assumes that E^{XC} at any point in space is a function of ρ_1 at that point only, and it is given by the electron density of a corresponding homogeneous electron gas. The approach usually refers to the exchange functional of Slater and to the correlation functional proposed by Vosko, Wilk and Nusair.¹⁵

However, molecular systems are different from a homogeneous electron gas because they have spatial varying electron densities. *Generalized gradient approximations* (GGA) take into account this feature by making E^{XC} dependent not only on ρ_1 but also on its gradient $\nabla\rho_1(\mathbf{r})$. These semi-local approximations represent significant improvements over local approaches but they are usually still not enough for accurate description of many molecular properties.^{14b} Recently, a new class of functionals based on GGAs was developed by including additional non-local information beyond $\nabla\rho_1(\mathbf{r})$. These methods, termed meta-GGAs (M-GGAs), represent significant improvement in the accuracy of several properties, with performances sometimes comparable to hybrid functionals.

Hybrid density functionals, H-GGAs, combine E^{XC} of a conventional GGA with a percentage of Hartree-Fock exchange. The weight factor for the components of the functionals that are mixed is fitted semi-empirically for a representative set of molecules.^{10b} These functionals have allowed tremendous improvement over GGAs, with accuracy often comparable to that of post-Hartree-Fock methods. Hybrid meta-GGA methods (HM-GGAs) comprise a new class of functionals based on a similar concept to meta-GGAs, with the difference of deriving from M-GGAs rather than GGA functionals.

For the treatment of all but the smallest systems, non-covalent interactions play important role for structure, energetics and various properties. In general, although hybrid functionals normally give reliable results for covalent and hydrogen bonds, a crucial drawback of all local and semi-local DFT formulations is their inability to provide the correct dependence of the dispersion interaction energy on the interatomic and intermolecular distances. Several approaches have been developed to tackle this problem.¹⁶ In this work, we use only two widely accepted methods (see Chapter 2), but a systematic investigation on the accuracy of the available schemes is highly desirable, in particular for electric properties like dipole moments and polarizabilities.

Finally, we carefully note that, unlike post-Hartree-Fock methods, no procedure has been devised for improving the approximate DFT energy functionals in a systematic, controlled manner, making possible to improve the description of the system towards the exact solution. In view of this drawback, the electron density generated by DFT has been systematically studied by comparison with post-Hartree-Fock methods, in an attempt to identify the correlation effects that are covered by particular density functionals.¹⁷ Fig. 1.1 indicates that some functionals, in particular CAM-B3LYP, are able to provide electron densities very similar to those calculated using highly correlated Hamiltonians.

Because DFT methods provide a very efficient manner to include electronic correlation effects, though in a rather incomplete empirical approach, it is desirable to identify the most accurate functionals able to estimate materials properties, using calculations of high-level electronic correlation as benchmarks. For many systems, it has been founded that the accuracy of post-Hartree-Fock methods is not sufficiently higher than that of DFT to justify the tremendous increase in computational cost. Thus, the approach used in Chapter 2 is to benchmark DFT formulations against highly correlated methods in order to select the most efficient density functional for calculation of polarizabilities, i.e. to select the functional that maximizes the accuracy/cost ratio for this property.

1.2.5. Periodic boundary conditions

Because the potential energy of an infinite crystal is a periodic function with the same periodicity as the crystal lattice, the Schrödinger equation for such system must also be translation invariant. This is equivalent to the requirement that after a translation by any direct-lattice vector \mathbf{g} , the solutions of the equation

$$\mathbf{H}(\{\mathbf{r} - \mathbf{g}\}; \{\mathbf{R} - \mathbf{g}\})\Psi_{el}(\{\mathbf{r} - \mathbf{g}\}; \{\mathbf{R} - \mathbf{g}\}) = E\Psi_{el}(\{\mathbf{r} - \mathbf{g}\}; \{\mathbf{R} - \mathbf{g}\}) \quad (1.23)$$

coincide with those of Eqn. 1.7, when a periodic potential is assumed.

It has been demonstrated that the eigenfunctions of (1.23) must also obey the Bloch theorem:¹⁸

$$u(\mathbf{r} + \mathbf{g}; \mathbf{k}) = e^{i\mathbf{k}\cdot\mathbf{g}}u(\mathbf{r}; \mathbf{k}) \quad (1.24)$$

This equation provides a relationship between the values of an eigenfunction at equivalent points in the crystal lattice and indicates that its periodicity is generally different from that of the lattice. A function that satisfies (1.24) is called *Bloch function* and depends not only on the \mathbf{r} position, but also on the reciprocal space *wave vector* \mathbf{k} , which is a parameter labelling different solutions.

Fortuitously, the use of Bloch functions as basis set allows one to solve the Schrödinger equation for a periodic system in reciprocal space at a finite number of \mathbf{k} points. The solutions $\{\varphi(\mathbf{r}; \mathbf{k})\}$ are called crystalline orbitals and are linear combinations of one-electron Bloch functions u_μ :

$$\varphi_i(\mathbf{r}; \mathbf{k}) = \sum_{\mu=1}^K C_{\mu i}(\mathbf{k})u_\mu(\mathbf{r}; \mathbf{k}) \quad (1.25)$$

In principle, if an infinite basis set was considered, atomic orbitals and plane waves would be equivalent choices to represent Bloch functions, but they are not equivalent in the practical case of finite basis. In this work, we prefer the use of atomic orbitals because they are linked to the chemical concept of a crystal composed by its building blocks: atoms, functional groups and molecules. The one-electron local basis sets used in periodic calculations are similar to that used in molecular calculations, with the additional requirement that $u_\mu(\mathbf{r}; \mathbf{k})$ must obey (1.24).^{18a}

For practical reasons, most of the periodic calculations are performed within DFT approaches but the debate is still open about the most appropriate functionals to be applied for different properties and chemical systems. LDA is still popular, as well as various GGA and H-GGA methods. In a few cases, Hartree-Fock is preferred. Perturbation theory applied to these wavefunctions are possible, but at enormous computational costs.^{18b}

Present first-principles implementations for periodic systems have provided valuable information on $\rho_1(\mathbf{r})$, but also on the full γ_1 matrix.¹⁹ This helps crystallographers for the analysis and interpretation concerning Bragg peaks and Compton profiles, including their dependence on non-ambient

conditions, such as pressure, electric and magnetic fields, and mechanical stress. However, discrepancies from experiment require advanced description of the Hamiltonians, in particular the inclusion of excited determinants in the frame of post-Hartree-Fock procedures. Larger atomic basis sets are sometimes required, in particular for accurate estimation of electric properties. Plane waves provide a reference in this respect. Results based on atomic orbitals can approach the plane-wave results only when extensive sets, including polarization and possibly diffuse functions, are used.

1.2.6. Calculations under electric fields

A number of molecular properties, including (hyper)polarizabilities, can be formulated in terms of derivatives of the energy E , with respect to perturbation parameters.^{10c} In general, let us write E as a Taylor expansion in some perturbation vector \mathbf{X} :

$$E(\mathbf{X}) = E(\mathbf{0}) + \left. \frac{\partial E}{\partial \mathbf{X}} \right|_{\mathbf{X}=\mathbf{0}} \cdot \mathbf{X} + \frac{1}{2!} \left. \frac{\partial^2 E}{\partial \mathbf{X}^2} \right|_{\mathbf{X}=\mathbf{0}} \cdot \mathbf{X}^2 + \frac{1}{3!} \left. \frac{\partial^3 E}{\partial \mathbf{X}^3} \right|_{\mathbf{X}=\mathbf{0}} \cdot \mathbf{X}^3 + \dots \quad (1.26)$$

If \mathbf{X} refers to an electric field applied to the molecule, the first derivative defines the permanent dipole moment $\boldsymbol{\mu}$, the second derivative defines the polarizability $\boldsymbol{\alpha}$, the third derivative defines the first-order hyperpolarizability $\boldsymbol{\beta}$, and so on.

Derivative techniques consider the energy in the presence of the perturbation \mathbf{X} , perform differentiation of the energy n times to derive the n th-order property, and make the perturbation strength go to zero.^{10c} This can be done either analytically or numerically.

Because differentiation of the energy with respect to a perturbation is equivalent to differentiation of the expectation value of the corresponding Hamiltonian, Eqn. 1.26 provide a simple manner to calculate many properties through numerical differentiation. All that is required is a calculation of the energy in the absence of the perturbation, and a modification of the Hamiltonian to include the perturbation.^{10b} For example, the first derivative in 1.26 can be computed as

$$\left. \frac{\partial E}{\partial \mathbf{X}} \right|_{\mathbf{X}=\mathbf{0}} = \frac{\partial}{\partial \mathbf{X}} \langle \Psi_{el} | \mathbf{H}' | \Psi_{el} \rangle |_{\mathbf{X}=\mathbf{0}} = \lim_{\mathbf{X} \rightarrow 0} \frac{\langle \Psi_{el} | \mathbf{H}' | \Psi_{el} \rangle - \langle \Psi_{el} | \mathbf{H} | \Psi_{el} \rangle}{\mathbf{X}} \quad (1.27)$$

where \mathbf{H} is the perturbation-free Hamiltonian, \mathbf{H}' includes the perturbation operator, and the expectation values are written using Dirac notation.^{10a}

This procedure is called *finite-field approach* and (1.27) must be solved for each component of the particular property, which is generally a tensor. Of course, the approach can be easily generalized for higher derivatives.

Computationally, it is usually more convenient to derive analytic expressions that allow direct calculation of higher-order energy derivatives. In the framework of the so-called *coupled-perturbed Hartree-Fock* procedure (CPHF), this can be done by, additionally to the energy expression (1.26), expanding also the Hartree-Fock Hamiltonian and its eigenfunctions in terms of the perturbation

parameter \mathbf{X} .^{10c} The perturbed molecular orbitals $\{\varphi'\}$ are given by a simple unitary transformation of the unperturbed orbitals:

$$\varphi'_i(\mathbf{r}) = \sum_{j=1}^K U_{ji} \varphi_j(\mathbf{r}) \quad (1.28)$$

The U_{ji} matrix elements describes how the molecular orbitals $\varphi_j(\mathbf{r})$ change upon perturbation, i.e.

$$\varphi_j(\mathbf{r}) \rightarrow \mathbf{X} \sum_{j=1}^K U_{ji}^{(1)} \varphi_j(\mathbf{r}) + \mathbf{X}^2 \sum_{j=1}^K U_{ji}^{(2)} \varphi_j(\mathbf{r}) + \mathbf{X}^3 \sum_{j=1}^K U_{ji}^{(3)} \varphi_j(\mathbf{r}) + \dots \quad (1.29)$$

where $U_{ji}^{(n)}$ are the elements that characterize the n th-order unitary matrix $\mathbf{U}^{(n)}$. These elements contain the derivatives of the molecular orbitals with respect to the perturbation and can be expressed in closed form as functions of the atomic orbital expansion (1.13). The size of $\mathbf{U}^{(n)}$ is the number of occupied molecular orbitals times the number of virtual orbitals, but the CPHF equations are linear and can be solved by standard iterative procedures.^{10c}

There is one CPHF equation to be solved for each perturbation. In the case \mathbf{X} is a homogeneous electric field, i.e. $\mathbf{X} = X\mathbf{r}$, there will be in general three equations. In this case, the perturbation operator that augments the Hamiltonian \mathbf{H} to produce \mathbf{H}' will be simply \mathbf{r} . The permanent dipole moment $\boldsymbol{\mu}$ is shown to be:^{10c}

$$\boldsymbol{\mu} = -\left. \frac{\partial E}{\partial \mathbf{X}} \right|_{\mathbf{X}=\mathbf{0}} = -\langle \Psi_{el} | \mathbf{r} | \Psi_{el} \rangle - 2 \left\langle \frac{\partial \Psi_{el}}{\partial \mathbf{X}} \middle| \mathbf{H} \middle| \Psi_{el} \right\rangle \quad (1.30)$$

Eqn. 1.30 reduces to the well-known quantum-mechanical expression for the dipole moment as soon as the basis functions are independent of the electric field, which is normally the case for small field magnitudes. This equation holds for Hartree-Fock and all correlated wavefunctions previously discussed. However, the analytical expression for second order properties, in particular the polarizability $\boldsymbol{\alpha}$, depends on whether the wavefunction is variationally optimized with respect to *all* parameters or not. This is indeed the case for Ψ_{HF} , and $\boldsymbol{\alpha}$ is expressed as^{10c}

$$\boldsymbol{\alpha} = -\left. \frac{\partial^2 E_{HF}}{\partial \mathbf{X}^2} \right|_{\mathbf{X}=\mathbf{0}} = -2 \left\langle \frac{\partial \Psi_{HF}}{\partial \mathbf{X}} \middle| \mathbf{r} \middle| \Psi_{HF} \right\rangle \quad (1.31)$$

Eqn. 1.31 shows that only the first-order change in Ψ_{HF} is necessary. For wavefunctions not completely optimized with respect to all parameters, CI, CC and MP, the second derivative of the energy assumes the more general form^{10c}

$$\frac{1}{2} \frac{\partial^2 E}{\partial \mathbf{X}^2} \Big|_{\mathbf{x}=0} = \left\langle \frac{\partial^2 \Psi_{el}}{\partial \mathbf{X}^2} \Big| \mathbf{H} \Big| \Psi_{el} \right\rangle + 2 \left\langle \frac{\partial \Psi_{el}}{\partial \mathbf{X}} \Big| \mathbf{r} \Big| \Psi_{el} \right\rangle + \left\langle \frac{\partial \Psi_{el}}{\partial \mathbf{X}} \Big| \mathbf{r} \Big| \frac{\partial \Psi_{el}}{\partial \mathbf{X}} \right\rangle \quad (1.32)$$

This expression can be computed analytically only for methods for which second derivatives of Ψ_{el} are available in closed form. This usually excludes CI and CC methods.

Finally, we note that the CPHF procedure may be generalized to higher order. Extending the expansion to third-order allows one to derive an equation for the third-order change in the molecular orbitals, which yields the hyperpolarizability β . Analogous formulation for DFT yields the coupled-perturbed Kohn-Sham equations.^{10c}

1.2.7. Open-shell determinants and spin operators

So far, we have described the electronic spin by two spin functions, $\alpha(\omega)$ and $\beta(\omega)$, and considered *restricted Slater determinants* that are formed from two spin orbitals whose spatial parts are restricted to be the same, see Eqn. 1.10. Furthermore, Eqn. 1.14 that gives $\rho_1(\mathbf{r})$ in terms of atomic orbitals is valid only for *closed-shell determinants*, those in which each spatial orbital $\varphi_i(\mathbf{r})$ is doubly occupied. In view of the *open-shell* systems considered in Chapter 3, we now discuss spin in some detail and generalize (1.14) for open-shell determinants.

The spin angular momentum of a single electron is the vector operator^{10a}

$$\mathbf{s} = s_x i + s_y j + s_z k \quad (1.33)$$

in Cartesian coordinate system. The squared magnitude of \mathbf{s} is the scalar operator \mathbf{s}^2 . The spin functions characterizing the complete set of spin states of the electron are simultaneous eigenfunctions of \mathbf{s}^2 and a single component of \mathbf{s} , say s_z . That is

$$\begin{aligned} \mathbf{s}^2 \tau_s^{m_s}(\omega) &= s(s+1) \tau_s^{m_s}(\omega) \\ s_z \tau_s^{m_s}(\omega) &= m_s \tau_s^{m_s}(\omega) \end{aligned} \quad (1.34)$$

where the eigenvalues are characterized by the quantum numbers s , which describes the total spin of the electron ($s = 1/2$) and m_s , which describes only its z spin-component ($m_s = \pm 1/2$). Thus, the complete set of spin states for the single electron is simply $\{\tau_{s=1/2}^{m_s=1/2}, \tau_{s=1/2}^{m_s=-1/2}\} = \{\alpha, \beta\}$. For an N -electron system, the total spin angular momentum operator \mathbf{S} is the vector sum of the spin vectors \mathbf{s} of each electron:^{10a}

$$\mathbf{S} = \sum_{i=1}^N \mathbf{s}(i) \quad (1.35)$$

Of course, this equation implies that \mathbf{S}_z is simply the sum of the \mathbf{s}_z component of each electron. The squared magnitude of the total spin is

$$\mathbf{S}^2 = \sum_{i=1}^N \sum_{j=1}^N \mathbf{s}(i) \cdot \mathbf{s}(j) \quad (1.36)$$

In the nonrelativistic treatment, the exact eigenfunctions $\Psi_{el}(\{\mathbf{x}\})$ of the Hamiltonian operator (1.8) are also eigenfunctions of \mathbf{S}^2 and \mathbf{S}_z :

$$\begin{aligned} \mathbf{S}^2 \Psi_{el,S}^{M_S}(\{\mathbf{x}\}) &= S(S+1) \Psi_{el,S}^{M_S}(\{\mathbf{x}\}) \\ \mathbf{S}_z \Psi_{el,S}^{M_S}(\{\mathbf{x}\}) &= M_S \Psi_{el,S}^{M_S}(\{\mathbf{x}\}) \end{aligned} \quad (1.37)$$

where S and M_S are the quantum numbers describing the total spin and its z component of the particular N -electron state $\Psi_{el,S}^{M_S}(\{\mathbf{x}\})$. The number S assumes one of the values $0, 1/2, 1, 3/2, \dots$, while M_S assumes $2S+1$ values, $-S, -S+1, -S+2, \dots, S-2, S-1, S$. The state characterized by a particular S is said to have multiplicity $2S+1 = 1, 2, 3, \dots$ and it is called singlet, doublet, triplet, ..., accordingly. However, we note that, unlike the exact wavefunctions $\Psi_{el,S}^{M_S}$, approximate solutions of the Schrödinger equation, in particular single-Slater determinants, are not necessarily pure spin states, i.e. they are not necessarily eigenfunctions of \mathbf{S}^2 and \mathbf{S}_z simultaneously.

It is usual to refer to Slater determinants by the number of open shells they contain. Because all the electron spins are paired in a closed-shell determinant, it is not surprising that it is in fact a pure singlet state. Open-shell determinants, on the other hand, are generally not eigenfunctions of \mathbf{S}^2 . However, for open-shell restricted determinants, it is usually possible to form *spin-adapted configurations* that are eigenfunctions of \mathbf{S}^2 by taking appropriate linear combinations of non-pure spin states.^{10a} Unrestricted determinants cannot be spin-adapted. For this reason, they are said to be *spin-contaminated* solutions.

Unrestricted determinants are formed from spin orbitals having different spatial orbitals for different spins. Given two sets of K orthonormal spatial orbitals $\{\varphi^\alpha(\mathbf{r})\}$ and $\{\varphi^\beta(\mathbf{r})\}$, one can form an orthonormal set of $2K$ unrestricted spin orbitals:

$$\chi(\mathbf{x}) = \begin{cases} \varphi_i^\alpha(\mathbf{r}) \cdot \alpha(\omega) \\ \varphi_i^\beta(\mathbf{r}) \cdot \beta(\omega) \end{cases} \quad (1.38)$$

It is possible to show that unrestricted wavefunctions can be expanded in terms of pure spin states of higher multiplicities,^{10a} thus the expectation value of \mathbf{S}^2 for an unrestricted solution is always too large because the contaminant spin states have larger values of S . In spite of spin contamination, unrestricted determinants are often used as first approximations for pure spin states with $S \geq 2$ because they certainly have lower energies than the corresponding restricted wavefunctions. Afterwards, the contaminations can be minimized, typically using annihilation operators.^{10b}

For unrestricted wavefunctions, because electrons with α and β spin have different spatial distributions, it is convenient to define the one-electron spin density $\rho_1^S(\mathbf{r})$ according to (1.6). The generalization of (1.14) and (1.15) is straightforward, and it yields the following representation of $\rho_\alpha(\mathbf{r})$ and $\rho_\beta(\mathbf{r})$ in the basis of the atomic orbitals $\{\phi(\mathbf{r})\}$:

$$\rho_\tau(\mathbf{r}) = \sum_{\mu=1}^K \sum_{\delta=1}^K \mathbf{P}_{\mu\delta}^\tau \phi_\mu^*(\mathbf{r}) \cdot \phi_\delta(\mathbf{r}), \quad \tau = \alpha, \beta \quad (1.39)$$

where the density matrices $\mathbf{P}_{\mu\delta}^\tau$ are defined as:

$$\mathbf{P}_{\mu\delta}^\tau = \sum_{i=1}^{N_\tau} C_{\mu i}^{*\tau} C_{\delta i}^\tau, \quad \tau = \alpha, \beta \quad (1.40)$$

In the basis of the $\{\phi(\mathbf{r})\}$ orbitals, $\rho_1(\mathbf{r})$ and $\rho_1^S(\mathbf{r})$ are simply:

$$\begin{aligned} \rho_1(\mathbf{r}) &= \mathbf{P}^\alpha + \mathbf{P}^\beta \\ \rho_1^S(\mathbf{r}) &= \mathbf{P}^\alpha - \mathbf{P}^\beta \end{aligned} \quad (1.41)$$

1.3. Electron densities from high-resolution X-ray diffraction

The X-ray diffraction experiment do not provide directly the one-electron density of a crystalline material because only a finite number of structure factors can be collected and their phases cannot be measured. Therefore, $\rho_1(\mathbf{r})$ is usually reconstructed by fitting a model against the collected intensities. In this section, we discuss how this can be done within the kinematic approximation.

1.3.1. Elastic X-ray scattering and the independent-atom formalism

Upon interaction with crystalline matter, X-ray photons are either scattered or absorbed by its constituent atoms.^{20a} However, it is usually convenient to treat the material as a purely mathematical space lattice, consisting of identical scattering points. When plane waves sweep through, each lattice point becomes the source of spherically scattered waves whose amplitude diminishes as the distance to the point increases. This phenomenon yields non-negligible intensities only in discrete directions, due to constructive and destructive interference of the wavelets scattered by different lattice points, and it can be expressed by the Laue equations.^{20b,c} The resulting scattered intensity in a particular direction can only be predicted when the lattice points are replaced by the actual group of atoms that form each unit cell of the crystal structure.

In most that follows, we consider the incident X-ray waves hardly modified by the crystal as they passes through. This condition is called *kinematical approximation* and neglects multiple-scattering effects that may become important.^{20a} Furthermore, we suppose that no absorption either of the incident or

the scattered radiation takes place within the crystal. Finally, we are mainly interested in the elastic and coherent scattering.

Quantum-mechanically, the total scattering of an X-ray photon by a single atom contains both elastic and inelastic components. The inelastic, incoherent scattering is known as the Compton effect and, as anticipated in section 1.1, can be used to model the off-diagonal terms of the first-order density matrix γ_1 . The formalism of Compton scattering can be found in textbooks²⁰ and it is not further considered here. Instead, the electric-field vector scattered elastically by a free particle of mass m and electric charge e in a direction defined by the polar angle ϕ and at a distance R from the particle was first given by J. J. Thomson as^{20b}

$$\mathbf{E}(\phi, t) = \mathbf{E}_0 \frac{e^2}{mc^2} \frac{\sin \phi}{R} \exp[i\omega(t - R/c)] \quad (1.42)$$

where $\mathbf{E}_0 \exp(i\omega t)$ is the electric vector incident at the particle at the time t . Eqn. 1.42 shows that the intensity scattered elastically and coherently by an atom is essentially determined by its electron density distribution because the electrons, much lighter particles, scatter X-rays more efficiently than nuclei.

According to (1.42), when $E_0 = 1$, the amplitude of the spherical wave radiated at unit distance by a free point electron in the $\phi = 0$ direction is e^2/mc^2 . This is the *Thomson scattering length* of the electron that assumes the value $2.82 \times 10^{-5} \text{Å}$, and it is usually taken as the unit of scattered amplitude.²⁰ For an ensemble of N non-interacting electrons, interference occurs between waves scattered by the different centers. If the incident beam defines the direction of the wave vector \mathbf{k} and the diffracted beam the direction of \mathbf{k}' , the phase difference between the scattered wave from an electron at the origin and one at \mathbf{r}_j is $\mathbf{K} \cdot \mathbf{r}_j$, where the familiar \mathbf{K} *scattering vector* is equal to $\mathbf{k} - \mathbf{k}'$ and has length $4\pi(\sin\theta)/\lambda$.^{20a,c} Thus, the amplitude $A(\mathbf{K})$ scattered elastically by the N non-interacting electrons assumes the form:

$$A(\mathbf{K}) = \frac{e^2}{mc^2} \sum_{j=1}^N \exp(i\mathbf{K} \cdot \mathbf{r}_j) \quad (1.43)$$

For a continuous electron density distribution $\rho_1(\mathbf{r})$, the summation over waves of different phase must be replaced by an integral.^{20c} Therefore, the amplitude of the elastic and coherent X-ray scattering at a reciprocal-space direction \mathbf{K} is the Fourier transform of the one-electron density:

$$A(\mathbf{K}) = FT[\rho_1(\mathbf{r})] = \int \rho_1(\mathbf{r}) \exp(i\mathbf{K} \cdot \mathbf{r}) d\mathbf{r} \quad (1.44)$$

where e^2/mc^2 has been taken as the scattering unit.

Furthermore, electrons in atoms occupy discrete energy levels. If the energy of the X-ray photons are not tremendously larger than the binding energy of the atomic electrons, the response of these electrons is reduced by virtue of the fact they are bound. Therefore, we expect a reduction on the scattering length of an atom in this condition. The correction to $A(\mathbf{K})$ is called *anomalous dispersion* and have both real and imaginary components:^{20a,d}

$$A^\omega(\mathbf{K}) = A(\mathbf{K}) + f'(\omega) + if''(\omega) \quad (1.45)$$

where f' and f'' are known as the dispersion corrections to $A(\mathbf{K})$. It is typically necessary to correct the X-ray scattering amplitudes for anomalous dispersion before the calculation of $\rho_1(\mathbf{r})$ by Fourier inversion of (1.44).

To emphasize the assumption of non-interacting electrons, the result (1.44) is referred to as the *form-factor approximation*.^{20c,d} When $\rho_1(\mathbf{r})$ is the one-electron density of a crystal unit cell, $FT[\rho_1(\mathbf{r})]$ is known as the *structure factor*, $F(\mathbf{K})$.

The density distribution $\rho_1(\mathbf{r})$ within a unit cell is determined from X-ray diffraction intensities by introducing an electron density model that yields theoretically computed structure factors known in both magnitude and phase as a function of some adjustable, refinable parameters. The parameters are evaluated by minimizing the difference between the structure-factor amplitudes calculated from the model and measured experimentally, using a least-squares refinement procedure.^{20d} An alternative to this method is represented by the maximization of the information entropy, which however would not return an electron density separated from the thermal smearing.²¹

The electron density of the crystal unit cell is approximated by a summation over discrete densities, typically taken as *pseudo-atomic densities* centered at the corresponding nuclear positions $\{\mathbf{R}_k\}$:

$$\rho_1(\mathbf{r}) = \sum_{k=1}^M \rho_{1,k}(\mathbf{r} - \mathbf{R}_k) \quad (1.46)$$

where M denotes the number of atomic centers in the unit cell. Substitution of (1.46) into (1.44) yields the structure factor expression²⁰

$$F(\mathbf{K}) = \sum_{k=1}^M f_k(\mathbf{K}) \exp(i\mathbf{K} \cdot \mathbf{R}_k) \quad (1.47)$$

in which $f_k(\mathbf{K})$ is the Fourier transform of the pseudo-atomic density $\rho_{1,k}(\mathbf{r})$ at \mathbf{K} . For atomic densities constructed from Slater-type or Gaussian-type orbitals, $f_k(\mathbf{K})$ can be expressed in simple closed form.^{20d} The *atomic scattering factor* is represented in Fig. 1.3 for the F, C and H atoms, along with the individual contributions from their core and valence electrons. The inverse relation between direct and reciprocal space is clear, as more compact electron densities have the more diffuse scattering

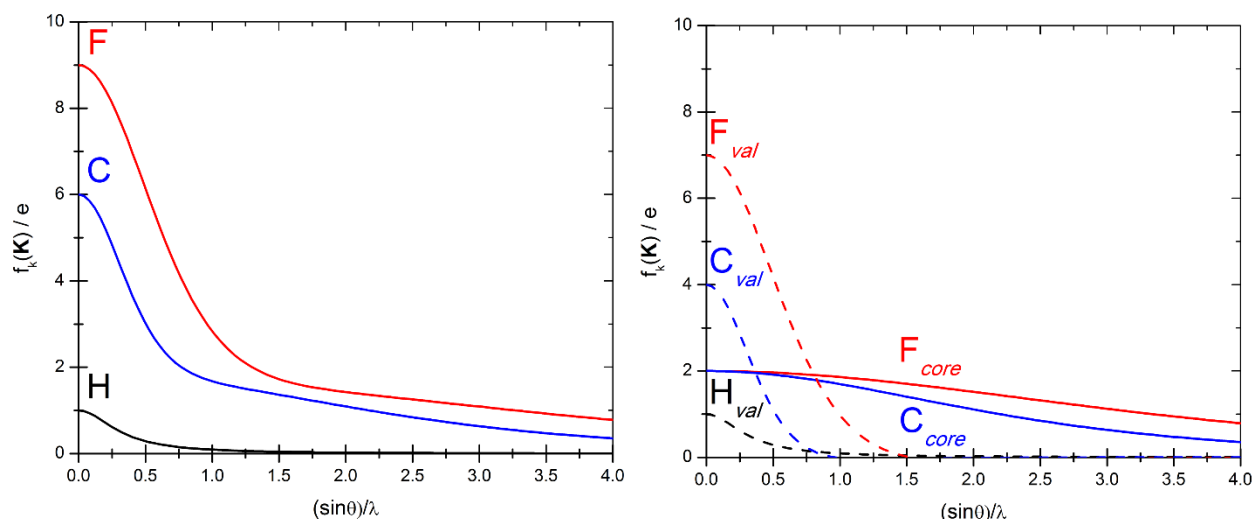


Figure 1.3. Atomic scattering factors and individual core and valence contributions to the total scattering for fluorine, carbon and hydrogen.

factors. Moreover, the scattering of the valence electrons are concentrated in the low-order region of the reciprocal space, while the core scattering persists to high-resolution. Of course, the scattering of hydrogen is rather small and concentrated at low values of $(\sin\theta)/\lambda$ because this atom has only one valence electron.

In X-ray crystal structure determination, the atomic densities are spherically symmetric, with a radial dependence equal to that of the Hartree-Fock ground-state atom. Only atomic coordinates and thermal parameters are refined against the experimental structure-factor amplitudes. This characterizes the so-called *independent-atom model* (IAM). Because the electron density distributions assume maximum values at nuclei, the IAM is a remarkably good approximation for the heavier atoms, for which the valence electrons contribute only to a minor part of the total scattering. However, IAM is much less accurate for lighter atoms, in particular for hydrogen, which lacks inner electronic shells. The mean of the electron density of H atoms covalently connected to heavier elements is displaced inwards into the X–H bond because of the overlap density involved in those interactions. Consequently, when an IAM hydrogen scattering factor is used in the least-squares refinement to adjust the atomic positions, the centroid of the electron density associated with the H atom is shifted in the direction of the bond, thus producing too-short X–H bonds. It has been demonstrated that this apparent shortening is far beyond the precision of X-ray structure determination and that it is of significance for second-row elements as well.^{20d} Finally, IAM assumes all atoms in the unit cell to be neutral and it is unable to describe the redistribution of the atomic densities due to chemical bonding effects.

1.3.2. Generalized scattering factors and Hansen-Coppens formalism

A very simple modification of the IAM that allows for charge transfer between atoms is the κ -*formalism*. It separates the atomic core density, kept fixed with respect to the neutral atom, from the atomic valence density, which can expand or contract with respect to the neutral atom and for which the electronic population can accordingly be refined. The model represents substantial improvement over the IAM, despite the refinement of only two more parameters per atom, the valence population

P_{val} and the exponent κ that scales the radial coordinate of the valence density function.^{20d} Thus, the pseudo-atomic density is formulated as

$$\rho_{1,k}(r) = \rho_{1,k}^{core}(r) + P_{val} \kappa^3 \rho_{1,k}^{val}(\kappa r) \quad (1.48)$$

When $\kappa > 1$, the same density is obtained at a smaller value of r , therefore the valence shell is contracted with respect to the neutral atom. Conversely, when $\kappa < 1$, the valence shell is relatively expanded. The factor κ^3 satisfies normalization requirements.^{20d} The assumption of unperturbed core electron density is amply supported. However, very-high-resolution studies suggest that small perturbations predicted by theory are also accessible experimentally.²²

The κ -formalism yields atomic charges in good agreement with electronegativity concepts and molecular dipole moments close to those derived from other experiments or calculated from first-principles.^{20d} However, it allows only a crude representation of $\rho_1(\mathbf{r})$. Nowadays, it is used only as an intermediate step during a multi-step refinement procedure.² An accurate treatment of X-ray scattering must also contain non-spherical density functions.

An extremely useful guidance for improving the scattering formalism upon the κ -formalism can be obtained from Eqn. 1.14 that expresses the one-electron density as combination of products of atomic orbitals $\phi_\mu(\mathbf{r})$. According to (1.14), the generalized scattering factor $f_{\mu\delta}$ is the Fourier transform of an atomic-orbital product:²³

$$f_{\mu\delta}(\mathbf{K}; \mathbf{R}) = \int \phi_\mu^*(\mathbf{r}) \cdot \phi_\delta(\mathbf{r}) \exp(i\mathbf{K} \cdot \mathbf{r}) d\mathbf{r} \quad (1.49)$$

The orbitals ϕ_μ and ϕ_δ are either on the same atomic center or on two different centers, and \mathbf{R} is the inter-nuclear vector for the two-center case. For $\mu = \delta$ and $\mathbf{R} = \mathbf{0}$, $f_{\mu\delta}$ is the scattering by a part of the atomic density function; for $\mu \neq \delta$ and $\mathbf{R} = \mathbf{0}$, $f_{\mu\delta}$ is the scattering contribution by two distinct orbitals in the same atom, the product of which is associated with a hybridized density function; for $\mathbf{R} \neq \mathbf{0}$, $f_{\mu\delta}$ may be seen as scattering from the overlap density in the bond.²³

The nuclear centered pseudo-atomic models represented by Eqn. 1.46 do not account explicitly for the two-center terms of (1.49). However, this is not a severe limitation because the bonding densities usually project efficiently in the atomic functions, provided they are sufficiently diffuse.^{20d} Additionally, non-atom-centered density models necessarily have “ghost” charge clouds located between atoms and in lone-pair regions, thus hampering straightforward interpretation in terms of chemically intuitive building blocks.

A number of atom-centered deformation-density models are available.²⁴ In most of them, the pseudo-atomic units are described by a multipole expansion that gives the best possible fit to the structure-factor amplitudes within the approximation (1.46). Among the so-called *multipolar models*, the Hansen-Coppens formalism^{24c} is particularly useful to us because of the usage of *local coordinate systems*. Each set of atomic functions is defined with respect to a Cartesian system, which is

independent from the unit-cell framework and from the reference systems of all other atoms. Proper choice of local reference for a pseudo-atom, defined using other pseudo-atoms in the unit cell, allows one to export atomic electron densities from relatively simple molecules (usually experimentally refined or theoretically calculated with high accuracy) to atoms belonging to much larger systems (for which experimental refinement or theoretical prediction cannot be performed so accurately). In fact, the transferability of multipolar densities characterizes most applications of modern electron density analysis on the field of biocrystallography.²⁵ Furthermore, local coordinate systems allow one to impose chemical equivalences to atoms not crystallographically equivalent, and to define constraints or restraints if a pseudo-symmetry is present in the molecule but not coincide with a crystallographic symmetry.⁴

The Hansen-Coppens approach augments each atomic electron density of the κ -formalism with deformation density terms that are products of radial and angular density functions:^{20d}

$$\rho_{1,k}^{def}(\mathbf{r}) = \sum_{l=0}^{l_{max}} \kappa'^3 R_l(\kappa' r) \cdot \sum_{m=0}^l P_{lm\pm} d_{lm\pm}(\theta, \vartheta) \quad (1.50)$$

The parameters $P_{lm\pm}$ and κ' can be refined within a least-squares procedure together with the usual κ and P_{val} parameters of the κ -formalism, as well as with atomic positions and thermal parameters. The angular functions $d_{lm\pm}$ are real linear combinations of the well-known imaginary spherical harmonics $Y_{lm}(\theta, \vartheta)$.¹² They can be written as

$$\begin{cases} d_{lm+}(\theta, \vartheta) = N_{lm} L_l^m(\cos \theta) \cos(m\vartheta) \\ d_{lm-}(\theta, \vartheta) = N_{lm} L_l^m(\cos \theta) \sin(m\vartheta) \end{cases} \quad (1.51)$$

with $0 \leq m \leq l$. The functions $L_l^m(\cos \theta)$ are the associated Legendre polynomials. The normalization constant N_{lm} ensures that a population parameter $P_{00} = 1$ for the spherically symmetric function d_{00} corresponds to one electron, and that the population parameters $P_{lm\pm}$ of non-spherical functions ($l > 0$) represent a shift of density from the negative to the positive regions of the corresponding $d_{lm\pm}$ harmonics.^{20d}

The spherical harmonic functions to be included in the description of a particular pseudo-atom may be symmetry restricted, depending not only on the crystallographic symmetry of the site, but also on the local symmetry imposed by a constraint.²⁶ The function d_{00} is of course spherically symmetric. For $l \neq 0$ and $m = 0$, the ϑ dependence disappears and the functions are cylindrically symmetric around the Cartesian z axis. Functions with l even are symmetric with respect to inversion through the origin of the local reference, while the functions with l odd are antisymmetric.^{20d} The monopole d_{00} is usually omitted for first- to third-row elements, but it is often necessary to describe the outer s-electron shell of transition metals, which is significantly more diffuse than the outermost d-subshell.

The choice of the radial functions of both spherical and aspherical parts of the total pseudo-atomic density $\rho_{1,k}(\mathbf{r})$ is crucial for a successful modelling of the crystalline electron density distribution. The core and spherical valence densities are taken from the isolated atom and modified by the κ expansion-contraction parameter. Typically, they are linear combinations of products of atomic Slater-type Hartree-Fock orbitals,^{27a} but relativistic effects can also be taken into account if necessary.^{27b,c} The radial deformation densities $R_l(\kappa'r)$ must instead be more diffuse to describe density accumulation in the bond regions. They are defined as^{20d}

$$R_l(\kappa'r) = \frac{(2\zeta_l)^{n_l+3}}{(n_l+2)!} (\kappa'r)^{n_l} \exp(-2\kappa'\zeta_l r) \quad (1.52)$$

The κ' parameter is generally numerically different from the κ applied to the spherical valence, as in Eqn. 1.48, and may be selected to vary among the different deformation functions on a particular atom. ζ_l assumes a value for each electronic subshell of the isolated atom, as optimized by Clementi and Raimondi.^{27d} The integer coefficient n_l is chosen for each subshell according to the rules of multiplication of spherical harmonic functions.^{20d}

For transition metals, it is sometimes preferable to use Hartree-Fock-orbital densities^{27a} for the higher multipoles as for the core and spherical valence because the rather contracted nature of the d-subshell makes the densities constructed from combinations of Slater-type orbitals more adequate.

The sum of the direct Fourier transform of Eqns. 1.48 and 1.50 yields the atomic scattering factor corresponding to the Hansen-Coppens multipolar pseudo-atom.^{20d} Due to Fourier-invariance of the spherical harmonics, its analytical expression is

$$f_k(\mathbf{K}) = f_{k,core}(K) + P_{val}f_{k,val}(K/\kappa) + 4\pi \sum_{l=0}^{l_{max}} i^l J_l(H/\kappa') \cdot \sum_{m=0}^l P_{lm\pm} d_{lm\pm}(\beta, \gamma) \quad (1.53)$$

where J_l is the l th-order Fourier-Bessel transform of R_l , and $d_{lm\pm}(\beta, \gamma)$ are reciprocal-space spherical harmonic functions with β and γ being the angular coordinates of \mathbf{K} . When the expansion (1.53) is truncated at $l = 0$, P_{val} is made equal to the number of valence electrons of the isolated atom, and $\kappa = 1$, the IAM is recovered.

Obviously, the physical content of the experimentally refined pseudo-atoms is subject to data quality, approximations and inadequacies inherent to the scattering model and ambiguities associated with the least-squares refinement.²⁸ Extremely accurate diffracted X-ray intensities, measured up to relatively high-resolution and at sufficiently low temperature are mandatory for meaningful electron density determination and analysis. High resolution is needed to precisely locate core-density maxima and adequately deconvolute thermal smearing effects from density deformations due to chemical bonding. Low temperature is required to minimize thermal diffuse scattering and thus increase the signal-to-noise ratio of the reflections.^{2,28}

1.3.3. Extended electron density models

Electron density distributions reconstructed using the Hansen-Coppens formalism does not necessarily adhere to quantum-mechanical requirements such as nuclear-cusp condition and proper asymptotic behaviour. However, this does not limit its applicability because extremely accurate radial wavefunctions have been used to improve the pseudo-atomic description at both regions, very close and very far from the nuclei.^{27e,f} Additional requirements, such as positivity, can be imposed by constraints.

Despite the large number of refinable parameters, the traditional Hansen-Coppens formalism is known to be not flexible enough and to produce bias in the resulting electron density. This becomes evident when comparing theoretically calculated electron densities with those obtained by applying multipolar models to the theoretical structure factors.²⁸ In view of these results, modified and extended formalisms have been proposed.

However, as anticipated, the pseudo-atom expansion (1.46) does not explain exactly the X-ray scattering due to overlap densities in the bond region between two atomic centers. Consequently, within multipolar formalisms, higher multipoles than those based on pure orbital assumptions are necessary to obtain satisfactory, though not exact or unique, convergence of the expansion.² For example, it is common to obtain significant octupole populations for C, N and O atoms. For transition metal atoms, the electron density is highly of one-center type because of the low overlap with the ligand density. For these atoms, hexadecapolar functions usually suffice.⁴ This feature motivates the first extension of the Hansen-Coppens formalism that is to include at least a few more harmonics in the series, usually truncated at the $l_{max} = 4$ level. This could be of particular importance in modelling the experimental electron density of compounds containing actinides or lanthanides²⁹

As discussed, electron densities undergo contractions and expansions from their ground state due to interactions with other atoms or molecules in the crystal. An atom involved in chemical bonds is anisotropically distorted, and one could consider, even in the same electronic shell, the possibility of different contraction-expansion in different directions. Of course, this implies much more parameters as each multipole lm has now a different radial function along with its particular κ' -scaling.⁴ An intermediate level of flexibility would be to use the contraction-expansion parameter as they appear in (1.50), but without imposing $\kappa'_l = \kappa'$.

The evidences for core-polarization observed in very-high-resolution X-ray diffraction experiments have opened the possibility to perform core-electron density refinements.²² Apart from the very small extents of core deformations, the core refinement within the Hansen-Coppens formalism is not particularly different from that of the valence density. Thus, in a minimal refinement of core density, one would simply include the core population P_{core} in (1.50) as a refinable variable. Notably, within the closely related Stewart formalism, P_{core} parameters are already routinely refined for each electronic shell but the aspherical density is superimposed on the spherical one without treating explicitly the expansion or contraction of the valence shell.³⁰ Furthermore, it has been encoded using a single crystal-coordinate system, rather than individual local-coordinate references.^{30b} Additional steps would be to refine a scaling factor κ_{core} together with P_{core} to account for the contraction-expansion of the core with respect to that of the unperturbed atom, then to refine a full set of multipoles starting from orbital

products of the atomic wavefunctions. In an extremely flexible approach, the refinement of different sets of multipoles and κ factors for each electronic shell of the core could be considered.⁴

With all these possibilities, Eqn. 1.50 becomes

$$\rho_{1,k}^{def}(\mathbf{r}) = \sum_{n=1}^{n_{max}} \left[P_n \kappa_n^3 \rho_n(\kappa_n r) + \sum_{l=0}^{l_{max}} \sum_{m=0}^l \kappa'_{nlm} {}^3R_{nlm}(\kappa'_{nlm} r) P_{lm\pm} d_{lm\pm}(\theta, \vartheta) \right] \quad (1.54)$$

Of course, flexible models imply many more parameters to describe small portion of the residual density left by a traditional multipolar refinement. Most of these approaches require extremely accurate, ultra-high-resolution data, much more than what is often available, and can possibly be applied only to highly symmetric and simple crystal structures. Moreover, the noise accompanying a residual map could hide systematic effects that are incidentally absorbed by too-flexible models, thus spoiling the interpretation of subtle features of the electron density distributions. In such circumstances, *residual-density analyses* could reveal systematic errors not only due to improperly corrected diffraction intensities, but also because of deficiencies in the density models. The state-of-the-art residual analysis uses the statistical test proposed by Meindl and Henn³¹ to ascertain whether only normally distributed noise affects the residual electron density in the unit cell.

Larger precision than that provided by (1.54) would require models much more computationally expensive not only for the refinement, but also for the calculation of density-derived properties.²⁸ At this point, the calculation of molecular orbitals constrained to X-ray diffraction intensities become more competitive.

1.3.4. X-ray constrained wavefunctions

An X-ray constrained wavefunction is one that, other than minimizing the associated energy, as stated by Eqns. 1.7 and 1.12, reproduces a set of experimentally collected X-ray structure-factor amplitudes within a predefined precision. The first attempt to constrain a wavefunction to experimental measures dates back to 1963, when Hartree-Fock Slater-type molecular orbitals were constrained to reproduce the experimental dipole moment of the HF molecule.^{32a} Since then, many methods have appeared. We postpone a brief literature review to Chapter 4. For a rather detailed description of previous methods, the reader is referred to Refs. 6a and 32b. Here, we only describe the most promising strategy, the one developed by Jayatilaka and co-workers.^{6a}

The most important reason to determine an X-ray constrained wavefunction is to condense the experimental data into an object that, unlike the pseudo-atomic expansion (1.46), is of quantum-mechanical significance. The fact that the object is a wavefunction has the advantage of allowing the derivation of properties rather different from those used to construct the model.^{32b}

Noteworthy, according to the Hohenberg-Kohn theorem,^{13a} the one-electron density suffices to determine all ground-state properties, but the corresponding functionals are usually unknown. Indeed, this is another reason to extract molecular orbitals from X-ray diffracted intensities: to learn something about the relationship between the one-electron density and the ground-state wavefunction.^{32c-e}

The strategy proposed by Jayatilaka provides a single-Slater determinant in the form of Eqn. 1.11 for which the spatial molecular orbitals $\varphi_i(\mathbf{r})$ are constrained to X-ray diffraction data.^{6a} It is necessary not only to minimize the energy associated with the Hartree-Fock Hamiltonian (1.17), but also to reproduce a set of collected structure-factor amplitudes within a predetermined agreement. This is achieved by searching for the orbitals $\{\varphi(\mathbf{r})\}$ that minimize the following functional:

$$L[\{\varphi\}] = E[\{\varphi\}] + \lambda (\chi^2[\{\varphi\}] - \Delta) \quad (1.55)$$

where $[\{\varphi\}]$ indicates the functional dependence on the set of occupied molecular orbitals $\{\varphi(\mathbf{r})\}$, and E is the energy associated with the Slater determinant for a suitably chosen crystal unit. λ is the Lagrange multiplier representing the strength of the constraint associated with the experimental data. Δ is the desired agreement between the structure-factor amplitudes experimentally measured, $F_{\mathbf{K},obs}$, and those calculated from the model wavefunction, $F_{\mathbf{K},calc}$. χ^2 is the agreement statistics between $F_{\mathbf{K},calc}$ and $F_{\mathbf{K},obs}$.^{6a}

$$\chi^2 = \frac{1}{N_r - 1} \sum_{\mathbf{K}} \frac{(\eta |F_{\mathbf{K},calc}| - |F_{\mathbf{K},obs}|)^2}{\sigma_{\mathbf{K},obs}^2} \quad (1.56)$$

with N_r as the number of experimental reflections and $\sigma_{\mathbf{K},obs}$ as the standard uncertainty associated with the experimental structure-factor amplitude $F_{\mathbf{K},obs}$, i.e. $\sigma_{\mathbf{K},obs} = \sigma(F_{\mathbf{K},obs})$. All the calculated structure factors are multiplied by an overall \mathbf{K} -independent scale factor η .³³

Following Jayatilaka, the set of structure-factor amplitudes $\{F_{\mathbf{K},calc}\}$ can be computed by assuming that the crystal is an ensemble of *non-interacting crystal units*.^{6a} This allows writing the global wavefunction for the crystal as

$$\Psi_{cell}(\mathbf{x}_1, \mathbf{x}_2, \dots, \mathbf{x}_N) = \prod_{k=1}^{N_u} \Psi_k(\mathbf{x}_1, \mathbf{x}_2, \dots, \mathbf{x}_{N_k}) \quad (1.57)$$

where N and N_k are the number of electrons in a crystal unit cell and in the crystal unit k , respectively, whereas N_u is the number of crystal units in an unit cell. The crystal-unit wavefunctions Ψ_k assume the single-Slater-determinant form of (1.11) and, apart from being related to each other by the crystal symmetry operations, they are formally identical to a reference wavefunction for the crystal fragment, Ψ_0 . Since we are particularly interested in molecular crystals and in the effects of the crystalline environment on isolated molecular units, it is convenient to use Ψ_0 for a molecule or maybe a small set of molecules. Eqn. 1.57 is exact, but an approximation is introduced when Ψ_0 is calculated for the crystal unit in isolation.

For practical calculations, the atomic orbital approximation (1.13) is used to obtain Ψ_0 . Finding the $\varphi_i(\mathbf{r})$ molecular orbitals that minimize the functional (1.55) is equivalent to solve self-consistently a set of N one-electron eigenvalue problems very similar to (1.16). The presence of the experimental

constraint merely adds an extra contribution to the one-electron operator \mathbf{f}_i .^{6a} If the Lagrange multiplier λ equals zero in (1.55), the usual Hartree-Fock equations are recovered, λ is simply chosen sufficiently large to give the desired agreement Δ .

In order to properly compute the set of structure-factor amplitudes $\{F_{\mathbf{k},calc}\}$, one must take into account the effect of the atomic thermal vibrations, which smear the electron density from that calculated for fixed nuclei. There are a number of choices for the atomic thermal parameters.³⁴ Additionally, the effect of secondary extinction must be corrected before comparison with $\{F_{\mathbf{k},obs}\}$. This effect has been analysed in some detail,^{35a} but typically the simplest empirical method^{35b} is used.

Owing to the experimental errors in the collected intensities, it is not necessary to force χ^2 equal to zero, but it is better to set the value of the desired agreement Δ equal to 1, so that, at the end of the calculations, the computed values are on average within one standard deviation of the experimental data. However, the convergence towards the desired agreement is not always fast and straightforward.³⁶ In order to avoid that large values of λ produce only minimal improvements in the χ^2 statistics and large unphysical changes of the energy, the following termination criteria have been recently proposed:³³

$$\left\{ \begin{array}{l} \chi^2 < 1 \\ \left(\frac{\Delta\chi^2}{\Delta\lambda} \right)_i = \frac{\chi_i^2 - \chi_{i-1}^2}{\lambda_i - \lambda_{i-1}} > -5 \times 10^{-1} \\ \frac{|E_{\lambda_i} - E_{\lambda=0}|}{|E_{\lambda=0}|} > 5 \times 10^{-4} \end{array} \right. \quad (1.58)$$

While the first criterion is the traditional one that checks if the statistical agreement $\Delta = 1$ has been reached, the second one avoids that a very large Lagrange multiplier produces only very small improvements in the statistics. The third criterion assures that the energy does not excessively change compared to the unconstrained situation. Although these criteria are quite reliable and well defined, the termination of the fitting procedure in the X-ray constrained approaches is still an open problem and it will deserve further investigations in the future.

In principle, the X-ray constrained wavefunction approach is capable to produce all the properties obtained from first-principle calculations, including those that require highly correlated Hamiltonians and largely extended basis sets to be estimated accurately, with the advantage of including, at least partially, crystal-field effects through the experimental constraint. Comparison with calculations is facilitated by the fact that the same level of theory can be used. However, in practice, acceptable convergence can only be achieved when rather small basis sets are used.³³

Nevertheless, Jayatilaka has calculated “in-crystal” electric properties of simple organic molecules using his constrained wavefunction method.^{36a,b} He concluded that *despite the fact that a constrained wavefunction is only a single-Slater determinant that minimizes the Hartree-Fock energy, the additional experimental constraint results in a wavefunction that reflects the effects of both electron correlation and*

intermolecular interactions experienced by the molecule in the crystal.^{32b} Our preliminary work on deconvoluting electronic correlation from crystal field effects shows that the experimental constraint is not capable to recover these features in full. Furthermore, the perturbation caused by intermolecular interactions seems to be more easily recovered than correlation effects, see Chapter 4.

Significant challenges remain in the field of experimentally constrained wavefunctions.^{32b} From the technical point of view, not only the termination criteria is an open question, but also how to make the method faster and more reliable, so larger basis sets and possibly better wavefunctions than the single-Slater approximation can be considered. The most exciting scientific opportunities concern the prediction of new properties. Reasonable spin densities have been calculated from X-ray constrained open-shell determinants.^{36c}

It is clear that, for accurate description of electron density distributions, the nuclear degrees of freedom must be accurately known as well. A very efficient approach is to refine nuclear positions and displacement parameters against X-ray diffraction data using multipolar models. Atomic coordinates are then used in constrained or unconstrained wavefunction methods without change. Eventually, atomic displacement parameters may be used to thermally smear the partitioned atomic densities. For some applications, even an IAM refined against experimental structure factors can be used without further optimization. However, a remarkably accurate procedure for crystal structure refinement have appeared, it is called *Hirshfeld method*.³⁷ Aspherical pseudo-atomic electron densities are obtained by partitioning a quantum-mechanical molecular density using the Hirshfeld scheme.^{41b} Then, atomic positions and displacement parameters are adjusted to fit the X-ray diffraction data. After that, a new electron density could be calculated at the new nuclear positions, and the parameters re-refined until no change is observed. The computational cost is of course dominated by the quantum-mechanical determination of the electronic wavefunctions, but the method is able to produce parameters very close to those observed for neutron diffraction experiments, even for H atoms.^{32b}

1.3.5. X-ray diffraction under electric fields

X-ray diffraction is a established technique for revealing the electronic nature and behaviour of solids upon application of a number of external perturbations.³⁸ We are interested in X-ray diffraction under electric fields due to the possibility of deriving electric response properties, in particular (hyper)polarizabilities, see next section. However, no experiment under electric field was performed for this thesis.

The response of a crystal to an externally applied electric field can be separated into two main contributions.^{39a} The first is a polarization of the electron density distribution. The second corresponds to a change of molecular geometry and thermal displacement parameters due to internal strain, which may be accompanied by a break of the crystal symmetry. As shown in Fig. 1.4 for the water molecule, the displacement of nuclei and electron density under the influence of an external field changes the scattered intensity, in particular at lower angles. Thus, a proper description of X-ray scattering by a crystal under external electric fields must take into account the two distinct responses.

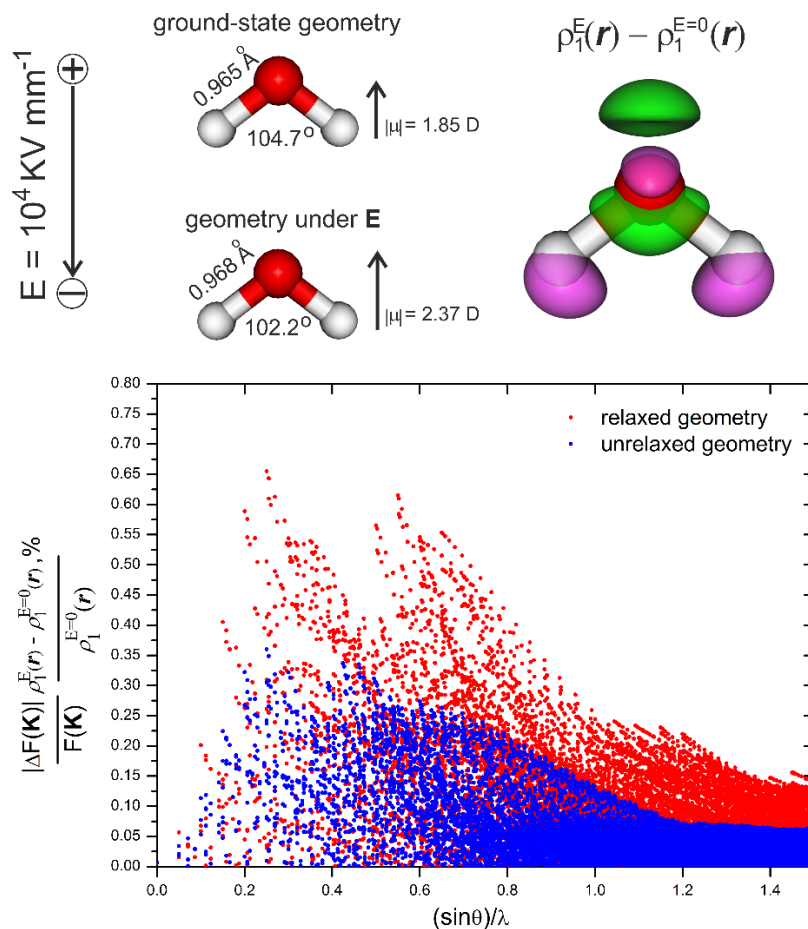


Figure 1.4. Effect of an applied electric field on molecular geometry, electron density distribution and structure-factor amplitudes. For the electron density difference surfaces, $\rho_1^E(\mathbf{r})$ denotes the one-electron density calculated under the applied field, but using the ground-state, unrelaxed geometry, thus only the effect of electronic polarization is considered. Isodensity surfaces are shown at the values of ± 0.002 au, with the positive surface in green and the negative one in magenta. For the structure-factor differences, in the unrelaxed case (blue points), the ground-state geometry is used to calculate both densities, $\rho_1^E(\mathbf{r})$ and $\rho_1^{E=0}(\mathbf{r})$, while in the relaxed one (red points), $\rho_1^E(\mathbf{r})$ is calculated using the geometry optimized under the electric field. Therefore, the relaxed situation takes into account both effects, electronic polarization and nuclear geometry changes. Calculations were performed at the B3LYP/d-aug-cc-pVDZ level of theory.

The understanding of how specific features of the structural framework respond to the electric field is still a challenge for modern X-ray diffraction. However, a quantum-mechanical description of the X-ray scattering by crystals under an external field was already proposed. Therefore, expressions for the electric field induced changes to atomic scattering and structure factors are available.^{39a,b} This formalism shows that the applied field disturbs mainly the valence electronic shells, as illustrated by the structure-factor differences shown in Fig. 1.4. The pure electron polarization gives approximately as much contribution to the diffracted intensities as the changes related to the displacement of the atoms from their ground-state equilibrium positions. Furthermore, probing the changes in the diffracted intensities is not a trivial task as they are overall small, in the range of 10^{-5} to 10^{-4} e per atom in the unit cell, for the field magnitudes typically used in nowadays X-ray experiments ($1 - 10$ kV mm^{-1}). For this reason, only a few experimental studies exist dealing with the electronic and structural changes induced by electric fields in crystals. Synchrotron radiation is usually required to reduce the statistical error of the intensities and to accumulate a number of photons sufficient to detect the effect in a reasonable time.

Nevertheless, chemical bond distortions induced by electric fields have been correlated to indicators available from the analysis of the accurate ground-state electron density in simple inorganic crystals such as α -GaPO₄ and Li₂SO₄·H₂O.^{39c} Interestingly, interactions predominantly ionic have been observed to be more sensitive to the applied fields than those characterized by largely covalent contributions. For example, the distortion of the Li–O closed-shell interaction is proportional to the projection of the electric field on the bond path.

These pioneering investigations are certainly the beginning of a comprehensive analysis of bond sensitivity to an applied electric field. As will be discussed in next section, this is highly desirable in view of the possibility to elucidate microscopic mechanisms governing the phenomena of dielectric polarization, piezo-, ferro- and pyroelectricity.^{39c} Finally, optical pulses have been recently used to initiate structural or electronic changes in materials. The measurement of diffraction intensities from different delay times of the X-ray pulse with respect to the excitation laser provides transient atomic positions or electron density distributions.^{38b}

1.4. Molecular and crystal properties from electron densities

So far, we have considered methods to obtain accurate electron density distributions, either from theory or from experiment. Now, we turn to the analysis of $\rho_1(\mathbf{r})$ and its applications to rationalize chemical bonding and molecular or crystal properties.

1.4.1. Topological analysis of electron density distributions

The hypothesis that the molecular structure is a collection of atoms linked by a network of bonds is routinely adopted by chemists. It is extremely useful for simplified descriptions of phenomena like chemical reactions or bonding mechanisms, and to predict molecular geometries. However, it suffers from the fundamental drawback of being not directly related to the quantum mechanics that governs the motion of nuclei and electrons in a molecular system. As noted by R. F. W. Bader, chemists have an understanding based on a scheme that is both powerful and, because of its empirical nature, limited. What remains is to show that atomic domains do exist and their properties can be predicted by quantum mechanics.^{40a} Typically, some experimental procedures are available for determination of a molecular or crystal property, but in general, measurements cannot probe the properties of particular atoms or groups of atoms in materials.

Although it has been demonstrated that a quantum-mechanical definition of atoms in molecules is possible,^{41a} many partitioning schemes have been devised and applied, depending on the properties of interest.⁴¹ They can be realized in real or Hilbert space, and are usually classified as *fuzzy-boundary* or *discrete-boundary* schemes. In the latter, the electron density at each point in space is assigned to a specific atomic domain, whereas in the former, the density at a point may be assigned to overlapping functions centered at different domains. In this respect, the pseudo-atom formalisms represented by (1.46) could be seen as a fuzzy-boundary scheme, because the electron density at a point within the unit cell is reconstructed as a sum of density contributions, either spherical or aspherical, from different pseudo-atoms.

Hilbert-space based partitioning schemes have the disadvantage of being built upon an object that is generally imaginary and that is a function of the four $\mathbf{x} = \{\mathbf{r}, \omega\}$ coordinates of each electron of the system. Additionally, many of the concepts related to chemical bonding, such as covalency, ionicity, aromaticity and resonance, and to atomic or functional-group properties, such as charge and volume, are typically difficult to recover or not unambiguously defined using many-electron wavefunctions.⁴² It is however generally recognized that the analysis of electron density distributions may provide both chemically appealing and physically founded answers to some of these concepts. This is the reason as to why $\rho_1(\mathbf{r})$, a relatively simple three-dimensional real-space based function, is preferable. Furthermore, the topological analysis of $\rho_1(\mathbf{r})$ as proposed by *Quantum Theory of Atoms in Molecules* (QTAIM) is special because it is capable to provide visual representation of many chemical concepts.⁴⁰

The principles of QTAIM are well detailed,⁴⁰ and an enormous literature describes the characterization of chemical bonds in terms of topological analysis of $\rho_1(\mathbf{r})$, despite the well-documented problems with this scheme.⁴³ We limit our discussion to a few concepts that will prove to be of relevance in the next chapters. In particular, we briefly consider the topological definition of an atom in a molecule or crystal, and how this yields atomic or functional-group properties. Of relevance for Chapter 3 is also the topology of $\nabla^2\rho_1(\mathbf{r})$, the Laplacian of the electron density, which maps the curvature of $\rho_1(\mathbf{r})$ at each point in space. Nevertheless, topological analysis of other real-space scalar functions, such as electrostatic potential and electron localization function, along with its associated partitioning into disjoint domains has also offered significant insights into the nature of many chemical concepts.^{44a,b} Sometimes, the topology of vector fields like the Ehrenfest force field has also shed some light into chemical bonding phenomena.^{44c} Not all of these functions are available experimentally nor can be obtained directly from $\rho_1(\mathbf{r})$. For this reason, the most general indicators are based on density matrices.⁴² Noteworthy, QTAIM has been applied extensively also to electron density models fitted against experimental structure-factor amplitudes. In this case, obviously ignoring nuclear motion.

The QTAIM topological analysis leads to an *exact* partitioning scheme, in the sense that the electron density at any point in space is necessarily attributed to one, and only one, *atomic domain* or *atomic basin*, which is thus defined as a region in which all the electrons are bound to a particular nucleus. Moreover, the atomic basins can be regarded as *open quantum subsystems*, because they are free to exchange charge and momentum with their neighbours, and the sum of the energies of the individual atoms equals the total quantum-mechanical energy of the system.⁴⁰ QTAIM also provides fairly *additive* and *transferable* atomic domains. The first feature is related to the fact that the atomic values for a property should, when summed over all atoms, yield the average molecular property, whereas the latter accounts for the observation that, within certain series of molecules, the atoms, functional groups and their properties are exportable from one molecule to another.^{40a}

The topological features of $\rho_1(\mathbf{r})$ are conveniently summarized in terms of the number and kind of its *critical points*. The *gradient vector field* of the electron density, $\nabla\rho_1(\mathbf{r})$, vanishes at any critical point, and whether it is a maximum, a minimum or a saddle depends on the three independent curvatures of ρ_1 at this point.⁴⁰ All the curvatures are of the same sign for local maxima and minima, while one of the curvatures has opposite sign for saddles. A critical point is classified as (ω, σ) , where the *rank* ω at this point is equal to the number of nonzero independent curvatures, and its *signature* σ is the algebraic sum of the signs of the curvatures. Because $\rho_1(\mathbf{r})$ is a three-dimensional function, molecular structures are defined in terms of critical points with $\omega = 3$. There are only four possible signature values for critical points with rank three.⁴⁰

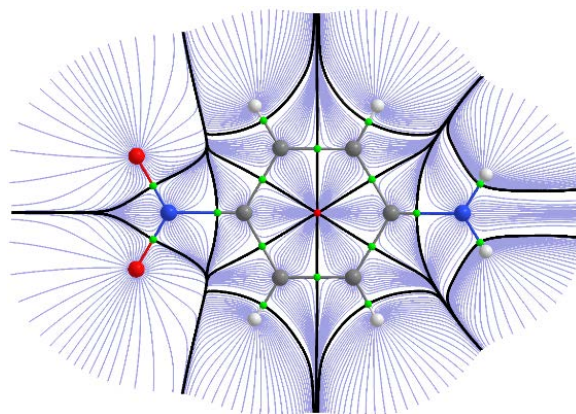


Figure 1.5. The QTAIM partitioning of the molecular p-nitroaniline electron density, as obtained from a DFT calculation. Gradient paths and interatomic surfaces are shown for all atomic basins. Bond critical points are small green spheres and the ring critical point is the small red one. Larger spheres represent nuclear attractors and the line connecting each pair of atoms is the bond path.

Local maxima of ρ_1 are critical points of $(3, -3)$ type, and are recognized as *nuclear attractors*. Notably, derivatives of the electron density distribution at nuclei are formally not defined because the gradient is discontinuous at nuclear cusps. However, because the exact $\rho_1(\mathbf{r})$ is approximated by a sum of atomic orbital products, see Eqn. 1.14, that are typically linear combinations of Gaussian functions, the critical point at nuclear position is easily defined in practice. Non-nuclear maxima were also found in some cases, normally very far from the nuclear sites, their interpretation is still debatable though.⁴⁵

Critical points of the $(3, -1)$ type correspond to maxima of ρ_1 in the plane defined by the directions of negative curvatures, and to minima along the direction of the third curvature. These saddles are defined as *bond critical points*, normally found between every pair of nuclei linked by a chemical bond. Conversely, at $(3, +1)$ points, ρ_1 is a minimum in the plane defined by the positive curvatures, while it is a maximum along the direction of the third one. These saddles are found at the center of a ring of bonded atoms and are called *ring critical points*. Finally, a $(3, +3)$ critical point is a local minimum. It is known as *cage critical point* because it is found at the center of a cage formed by atoms linked through chemical bonds.

An atomic domain in the scalar field $\rho_1(\mathbf{r})$ is defined by boundaries constructed from its associated $\nabla\rho_1(\mathbf{r})$ field.⁴⁰ The topology of the electron density distribution allows atomic basins Ω to be separated by interatomic surfaces defined such that all gradient vectors at any point on the surface S are perpendicular to the vector \mathbf{n} normal to the surface, i.e.

$$\nabla\rho_1(\mathbf{r}) \cdot \mathbf{n}(\mathbf{r}) = 0, \quad \forall \mathbf{r} \in S(\Omega, \mathbf{r}) \quad (1.59)$$

where $S(\Omega, \mathbf{r})$ is referred to as a *zero-flux surface*, because it is not crossed by any trajectory of $\nabla\rho_1(\mathbf{r})$. It is these surfaces that separate atomic domains and define the volume of the basins. Fig. 1.5 shows the gradient density partitioning for the p-nitroaniline molecule. Blue lines represent all the gradient trajectories, which terminate at nuclear attractors. The solid black lines are the interatomic surfaces. Two nuclei are connected by lines of maximum electron density, the *bond paths*. The collection of bond paths, defines the particular *molecular graph*.⁴⁰

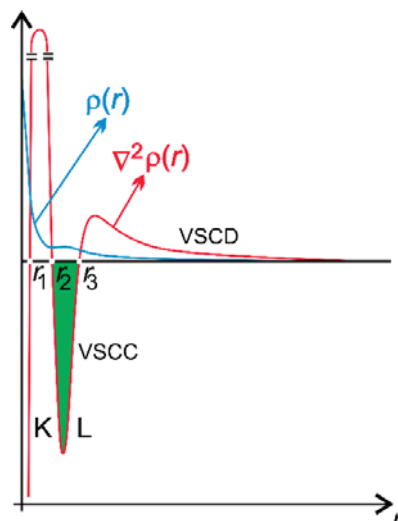


Figure 1.6. The hypothetical electron density of a second row element along with its corresponding Laplacian function. The green area is the valence shell charge concentration region of the atom. The region from the origin to r_2 corresponds to the K shell, after that, the L shell extends to infinity.

The chemical interpretation of the bond paths is still not completely clear. In the potential energy distribution of an equilibrium geometry, the bond paths certainly indicate directions of energy lowering, thus corresponding to chemical bonds. Because of the homeomorphism between this function and the electron density distribution, Bader has argued that the presence of a bond path in $\rho_1(\mathbf{r})$ assures the presence of chemical bonding.^{46a} However, because the homeomorphism between these two distributions is only visual, and not formally demonstrable, this interpretation has been strongly criticized.^{46b} In fact, bond paths are frequently found between atoms that chemists would hardly considered to be bound.^{46c,d}

As anticipated, the electron density distribution is not the only function from which chemical information can be extracted. Indeed, its Laplacian contains information complementary to that contained in $\rho_1(\mathbf{r})$, and it is usually useful to reveal the deep fine structure of the electron density distribution.⁴⁰ The Laplacian of the electron density, $\nabla^2\rho_1(\mathbf{r})$, is the scalar field defined in Cartesian coordinates as

$$\nabla^2\rho_1(\mathbf{r}) = \frac{\partial^2\rho_1(\mathbf{r})}{\partial x^2} + \frac{\partial^2\rho_1(\mathbf{r})}{\partial y^2} + \frac{\partial^2\rho_1(\mathbf{r})}{\partial z^2} \quad (1.60)$$

that is invariant with respect to the choice of coordinate axes, and has a topology of its own, usually more complicated than that of $\rho_1(\mathbf{r})$. The function determines whether the electronic charge at a point in space is relatively concentrated or depleted. When $\nabla^2\rho_1(\mathbf{r}) < 0$, the electron density is *locally concentrated* at \mathbf{r} ; when $\nabla^2\rho_1(\mathbf{r}) > 0$, it is *locally depleted* at that point. This outstanding feature of the Laplacian is responsible to reveal the shell structure of an atom, which is not evident in the electronic distribution through space. Fig. 1.6 shows the Laplacian of a typical electron density for a second row atom. While $\rho_1(\mathbf{r})$ decreases quite monotonically and seems to be featureless, $\nabla^2\rho_1(\mathbf{r})$ oscillates heavily around zero. In fact, the zeroes of the Laplacian are nodes confining regions of charge concentration or depletion. The region from the origin to the point r_2 corresponds to the K atomic shell. The second shell L extends from this point to infinity.^{40b}

The outermost region of negative Laplacian is called the *valence shell charge concentration* (VSCC). Analyses of this region has been extremely elucidative for rationalize properties of materials using their electron density distributions.⁴⁷ In Chapter 3, we apply this tool for help understanding the magnetism of metal-organic polymers. Here, we simply note that, because it is intuitive to associate a positive value to a concentration of charge and a negative value to depletion, topological analyses are typically performed in terms of $L(\mathbf{r}) = -\nabla^2 \rho_1(\mathbf{r})$, rather than the Laplacian itself.⁴⁰ The VSCC regions of $L(\mathbf{r})$ are usually characterized by $(3, -3)$ critical points, corresponding to *non-bonding maxima*, and by $(3, +1)$ and $(3, -1)$ saddles, corresponding to depletion along particular directions. Inside the VSCC all critical points will have at least one negative curvature, thus $(3, +3)$ points can never be encountered. In analogy to the molecular graph, the topological object constituted by the critical points of $L(\mathbf{r})$ are called *atomic graph*. Noteworthy, for many molecules, the $(3, -3)$ critical points within the VSCC provide a one-to-one mapping of electron pairs of the Lewis model. In fact, this has been used to support the Valence Shell Electron Pair Repulsion Model (VSEPR) of Gillespie.⁴⁸ However, this mapping is only visual, as no analysis of the two-electron density supports the existence of localized electron pairs.^{40b}

The QTAIM topological partitioning of the real, molecular or crystal, space into atomic domains Ω enables the partitioning of the corresponding electronic properties into atomic or functional group contributions. The expectation value of an operator \mathbf{A} averaged over all space is the sum of the expectation values of this operator averaged over all the atoms in the molecule or crystal:^{40c}

$$\langle \mathbf{A} \rangle = \sum_{\Omega=1}^{N_{atoms}} \left(\int_{\Omega} \left\{ \frac{N}{2} \int [\Psi_{el}^* \mathbf{A} \Psi_{el} + (\mathbf{A} \Psi_{el})^* \Psi_{el}] d\mathbf{x}_2, \dots, d\mathbf{x}_N \right\} d\mathbf{r} \right) \quad (1.61)$$

Because we are particularly interested in cases where \mathbf{A} is a simple non-imaginary multiplier, usually some function of the coordinate \mathbf{r} , Eqn. 1.61 reduces to¹

$$\langle \mathbf{A} \rangle = \sum_{\Omega=1}^{N_{atoms}} \left(\int_{\Omega} \mathbf{A} \rho_1(\mathbf{r}) d\mathbf{r} \right) \quad (1.62)$$

1.4.2. Atomic and molecular electric properties

Electrical properties of materials span a wide field⁴⁹ in which their prediction in molecules, as found either in an infinitely diluted gas or in a crystal, has for long been of interest. All these properties result of the forces that the electric charges exert on each other in a molecular material, and are observables of the charge distribution. However, while some of them, like electrostatic moments and interaction energies, are consequence of the “intrinsic” interactions among nuclei and electrons, others, such as (hyper)polarizabilities, measure how the charge distribution changes as a result of interactions with external stimuli, in particular an electric field. In view of their importance for Chapter 2, this and the next section are devoted to analyse the most relevant aspects of estimation of electric dipole moments and first-order polarizabilities along with some of their applications in materials science.

Electrostatic moments are relevant because they provide concise information about the charge distribution within a material, with the advantage of being available from a variety of theoretical and experimental techniques.^{50a} Additionally, as discussed in Chapter 2, they find applications on quantitative rationalization of intra- and intermolecular interactions in molecular crystals or aggregates. Electrostatic moments can be fundamentally defined as expectation values of multipole moment operators. In Cartesian coordinates, the components of the multipole moment tensors are^{10b}

$$\langle \mathbf{x}^l \mathbf{y}^m \mathbf{z}^n \rangle = \sum_{k=1}^M Z_k x_k^l y_k^m z_k^n - \int x^l y^m z^n \rho_1(\mathbf{r}) d\mathbf{r} \quad (1.63)$$

where l , m and n are integers larger than or equal to zero, and the sum $l + m + n$ determines the type of moment, i.e. monopole, dipole, quadrupole, etc. The monopole moment corresponds to the charge and it is simply $q = \langle \mathbf{1} \rangle$, a quantity that, unlike higher moments, is independent of the coordinate system and its origin. The dipole moment $\boldsymbol{\mu}$ has three components that can be calculated from Eqn. 1.63, depending on which of l , m or n is one, with the others set equal to zero. For example, the x component is usually denoted by μ_x , and equals $\langle x \rangle$. Analogously, higher moments can be computed from (1.63) by considering the integers l , m and n that yield their corresponding tensor components.

(Hyper)polarizabilities are the fundamental properties that determine most of the optical behaviour of the materials. They are the quantities defined at atomic and molecular levels that yield the corresponding electric susceptibilities through lattice summation. As for electrostatic moments, they are available from both theory and experiment, but, with a few exceptions, measures are not capable to provide all their tensor components.^{50b} As anticipated in Eqn. 1.26, the (hyper)polarizabilities can be defined in terms of energy derivatives when the perturbation vector \mathbf{X} is an electric field. Because the first derivative of the energy with respect to the field is the dipole moment, it may be useful to express (hyper)polarizabilities as derivatives of $\boldsymbol{\mu}$. For example, the α_{ij} component of the polarizability tensor can be alternatively defined as

$$\alpha_{ij} = -\frac{\partial^2 E}{\partial X_i \partial X_j} = \frac{\partial \mu_j}{\partial X_i} \quad (1.64)$$

Noteworthy, optical properties are generally dependent on the frequency of the oscillating electric field used to probe them. However, the polarizabilities considered in this thesis are calculated under *static electric fields*. Furthermore, *nuclear relaxations*, which also affect optical properties, are not considered as well. Although sometimes small, these effects may hamper a direct comparison with experimental data.^{50c}

Because we are interested in identifying the most important atoms and functional groups that determine particular properties of a molecule or a crystalline material, it is useful to partition the electrostatic moments and (hyper)polarizabilities into their atomic contributions.

The pseudo-atom formalism (1.46) is itself an atomic partitioning. Provided that a suitable deformation density is considered, the electrostatic moments can be easily calculated for each pseudo-atom from the parameters refined against either measured or calculated structure-factor amplitudes.^{20d} However, because these parameters correlate, sometimes strongly, within a refinement, and different combinations of parameters may describe the same electron density distribution, a better estimation of atomic moments is obtained from an *a posteriori* partitioning of the total electron density.

Interestingly, the application of partitioning schemes to estimate linear optical properties of atoms and functional groups in molecules or crystals has a long history. In particular, several approaches have been proposed for the calculation of *distributed atomic polarizabilities*, i.e. the atomic polarizability tensors within a molecule or molecular aggregate.⁵¹ Notably, Bader and co-workers have calculated QTAIM-partitioned polarizabilities and used them to evaluate intermolecular interaction energies and transferability of electric properties.⁵² Keith's generalization of Bader's method removed the origin dependence from the QTAIM definition of atomic dipoles and polarizabilities, thus making these quantities transferable to other systems.^{53a} The procedure has been recently modified and implemented in a program called *PolaBer*,^{53b} used to obtain most of the results shown in Chapter 2. Furthermore, *PolaBer* extends the quantities computed from atomic polarizabilities, including the evaluation of bond polarizabilities and refractive indices in crystals.^{53b-f}

The fuzzy Hirshfeld scheme has also been applied to extract molecular polarizabilities in clusters or atomic polarizabilities in large molecular systems such as fullerenes, metallic nanoparticles and proteins.⁵⁴ However, a disadvantage of the Hirshfeld scheme, at least in the current implementations, is that the atomic polarizabilities remain origin-dependent.

We now consider how distributed atomic dipole moments and polarizabilities can be computed from the QTAIM partition of the total molecular or crystal charge density distribution. As stated in Eqn. 1.61, QTAIM defines the expectation value of an observable over each atom in the system. Thus, the average value of the dipole moment $\boldsymbol{\mu}$ over the molecule or the crystal is given as a sum of atomic contributions $\boldsymbol{\mu}(\Omega)$. Each atomic moment consists of an origin-independent *polarization* term $\boldsymbol{\mu}_p(\Omega)$, and an origin-dependent *charge-translation* term $\boldsymbol{\mu}_c(\Omega)$.^{52a} That is,

$$\boldsymbol{\mu}(\Omega) = \boldsymbol{\mu}_p(\Omega) + \boldsymbol{\mu}_c(\Omega) = - \int_{\Omega} [\mathbf{r} - \mathbf{R}_{\Omega}] \rho_1(\mathbf{r}) d\mathbf{r} + [\mathbf{R}_{\Omega} - \mathbf{R}_0] q(\Omega) \quad (1.65)$$

where $q(\Omega)$ is the net charge of the atomic basin Ω , \mathbf{R}_{Ω} is the nuclear position vector of the basin and \mathbf{R}_0 is the arbitrary origin of the molecular or crystal coordinate system. Unless $q(\Omega)$ is zero, $\boldsymbol{\mu}_c(\Omega)$ is dependent on \mathbf{R}_0 . Thus, the atomic dipole moment $\boldsymbol{\mu}(\Omega)$ is not generally meaningful because it is origin-dependent, just as the total $\boldsymbol{\mu}$ is not meaningful for charged molecules. However, the origin-dependent charge-translation term can be converted to an origin-independent definition:^{53a}

$$\boldsymbol{\mu}_c(\Omega) = [\mathbf{R}_{\Omega} - \mathbf{R}_0] q(\Omega) = \sum_{\Lambda=1}^{N_{atoms}} [\mathbf{R}_{\Omega} - \mathbf{R}_{BCP}] q(\Omega|\Lambda) \quad (1.66)$$

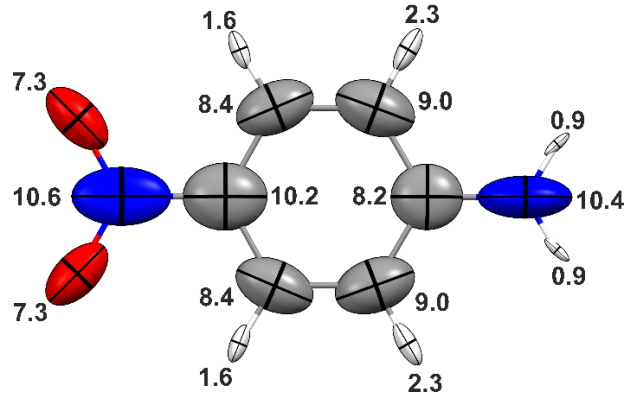


Figure 1.7. Distributed atomic polarizability ellipsoids obtained after QTAIM partitioning of the molecular p-nitroaniline electron density, as obtained from a DFT calculation. The isotropic polarizabilities, obtained as the arithmetical average of the main diagonal tensor components, are shown in au. The scaling factor for the ellipsoids is 0.3 \AA^{-2} .

in which $q(\Omega|\Lambda)$ is called a *bond charge*, and can be interpreted as the charge induced at the basin Ω due to its interaction with the basin Λ . \mathbf{R}_{BCP} is the position vector of the bond critical point connecting the basins Ω and Λ , and the summation runs over all basins connected to Ω through a bond critical point. All quantities in Eqn. 1.66 are uniquely determined by the total charge density distribution partitioned according to the zero-flux surfaces (1.59) of QTAIM. The bond charges can be obtained by imposing a series of constraints on the atomic and molecular charges.^{53a,b}

As for the dipole moment, the molecular polarizability tensor can be decomposed into additive atomic contributions:^{53a}

$$\boldsymbol{\alpha} = \sum_{\Omega=1}^{N_{\text{atoms}}} \boldsymbol{\alpha}(\Omega) = \sum_{\Omega=1}^{N_{\text{atoms}}} [\boldsymbol{\alpha}_p(\Omega) + \boldsymbol{\alpha}_c(\Omega)] \quad (1.67)$$

where $\boldsymbol{\alpha}_p(\Omega)$ and $\boldsymbol{\alpha}_c(\Omega)$ are the polarization and charge-translation atomic polarizability tensors that arise from the derivation of the corresponding $\boldsymbol{\mu}_p(\Omega)$ and $\boldsymbol{\mu}_c(\Omega)$ atomic dipole moments with respect to the applied electric field, according to Eqn. 1.64. Given the linear response of the electron density with respect to a sufficiently small field, (1.64) can be calculated numerically, using wavefunctions computed at finite electric fields. Thus, the atomic polarizability components $\alpha_{ij}(\Omega)$ are evaluated as:

$$\alpha_{ij}(\Omega) = \lim_{E_i \rightarrow 0} \frac{\mu_j^{E_i}(\Omega) - \mu_j^0(\Omega)}{E_i} \quad (1.68)$$

in which $\mu_j^{E_i}(\Omega)$ is the dipole moment component of the atomic basin Ω along the j direction computed with an applied electric field in direction i . Because polarizabilities have dimensions of volume, the atomic and molecular tensors can be visualized as ellipsoids in the same three-dimensional space as the molecule, assuming $1 \text{ \AA}^3 \equiv 1 \text{ \AA}$, although a scaling factor is usually applied to reduce the size of the polarizability ellipsoids for visualization purposes.^{53b} Fig. 1.7 shows atomic ellipsoids for the p-nitroaniline molecule, as obtained from an isolated-molecule calculation at the CAM-B3LYP/aug-cc-pVDZ level of theory.

However, the use of this procedure to compute atomic polarizabilities through Eqn. 1.68 introduces an important drawback: because the ground-state molecular electron density $\rho_1^0(\mathbf{r})$ and the corresponding field-perturbed densities $\rho_1^{Ej}(\mathbf{r})$ are “independently” partitioned into their atomic contributions, there is no guarantee that the corresponding atomic basins are kept constant in the process. Indeed, within this methodology, it is very common to observe changes in atomic charge and volume of a basin when going from $\rho_1^0(\mathbf{r})$ to $\rho_1^{Ej}(\mathbf{r})$. Such changes can be regarded as the deviation of the method from a perfect *atomic response theory*, and result in slightly asymmetric atomic polarizability tensors. Even though the lack of symmetry can be easily corrected through *a posteriori* tensor symmetrization, this by no means guarantees that the QTAIM basins have been retained. Interestingly, an alternative scheme that removes this drawback has been recently proposed and applied to compute and visualize Hirshfeld-based distributed polarizabilities.^{54d}

Nevertheless, it has been demonstrated that QTAIM distributed polarizabilities obtained through Eqns. 1.65-67 are remarkably exportable among some series of molecules, including amino acids and organic optical materials.^{53c} Furthermore, this approach has been successfully applied to understand the origin of the refractive indices of molecular crystals in terms of their most fundamental building-blocks, i.e. atoms and functional groups.^{53d}

1.4.3. Crystalline electric properties

High-resolution X-ray diffraction is an established technique for determination of molecular electrostatic moments in crystals, with the advantage of providing not only magnitudes, but also all their tensor components. Nowadays, these experimental values are often used to benchmark theoretical predictions.^{20d,50a} Some time ago, it was proposed that the first-order polarizability α and hyperpolarizability β could be estimated for molecules in crystals using respectively the quadrupole and octupole electrostatic moments obtained from the electron density model fitted against experimental X-ray diffracted intensities.⁵⁵ However, application of this method to organic non-linear optical materials revealed that many of the diagonalized tensor components of α and β calculated from X-ray diffraction differ by more than an order of magnitude from theoretical results. Indeed, it was later shown that the one-electron density $\rho_1(\mathbf{r})$, obtained from the usual multipolar pseudo-atom formalisms, does not yield accurate response properties because electronic correlation is included only partially.^{36a} Instead, Jayatilaka and Cole have pursued the X-ray constrained wavefunction approach to derive much more accurate $\rho_1(\mathbf{r})$ distributions for a few optical materials, including a metal-organic non-linear compound.⁵⁶ The “experimental” wavefunctions yielded remarkably accurate electric properties, indicating the possibility to use constrained molecular orbitals to help engineering this kind of materials. As discussed in Chapter 4, in case a scheme is further assumed to localize the constrained orbitals in particular atoms or functional groups, they can be exported to much larger systems, thus allowing accurate prediction of their electric properties too, which is currently challenging for both theory and experiment.

When the molecular electrostatic moments of a charge density distribution are estimated from first-principles in an infinitely diluted gas, the agreement with experimental results obtained in crystals, or with equivalent simulations performed under periodic boundary conditions, is often poor.^{50a} This is

because, not surprisingly, electric moments are typically affected by short- and long-range crystal field effects. For example, in the crystalline phase, molecules tend to line up in order to maximize their electrostatic attractions, hence often enhancing their dipole moments due to induced polarization of their electron density distributions.^{59c} This *dipole moment enhancement* observed when going from a gas-phase molecule to an aggregated environment has been investigated in quite some detail for 2-methyl-4-nitroaniline, one of the molecular prototypes for linear and non-linear optical materials. A careful diffraction study by Spackman reported a significant enhancement of 30-40%.^{57a} While various theoretical studies indicate 30% as typical dipole moment enhancement for hydrogen-bonded systems,^{57b} many diffraction experiments result in enhancements greater than 100%. However, it is recognized that molecular moments are highly dependent on the multipole model fitted against the X-ray diffracted intensities, and several studies reporting incredibly large enhancements were performed treating the thermal motion of hydrogen atoms as isotropic and without incorporating neutron diffraction estimates of X–H distances.

The redistribution of electronic charge that molecules undergo upon aggregation to other molecules or, ultimately, crystallization has also important consequences for estimation of optical properties. Studies on organic non-linear optical materials have revealed that the hyperpolarizability of a molecule typically enhances by a factor of three when a hydrogen-bonded cluster is considered in its surrounding.^{57c,d} Instead, the first-order polarizability α is much less variable, thus being determined in a great extent by the intramolecular connectivity rather than the intermolecular forces.

Crystal-orbital or plane-wave-based calculations are in principle the correct approaches to model the crystalline effects, and therefore, to accurately estimate electrostatic and response properties of molecules in crystals. However, some problems affect these methods: a) the amount of electronic correlation that one can introduce is limited; b) convergence often fails when Bloch-type functions use diffuse atomic orbitals; c) plane-wave calculations exclude very localized core-orbital functions and therefore their contribution to the properties, which can be quite substantial for hyperpolarizabilities, for example. In order to overcome these drawbacks, the so-called supermolecule or cluster method have emerged.⁵⁸ Within this approach, the property of interest of several interacting molecules are evaluated as a whole, just like in standard molecular calculations. The properties of the molecules embedded in a crystal are estimated to be those of a particular molecule in the cluster, usually chosen as the “central” one around which the aggregate is constructed. The electron density of this molecule is extracted from the total cluster density by applying a partitioning scheme. In fact, by comparing the electric properties of an isolated molecule and that of the molecular cluster, one gains insight into the role of short and medium-range intermolecular interactions, crucial for the design of optical materials.⁵⁸ However, this approach suffers from include the crystal field effects only partially as long-range interactions are neglected. Furthermore, the choice of the molecular aggregate that yield accurate molecular properties is usually not unique, a computationally costly pre-screening of at least a few clusters are typically necessary.

An alternative strategy to include crystal field effects in a single-molecule calculation or long-range effects in a molecular aggregate, thus allowing the estimation of crystal properties from their molecular building-blocks, is firstly to construct an *oriented-gas model*, one in which non-interacting identical

molecules or aggregates lie side-by-side and the solid-state properties are simply appropriate combinations of the molecular ones.⁵⁸ Afterwards, the effects of the surroundings are semi-empirically approximated by using *local-field factors*. Since molecular crystals feature in general only non-covalent intermolecular interactions, classical electrostatic models have been successfully adopted to estimate dipole moment enhancements and, ultimately, the electric response properties of crystals starting from a simple gas-phase calculation.^{36a,59}

For the purpose of defining the local-field factor, a crystal may be represented as an array of equal dipoles distributed over a space lattice.⁵⁹ A molecule k embedded in the crystal experiences a local-electric field \mathbf{E}_{local} that, in general, is a sum of any externally applied field \mathbf{E} , and the internal field that results from the dipole moments of all other N molecules in the unit cell,^{59a,b} i.e.

$$\mathbf{E}_{local}(k) = \mathbf{E} + \sum_{k'=1}^N \mathbf{L}(k, k') \cdot \boldsymbol{\mu}(k') \quad (1.69)$$

where k' represents the sites that are symmetry-related to k in the crystal. In general, the *Lorentz tensors* $\mathbf{L}(k, k')$ depend on the unit cell parameters, and the positions and orientations of the k' dipoles relative to the lattice site k at which the field is determined. Many approaches, either in direct or reciprocal space, can be used to perform the lattice summation in (1.69), but the Ewald method is typically chosen.^{59b}

For relatively small values of \mathbf{E}_{local} , the dipole moment $\boldsymbol{\mu}^{ind}$ induced at a particular molecule k depends only on its first-order polarizability, and can be computed as:

$$\boldsymbol{\mu}^{ind}(k) = \boldsymbol{\alpha} \cdot \mathbf{E}_{local} \quad (1.70)$$

The dipole moment of the molecule embedded in a crystal or molecular cluster can be estimated as a simple sum of its permanent dipole moment $\boldsymbol{\mu}$, calculated in gas-phase, with the induced dipole $\boldsymbol{\mu}^{ind}$. Therefore, Eqns. 1.69 and 1.70 allow the estimation of “in-crystal” dipole moments from the knowledge of the polarizability of the constituent molecules and the symmetry operations used to construct the aggregate, which determine the $\mathbf{L}(k, k')$ tensors.

The formalism using (1.69) and (1.70) is usually called *rigorous local field theory* (RLFT), and can be straightforwardly extended to compute atomic and functional-group induced dipole moments $\boldsymbol{\mu}^{ind}(\Omega, k)$ in the k molecule of the crystal, provided that a partitioning scheme is used to calculate $\boldsymbol{\mu}(\Omega)$ and $\boldsymbol{\alpha}(\Omega)$. In this case, the *molecular point-dipole* realization of RLFT, i.e. the one in which each molecule is considered as a point dipole (RLFT1), would be replaced by a *distributed* atomic or functional-group point-dipole treatment, in which n atomic dipoles are distributed over the molecule (RLFT n). The relative accuracy of these approximations depend on the size and shape of the molecules. For small compounds, such as urea or benzene,^{59f,g} RLFT1 and RLFT n do not differ substantially, whereas RLFT n is typically more accurate to describe the anisotropies of larger systems, as shown for *m*-nitroaniline.^{59d}

The first-order polarizabilities of the molecule embedded in its environment can be calculated through numerical differentiation of the induced dipole moments estimated through RLFT. Thus, the components $\alpha_{ij}(\Omega)$ of the polarizability calculated for the molecule in isolation are perturbed and become $\alpha'_{ij}(\Omega)$ in the crystal. Analogously to Eqn. 1.68, $\alpha'_{ij}(\Omega)$ can be computed as:

$$\alpha'_{ij}(\Omega) = \lim_{E_i \rightarrow 0} \frac{[\alpha_{ij}(\Omega) \cdot E_{i,local}]^{E_i} - [\alpha_{ij}(\Omega) \cdot E_{i,local}]^0}{E_i} \quad (1.71)$$

Although the local electric field of Eqn. 1.69 is just a zero-order approximation, only few works have attempted to iterate the process, using the dipole moment of the embedded molecule to compute an improved approximation to the electric field.^{59c,d} Notably, we used this iterative procedure in Chapter 2, finding convergence on dipole moments and polarizabilities within 3-4 cycles for amino acid aggregates.

Within RLFT, the first-order electric susceptibility tensor χ of a molecular crystal with N molecules per unit cell can be written as:

$$\chi = \sum_{k=1}^N \sum_{k'=1}^N (\mathbf{a}^{-1} - \Gamma)_{kk'}^{-1} \quad (1.72)$$

where $\Gamma_{kk'}$ and \mathbf{a} are matrices of order $3N$ whose 3×3 submatrices are respectively the Lorentz tensors $\mathbf{L}(k, k')$ and $\mathbf{a}_k \delta_{kk'}$, in which \mathbf{a}_k is the dimensionless reduced polarizability tensor of molecule k , $\alpha_k / \epsilon_0 V_{cell}$.^{36a} The permittivity tensor is simply obtained as $\boldsymbol{\epsilon} = \mathbf{1} + \chi$, and the three crystalline refractive indices n_i can be calculated from the eigenvalues ϵ_i of the permittivity, $n_i = \sqrt{\epsilon_i}$.

The electric susceptibility tensor and refractive indices of crystalline urea have been estimated from a variety of approaches.^{53b} Among them, RLFT resulted in values very close to the periodic first-principles methods, as well as to the experimental values extrapolated to zero frequency. Interestingly, the application of RLFT to a urea molecule in a cluster overcorrects the refractive indices.

Nevertheless, we note that an isotropic refractive index n_{ISO} suffices for many applications, not only when dealing with molecules in liquids or gases, which are randomly oriented, but also for determination of mean optical properties in crystalline materials. In such cases, the well-known *Clausius-Mossotti equation* is useful for estimating the isotropic molecular polarizabilities from measures of n_{ISO} ,

$$\frac{n_{ISO}^2 - 1}{n_{ISO}^2 + 2} = \frac{1}{3\epsilon_0} \frac{N}{V} \alpha_{ISO} \quad (1.73)$$

in which N/V is the number density or concentration of the material.^{20e} However, this equation is not particularly useful to estimate mean refractive indices of molecules in aggregates from their polarizabilities calculated in an infinitely diluted gas.

1.4.4. Magnetic properties of metal-organic materials

Research in molecular magnetism involves engineering and synthesis of materials exhibiting preconceived magnetic behavior, often applying strategies based on the quantum-mechanical nature of the phenomena.⁶⁰ Although several classes of materials, including organic free radicals, exhibit magnetic behavior,^{61a} of particular appeal are metal-organic coordination compounds in which the magnetic centers are transition-metal ions, and the metal-organic or organometallic building blocks are connected through covalent bonds, coordination interactions and weaker intermolecular bonds. The interplay between chemical interactions of different strength may lead to materials exhibiting single-molecule magnetic behavior, low-dimensional magnetism or three-dimensional long-range magnetic ordering.^{60a} For example, copper(II) pyrazine nitrate and halide coordination polymers have been for long explored as materials,⁶² even though sometimes based solely on empirical knowledge.

Therefore, the understanding of magnetic coupling mechanisms, as required to design new materials with enhanced properties, relies intimately on the strength and nature of intra- and intermolecular interactions, fields in which electron density analysis has obviously a lot to contribute.

The magnetic properties of molecular systems in that there is a unique magnetic center is well described in literature,^{60a} and not further considered here. Instead, we focus on compounds where several magnetic centers interact. The magnetic coupling models applied to these systems rely on *superexchange interactions* between two paramagnetic centers whose atomic wavefunctions overlap. However, for systems with large metal-metal separation, like in ligand-bridged polymetallic systems, no direct bonding can take place between the two metals, and the magnetic interactions are mediated by diamagnetic, ideally closed-shell ligands, acting as couplers, rather than as mere spacers.

The simplest realization of superexchange magnetic interactions can be encountered in dinuclear transition-metal complexes, among them, copper(II) compounds being widely investigated.^{60a} In these cases, two Cu(II) cations in the same molecule are bridged by a diamagnetic ligand that couples the metallic centers. Because of the magnetic coupling, the total spin quantum number S , which assumes the values 0 or 1, is preferred to describe the phenomena, rather than the local spins $S_{\text{Cu}} = 1/2$ (see Eqn. 1.37). The energy of the two pair states are generally not the same, but separated by an energy gap defined as^{60a}

$$J = E_{S=0} - E_{S=1} \quad (1.74)$$

where J is the *exchange-coupling constant* of the particular magnetic interaction. When the state with $S = 0$ is the ground-state, the interaction is *antiferromagnetic* ($J < 0$), whereas when the ground-state is characterized by $S = 1$, the interaction is a *ferromagnetic* one ($J > 0$). In the absence of intermolecular interactions and any other magnetic phenomena,^{60a} the macroscopic *magnetic susceptibility* is straightforwardly given by

$$\chi(T) [\text{emu mol}^{-1}] = \frac{2N_a g^2 \mu_B^2 \mu_0}{k_B T [3 + \exp(-2J/k_B T)]} \quad (1.75)$$

in which the g factor can be calculated from the well-known Landé equation,^{20c} but it is also available from magnetization measurements.⁶² N_a is the Avogadro's number, μ_B is the Bohr magneton, k_B is the Boltzmann constant, and μ_0 is the permeability of free-space ($4\pi \times 10^{-7}$). Therefore, for the rather simple dinuclear complexes, Eqn. 1.75 provides a one-to-one relationship between susceptibility, the quantity that characterizes the magnetic behavior of the material, and exchange-coupling constant, the energy gap that characterizes the magnetic interaction at the molecular level.

When different pair exchange interactions take place, as it is often the case not only for polynuclear magnetic complexes or polymers, but also for mono- or dinuclear compounds interacting through intermolecular interactions, the *low-spin-high-spin energy gap* (1.74) cannot be identified with a single type of dimeric interaction, thus the J parameter yielding the susceptibility in (1.75) averages all possible microscopic coupling constants. For such systems, crystalline orbital calculations must be performed on a series of ferro- and antiferromagnetic phases in order to find the individual pair coupling constants as the solution of a system of equations.^{63a} Alternatively, a method has been proposed to estimate the crystalline susceptibility from gas-phase calculations on selected dinuclear building blocks that are afterwards used to construct the magnetic structure.^{63b}

Even for an *extended magnetic material*, the theoretical calculation of pair exchange-coupling constants, using *dinuclear models* properly extracted from the crystal structure, is still worthwhile because it allows us to distinguish the most relevant magnetic interactions from those that contribute only marginally to the crystal susceptibility.

Let us consider an open-shell system composed by two paramagnetic centers, each with one unpaired electron that, in an unrestricted treatment, occupies one of the two orthogonal magnetic spatial orbitals $\varphi_{i=1,2}$. A spin eigenfunction that describes the singlet ($S = 0$) state assumes the form:^{64a}

$$\Psi_{S=0}^{M_S=0} = \frac{1}{\sqrt{2}} (|\varphi_1\alpha\varphi_2\beta\rangle + |\varphi_1\beta\varphi_2\alpha\rangle) \quad (1.76)$$

While the spin eigenfunctions describing the triplet ($S = 1$) states can be written as:

$$\begin{aligned} \Psi_{S=1}^{M_S=0} &= \frac{1}{\sqrt{2}} (|\varphi_1\alpha\varphi_2\beta\rangle - |\varphi_1\beta\varphi_2\alpha\rangle) \\ \Psi_{S=1}^{M_S=+1} &= |\varphi_1\alpha\varphi_2\alpha\rangle \\ \Psi_{S=1}^{M_S=-1} &= |\varphi_1\beta\varphi_2\beta\rangle \end{aligned} \quad (1.77)$$

where Dirac notation have been used for the Slater determinants. Therefore, the calculation of the exchange-coupling constant as the energy gap between the singlet and triplet states, as shown in Eqn. 1.74, necessarily involves at least one wavefunction, $\Psi_{S=0}^{M_S=0}$, that cannot be expressed as a single-Slater determinant. For this reason, *multi-configurational approaches* are in principle the recommended methods, but, apart from become prohibitively costly, depending on the dinuclear model of interest, the selection of the *active space* is never straightforward because it usually requires knowledge of the magnetic mechanism involved, an information typically not available beforehand.

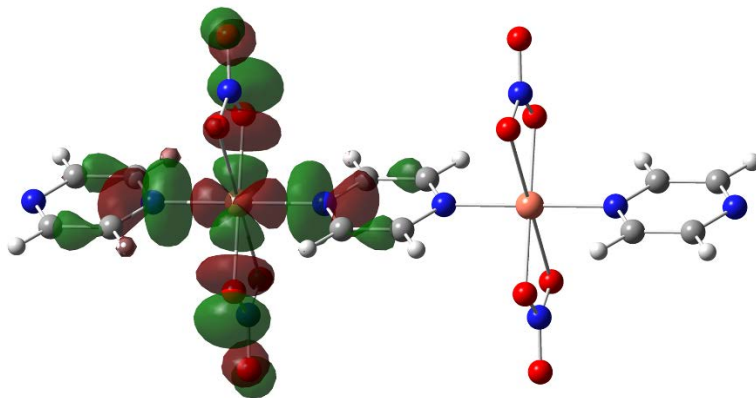


Figure 1.8. A broken-symmetry orbital for a dinuclear model extracted from the Cu(II) pyrazine dinitrate coordination polymer. Small contributions (not shown) can be found at the second metallic center and at the corresponding nitrates.

A possible alternative was proposed by Noodleman,⁶⁵ who suggested to construct single-Slater determinants of mixed spin states that are not intended to represent the true singlet wavefunction (as they are not spin eigenfunctions), but are used to estimate the energy and the properties of the correct singlet. These wavefunctions are called *broken-symmetry solutions* because they are typically characterized by lowered symmetry with respect to that of the nuclear geometry (see Fig. 1.8). For the dinuclear model represented by the states (1.76) and (1.77), the broken-symmetry solutions assume the form:^{64a}

$$\begin{aligned}\Psi_{BS}^{M_S=0} &= |\varphi_1\alpha\varphi_2\beta\rangle \\ \Psi_{BS'}^{M_S=0} &= |\varphi_1\beta\varphi_2\alpha\rangle\end{aligned}\tag{1.78}$$

which can be written as linear combinations of $\Psi_{S=0}^{M_S=0}$ and $\Psi_{S=1}^{M_S=0}$. Within unrestricted Hartree-Fock theory, Noodleman has shown that the energy of (1.78) is related to that of the true singlet and triplet states.^{65a} From this relation, the following expression for the exchange-coupling constant can be deduced:

$$J = 2(E_{BS} - E_{S=1})\tag{1.79}$$

Although capable of predicting the right sign of J , Hartree-Fock theory is generally not quantitatively accurate.⁶⁴ However, the extension of the broken-symmetry approach to unrestricted Kohn-Sham theory is still debatable, and the following relation is frequently used to estimate coupling constants using DFT calculations:^{64a,b}

$$J = E_{BS} - E_{S=1}\tag{1.80}$$

Fortunately, application of (1.80) to dinuclear systems simulated at DFT level using hybrid functionals has found exchange-coupling constants that yield susceptibilities in excellent agreement with experimentally reported values.^{62,66}

Even though the variety of structural and magnetic data available for polynuclear transition-metal complexes has established some structure-property relationships,^{64a,67} the prediction of their magnetic behavior, in particular their exchange-coupling constants and hence their susceptibilities, is far from trivial, mainly due to the intricate interplay between different factors that determine the exchange processes. From this perspective, the knowledge of the electronic structure of polymetallic materials is of particular importance, given that the spin density determines the sign and magnitude of the coupling constants.^{68a} Among the experimental techniques available to determine electronic spin density distributions, single-crystal polarized neutron diffraction stands apart because it affords enormous possibilities to understand the magnetic mechanisms at the atomic and molecular levels. It allows reconstruction of the periodic spin density by fitting either a set of atomic wavefunctions or a multipolar model at various levels of sophistication.^{68b,c} Noteworthy, the reconstruction of spin-resolved electron densities is possible nowadays by combining polarized neutron and high-resolution X-ray diffractions.⁹ From the theoretical side, spin density distributions can be found for very large or even periodic systems thanks to DFT.^{68a} These studies are crucial because the interpretation of magnetic measurements at the atomic and molecular level is not trivial, especially for systems containing many paramagnetic centers. In such cases, theoretical spin densities and orbital analyses have been demonstrated to be very important.^{66,67}

Nevertheless, the determination and analysis of the position densities $\rho_1(\mathbf{r})$ alone, either theoretical or experimental, have played an important role in advancing chemical bond theory, which directly impacts the understanding of superexchange mechanisms. Notably, a method has been developed to calculate the occupancy of the transition-metal valence orbitals from the refined multipole population parameters.^{69a} Because in a transition-metal complex the overlap density in the metal–ligand coordinative bond is usually small, the valence electron density of the transition metal can, to a good approximation, be described using only the corresponding one-center density terms in Eqn. 1.14. This enables to equate the electron density of the d orbitals at the metal, expressed as atomic orbital products, with the pseudo-atomic deformation density (1.50).^{20d} Because all d orbitals are invariant with respect to inversion through the nuclear position, only the terms with l even in (1.50) contribute to the density of the d orbitals. If it is further assumed that the radial dependency of the valence density is the same in both orbital product and multipolar descriptions, the atomic d-orbital populations and the multipolar populations are simply related by:

$$\mathbf{P}_{ij}^T = \mathbf{M}^{-1} \mathbf{P}_{lm\pm}^T \quad (1.81)$$

where \mathbf{P}_{ij} represents the row vector of the 15 unique elements of the symmetric 5×5 matrix whose elements are the population coefficients for the products of the five d orbitals, and $\mathbf{P}_{lm\pm}$ is the row vector containing the coefficients of the 15 spherical harmonic density functions $d_{lm\pm}$ with $l = 0, 2$ or 4. The 15×15 transformation matrix \mathbf{M} can be found in Ref. 20a.

Because the parameters $P_{lm\pm}$ depend on the local coordinate system, the d-orbital occupancies are necessarily dependent on this choice. For highly symmetric environments, such as perfect octahedral or tetrahedral, the choice of local axes is unambiguous and dictated by ligand-field theory considerations. For example, in the former, the x , y and z axes are oriented along the metal–ligand

directions, while in the latter, they are oriented along the fourfold improper axes bisecting the ligands. For environments characterized by much lower or distorted symmetries, the local reference system may not be obvious from the ligand positions. In these cases, it has been proposed that the best local coordinate system is the one with the smallest crossed d-orbital populations, i.e. the one that minimizes the P_{ij} terms with $i \neq j$ in Eqn. 1.81.^{69b}

Accurate analyses of multipolar densities fitted against experimental structure-factor amplitudes have been performed on a few magnetic polynuclear materials.⁶¹ While most of these studies focuses on the QTAIM topological analysis of the metal–metal interactions, thus providing potential magnetic exchange pathways, and on population analysis at the metallic centers, thus identifying the magnetic orbital, in Chapter 3 we show that much more information can be extracted from $\rho_1(\mathbf{r})$. If analysed in conjunction with the spin density and the orbitals bearing the unpaired electrons, parameters readily available from multipolar-fitted electron densities can help elucidating the mechanism of the magnetic exchange. This is highly desirable as a tool not only to rationalize the magnetic phenomena at the level of the building blocks that compose the material, but also to tune their properties accordingly.

1.4.5. Other properties from electron densities

X-ray diffraction and DFT calculations are quite mature techniques to obtain a number of properties from the electron density distribution of materials in their crystalline phases. However, some of these properties have been recently investigated under a refreshing point of view, particularly focused on their applications to rationalize materials behaviour. For example, the *electrostatic potential* of a molecule in a crystal, which can be obtained from both periodically calculated and multipolar fitted charge distributions,^{70a} has been used to identify the most favourable binding sites for guests and counter-ions in metal-organic frameworks, thus providing a tool for rationally design these materials that envisages their application as gas-storage systems.^{70b}

Another example is the *interaction energies* among molecules, which have for long been of interest in the field of biomolecule modelling, but only recently have been investigated under a materials science perspective.^{71a} Spackman introduced a computational approach to accurately estimate intermolecular interaction energies that include the popular electrostatic, polarization, dispersion and exchange-repulsion terms, along with a graphical representation of their topology and strength in molecular crystals.^{71b} These so-called energy frameworks highlight the directions related to the strongest interactions, thus providing a direct visualisation of the most fundamental building blocks in the material. Furthermore, the approach has been applied to examine *mechanical properties* in molecular crystals, in particular bending and shearing, known to be directly related to the anisotropy of the intermolecular interactions in the crystal.^{71c}

From the side of the materials, organic crystals containing larger molecules have been constantly investigated. Experimental and theoretical *databanks of atomic and functional-group multipolar moments* have been created to improve the traditional structure refinement of biomolecules and to estimate their electrostatic properties in crystals.⁷² Because the size of the systems for which experiments are performed typically excludes straightforward application of most high-accuracy quantum-mechanics methods, a number of *embedding strategies* for multi-level simulations has been developed, often based on DFT.⁷³

Experimental and theoretical electron density distributions have been also used to understand and control the materials behaviour of extended inorganic solids. Scherer, investigating the series of carbides Sc_3TC_4 ($T = Fe, Co$ and Ni), has shown that the Laplacian distribution in the T metal VSCC region, which reflects the occupation of the d orbitals, varies significantly along the series, even though the compounds are closely related structurally.⁴⁷ The atomic graph of T has been correlated to the *density of states* and the *band structure* in these crystals, which has enabled unveiling the mechanism governing the structural phase transition that occurs in the Co congener at low temperature, and that makes this species a one-dimensional *superconductor*.⁷⁴

Apart from carbides, many other challenging materials have been investigated. For example, Iversen has focused on *thermoelectric*, *magnetic* and *porous* compounds.⁷⁵ Most of these studies are still highly demanding because the presence of heavy atoms or structural disorder in the crystals require sophisticated experimental and theoretical techniques to obtain accurate electron density distributions. However, as both theoretical and experimental techniques continue to evolve, the importance of electron density analyses in material science also increases. Nevertheless, Pinkerton have been involved in developing the hardware and software, as well as the experimental protocols necessary for “in-house” collection of low-temperature, high-resolution X-ray diffraction data for accurate electron density analysis in crystals containing elements as heavy as the actinides.²⁹ All research on materials crystallography takes advantage of such advances because the main question of how the chemical bonding determines materials properties can now be partially answered on a quantitative basis.

References

1. McWeeny, R.; Sutcliffe, B. T. *Methods of Molecular Quantum Mechanics*; Academic Press: London, **1969**.
2. Gatti, C.; Macchi, P. A Guided Tour through Modern Charge Density Analysis. In *Modern Charge-Density Analysis*; Gatti, C.; Macchi, P. (Eds.); Springer: Netherlands, **2012**; p 1-78.
3. Marx, D.; Hutter, J. *Ab Initio Molecular Dynamics*; Cambridge University Press: Cambridge, **2012**.
4. Macchi, P. *Cryst. Rev.* **2013**, *19*, 58-101.
5. (a) Gillet, J.-M.; Becker, P. J.; Cortona, P. *Phys. Rev. B*, **2001**, *63*, 235115. (b) Gillet, J.-M. *Acta Cryst. Sect. A*, **2007**, *63*, 234-238.
6. (a) Jayatilaka, D.; Grimwood, D. J. *Acta Cryst. Sect. A*, **2001**, *57*, 76-86. (b) Clinton, W. L.; Massa, L. J. *Phys. Rev. Lett.* **1972**, *29*, 1363-1366.
7. (a) Bader, R. F. W.; Gatti, C. *Chem. Phys. Lett.* **1998**, *287*, 233-238. (b) Gatti, C.; Cargnoni, F.; Bertini, L. *J. Comput. Chem.* **2003**, *24*, 422-436.
8. Farrugia, L. J.; Macchi, P. *J. Phys. Chem. A*, **2009**, *113*, 10058-10067.
9. Deutsch, M.; Claiser, N.; Pillet, S.; Chumakov, Y.; Becker, P.; Gillet, J.-M.; Gillon, B.; Lecomte, C.; Souhassou, M. *Acta Cryst. Sect. A*, **2012**, *68*, 675-686.
10. (a) Szabo, A.; Ostlund, N. S. *Modern Quantum Chemistry: Introduction to Advanced Electronic Structure Theory*; Dover Publications Inc.: New York, **1996**. (b) Cramer, C. J. *Essentials of Computational Chemistry: Theory and Models*; John Wiley & Sons: Chichester, **2004**. (c) Jensen, F. *Introduction to Computational*

Chemistry; John Wiley & Sons: Chichester, **2007**. (d) Helgaker, T.; Jorgensen, P.; Olsen, J. *Molecular Electronic-Structure Theory*; Wiley: Chichester, **2000**.

11. (a) Helgaker, T.; Ruden, T. A.; Jorgensen, P.; Olsen, J.; Klopper, W. *J. Phys. Org. Chem.* **2004**, *17*, 913-933. (b) Wiberg, K. B.; Hadad, C. M.; LePage, T. J.; Breneman, C. M.; Frisch, M. *J. Phys. Chem.* **1992**, *96*, 671-679. (c) Velders, G. J.; Feil, D.; *J. Phys. Chem.* **1992**, *96*, 10725-10735. (d) Gatti, C.; MacDougall, P. J.; Bader, R. F. W.; *J. Chem. Phys.* **1988**, *88*, 3792-3804.

12. Pauling, L.; Bright Wilson Jr., E. *Introduction to Quantum Mechanics with Applications to Chemistry*; Dover Publications Inc.: New York, **1963**.

13. (a) Hohenberg, P.; Kohn, W. *Phys. Rev. B.* **1964**, *136*, 864-871. (b) Kohn, W.; Sham, L. J. *Phys. Rev. A* **1965**, *140*, 1133-1138.

14. (a) Burke, K.; Wagner, L. O. *Int. J. Quantum Chem.* **2012**, *113*, 96-101. (b) Sousa, S. F.; Fernandes, P. A.; Ramos, M. J. *J. Phys. Chem. A* **2007**, *111*, 10439-10452.

15. (a) Slater, J. C. *Phys. Rev.* **1951**, *81*, 385-390. (b) Vosko, S. H.; Wilk, L.; Nusair, M. *Can. J. Phys.* **1980**, *58*, 1200-1211.

16. Grimme, S. *WIREs Comput. Mol. Sci.* **2011**, *1*, 211-228.

17. (a) He, Y.; Grafenstein, J.; Kraka, E.; Cremer, D. *Mol. Phys.* **2000**, *98*, 1639-1658. (b) Polo, V.; Kraka, E.; Cremer, D. *Mol. Phys.* **2002**, *100*, 1771-1790.

18. (a) Dovesi, R.; Civalleri, B.; Orlando, R.; Roetti, C.; Saunders, V. *Rev. Comput. Chem.* **2005**, *21*, 1-125. (b) Pisani, C.; Maschio, L.; Casassa, S.; Halo, M.; Schütz, M.; Usvyat, D. *J. Comput. Chem.* **2008**, *29*, 2113-2124.

19. Pisani, C.; Dovesi, R.; Erba, A.; Giannozzi, P. Electron Densities and Related Properties from the Ab-initio Simulation of Crystalline Solids. In *Modern Charge-Density Analysis*; Gatti, C.; Macchi, P. (Eds.); Springer: Netherlands, **2012**; p 79-132.

20. (a) Als-Nielsen, J.; McMorrow, D. *Elements of Modern X-ray Physics*; John Wiley & Sons: Chichester, **2011**. (b) James, R. W. *The Optical Principles of the Diffraction of X-rays*; G. Bell and Sons: London, **1962**. (c) Cohen-Tannoudji, C.; Diu, B.; Laloë, F. *Quantum Mechanics*; Hermann and Wiley & Sons: Paris, **1977**. (d) Coppens, P. *X-Ray Charge Densities and Chemical Bonding*; Oxford University Press: New York, **1997**. (e) Kittel, C. *Introduction to Solid State Physics*; John Wiley & Sons: USA, **2005**.

21. Roversi, P.; Irwin, J. J.; Bricogne, G. *Acta Cryst. Sect. A* **1998**, *54*, 971-996.

22. (a) Fischer, A.; Tiana, D.; Scherer, W.; Batke, K.; Eickerling, G.; Svendsen, H.; Bindzus, N.; Iversen, B. B. *J. Phys. Chem. A* **2011**, *115*, 13061-13071. (b) Bindzus, N.; Straaso, T.; Wahlberg, N.; Becker, J.; Bjerg, L.; Dippel, A.-C.; Iversen, B. B. *Acta Cryst. Sect. A* **2014**, *70*, 39-48.

23. Stewart, R. F. *J. Chem. Phys.* **1969**, *51*, 4569-4577.

24. (a) Dawson, B. *Proc. Roy. Soc. (London) Series A* **1967**, *298*, 255-263. (b) Kurki-Suonio, K. *Acta Cryst. Sect. A* **1968**, *24*, 379-390. (c) Hirshfeld, F. L. *Acta Cryst. Sect. B* **1971**, *27*, 769-781. (d) Stewart, R. F. *J. Chem. Phys.* **1972**, *57*, 1664-1668. (e) Hansen, N. K.; Coppens, P. *Acta Cryst. Sect. A* **1978**, *34*, 909-921.

25. Jelsch, C.; Domagala, S.; Guillot, B.; Liebschner, D.; Fournier, B.; Pichon-Pesme, V.; Lecomte, C. Frontier Applications of Experimental Charge Density and Electrostatics to Bio-macromolecules. In *Modern Charge-Density Analysis*; Gatti, C.; Macchi, P. (Eds.); Springer: Netherlands, **2012**; p 527-551.

26. Kurki-Suonio, K. *Isr. J. Chem.* **1977**, *16*, 115-123.
27. (a) Clementi, E.; Roetti, C. *Atom. Data Nucl. Data Tab.* **1974**, *14*, 177-478. (b) Su, Z.; Coppens, P. *Acta Cryst. Sect. A* **1998**, *54*, 646-652. (c) Macchi, P.; Coppens, P. *Acta Cryst. Sect. A* **2001**, *57*, 656-662. (d) Clementi, E.; Raimondi, D. L. *J. Chem. Phys.* **1963**, *38*, 2686-2689. (e) Bunge, C. F.; Barrientos, J. A.; Bunge, A. V. *Atom. Data Nucl. Data Tab.* **1993**, *53*, 113-162. (f) Volkov, A.; Macchi, P. The PBE/QZ4P Zora Wavefunction Databank. *Unpublished work* **2006**.
28. Gillet, J.-M.; Koritsanszky, T. Past, Present and Future of Charge Density and Density Matrix Refinements. In *Modern Charge-Density Analysis*; Gatti, C.; Macchi, P. (Eds.); Springer: Netherlands, **2012**; p 181-211.
29. (a) Zhurov, V. V.; Zhurova, E. A.; Pinkerton, A. A. *Inorg. Chem.* **2011**, *50*, 6330-6333. (b) Zhurov, V. V.; Zhurova, E. A.; Stash, A. I.; Pinkerton, A. A. *J. Phys. Chem. A* **2011**, *115*, 13016-13023.
30. (a) Jeffrey, G. A.; Piniella, J. F. (Eds.) *The Application of Charge Density Research to Chemistry and Drug Design*; Plenum Press: New York, **1991**. (b) Stewart, R. F.; Spackman, M. A.; Flensburg, C. *VALRAY – User’s Manual*; Pittsburgh and Denmark, **2000**.
31. (a) Meindl, K.; Henn, J. *Acta Cryst. Sect. A* **2008**, *64*, 404-418. (b) Meindl, K.; Henn, J. *Struct. Bond.* **2012**, *147*, 143-192.
32. (a) Mukherji, A.; Karplus, M. *J. Chem. Phys.* **1963**, *38*, 44-48. (b) Jayatilaka, D. Using Wavefunctions to Get More Information Out of Diffraction Experiments. In *Modern Charge-Density Analysis*; Gatti, C.; Macchi, P. (Eds.); Springer: Netherlands, **2012**; p 213-257. (c) Grimwood, D. J.; Jayatilaka, D. *Acta Cryst. Sect. A* **2001**, *57*, 87-100. (d) Bytheway, I.; Grimwood, D. J.; Jayatilaka, D. *Acta Cryst. Sect. A* **2002**, *58*, 232-243. (e) Grimwood, D. J.; Bytheway, I.; Jayatilaka, D. *J. Comput. Chem.* **2003**, *24*, 470-483.
33. (a) Genoni, A. *J. Phys. Chem. Lett.* **2013**, *4*, 1093-1099. (b) Genoni, A. *J. Chem. Theory Comput.* **2013**, *9*, 3004-3019.
34. (a) Stewart, R. F. *J. Chem. Phys.* **1969**, *51*, 4569-4577. (b) Coppens, P.; Willoughby, T. V.; Csonka, L. N. *Acta Cryst. Sect. A* **1971**, *27*, 248-256. (c) Tanaka, K. *Acta Cryst. Sect. A* **1988**, *44*, 1002-1008.
35. (a) Becker, P. J.; Coppens, P. *Acta Cryst. Sect. A* **1974**, *30*, 129-147. (b) Larson, A. C. The Inclusion of Secondary Extinction in Least-Squares Refinement in Crystal Structures. In *Crystallographic Computing*; Ahmed, F. R.; Hall, S. R.; Huber, C. P. (Eds.); Munksgaard: Copenhagen, **1970**; p 291-294.
36. (a) Whitten, A. E.; Jayatilaka, D.; Spackman, M. A. *J. Chem. Phys.* **2006**, *125*, 174505. (b) Jayatilaka, D.; Munshi, P.; Turner, M. J.; Howard, J. A.; Spackman, M. A. *Phys. Chem. Chem. Phys.* **2009**, *11*, 7209-7218. (c) Húdak, M.; Jayatilaka, D.; Perainova, L.; Biskupic, S.; Kozisek, J.; Bucinsky, L; *Acta Cryst. Sect. A* **2010**, *66*, 78-92.
37. Jayatilaka, D.; Dittrich, B. *Acta Cryst. Sect. A* **2008**, *64*, 383-393.
38. (a) Destro, R.; Lo Presti, L.; Soave, R.; Goeta, A. E. Multi-temperature Electron Density Studies. In *Modern Charge-Density Analysis*; Gatti, C.; Macchi, P. (Eds.); Springer: Netherlands, **2012**; p 659-696. (b) Elsaesser, T.; Woerner, M. Transient Charge Density Maps from Femtosecond X-ray Diffraction. In *Modern Charge-Density Analysis*; Gatti, C.; Macchi, P. (Eds.); Springer: Netherlands, **2012**; p 697-714. (c) Macchi, P.; Casati, N. Electron Density in Molecules Under High Pressure. *Sagamore XVIII Conference on Charge, Spin and Momentum Densities*. Santa Margherita de Pula. **2015**.

39. (a) Tsirelson, V. G.; Gorfman, S. V.; Pietsch, U. *Acta Cryst. Sect. A* **2003**, *59*, 221-227. (b) Gorfman, S. V.; Tsirelson, V. G.; Pietsch, U. *Acta Cryst. Sect. A* **2005**, *61*, 387-396. (c) Schmidt, O.; Gorfman, S.; Bohaty, L.; Neumann, E.; Engelen, B.; Pietsch, U. *Acta Cryst. Sect. A* **2009**, *65*, 267-275.
40. (a) Bader, R. F. W. *Atoms in Molecules – A Quantum Theory*; Clarendon Press: Oxford, **1990**. (b) Popelier, P. *Atoms in Molecules – An Introduction*; Pearson Education Ltd.: Harlow, **2000**. (c) Matta, C. F.; Boyd, R. J. (Eds.) *The Quantum Theory of Atoms in Molecules: From Solid State to DNA and Drug Design*; Wiley-VCH: Weinheim, **2007**.
41. (a) Bader, R. F. W.; Beddall, P. M. *J. Chem. Phys.* **1972**, *56*, 3320-3329. (b) Hirshfeld, F. L. *Theor. Chim. Acta* **1977**, *44*, 129-138. (c) Guerra, C. F.; Handegraaf, J. W.; Baerends, E. J.; Bickelhaupt, F. M. *J. Comput. Chem.* **2004**, *25*, 189-210. (d) Stone, A. J.; Alderton, M. *Mol. Phys.* **2002**, *100*, 221-233. (e) Mulliken, R. S. *J. Chem. Phys.* **1955**, *23*, 1833-1846 and 2338-2347. (f) Lödwin, P.-O. *Adv. Quantum Chem.* **1970**, *5*, 185-199. (g) Reed, A. E.; Weinstock, R. B.; Weinhold, F. *J. Chem. Phys.* **1985**, *83*, 735-747.
42. Martín-Pendás, A.; Kohout, M.; Blanco, M. A.; Francisco, E. Beyond Standard Charge Density Topological Analyses. In *Modern Charge-Density Analysis*; Gatti, C.; Macchi, P. (Eds.); Springer: Netherlands, **2012**; p 303-358.
43. Cassam-Chenaï, P.; Jayatilaka, D. *Theor. Chem. Acc.* **2001**, *105*, 213-218.
44. (a) Gadre, S.; Shrivastava, I. H. *J. Chem. Phys.* **1991**, *94*, 4384-4390. (b) Becke, A. D.; Edgecombe, K. E. *J. Chem. Phys.* **1990**, *92*, 5397-5404. (c) Martín-Pendás, A.; Trujillo, J. H. *J. Chem. Phys.* **2012**, *137*, 134101.
45. Martín-Pendás, A.; Blanco, M. A.; Costales, A.; Sánchez, P. M.; Luaña, V. *Phys. Rev. B* **1999**, *83*, 1930-1933.
46. (a) Bader, R. F. W. *J. Phys. Chem. A* **1998**, *102*, 7314-7323. (b) Martín-Pendás, A.; Francisco, E.; Blanco, M. A.; Gatti, C. *Chem. Eur. J.* **2007**, *13*, 9362-9371. (c) Macchi, P. *Chimia* **2009**, *63*, 1-6. (d) Macchi, P.; Sironi, A. *Coord. Chem. Rev.* **2003**, *238*, 383-412.
47. Scherer, W.; Eickerling, G.; Hauf, C.; Presnitz, M.; Scheidt, E.-W.; Eyert, V.; Pöttgen, R. On the Interplay Between Real and Reciprocal Space Properties. In *Modern Charge-Density Analysis*; Gatti, C.; Macchi, P. (Eds.); Springer: Netherlands, **2012**; p 359-385.
48. (a) Gillespie, R. J.; Robinson, E. A. *Chem. Soc. Rev.* **2005**, *34*, 396-407. (b) Gillespie, R. J. *Coord. Chem. Rev.* **2000**, *197*, 51-69.
49. (a) Solymar, L.; Walsh, D.; Syms, R. R. A. *Electrical Properties of Materials*; Oxford University Press: Oxford, **2014**. (b) Hummel, R. E. *Electronic Properties of Materials*; Springer: New York, **2011**.
50. (a) Spackman, M. A. *Chem. Rev.* **1992**, *92*, 1769-1797. (b) Bonin, K. D.; Kresin, V. *Electric-Dipole Polarizabilities of Atoms, Molecules and Clusters*; World Scientific: Singapore, **1956**. (c) Bishop, D. M.; Kirtman, B. *J. Chem. Phys.* **1992**, *97*, 5255-5256.
51. (a) Applequist, J.; Carl, J. R.; Fung, K.-K. *J. Am. Chem. Soc.* **1972**, *94*, 2952-2960. (b) Applequist, J. *Acc. Chem. Res.* **1977**, *10*, 79-85. (c) Miller, K. J. *J. Am. Chem. Soc.* **1990**, *112*, 8533-8542. (d) No, K. T.; Cho, K. H.; Jhon, M. S.; Scheraga, H. A. *J. Am. Chem. Soc.* **1993**, *115*, 2005-2014. (e) van Duijnen, P. Th.; Swart, M. *J. Phys. Chem. A*, **1998**, *102*, 2399-2407. (f) Maple, J. R.; Ewig, C. S. *J. Chem. Phys.* **2001**, *115*, 4981-4988. (g) Ewig, C. S.; Waldman, M.; Maple, J. R. *J. Phys. Chem. A*, **2002**, *106*, 326-334. (h) in het Panhuis, M.; Munn, R. W.; Popelier, P. L. A. *J. Chem. Phys.* **2004**, *120*, 11479-11486.

52. (a) Bader, R. F. W.; Larouche, C.; Gatti, C.; Carroll, M. T.; MacDougall, P. J. *J. Chem. Phys.* **1987**, *87*, 1142-1152. (b) Laidig, K. E.; Bader, R. F. W. *J. Chem. Phys.* **1990**, *93*, 7213-7224. (c) Bader, R. F. W.; Keith, T. A.; Gough, K. M.; Laidig, K. E. *Mol. Phys.* **1992**, *75*, 1167-1189. (d) Jansen, G.; Hättig, C.; Hess, B. A.; Ángyán, J. G. *Mol. Phys.* **1996**, *88*, 69-92. (e) Hättig, C.; Jansen, G.; Hess, B. A.; Ángyán, J. G. *Mol. Phys.* **1997**, *91*, 145-160. (f) in het Panhuis, M.; Popelier, P. L. A.; Munn, R. W.; Ángyán, J. G. *J. Chem. Phys.* **2001**, *114*, 7951-7961. (g) Stone, A. J.; Hättig, C.; Jansen, G.; Ángyán, J. G. *Mol. Phys.* **1996**, *89*, 595-605.
53. (a) Keith, T. A. Atomic Response Properties. In *The Quantum Theory of Atoms in Molecules: From Solid State to DNA and Drug Design*; Matta, C. F.; Boyd, R. J. (Eds.); Wiley-VCH: Weinheim, **2007**; p 61-94. (b) Krawczuk, A.; Pérez, D.; Macchi, P. *J. Appl. Cryst.* **2014**, *47*, 1452-1458. (c) Krawczuk, A.; Pérez, D.; Stadnicka, K.; Macchi, P. *Trans. Am. Cryst. Assoc.* **2011**, *42*, 1-25. (d) Chimpri, A. S.; Gryl, M.; Dos Santos, L. H. R.; Krawczuk, A.; Macchi, P. *Cryst. Growth Des.* **2013**, *13*, 2995-3010. (e) Krawczuk, A.; Macchi, P. *Chem. Central J.* **2014**, *8*, 68. (f) Macchi, P.; Krawczuk, A. *Comput. Theor. Chem.* **2015**, *1053*, 165-172.
54. (a) Krishtal, A.; Senet, P.; Yang, M.; Van Alsenoy, C. *J. Chem. Phys.* **2006**, *125*, 034312. (b) Krishtal, A.; Senet, P.; Van Alsenoy, C. *J. Chem. Theory Comput.* **2008**, *4*, 426-434. (c) Marenich, A. V.; Cramer, C. J.; Truhlar, D. G. *Chem. Sci.* **2013**, *4*, 2349-2356. (d) Otero, N.; Van Alsenoy, C.; Pochan, C.; Karamanis, P. *J. Comput. Chem.* **2015**, *36*, 1831-1843.
55. (a) Fkyerat, A.; Guelzim, A.; Baert, F.; Paulus, W.; Heger, G.; Zyss, J.; Périgaud, A. *Acta Cryst. Sect. B* **1995**, *51*, 197-209. (b) Fkyerat, A.; Guelzim, A.; Baert, F.; Zyss, J.; Périgaud, A. *Phys. Rev. B* **1996**, *53*, 16236. (c) Hamzaoui, F.; Zanoun, A.; Vergoten, G. *J. Mol. Struct.* **2004**, *697*, 17-22.
56. (a) Hickstein, D. D.; Cole, J. M.; Turner, M. J.; Jayatilaka, D. *J. Chem. Phys.* **2013**, *139*, 064107. (b) Cole, J. M.; Hickstein, D. D. *Phys. Rev. B* **2013**, *88*, 184105.
57. (a) Whitten, A. E.; Turner, P.; Klooster, W. T.; Piltz, R. O.; Spackman, M. A. *J. Phys. Chem. A* **2006**, *110*, 8763-8776. (b) Dittrich, B.; Jayatilaka, D. *Struct. Bond.* **2002**, *147*, 27-46. (c) Balakina, M. Y.; Nefediev, S. E. *Int. J. Quantum Chem.* **2006**, *106*, 2245-2253. (d) Balakina, M. Y.; Fominykh, O. D. *Int. J. Quantum Chem.* **2008**, *108*, 2678-2692.
58. (a) Champagne, B.; Bishop, D. M. *Adv. Chem. Phys.* **2003**, *126*, 41-92. (b) Wu, K.; Snijders, J. G.; Lin, C. *J. Phys. Chem. B* **2002**, *106*, 8954-8958.
59. (a) Dunmur, D. A. *Mol. Phys.* **1972**, *23*, 109-115. (b) Cummins, P. G.; Dunmur, D. A.; Munn, R. W.; Newham, R. J. *Acta Cryst. Sect. A* **1976**, *32*, 847-853. (c) Spackman, M. A.; Munshi, P.; Jayatilaka, D. *Chem. Phys. Lett.* **2007**, *443*, 87-91. (d) Reis, H.; Papadopoulos, M. G.; Calaminici, P.; Jug, K.; Köster, A. M. *Chem. Phys.* **2000**, *261*, 359-371. (e) Reis, H.; Raptis, S. G.; Papadopoulos, M. G. *Chem. Phys.* **2001**, *263*, 301-316. (f) Reis, H.; Raptis, S. G.; Papadopoulos, M. G.; Janssen, R. H. C.; Theodorou, D. N.; Munn, R. W. *Theor. Chem. Acc.* **1998**, *99*, 384-390. (g) Reis, H.; Papadopoulos, M. G.; Munn, R. W. *J. Chem. Phys.* **1998**, *109*, 6828-6838.
60. (a) Kahn, O. *Molecular Magnetism*; Wiley-VCH: New York, **1993**. (b) Miller, J. S.; Drillon, M. (Eds.); *Magnetism: Molecules to Materials*; Wiley-VCH: Weinheim, **2001**.
61. (a) Pillet, S.; Souhassou, M.; Lecomte, C. *Acta Cryst. Sect. A* **2004**, *60*, 455-464. (b) Overgaard, J.; Hibbs, D. E.; Rentschler, E.; Timco, G. A.; Larsen, F. K. *Inorg. Chem.* **2003**, *42*, 7593-7601. (c) Overgaard, J.; Walsh, J. P. S.; Hathwar, V. R.; Jorgensen, M. R. V.; Hoffman, C.; Platts, J. A.; Piltz, R.; Winpenny, R. E. P. *Inorg. Chem.* **2014**, *53*, 11531-11539. (d) Pillet, S.; Souhassou, M.; Mathonière, C.; Lecomte, C. *J. Am. Chem. Soc.* **2004**, *126*, 1219-1228.

62. (a) Manson, J. L.; Conner, M. M.; Schlueter, J. A.; McConnell, A. C.; Southerland, H. I. et al. *Chem. Mat.* **2008**, *20*, 7408-7416. (b) Lapidus, S. H.; Manson, J. L.; Liu, J.; Smith, M. J.; Goddard, P. et al. *Chem. Comm.* **2013**, *49*, 3558-3560. (c) Lancaster, T.; Blundell, S. J.; Brooks, M. L.; Baker, P. J.; Pratt, F. L.; Manson, J. L.; Landee, C. P.; Baines, C. *Phys. Rev. B* **2006**, *73*, 020410.
63. (a) Reinhardt, P.; Moreira, I. P. R.; de Graaf, C.; Dovesi, R.; Illas, F. *Chem. Phys. Lett.* **2000**, *319*, 625-630. (b) Deumal, M.; Bearpark, M. J.; Novoa, J. J.; Robb, M. A. *J. Phys. Chem. A* **2002**, *106*, 1299-1315.
64. (a) Ruiz, E.; Alvarez, S.; Rodríguez-Forteza, A.; Alemany, P.; Pouillon, Y.; Massobrio, C. Electronic Structure and Magnetic Behavior in Polynuclear Transition-Metal Compounds. In *Magnetism: Molecules to Materials II*; Miller, J. S.; Drillon, M. (Eds.); Wiley-VCH: Weinheim, **2003**; p 227-279. (b) Ruiz, E.; Cano, J.; Alvarez, S.; Alemany, P. *J. Comput. Chem.* **1999**, *20*, 1391-1400. (c) Ruiz, E. *Struct. Bond.* **2004**, *113*, 71-102.
65. (a) Noodleman, L. *J. Chem. Phys.* **1981**, *74*, 5737-5743. (b) Noodleman, L.; Peng, C. Y.; Case, D. A.; Mouesca, J.-M. *Coord. Chem. Rev.* **1995**, *144*, 199-244.
66. (a) Desplanches, C.; Ruiz, E.; Rodríguez-Forteza, A.; Alvarez, S. *J. Am. Chem. Soc.* **2002**, *124*, 5197-5205. (b) Cauchy, T.; Ruiz, E.; Jeannin, O.; Nomura, M.; Fourmigué, M. *Chem. Eur. J.* **2007**, *13*, 8858-8866.
67. (a) Richardson, H. W.; Wasson, J. R.; Hatfield, W. E. *Inorg. Chem.* **1977**, *16*, 484-486. (b) de Biani, F. F.; Ruiz, E.; Cano, J.; Novoa, J. J.; Alvarez, S. *Inorg. Chem.* **2000**, *39*, 3221-3229.
68. (a) Ruiz, E.; Cirera, J.; Alvarez, S. *Coord. Chem. Rev.* **2005**, *249*, 2649-2660. (b) Schweizer, J.; Ressouche, E. Neutron Scattering and Spin Densities in Free Radicals. In *Magnetism: Molecules to Materials I*; Miller, J. S.; Drillon, M. (Eds.); Wiley-VCH: Weinheim, **2001**; p 325-355. (c) Gillon, B. Spin Distributions in Molecular Systems with Interacting Transition Metal Ions. *Ibid.* p 357-378.
69. (a) Holladay, A.; Leung, P.; Coppens, P. *Acta Cryst. Sect. A* **1983**, *39*, 377-387. (b) Sabino, J. R.; Coppens, P. *Acta Cryst. Sect. A* **2003**, *59*, 127-131.
70. (a) Volkov, A.; King, H. F.; Coppens, P.; Farrugia, L. J. *Acta Cryst. Sect. A* **2006**, *62*, 400-408. (b) Chimpri, A. S. *PhD Thesis*; Bern, **2013**.
71. (a) Dominiak, P. M.; Espinosa, E.; Ángyán, J. G. Intermolecular Interaction Energies from Experimental Charge Density Studies. In *Modern Charge-Density Analysis*; Gatti, C.; Macchi, P. (Eds.); Springer: Netherlands, **2012**; p 387-433. (b) Turner, M. J.; Grabowsky, S.; Jayatilaka, D.; Spackman, M. A. *J. Phys. Chem. Lett.* **2014**, *5*, 4249-4255. (c) Turner, M. J.; Thomas, S. P.; Shi, M. W.; Jayatilaka, D.; Spackman, M. A. *Chem. Comm.* **2015**, *51*, 3735-3738.
72. Bak, J. M.; Domagala, S.; Hübschle, C.; Jelsch, C.; Dittrich, B.; Dominiak, P. M. *Acta Cryst. Sect. A* **2011**, *67*, 141-153.
73. Wesolowski, T. A.; Shedge, S.; Zhou, X. *Chem. Rev.* **2015**, *115*, 5891-5928.
74. Eickerling, G.; Hauf, C.; Scheidt, E.-W.; Reichardt, L.; Schneider, C.; Muñoz, A.; Lopez-Moreno, S.; Romero, A. H.; Porcher, F.; André, G.; Pöttgen, R.; Scherer, W. *Z. Anorg. Allg. Chem.* **2013**, *639*, 1985-1995.
75. Overgaard, J.; Grin, Y.; Takata, M.; Iversen, B. B. Charge Density in Materials and Energy Science. In *Modern Charge-Density Analysis*; Gatti, C.; Macchi, P. (Eds.); Springer: Netherlands, **2012**; p 469-504.

Chapter 2

Distributed Atomic Polarizabilities of Amino Acids and their Hydrogen-Bonded Aggregates*

In this chapter, with the purpose of rationally designing linear optical materials, distributed atomic polarizabilities of amino acid molecules and their hydrogen-bonded aggregates are calculated in order to identify the most efficient functional groups, able to build-up larger electric susceptibilities in crystals. Moreover, we carefully analyse how the atomic polarizabilities depend on the one-electron basis set or the many-electron Hamiltonian, including both wavefunction and density functional theory methods. This is useful for selecting the level of theory that best combines high accuracy and low computational costs, very important in particular when using the cluster method to estimate susceptibilities of molecular-based materials.

2.1. Introduction, motivation and specific goals

The linear and non-linear optical responses are correlated to the electric (hyper)polarizabilities and susceptibilities at molecular and macroscopic levels, respectively. With the current computational resources, (hyper)polarizabilities of medium-size molecules in the gas-phase can be computed with satisfactory accuracy if sufficient electronic correlation is included and extended atomic basis sets are used. This has enabled the design of various molecular-based optical materials, but, as stated by Champagne and Bishop,¹ the knowledge acquired in the field of single-molecule (hyper)polarizability calculations must evolve to quantitatively rationalize optical properties of the solid state, a field which is far less advanced. In fact, with few exceptions, a useful electro-optical material will be in the solid state and, frequently, in a crystalline or partially crystalline phase. For this reason, the ultimate goal is the investigation of optical properties in periodically homogeneous systems.

As discussed in Chapter 1, calculations under periodic boundary conditions are the most adequate approaches to model crystalline effects. However, mainly because of the rather limited amount of electronic correlation that can be included within these methods, some alternatives have emerged, in particular the first-principles supermolecule or *cluster method*, and the semi-empirical *local-field factor* corrections. This techniques are fully explored in this chapter to help understanding the short- and long-range crystal field effects on distributed polarizabilities.

Because density functional theory (DFT) may be inappropriate for correct evaluation of the intermolecular dispersion forces, one of the goals of the present work is to identify the most accurate DFT functionals able to estimate optical properties in molecular assemblies, using calculations of high-level electron correlation as benchmarks. The performance of DFT have been rigorously investigated for the polarizabilities of large water clusters.² It was found that the accuracy of post-Hartree-Fock levels of theory was not sufficiently higher than that of DFT to justify the increased computational costs. In this chapter, we aim at extend this analysis to amino acid aggregates, through a careful estimation of the cost/benefits and the *marginal utility* of extending the level of theory.

*This chapter was taken and modified from Dos Santos, L. H. R.; Krawczuk, A.; Macchi, P. *J. Phys. Chem. A* **2015**, *119*, 3285-3298.

For us, it is also important to breakdown the molecular or crystal polarizability into its atomic or functional-group contributions. Visualizing and analysing atomic and bond polarizabilities of a system is useful because functional groups represent the way in which chemists reduce molecules for synthetic and engineering purposes. In fact, a given molecular property may especially originate from one particular group. In this respect, *transferability* is a key concept that allows exporting quantities, calculated with high accuracy in small molecules, to atoms or functional groups belonging to complex systems, like macromolecules, polymers or crystals,³ that would be too expensive to calculate *ab initio*.

Here, the QTAIM distributed atomic polarizabilities of amino acids and their hydrogen-bonded aggregates are calculated at different theoretical levels, using the method proposed by Keith within the “atomic response theory”,^{4a} which was modified and implemented in the *PolaBer* program.^{4b} We focus on the first-order polarizability tensor α due to its relative simplicity, its major role in both qualitative and quantitative considerations of reaction paths and molecular interactions, and, of course, its prominence in determining linear optical properties of materials. For this analysis, we have chosen the natural α -amino acids in their zwitterionic form, because the optical properties of their crystals, co-crystals, salts and metal hybrids have attracted much attention in the last few years.⁵

As anticipated in Chapter 1, while some components of the total polarizability tensors are measurable, either in the gas or in the condensed phase, no procedure is available for the experimental determination of polarizabilities of atoms in molecules. Therefore, for benchmarking the various DFT functionals, we use post-Hartree-Fock methods up to *coupled-cluster* (CC) techniques, known to deliver highly accurate polarizabilities.²

Another purpose of our work is testing the efficiency of Gaussian-type basis sets for the calculations of distributed polarizabilities. Both Pople and Dunning families are considered. These investigations allow us to propose a protocol for the evaluation of optical properties of molecular materials that is both quality- and cost-oriented.

The last goal of our study is to quantify the perturbation of hydrogen bonds on the molecular polarizabilities, analysing the most common aggregation modes of amino acids in the solid state.

2.2. Theoretical methods

Electron densities were obtained by molecular-orbital wavefunction calculations at various levels of approximation. We used the glycine molecule and three hydrogen-bonded dimers as references in order to test various basis-set expansions and to compare results from different DFT functionals against those from coupled-cluster (CC), configuration interaction (CI) or perturbation methods (second-order Møller-Plesset, MP2). Firstly, the polarizabilities of the glycine monomer and the dimers were investigated with increasing level of electron correlation, up to coupled-cluster singles-and-doubles (CCSD), and increasing basis-set rank, up to quadruple-zeta quality including diffuse and polarization functions. Secondly, the polarizability of the glycine monomer was calculated using various density functionals and then compared against results at the highest electron-correlated levels. Thirdly, results with basis sets from Pople and Dunning families were compared against each other at the CAM-B3LYP level of theory, found to be one of the best-performing functionals. Finally, all the

20 amino acids and some dimers were investigated at the CAM-B3LYP/d-aug-cc-pVDZ level, which was determined to be the best compromise between accuracy and computational costs.

When available, three-dimensional coordinates were taken from measured single-crystal neutron diffraction data and kept frozen. This choice is necessary because the most stable configuration of the amino acids in the gas-phase is the neutral one, whereas the zwitterionic forms are the most frequently observed species in liquid solutions and crystal phases. Because stationary points for the zwitterionic forms are normally not found in gas-phase potential energy surfaces, we could not use optimized geometries. For those amino acids in which X-ray structures only are available, the heavier atom positions were kept at measured values and the distances to the attached H atoms were normalized to the average neutron diffraction values. Because the crystal structure of lysine is not known, the calculations were performed for its cationic form, lysinium. Correlated calculations use the frozen-core approximation. All the wavefunction calculations were performed using the Gaussian 09 package^{6a} and the corresponding charge density distributions were partitioned in keeping with the QTAIM, using the AIMAll program.^{6b}

PolaBer^{4b} was used to calculate distributed atomic polarizabilities according to the procedure discussed in Chapter 1, section 1.4.2. The method is based on QTAIM partitioning of the ground-state electron density $\rho_1^0(\mathbf{r})$, and the field-perturbed densities $\rho_1^{E_j}(\mathbf{r})$ of a molecular system into their atomic contributions. The algorithm was already tested and proved a reliable way to breakdown the molecular α tensor into atomic contributions.^{5,7} Because QTAIM is an “exact” partitioning scheme, the sum of the atomic polarizabilities must coincide, a part for minor numerical imprecision, to the molecular polarizability calculated using the coupled-perturbed Hartree-Fock (CPHF) or Kohn-Sham (CPKS) equations.

In this chapter, atomic polarizability tensors are frequently visualized as ellipsoids in the same three-dimensional space as the molecule, assuming $1 \text{ \AA}^3 \equiv 1 \text{ \AA}$, but a scaling factor of 0.4 \AA^{-2} is applied to reduce the size of the ellipsoids for visualization purposes.

All the amino acids under study and their aggregates have C_1 symmetry. Therefore, the first-order polarizability tensors have six different non-zero components. We report the components of the diagonalized tensors (α_{11} , α_{22} , α_{33}). The isotropic polarizability was estimated as:

$$\alpha_{ISO} = \frac{1}{3} \text{Tr} \alpha = \frac{1}{3} (\alpha_{11} + \alpha_{22} + \alpha_{33}) \quad (2.1)$$

While the anisotropy of the polarizability tensor is typically estimated by:⁸

$$\Delta\alpha = \left\{ \frac{1}{2} [3\text{Tr}(\alpha^2) - (\text{Tr}\alpha)^2] \right\}^{1/2} \quad (2.2)$$

All polarizabilities are reported in atomic units unless stated otherwise. Sources of error on the calculated static polarizabilities are due to the incompleteness of both electronic correlation models and basis sets, and the limited accuracy of the atomic basin integration procedures.⁹

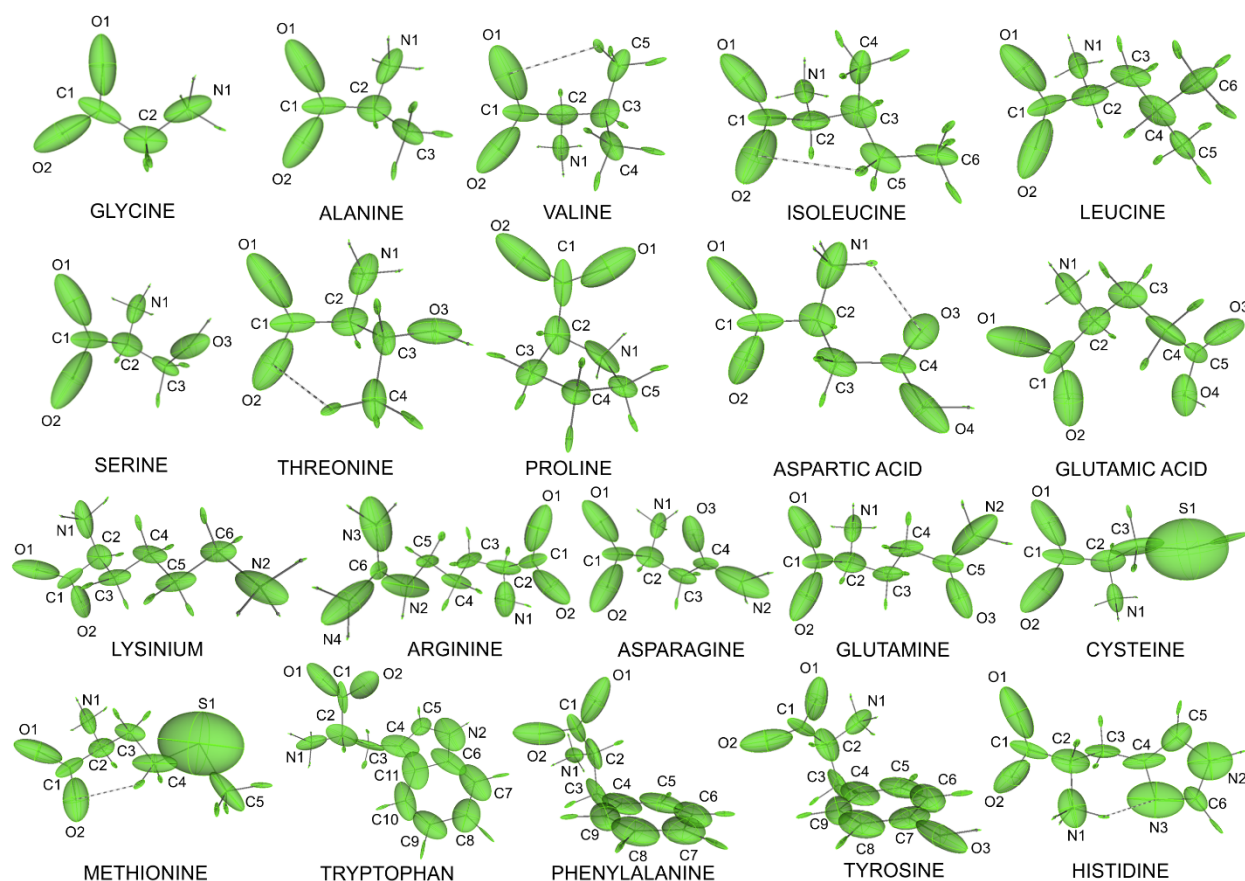


Figure 2.1. Atomic polarizability ellipsoids for the amino acids at the CAM-B3LYP/d-aug-cc-pVDZ level of theory. Intramolecular hydrogen bonds are shown as dashed lines.

2.3. Results and discussion

2.3.1. Atomic and functional-group polarizabilities in amino acid molecules

One of the main aims of our work is quantifying the contribution of individual atoms and, more importantly, of functional groups to specific optical properties, like the refractive index. Distributed atomic polarizabilities are particularly useful, because they enable reconstructing the polarizability of a functional group in a molecule by simple sum of the atomic tensors. Fig. 2.1 shows the polarizabilities for the twenty zwitterionic α -amino acids, calculated at the CAM-B3LYP/d-aug-cc-pVDZ level of theory. Noteworthy, atomic polarizabilities are extremely sensitive to the local chemical environment, being larger along the directions of covalently bonded atoms. For example, in the carboxylic groups, the polarizability ellipsoids of the oxygen atoms are stretched in the direction of the C–O bonds, because these bonds are highly polarizable due to the π -bonding character and the large electronegativity difference between their atoms. In the carbonylic groups, the oxygen polarizability is approximately symmetrical about the C–O bond axis, unless involved in a hydrogen bond. Instead, the polarizability ellipsoid of oxydrilic oxygen atoms is slightly rotated due to the O–H bond. The hydrogen atoms have extremely prolate ellipsoids along the X–H bond direction, but overall their polarizabilities are very small due to their low electronic populations. Intramolecular hydrogen bonds increase the polarizability of H atoms, besides them being more positively charged, and modify the shape and orientation of the polarizability tensor of the hydrogen bond acceptor.

Table 2.1. Average values of functional-group polarizabilities in the 20 amino acids. Standard deviations (SD) and maximum absolute differences (MAD) from the mean for polarizability features are given. In parenthesis are the amino acids for which the maximum differences occur. Calculations are at the CAM-B3LYP and MP2 levels of theory with the d-aug-cc-pVDZ basis set.^a

	Average		MAD			Average		MAD	
	CAM-B3LYP	MP2	CAM-B3LYP	MP2		CAM-B3LYP	MP2	CAM-B3LYP	MP2
COO⁻					OH				
α_{11}	14.9 ± 0.5	15.4 ± 0.6	1.6 (arg)	1.6 (arg)	α_{11}	5.3 ± 0.1	5.5 ± 0.1	0.2 (thr)	0.2 (asp)
α_{22}	26.9 ± 0.8	28 ± 1	1.8 (tyr)	1.6 (arg)	α_{22}	6.5 ± 0.6	6.4 ± 0.5	0.9 (tyr)	0.8 (glu)
α_{33}	28.8 ± 0.9	29.9 ± 0.9	1.6 (his)	1.9 (gly)	α_{33}	13 ± 2	14 ± 2	3 (tyr)	3 (tyr)
α_{iso}	23.5 ± 0.5	24.4 ± 0.5	1.2 (arg)	1.1 (arg)	α_{iso}	8.6 ± 0.4	8.7 ± 0.4	0.7 (tyr)	0.6 (ser)
$\Delta\alpha$	13.1 ± 0.7	13.7 ± 0.8	1.3 (try)	1.3 (tyr)	$\Delta\alpha$	8 ± 2	8 ± 2	3 (tyr)	3 (tyr)
$\alpha_{iso}/V_{0.001au}$	0.073	0.073	$\alpha_{iso}/V_{0.001au}$	0.058	0.058
NH₃⁺					C=O				
α_{11}	7.3 ± 0.8	7.4 ± 0.3	1.9 (cys)	0.8 (gly)	α_{11}	7.2 ± 0.3	7.3 ± 0.3	0.4 (glu)	0.4 (asn)
α_{22}	8 ± 1	8.6 ± 0.9	2.7 (his)	3.4 (his)	α_{22}	12.7 ± 0.9	13 ± 1	1.7 (asn)	2 (glu)
α_{33}	15 ± 1	14.5 ± 0.8	2.8 (cys)	1.5 (cys)	α_{33}	17 ± 1	17 ± 1	2 (gln)	2 (asp)
α_{iso}	10.1 ± 0.9	10.2 ± 0.3	2.3 (phe)	0.9 (cys)	α_{iso}	12.4 ± 0.4	12.6 ± 0.4	0.6 (gln)	0.6 (gln)
$\Delta\alpha$	6.8 ± 0.9	6.6 ± 0.9	1.7 (his)	1.6 (asp)	$\Delta\alpha$	8.9 ± 0.9	9 ± 1	1.4 (asp)	1 (asp)
$\alpha_{iso}/V_{0.001au}$	0.062	0.062	$\alpha_{iso}/V_{0.001au}$	0.072	0.072
Cα					N(sp²)H₂				
α_{11}	4.3 ± 0.3	4.3 ± 0.3	0.7 (try)	0.7 (pro)	α_{11}	7.9 ± 0.5	8.3 ± 0.6	0.6 (gln)	0.7 (gln)
α_{22}	7.8 ± 0.7	7.5 ± 0.7	2.0 (arg)	1.9 (arg)	α_{22}	9.1 ± 0.5	9.2 ± 0.6	0.8 (arg)	0.9 (arg)
α_{33}	10 ± 1	10 ± 1	3 (arg)	3 (arg)	α_{33}	17.4 ± 0.9	18.0 ± 0.9	1.6 (arg)	1.6 (arg)
α_{iso}	7.4 ± 0.3	7.3 ± 0.3	0.6 (thr)	0.5 (tyr)	α_{iso}	11.5 ± 0.4	11.8 ± 0.4	0.5 (arg)	0.6 (arg)
$\Delta\alpha$	5 ± 1	5 ± 1	3 (arg)	3 (arg)	$\Delta\alpha$	8.9 ± 0.9	8.9 ± 0.9	1.3 (arg)	1.3 (arg)
$\alpha_{iso}/V_{0.001au}$	0.15	0.15	$\alpha_{iso}/V_{0.001au}$	0.067	0.067
CH₃					(C₆)phenyl^b				
α_{11}	11.7 ± 0.4	11.5 ± 0.5	0.8 (ileu)	0.7 (met)	α_{11}	29.9 ± 0.7	30.9 ± 0.9	1.1 (try)	1.5 (try)
α_{22}	12.2 ± 0.3	12.2 ± 0.4	0.4 (val)	0.7 (ileu)	α_{22}	51 ± 3	55 ± 1	3 (phe)	1 (phe)
α_{33}	17 ± 2	17 ± 2	5 (met)	7 (met)	α_{33}	72 ± 5	77 ± 4	5 (phe)	4 (tyr)
α_{iso}	13.6 ± 0.7	13.6 ± 0.8	1.4 (met)	2.0 (met)	α_{iso}	51 ± 2	54 ± 1	3 (phe)	2 (try)
$\Delta\alpha$	5 ± 2	5 ± 2	4 (met)	6 (met)	$\Delta\alpha$	36 ± 5	39 ± 3	5 (phe)	4 (tyr)
$\alpha_{iso}/V_{0.001au}$	0.062	0.062	$\alpha_{iso}/V_{0.001au}$	0.11	0.11
C(sp³)H₂					S				
α_{11}	8.5 ± 0.9	8.5 ± 0.7	2.1 (cys)	1.6 (gly)	α_{11}	14 ± 1	15 ± 1
α_{22}	10 ± 1	10 ± 1	3 (tyr)	3 (tyr)	α_{22}	17.6 ± 0.1	17.8 ± 0.2
α_{33}	14 ± 2	14 ± 2	5 (met)	6 (met)	α_{33}	24.2 ± 0.8	24.7 ± 0.2
α_{iso}	11.0 ± 0.8	11 ± 1	1.6 (tyr)	2 (asp)	α_{iso}	18.8 ± 0.8	19.1 ± 0.6
$\Delta\alpha$	5 ± 2	5 ± 2	5 (met)	5 (met)	$\Delta\alpha$	8.6 ± 0.4	8.8 ± 0.9
$\alpha_{iso}/V_{0.001au}$	0.073	0.073	$\alpha_{iso}/V_{0.001au}$	0.089	0.089
C(sp³)H									
α_{11}	7.7 ± 0.9	7.8 ± 0.7	2.0 (pro)	1.9 (thr)					
α_{22}	9.3 ± 0.6	9.3 ± 0.5	1.4 (cys)	1.1 (asp)					
α_{33}	11 ± 1	11 ± 1	4 (arg)	4 (arg)					
α_{iso}	9.5 ± 0.6	9.5 ± 0.5	1.5 (thr)	1.2 (thr)					
$\Delta\alpha$	3 ± 1	3 ± 1	4 (arg)	3 (arg)					
$\alpha_{iso}/V_{0.001au}$	0.10	0.10					

^a $V_{0.001au}$ denotes the functional-group volume defined by an electron density isosurface of 0.001 au. SD and MAD values relative to the $\alpha_{iso}/V_{0.001au}$ ratio are omitted as they are very small.

^b The transferable features for the phenyl ring were calculated neglecting the H atoms as this allows one to export the group for molecules containing more than one substituent in the ring. The polarizability of the H atoms is anyway negligible compared to the entire group.

Fig. 2.1 also shows that each atom belonging to a functional group has very similar polarizabilities in all amino acids, suggesting a potentially good transferability. Table 2.1 gathers the average values for the diagonalized polarizability tensors of various functional groups. The standard deviation (SD) and the maximum absolute difference (MAD) from the mean are good indicators of the similarities. For the isotropic polarizability, α_{iso} , SD and MAD are sufficiently small (less than 10% and 15% from the average values, respectively) for all but the methyl and methylenic functional groups. The

anisotropy $\Delta\alpha$ is instead more variable. The worst outlier is methionine, for which the polarizability of the $-\text{CH}_2-$ and $-\text{CH}_3$ groups is significantly larger than the average among all other amino acids. This difference is due to the highly polarizable sulfur atom, which increases the polarizability of all the atoms chemically bounded to it.

The average polarizabilities of the groups can be taken as the *transferable functional group* and used to estimate the electric susceptibility of a material, without carrying out a full quantum-mechanical calculation. They are shown in Fig. 2.2 at the CAM-B3LYP/d-aug-cc-pVDZ level of theory. These quantities were constrained to the idealized symmetry of the fragment by averaging the pertinent components of the tensor. For example, the polarizability of the carboxylate group was averaged in order to respect the ideal C_{2v} symmetry of the fragment.

Table 2.2 shows the calculated molecular polarizability tensors, with full *ab initio* treatments (CAM-B3LYP and MP2) or with the transferable-groups. As benchmark, we take the polarizabilities derived, using the Clausius-Mossotti equation, from experimental measurements of molar refraction in aqueous solution.¹⁰ The differences between experimental and calculated values are within 6%, a good result given that calculations do not account for wavelength dispersion or solvent effects.¹¹ Our results are also in good agreement with other additive models of polarizabilities.^{11b}

The isotropic polarizabilities computed *via* the transferable groups (shown in Table 2.2 under the heading α_{iso}^{transf}) compare very well against the *ab initio* or the experimental values. For each amino acid, only small absolute differences occur, in the range of 1-3 au for most of the molecules, corresponding approximately to the propagated standard deviations of the transferable groups.

In order to confirm the validity of the transferable functional groups, we computed the polarizability of some molecules, for example β -alanine and α -aminoisobutyric acid, that contain the same functional groups but that are outside the set used to construct the database. The results in Table 2.3 indicate that the transferable groups pass this test as well, with good comparison against experimental values, when available.^{10b}

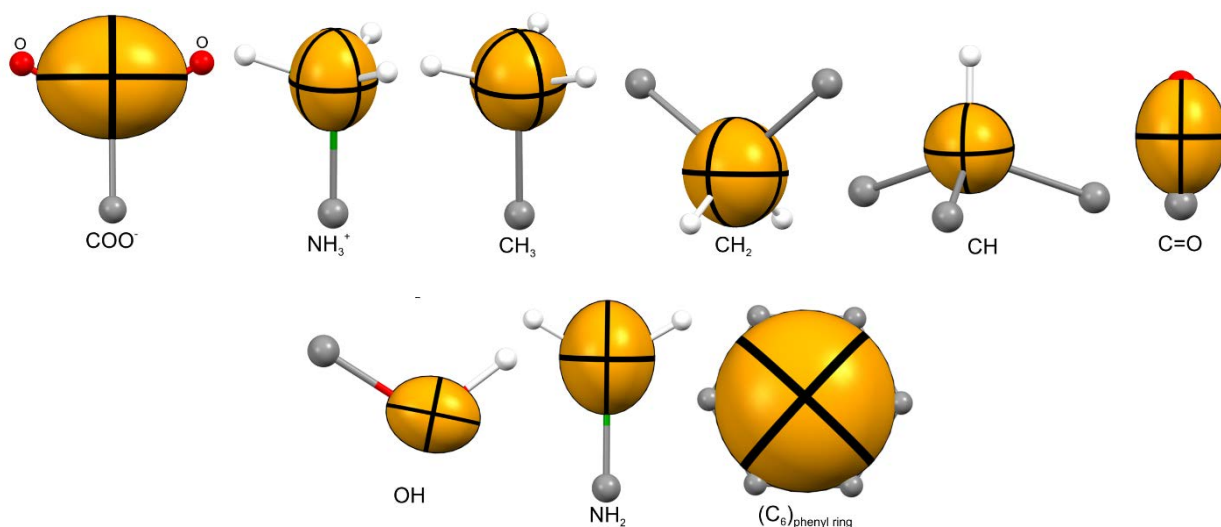


Figure 2.2. Polarizability ellipsoids for the main functional groups of the amino acids at the CAM-B3LYP/d-aug-cc-pVDZ level of theory. Ellipsoids are centered at the corresponding center of mass.

Table 2.2. Diagonalized tensor components for the polarizability of the amino acids calculated at CAM-B3LYP and MP2 levels of theory using the d-aug-cc-pVDZ basis set.

	CAM-B3LYP/d-aug-cc-pVDZ						MP2/d-aug-cc-pVDZ						Exptl. ^a
	α_{11}	α_{22}	α_{33}	α_{iso}	$\Delta\alpha$	α_{iso}^{transf}	α_{11}	α_{22}	α_{33}	α_{iso}	$\Delta\alpha$	α_{iso}^{transf}	α_{iso}
Glycine	35.78	49.31	57.88	47.66	19.30	45 ± 1	36.26	50.35	57.77	48.13	18.92	46 ± 1	44.3 ± 0.6
Alanine	47.32	58.45	65.12	56.96	15.58	57 ± 1	47.42	59.44	64.89	57.25	15.48	58 ± 1	55.9 ± 0.7
Valine	72.23	80.23	86.05	79.50	12.02	80 ± 2	72.10	80.05	86.85	79.67	12.79	81 ± 1	81.5 ± 0.4
Isoleucine	81.84	91.34	101.33	91.50	16.88	91 ± 2	82.33	91.31	102.10	91.91	17.15	92 ± 2	95.2 ± 0.6
Leucine	86.17	91.70	97.43	91.77	9.75	91 ± 2	86.94	92.12	98.04	92.37	9.62	92 ± 2	94.5 ± 0.4
Serine	53.06	63.82	69.10	62.00	14.16	63 ± 1	53.14	64.35	69.09	62.19	14.19	64 ± 1	61.2 ± 0.4
Threonine	61.73	78.13	79.36	73.07	17.05	72 ± 2	62.19	78.77	80.27	73.74	17.38	73 ± 1	73.7 ± 0.4
Proline	64.66	73.55	81.65	73.29	14.72	76 ± 2	64.98	74.31	82.39	73.89	15.09	77 ± 2	73.5 ± 0.4
Aspartic acid	59.04	75.52	86.75	73.77	24.14	75 ± 2	59.71	76.54	87.06	74.44	23.90	76 ± 1	...
Glutamic acid	74.12	89.84	95.38	86.45	19.10	86 ± 2	74.46	91.01	95.89	87.12	19.45	87 ± 2	90.4 ± 0.4
Lysinium	81.57	94.85	118.23	98.22	32.15	101 ± 2	81.60	95.15	117.13	97.96	31.06	102 ± 2	101.2 ± 0.5 ^b
Arginine	99.74	115.89	138.52	118.05	33.74	115 ± 2	101.16	117.81	140.67	119.88	34.36	116 ± 2	115.6 ± 0.2
Asparagine	70.49	77.53	89.90	79.31	17.02	78 ± 2	71.28	77.83	91.93	80.35	18.28	80 ± 1	79.8 ± 0.7
Glutamine	82.54	93.28	95.43	90.42	11.96	89 ± 2	83.02	94.91	95.94	91.29	12.44	91 ± 2	91.2 ± 0.6
Cysteine	57.26	71.38	87.13	77.92	25.88	76 ± 1	63.29	76.78	94.85	78.31	27.43	77 ± 1	...
Methionine	81.92	97.99	126.78	102.23	39.37	100 ± 2	82.52	98.49	128.26	103.09	40.21	101 ± 2	102.1 ± 0.1
Tryptophan	104.20	161.57	197.90	154.56	81.82	156 ± 2	106.51	161.07	201.39	156.32	82.48	150 ± 2	157.8 ± 0.5
Phenylalanine	96.19	122.64	150.18	123.00	46.76	119 ± 2	97.77	124.15	151.63	124.52	46.64	123 ± 2	122.9 ± 0.3
Tyrosine	95.25	132.60	153.86	127.24	51.39	127 ± 2	97.10	133.03	154.95	128.36	50.59	130 ± 2	...
Histidine	73.12	104.25	127.63	101.67	47.37	99 ± 1	74.28	105.47	128.48	102.75	47.12	100 ± 1	102.6 ± 0.4

^a Experimental values extracted from the molar refractions, measured in aqueous solution at $\lambda = 589$ nm and 25 °C, using the Clausius-Mossotti equation, from ref. 10a.

^b Reported value for lysine.

Table 2.3. Diagonalized tensor components for the polarizability of β -alanine and α -aminoisobutyric acid, calculated *ab initio*, at the CAM-B3LYP/d-aug-cc-pVDZ level of theory, and using the transferable-group treatment.

	CAM-B3LYP/d-aug-cc-pVDZ					Transferable-group treatment					Exptl. ^a
	α_{11}	α_{22}	α_{33}	α_{iso}	$\Delta\alpha$	α_{11}	α_{22}	α_{33}	α_{iso}	$\Delta\alpha$	α_{iso}
β -alanine	44.06	53.92	65.86	54.61	18.91	45.24	53.04	67.62	55.30	19.67	...
α -aminoisobutyric acid	56.21	66.23	69.68	64.04	12.11	61.79	68.65	74.35	68.26	10.89	67.34

^a Experimental value extracted from molar refraction, measured in aqueous solution at $\lambda = 578$ nm, using the Clausius-Mossotti equation, from ref. 10b.

Our analysis enables to ascertain the role of each functional group in the build-up of optical properties. The linear susceptibility of a crystal is proportional to the unit-cell polarizability per unit-cell volume, a “polarizability density”, which is approximately an additive function. Therefore, the most promising functional groups and amino acid molecules are those that maximize their α/V ratio. In principle, the isotropic molecular polarizability and the molecular volume should correlate linearly.^{3b} Fig. 3(a) shows the linear regression between the calculated α_{ISO} and the molecular volume $V_{0.001au}$ (*i.e.* determined by a 0.001 au isosurface of electron density). The regression coefficient is 0.98. However, for some amino acids the calculated isotropic polarizabilities exceed the correlation, see also Table 2.2. Cysteine, phenylalanine, tyrosine and tryptophan have in fact the largest $\alpha_{ISO}/V_{0.001au}$ ratio, see Fig. 3(b). For a proper estimation of the optical properties in the solid, one should consider the volume actually occupied by the molecule when embedded in the crystal, which depends on the packing ability, determined by the number of sites available for strong hydrogen bonding with the neighbours. Fig. 3(c) shows the polarizability density calculated as $Z\alpha_{ISO}/V_{unit-cell}$, where $V_{unit-cell}$ is the room-temperature unit-cell volume and Z is the number of molecules per unit cell. The polarizability

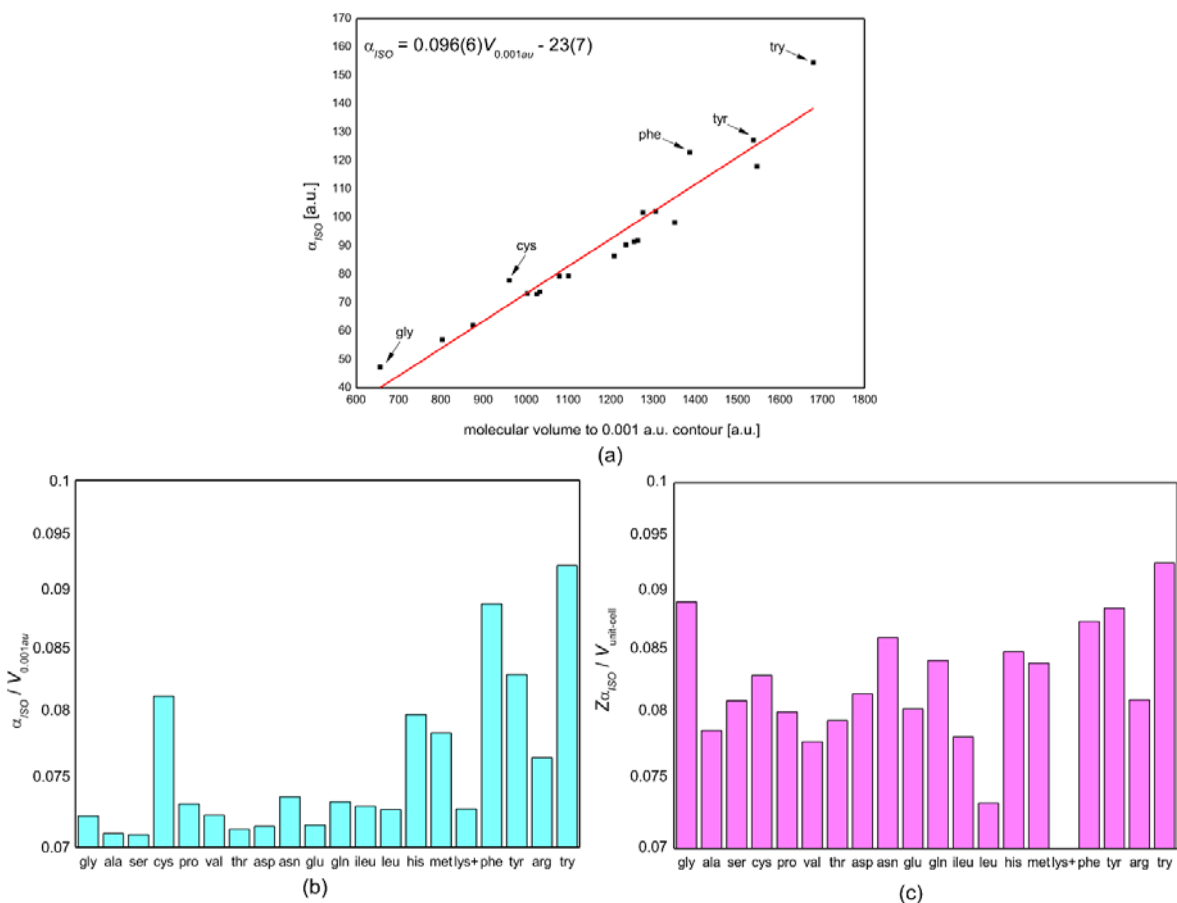


Figure 2.3. (a) Isotropic molecular polarizabilities plotted against the molecular volumes determined by a 0.001 au isosurface of electron density. (b) and (c) Polarizability densities for the amino acids. In (b), the molecular volume is defined by a 0.001 au isosurface of electron density, while in (c) it is defined by the room-temperature unit-cell volume. Z is the number of molecules per unit cell. All calculations were performed at the CAM-B3LYP/d-aug-cc-pVDZ level.

densities of glycine, tryptophan, phenylalanine and tyrosine are larger than those of the other molecules, addressing these amino acids as more promising for fabricating optical waveguides or other devices requiring high refractive index. Accurate experimental values are available only for few amino acids, whereas some preliminary periodic DFT calculations, confirm highest refractive indices for tryptophan, glycine, tyrosine and phenylalanine. With the exception of glycine, these molecules present aromatic rings, empirically well-known for large, though anisotropic, molecular polarizability. Even though high anisotropy is to be avoided in many optical applications, this is by no means a limitation on the use of the aromatic amino acids. In fact, molecules may pack in a crystal without alignment of the aromatic moieties, thus producing a rather isotropic susceptibility. The high $Z\alpha_{ISO}/V_{unit-cell}$ ratio for glycine is due to the relatively large contribution of the $C\alpha$ atom to the molecular polarizability and the high packing density when compared to other amino acid crystals. In fact, as shown in Table 2.1, the $C\alpha$ atom features the highest $\alpha_{ISO}/V_{0.001au}$ ratio of all functional groups, and in glycine, $C\alpha$ counts more than in all other amino acids.

Analogously to the molecular quantities, the polarizability densities of the individual functional groups are useful parameters for the rational design of efficient opto-electronic molecules, especially concerning polymer-based optical devices, as the optical properties of their molecular subunits can be easily tunable by appropriate functionalization.¹²

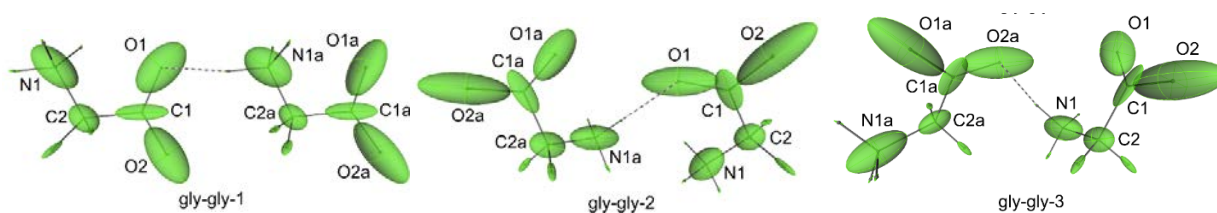


Figure 2.4. Atomic polarizability ellipsoids for glycine dimers at CAM-B3LYP/d-aug-cc-pVDZ level of theory. Hydrogen bonds are shown as dashed lines. The N...O distance is 2.97 Å in gly-gly-2 and 2.80 Å in gly-gly-1 and gly-gly-3.

Table 2.4. Polarizabilities of the glycine monomer and gly-gly dimers. The isotropic polarizability (α_{ISO}) and the anisotropy of polarizability ($\Delta\alpha$) are reported for the aug-cc-pVDZ, aug-cc-pVTZ and d-aug-cc-pVDZ basis sets using a variety of methods. In the dimers, the polarizabilities for the hydrogen bond donor and acceptor molecules are reported. Due to computational costs, full series of correlated calculation was performed only for gly-gly-1 with the aug-cc-pVDZ basis set.

Method		α_{ISO}						$\Delta\alpha$							
		aug-cc-pVDZ		aug-cc-pVTZ		d-aug-cc-pVDZ		aug-cc-pVDZ		aug-cc-pVTZ		d-aug-cc-pVDZ			
monomer		HF	41.29	41.63	41.80	13.86	13.67	13.72	CID	43.31	43.32	43.89	15.67	15.66	15.74
		CISD	43.44	43.39	44.03	16.09	15.75	15.91	CCD	45.24	45.27	45.89	16.89	17.04	17.22
		CCSD	46.70	46.45	47.38	19.10	18.48	18.87	MP2	47.38	47.75	48.13	19.15	18.96	18.92
Method		α_{ISO}						$\Delta\alpha$							
		aug-cc-pVDZ		aug-cc-pVTZ		d-aug-cc-pVDZ		aug-cc-pVDZ		aug-cc-pVTZ		d-aug-cc-pVDZ			
		donor	acceptor	donor	acceptor	donor	acceptor	donor	acceptor	donor	acceptor	donor	acceptor		
gly-gly-1		HF	41.54	40.49	42.03	40.65	42.01	40.62	14.88	16.17	15.17	16.30	14.88	16.09	
		CID	43.00	41.66	43.53	41.90	16.65	17.70	16.46	17.47	
		CISD	43.03	41.69	43.56	41.93	16.71	17.71	16.50	17.52	
		CCD	45.62	43.96	18.72	19.52	
		CCSD	46.88	45.11	20.35	21.37	
		MP2	47.73	45.75	48.17	45.83	48.51	46.04	20.51	21.37	20.53	21.37	20.47	21.31	
gly-gly-2		HF	42.41	41.36	42.63	41.52	42.83	41.67	16.63	17.44	16.17	17.20	16.40	17.17	
		MP2	49.46	47.44	49.63	47.62	50.13	47.88	22.72	22.93	22.26	22.69	22.38	22.62	
gly-gly-3		HF	41.91	40.84	42.27	41.02	42.36	41.15	9.51	16.80	9.33	16.63	9.14	16.95	
		MP2	48.92	46.82	49.39	46.32	49.46	47.05	13.41	22.29	13.49	21.76	13.12	22.11	

2.3.2. Electron correlation and basis-set effects

An important matter of debate is the role of electron correlation and basis-set completeness for the calculation of polarizabilities.¹³ In order to investigate how much they affect atomic polarizabilities, we have analysed an isolated glycine molecule and three dimers (Fig. 2.4), with increasing amount of electron correlation and basis-set functions. In all dimers, the molecules are connected through one N–H...O hydrogen bond: one of them is a “head-to-tail” aggregation, whereas the other two are “lateral” aggregations. Table 2.4 gathers the relevant features of molecular polarizability calculated at several levels, from Hartree-Fock (HF) to MP2 and CCSD, with augmented correlation-consistent basis sets. The isotropic polarizabilities, α_{ISO} , at CCSD and MP2 levels are *ca.* 10-15% larger than at the HF level. A similar trend is observed for $\Delta\alpha$. While α_{ISO} increases with the basis-set size, the largest $\Delta\alpha$ occurs for the smallest aug-cc-pVDZ basis set.

Compared with CCSD, the truncated CI methods (CID and CISD) underestimate the magnitude of the polarizability tensors and their anisotropy, providing only a smaller increment compared with HF. On the other hand, CCSD and MP2 give quite comparable α_{ISO} and $\Delta\alpha$. The trend for the monomer is replicated by the dimer gly-gly-1 calculated at many intermediate levels of theory (CID, CISD and CCD) using the aug-cc-pVDZ basis set. The increasing correlation level has a very similar effect on either the donor or the acceptor molecules, whose polarizabilities are easily determined using the distributed atomic ones.

The highest level of approximation is the iterative introduction of triple or even quadruple excitations (CCSDT or CCSDTQ models). However, the trend observed for gly-gly-1 may suggest that high-order correlation is not likely to play a significant role for larger aggregates because, on going from CCD to CCSD, α_{ISO} increases less for the dimer than for the monomer. As concluded by Hammond *et al.*² for water clusters at various coupled-cluster levels of theory, triple or higher excitations are less significant as the number of molecules increases. Noteworthy, the calculation of amino acid aggregates is currently very challenging at the CCSDT level of theory even with the smaller aug-cc-pVDZ basis set. While CCSDT/aug-cc-pVDZ calculations are feasible for the glycine monomer, this will likely not produce meaningful results due to the imbalance between a high-level correlation method and a small/medium size basis set.¹⁴

In light of these findings, MP2 results as the most efficient level of theory, i.e. the one with largest accuracy/cost ratio, to estimate the electronic correlation effects on the distributed polarizabilities. Therefore, we have selected the MP2 level for benchmarking the various basis sets (see below) and DFT functionals (see next section).

Concerning the selection of a basis set, Table 2.5 lists the results at the HF and MP2 levels of theory for very large basis sets, up to quadruple-zeta quality and several levels of augmentation¹⁵ within the Dunning family for the glycine monomer and the gly-gly-1 dimer. The number of diffuse functions is more important to achieve convergence than the valence splitting X for both α_{ISO} and $\Delta\alpha$: for the augmented basis sets aug-cc-pVXZ, change in α_{ISO} and $\Delta\alpha$ is still noticeable on going from the double- to the triple-zeta quality sets, whereas the d-aug-cc-pVXZ series is already converged with the double-zeta quality basis set ($X = D$).

We can conclude that d-aug-cc-pVDZ is the ideal basis set to calculate the polarizabilities of the larger amino acid aggregates, again adopting a criterion of largest accuracy/cost ratio, where cost is here represented by the basis-set rank.

Calculations of the glycine monomer and the gly-gly-1 dimer polarizabilities using the Pople family of basis set were also performed. The α_{ISO} convergence is extremely slow mainly because the smaller Pople basis sets lack the additional diffuse functions present instead in the Dunning family. Only the largest Pople basis set, namely 6-311++G(3df,3pd), would be satisfactory, but its rank is quite higher than d-aug-cc-pVDZ. For this reason, Pople basis sets are no further considered in our analysis.

Table 2.5. Polarizabilities and their anisotropies for the glycine monomer and the gly-gly-1 dimer at HF and MP2 levels of theory with the Dunning family of basis sets. In the dimer, the polarizabilities for the hydrogen bond donor and acceptor molecules are reported.

	Basis set	Rank	α_{ISO}				$\Delta\alpha$			
			HF		MP2		HF		MP2	
monomer	cc-pVDZ	95	32.63		35.95		12.72		16.63	
	cc-pVTZ	220	37.06		41.03		13.26		17.60	
	cc-pVQZ	425	39.29		43.92		13.65		18.40	
	m-aug-cc-pVDZ	115	38.27		44.16		14.01		19.17	
	m-aug-cc-pVTZ	240	40.11		45.84		14.15		19.37	
	m-aug-cc-pVQZ	445	40.88		46.59		13.99		19.21	
	aug-cc-pVDZ	160	41.29		47.38		13.86		19.15	
	aug-cc-pVTZ	345	41.63		47.75		13.67		18.96	
	aug-cc-pVQZ	630	41.71		47.75		13.66		18.84	
	d-aug-cc-pVDZ	225	41.80		48.13		13.72		18.92	
	d-aug-cc-pVTZ	470	41.80		47.97		13.72		18.85	
	d-aug-cc-pVQZ	835	41.75		47.81		13.67		18.81	

	Basis set	Rank	α_{ISO}				$\Delta\alpha$			
			HF		MP2		HF		MP2	
			donor	acceptor	donor	acceptor	donor	acceptor	donor	acceptor
gly-gly-1	cc-pVDZ	190	33.40	32.54	36.77	35.65	15.56	12.60	20.42	16.87
	cc-pVTZ	440	37.40	36.99	41.45	40.99	16.40	13.93	21.69	18.76
	m-aug-cc-pVDZ	230	38.59	37.52	44.69	42.64	14.02	14.96	19.55	20.03
	m-aug-cc-pVTZ	480	40.31	39.32	46.25	44.30	14.66	15.88	20.41	21.05
	aug-cc-pVDZ	320	41.54	40.49	47.73	45.75	14.88	16.17	20.51	21.37
	aug-cc-pVTZ	690	42.03	40.65	48.17	45.83	15.17	16.30	20.53	21.37
	d-aug-cc-pVDZ	450	42.01	40.62	48.51	46.04	14.88	16.09	20.47	21.31

2.3.3. Benchmarking of density functionals for distributed polarizabilities

Although the correct method to compute polarizabilities requires the explicit treatment of electronic correlation, for practical applications on large systems only DFT is feasible. Therefore, a functional is desirable that could provide results as close as possible to correlated calculations. We have evaluated the performances of the most popular density functionals for the calculation of distributed polarizabilities. The main features of the DFT schemes under investigation are described in Table 2.6, classified according to Sousa *et al.*^{16a} As discussed in the previous section, MP2 is taken as benchmark. The comparisons refer to calculations performed using the d-aug-cc-pVTZ basis set, one of the most complete basis set applied in this study, certainly guaranteeing basis-set convergence as discussed in the previous section.

α_{ISO} and $\Delta\alpha$ for glycine calculated with the different density functionals are plotted in Fig. 2.5. The LSDA and GGA-based functionals underperform all the other DFT methods, with a clear tendency to overestimate both α_{ISO} and $\Delta\alpha$. The meta-GGA functionals provide some improvement, with errors ranging approximately from 5% to 13% with respect to the MP2/d-aug-cc-pVTZ benchmark. Hybrid functionals, which include part of exact exchange, generally show good performance. Among them, the so-called long-range corrected ones, like CAM-B3LYP, or and the highly parameterized M06-2X and BMK functionals, predict the most accurate α_{ISO} and $\Delta\alpha$.

In view of these results and those presented in the previous section, we have selected the CAM-B3LYP/d-aug-cc-pVDZ level of theory to perform further calculations on dimers and small clusters. This is in keeping with the known limitations of “conventional” DFT that significantly overestimates (hyper)polarizabilities, especially for systems presenting long-chain lengths.¹⁷ In many cases, these drawbacks have been largely improved by applying long-range correction schemes^{18a-c} or highly parameterized functionals,^{18d} as confirmed by our results.

Table 2.6. Summary of the DFT functionals evaluated for the distributed polarizabilities of amino acids.^a

Type	Functional	χ	Exchange	Correlation
LSDA	SVWN	0	Slater	Vosko-Wilk-Nusair80
GGA	BP86	0	Becke88	Perdew86
	BLYP	0	Becke88	Lee-Yang-Parr
	BPW91	0	Becke88	Perdew-Wang91
	PBE	0	Perdew-Burke-Ernzerhof	Perdew-Burke-Ernzerhof
	HCTH	0	Hamprecht-Cohen-Tozer-Handy	Hamprecht-Cohen-Tozer-Handy
	mPWLYP	0	modified Perdew-Wang91	Lee-Yang-Parr
	mPWPBE	0	modified Perdew-Wang91	Perdew-Burke-Ernzerhof
	mPWPW91	0	modified Perdew-Wang91	Perdew-Wang91
	OLYP	0	OptX	Lee-Yang-Parr
M-GGA	BB95	0	Becke88	Becke95
	VSXC	0	Van Voorhis-Scuseria	Van Voorhis-Scuseria
	TPSS	0	Tao-Perdew-Staroverov-Scuseria	Tao-Perdew-Staroverov-Scuseria
H-GGA	B3P86	20	Becke88	Perdew86
	B3PW91	20	Becke88	Perdew-Wang91
	B3LYP	20	Becke88	Lee-Yang-Parr
	PBE0	25	Perdew-Burke-Ernzerhof	Perdew-Burke-Ernzerhof
	B97-2	21	B97-2	B97-2
	O3LYP	11.6	OptX	Lee-Yang-Parr
	X3LYP	21.8	Becke88 + Perdew-Wang91	Lee-Yang-Parr
	mPW1LYP	25	modified Perdew-Wang91	Lee-Yang-Parr
	mPW3PBE	25	modified Perdew-Wang91	Perdew-Burke-Ernzerhof
HM-GGA	TPSSh	10	Tao-Perdew-Staroverov-Scuseria	Tao-Perdew-Staroverov-Scuseria
	BMK	42	BMK	BMK
	M06-2X	54	M06-2X	M06-2X
LC-H-GGA	CAM-B3LYP ^b	19-65	Becke88	Lee-Yang-Parr
	LC-BLYP ^c	0-100	Becke88	Lee-Yang-Parr
	ω B97	0-100	modified B97	B97

^a χ denotes the percentage of Hartree-Fock exchange in the functional.

^b CAM- refers to the Coulomb attenuation method, ref. 16b.

^c LC- denotes the long-range correction of ref. 16c.

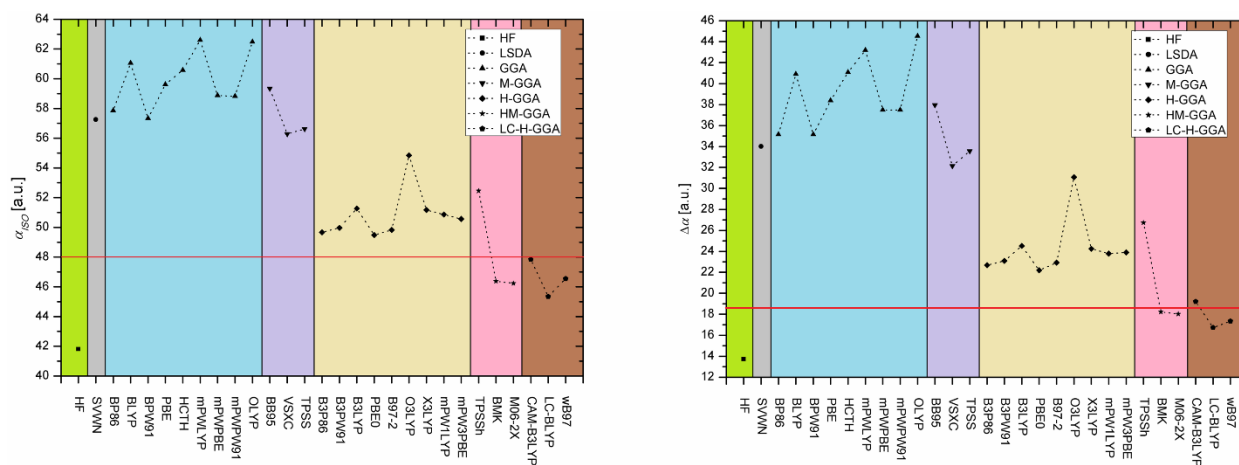


Figure 2.5. Isotropic polarizability and polarizability anisotropy of glycine calculated using various DFT functionals and comparison with the MP2 result (red line). All calculations employ the d-aug-cc-pVTZ basis set.

Table 2.7. Polarizabilities and their anisotropies for the hydrogen-bonded carboxylate and ammonium groups in the amino acid dimers and comparison with the corresponding values for the monomers at the CAM-B3LYP/d-aug-cc-pVDZ level of theory (percentage deviations from the monomer values are shown in parenthesis).

dimer	d(N...O) ^a	-COO ⁻				-NH ₃ ⁺			
		monomer		dimer		monomer		dimer	
		α_{ISO}	$\Delta\alpha$	α_{ISO}	$\Delta\alpha$	α_{ISO}	$\Delta\alpha$	α_{ISO}	$\Delta\alpha$
gly-gly-1	2.802			26.60(8%)	14.45(7%)			11.62(5%)	5.18(-24%)
gly-gly-2	2.970	24.56	13.47	26.54(8%)	19.10(42%)	11.06	6.89	11.97(8%)	7.68(11%)
gly-gly-3	2.807			25.66(4%)	17.44(29%)			11.56(5%)	5.83(-15%)
ala-ala-1	2.828			24.02(1%)	16.63(25%)			10.99(3%)	5.18(-25%)
ala-ala-2	2.849	23.79	13.32	24.31(2%)	16.12(21%)	10.63	6.93	11.73(10%)	7.63(10%)
leu-leu	2.678	23.33	12.90	22.63(-3%)	14.80(15%)	10.22	7.17	9.48(-7%)	6.04(-16%)
thr-thr	2.917	23.12	12.15	23.61(2%)	17.16(41%)	10.67	7.16	11.47(7%)	6.83(5%)
glu-glu	2.785	23.84	14.29	22.98(-4%)	13.58(-5%)	10.60	7.08	11.15(5%)	5.77(-19%)
cys-cys	2.780	23.93	13.83	23.65(-1%)	15.25(-11%)	7.57	5.65	7.83(3%)	5.33(-6%)
his-his	2.769	24.25	14.44	23.82(-2%)	15.58(8%)	10.89	5.04	11.76(8%)	6.68(20%)

^a d(N...O) denotes the distance in Å between the hydrogen bond donor N atom of the -NH₃⁺ group and the hydrogen-bond acceptor O atom of the -COO⁻ group.

2.3.4. Hydrogen bond effects on the distributed polarizability of amino acid aggregates

The intermolecular interactions play a significant role for the susceptibilities of molecular crystals, typically enhanced by the cooperative effect of mutually induced polarization. In order to investigate this phenomenon from the point of view of distributed atomic polarizabilities, we selected ten hydrogen-bonded amino acid dimers with N...O donor-acceptor distance in the range 2.68 – 2.97 Å, typical of medium-strength hydrogen bonds. The -COO⁻ and -NH₃⁺ group polarizabilities are summarized in Table 2.7, where they are also compared with the corresponding amino acid monomers.

The perturbation of the hydrogen bond linkage is quite significant in all cases. The polarizability of the -NH₃⁺ donor is typically increased (except for the leucine dimer), whereas that of the -COO⁻ acceptor is either increased or decreased. There is no strict correlation with the N...O distance, given that interactions also occur amongst other atoms of the donor or acceptor molecules, even if not directly involved in the hydrogen bridge. The perturbation is highly anisotropic, because the aggregation occurs along the hydrogen bond direction, therefore all atoms in the donor or acceptor molecule increase their polarizability component along this direction.

Since molecular crystals feature in general only non-covalent intermolecular interactions, classical electrostatic local-field factors based on point dipoles have been adopted to estimate the crystal susceptibilities starting from the gas-phase molecular (hyper)polarizabilities.¹⁹ However, it is important to check the consequences of neglecting the intermolecular interactions in the quantum-mechanical calculations, and accounting for them only through perturbative local-field corrections. The

distributed polarizability method is extremely useful in this respect, because it allows computing quantum-mechanically an entire aggregate and extracting the polarizabilities of individual molecules, after QTAIM partition. These quantities are then comparable with the approximated polarizabilities computed with the classical electrostatic perturbation of a gas-phase, isolated molecule. As discussed in Chapter 1, Munn and co-workers²⁰ have derived the so-called rigorous local field theory (RLFT), in which the local field experienced by a molecule in a crystal is calculated with point-dipole approximation, by summing the fields arising from the surrounding dipoles in the crystal. The induced dipole moment due to the embedding of the isolated molecule in a crystal lattice equals the field-induced polarization of the isolated molecule, according to Eqn. 1.70. The atomic components $\alpha_{ij}(\Omega)$ of the molecular polarizability tensor are then perturbed and become $\alpha'_{ij}(\Omega)$ in the crystal, which can be iteratively calculated following (1.71).

While the correctness of the RLFT approximation for the long-range interactions is out of discussion, the first coordination sphere requires more attention, because point electrostatic models may be inadequate. Therefore, we analysed some glycine dimers, in order to test whether RLFT properly explains the polarizability changes. Two RLFT models have been employed and compared against the results of the “exact” QTAIM partition of the dimer. In RLFT1, each glycine molecule is approximated by a single point-dipole and polarizability at the center of mass of the molecule. In RLFT3, each glycine molecule is represented by three functional group point-dipoles and polarizabilities, each at the corresponding center of mass. Table 2.8 and Fig. 2.6 show the dipole moment for the glycine monomer and for the hydrogen-bond donor and acceptor molecules in the gly-gly-1 dimer. The head-to-tail aggregation induces an increased dipole moment, while its direction changes only slightly. The dipole moments from the QTAIM partitioning of the electron density are used as benchmarks, given that they come from a quantum-mechanical calculation of the entire dimer.

Table 2.8. Components of the dipole moment (au) for the glycine monomer and for the hydrogen-bonded acceptor and donor molecules in the gly-gly-1 dimer, along with the predictions calculated using RLFT. Computations are at the CAM-B3LYP/d-aug-cc-pVDZ level of theory.

Monomer		μ_x	μ_y	μ_z	$ \mu $				
QTAIM	total	-1.39	0.15	4.47	4.69				
	COO ⁻	0.36	-0.23	2.53	2.57				
	NH ₃ ⁺	-1.19	0.34	0.49	1.33				
	CH ₂	-0.56	0.04	1.46	1.57				
Dimer		Donor				Acceptor			
		μ_x	μ_y	μ_z	$ \mu $	μ_x	μ_y	μ_z	$ \mu $
QTAIM	total	-1.34	0.15	5.20	5.37	-1.25	0.12	4.96	5.11
	COO ⁻	0.36	-0.24	2.73	2.76	0.53	-0.26	2.85	2.91
	NH ₃ ⁺	-1.14	0.32	0.81	1.43	-1.24	0.35	0.55	1.40
	CH ₂	-0.55	0.08	1.66	1.75	-0.53	0.03	1.56	1.65
RLFT3	total	-1.29	0.15	5.39	5.55	-1.20	0.12	5.01	5.15
	COO ⁻	0.35	-0.23	2.71	2.74	0.54	-0.25	2.96	3.02
	NH ₃ ⁺	-1.06	0.33	0.87	1.44	-1.20	0.34	0.54	1.36
	CH ₂	-0.58	0.06	1.81	1.90	-0.54	0.03	1.52	1.61
RLFT1	total	-1.36	0.14	4.94	5.13	-1.36	0.14	4.94	5.13

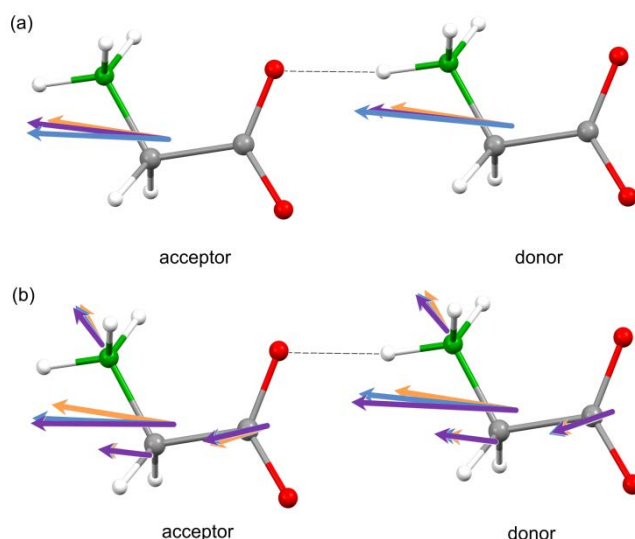


Figure 2.6. Dipole moments for the molecules in the gly-gly-1 dimer. Orange arrow: for the monomer; Blue arrow: calculated using QTAIM partition; Violet arrow: calculated using the RLFT models. (a) RLFT1 and (b) RLFT3.

The RLFT1 approximation [see Table 2.8 and Fig. 2.6(a)] does not distinguish the donor and the acceptor, of course because the two point dipoles and polarizability tensors are identical. This especially means underestimating the dipole moment of the donor. The RLFT3 model is instead able to differentiate the donor (with a larger dipole) from the acceptor, given that each group is treated separately. Nevertheless, RLFT3 is not completely correct because the dipole moment of the donor is overestimated with respect to the QTAIM results; see Table 2.8 and Fig. 2.6(b).

As indicated in Table 2.9, the RLFT1 and RLFT3 models yield similar polarizabilities, both of which overestimate the QTAIM results. Again, RLFT1 does not distinguish donor or acceptor, thus it does not predict the enhancement of the donor with respect to the acceptor. On the other hand, RLFT3 overestimates the polarizability component along the hydrogen bond direction, resulting in too large anisotropies. This is not a failure of the distributed model, which is obviously more accurate than the model with just a global molecular polarizability. Instead, it is the manifestation of another problem, so far not much discussed in the literature, namely the volume contraction. In fact, the molecule in isolation is, by default, integrated within the isosurface $\rho_1(\mathbf{r}) = 0.001 \text{ au}$, which however corresponds to a much larger volume than the molecule in aggregation. In the gly-gly-1 example, this is particularly true along the hydrogen bond direction, being the other two directions anyway unconstrained. It seems therefore necessary to adopt a correction when using gas-phase molecular polarizabilities in solid-state calculations: the molecular or group polarizabilities should be rescaled proportionally with the volume decrement.

In a small molecule such as glycine, the central or distributed polarizabilities methods do not differ substantially, whereas the distributed method should be more accurate in describing the anisotropies of larger molecules. In this sense, our results corroborate earlier findings for small molecules like urea and benzene,^{19a,b,c} whereas for a larger and more anisotropic molecule, *m*-nitroaniline, the spatial partitioning of the molecular response has been found to exert crucial influence on the crystal susceptibilities.^{19c}

Table 2.9. Polarizabilities for the glycine monomer and for the hydrogen-bonded donor and acceptor molecules in the gly-gly-1 dimer, along with the predictions calculated using RLFT. Computations at the CAM-B3LYP/d-aug-cc-pVDZ level of theory.

Monomer		α_{11}	α_{22}	α_{33}	α_{iso}	$\Delta\alpha$					
QTAIM	total	35.78	49.31	57.88	47.66	19.30					
	COO ⁻	15.71	27.69	30.32	24.57	13.49					
	NH ₃ ⁺	8.42	9.19	15.62	11.08	6.85					
	CH ₂	10.16	11.05	13.72	11.64	3.21					
Dimer		Donor					Acceptor				
		α_{11}	α_{22}	α_{33}	α_{iso}	$\Delta\alpha$	α_{11}	α_{22}	α_{33}	α_{iso}	$\Delta\alpha$
QTAIM	total	34.86	45.42	59.36	46.55	21.28	32.15	46.69	59.29	46.04	23.52
	COO ⁻	17.10	25.91	32.22	25.09	13.14	14.72	28.00	32.32	25.01	15.89
	NH ₃ ⁺	8.45	9.55	14.15	10.72	5.24	7.95	8.55	14.13	10.21	5.90
	CH ₂	9.30	9.96	12.99	10.75	3.41	9.48	10.14	12.84	10.82	3.08
RLFT3	total	33.41	48.62	64.71	48.91	27.13	33.41	48.36	64.18	48.65	26.65
	COO ⁻	15.40	28.05	31.04	24.83	14.38	14.36	26.54	36.24	25.71	19.01
	NH ₃ ⁺	8.33	10.19	16.52	11.68	7.43	8.44	9.01	16.05	11.16	7.39
	CH ₂	9.48	10.01	17.71	12.40	7.97	9.91	10.67	14.69	11.75	4.52
RLFT1		34.12	48.37	61.72	48.07	23.89	34.12	48.37	61.72	48.07	23.89

In conclusion, our analysis suggests that the classical local field approximation could be improved in order to better estimate the polarizability increase of an aggregation (crystal), by taking into account a more accurate treatment of the short-range interactions. This will be the subject of further research in our group, implementing a hybrid scheme where the local interactions are accounted quantum-mechanically and included in the distributed atomic polarizabilities (thus automatically including also the volume contraction), whereas the long-range ones are evaluated with the classical local field approximation.

2.3.5. Polarizabilities and refractive indices of amino acid salts

Amino acid salts have also attracted attention for their potential application as linear and non-linear optical materials.⁵ Among them, the organic salt L-histidinium hydrogen-oxalate has been investigated in our group. Its crystal structure is mainly characterized by three short-medium intermolecular hydrogen bonds: the first is a O–H...O bond [2.5052 (5) Å] between hydrogen-oxalates that originates anionic chains along the *a* crystallographic direction; the second is a N–H...O bond [2.6089 (7) Å] between two L-histidinium cations, through the imidazole nitrogen and the carboxylic oxygen, which produces L-histidinium helices, also along the *a* direction; the third is a N–H...O hydrogen bond [2.7982 (7) Å] between the ammonium group of the amino acid and the hydrogen-oxalate, thus connecting the chains and helices along the *c* crystallographic direction.^{5a} Here, we report the results of distributed atomic polarizabilities calculated for the ions of this species, focusing on the intermolecular factors that mainly affect the atomic and functional-group tensors, see Fig. 2.7.

From Figs. 2.7(a) and (c), we see that O5c (the acceptor in a hydrogen-oxalate dimer) slightly modifies the orientation and stretching of its polarizability tensor, due to the hydrogen bond. In general, the whole anion changes the shape of the polarizability tensor that becomes larger in the hydrogen-bond direction. However, α_{ISO} does not change significantly. In a hydrogen-oxalate dimer, the two anions have $\alpha_{ISO} = 49.4$ (donor) and 48.8 au (acceptor), whereas $\alpha_{ISO} = 48.3$ au for an isolated hydrogen-

oxalate. On the contrary, the anisotropy of the tensor is much more affected: $\Delta\alpha$ is 28.44 au for an isolated anion, but 34.76 au for the acceptor anion in a dimer and 34.05 for the central anion in a trimer (acting both as acceptor and donor, not shown in the figure). This means that the hydrogen-oxalate chain motif should produce larger crystal susceptibility along the direction of the chain (a axis) for two reasons: because the chains elongate along the direction of larger component of the anion polarizability; and because the hydrogen bond increases the anisotropy of the polarizability in the same direction by a factor of about 20%. The second important direction is c because the molecular plane of all hydrogen-oxalates is parallel to ac . In fact, the crystal susceptibilities calculated after summation of the polarizabilities of the four gas-phase anions as oriented in the unit cell, thus corresponding to a simple *oriented-gas model*, are $\chi_{11} = 0.50$, $\chi_{22} = 0.21$ and $\chi_{33} = 0.37$, showing that the hydrogen-oxalates would produce a large anisotropy. This is further increased if we use the polarizabilities of hydrogen-oxalates computed for the anion embedded in a chain.

On the other hand, the L-histidinium is itself more isotropic ($\Delta\alpha = 19.17$ in isolation). Moreover, it is not oriented to maximize the polarizability along any specific crystallographic direction. For this reason, the contribution to the susceptibility is rather isotropic, $\chi_{11} = 0.70$, $\chi_{22} = 0.64$ and $\chi_{33} = 0.67$, using the polarizabilities calculated for the isolated cation to construct an oriented-gas model). The isotropic molecular polarizability of L-histidinium is not much affected by the hydrogen bond, Figs. 2.7(b) and (d): $\alpha_{ISO} = 92.6$ and 86.5 au, for the donor and acceptor molecules, compared to an isotropic polarizability of 89.8 au for the isolated cation. However, the strong hydrogen bond that connects the two cations is highly directional (almost parallel to c). If we calculate the contribution to the susceptibility using a cation perturbed by two other molecules in the L-histidinium helices, then χ_{33} would be quite enhanced ($\chi_{11} = 0.67$, $\chi_{22} = 0.61$ and $\chi_{33} = 0.79$).

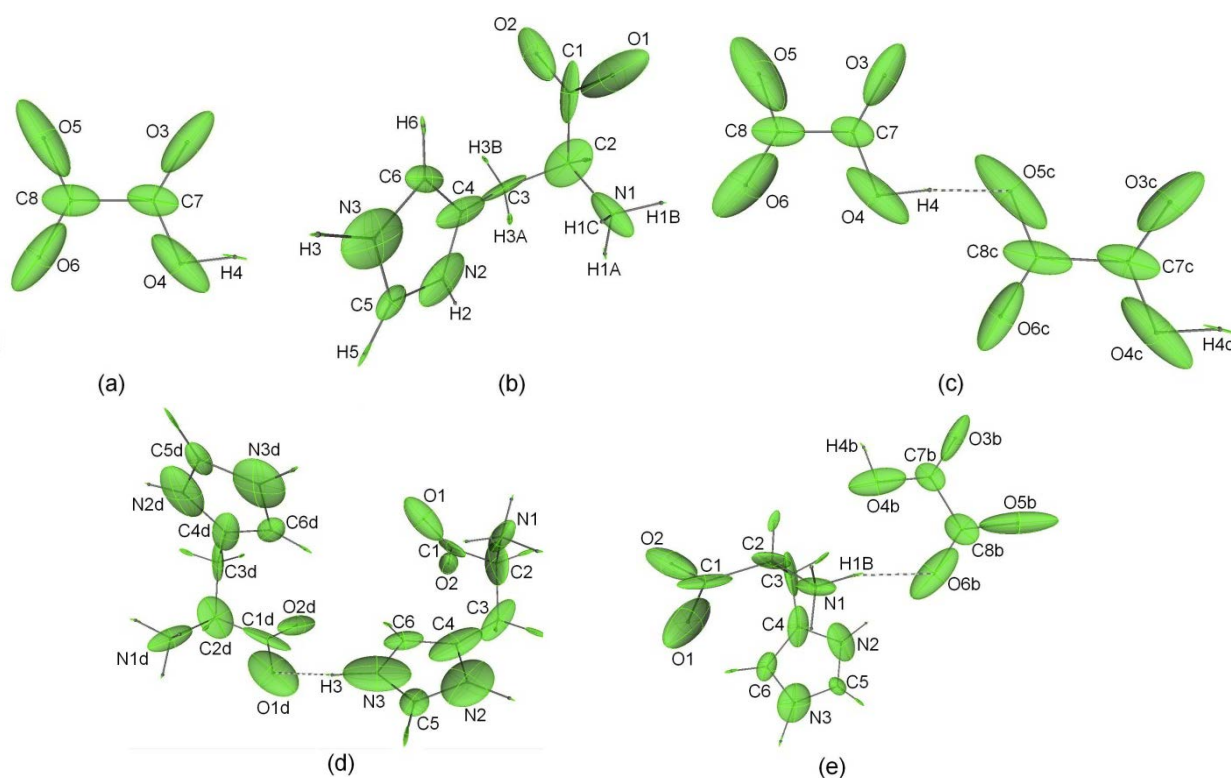


Figure 2.7. Atomic polarizability ellipsoids for (a) isolated hydrogen-oxalate, (b) isolated L-histidinium, (c) hydrogen-oxalate dimer, (d) L-histidinium dimer, and (e) L-histidinium hydrogen oxalate motif.

The combined effects of L-histidinium and hydrogen-oxalate produce the larger crystal susceptibilities, $\chi_{11} = 1.17$, $\chi_{22} = 0.82$ and $\chi_{33} = 1.16$, from which one calculate the corresponding refractive indices $n_a = 1.47$, $n_b = 1.35$ and $n_c = 1.47$. If we then consider local-field factors to account for the crystalline environment, i.e. increased polarizability due to induced electric moments of all molecules in the crystal, see Eqns. 1.69 and 70, the refractive indices become $n_a = 1.62$, $n_b = 1.43$ and $n_c = 1.61$, quite close to those calculated *ab initio* from couple-perturbed Kohn-Sham theory ($n_a = 1.58$, $n_b = 1.45$ and $n_c = 1.63$), although n_a results larger, as from the experimental determination ($n_a = 1.63$, $n_b = 1.50$ and $n_c = 1.60$).^{5a}

Further adjustment of the molecular polarizabilities are possible taking into account also the hydrogen bond between the cation and the anion, Fig. 2.7(e), which are however weaker than the two homo-ionic ones. The isotropic polarizability for the hydrogen-oxalate (hydrogen bond acceptor) is 45.8 au, smaller than the isolated anion, whereas α_{ISO} for L-histidinium (93.5 au) is larger than in isolation. The anisotropy of the hydrogen-oxalate is also increased by this interaction ($\Delta\alpha = 29.83$ au), which reduces the polarizability component along the direction perpendicular to the main plane of the molecule, i.e. in the direction of the b axis.

With this analysis, it can be concluded that the measured or calculated crystalline refractive indices reflect mainly the specific orientation of the molecular polarizabilities of the ions, especially of the hydrogen-oxalates. The perturbation of the hydrogen bonds is not large, but contributes to stretch the polarizability tensors in the ac plane. This features are in keeping with larger n_a and n_c , and smaller n_b refractive indices, and therefore with the significant birefringence of the material.

2.4. Conclusions and perspectives

We have carried out a detailed analysis of the distributed atomic and functional group polarizabilities in amino acids and some of their hydrogen-bonded aggregates. We focused on the contribution of each functional group to the build-up of molecular or supramolecular properties and the effect of intermolecular interactions.

First, we demonstrated a very good transferability of the functional-group polarizabilities. This enabled us to identify which group mostly contributes to the global dielectric constant of materials based on amino acids, which have recently attracted attention.⁵ In particular, we found that the C_α atom provides a rather large optical density. In keeping with experimental evidence, another highly active group is the aromatic ring, which is also quite anisotropic (a feature to be carefully considered in the case where low or high birefringence is desirable). On the other hand, the sulfur atom, although itself quite polarizable, does not produce a very large molar refraction, because its atomic basin has a large volume. However, sulfur plays the role of enhancing the polarizabilities of all neighboring atoms, therefore it indirectly contributes to increasing the molecular and the overall crystal refraction.

Our study was also intended to identify the most quality/cost efficient method to calculate molecular and atomic polarizabilities. Careful analysis demonstrated that a hybrid DFT functional with long-range Coulomb attenuation, like CAM-B3LYP, gives results very close to those obtained with coupled-cluster techniques. As for the basis set, augmentation with diffuse functions is vital and even more

important than valence splitting. Consequently, d-aug-cc-pVDZ is selected as the most efficient, at least for the series of molecules we investigated.

Another outcome of our analysis concerns the perturbation produced by medium strength intermolecular hydrogen bonds. A proper quantum-mechanical treatment of the first coordination is necessary to correctly estimate the effects of mutual polarization between two molecules. The classically adopted local field approximations, even in the more sophisticated distributed group model, overestimate the polarizabilities of molecules in aggregation. The reason is that calculations in the gas-phase assume a too large volume for a molecule and therefore overestimate its polarizability in condensed matter. Based on these evidences, we will develop a new hybrid procedure for estimation of the crystal susceptibilities, meaning that the first coordination sphere of the molecule in the crystal is computed quantum-mechanically and that the semi-empirical local field perturbation is considered only for longer-range interactions.

The distributed polarizabilities of transition metal-amino acid networks are currently been investigated by Ernst²¹ in quite some detail. These quantities are used to understand the effect of the coordination to metals on the optical properties of the amino acids, and how it affects the optical behaviour of the metallic centers, in view of establishing cost-efficient strategies to engineering this kind of materials, in a similar manner as done in this thesis to design hydrogen-bonded functional organic crystals. In particular, correlations have been established among the valence electronic distribution of the transition metals and their relatively large α/V ratio. Furthermore, the preferential occupancy of some d orbitals over the others are directly related to the polarizability anisotropy of the metal, a subtle observation that, although expected, has never been quantified before. Cluster and local-field approaches are also being systematically studied for these materials, in view of identifying the most efficient methods to include long- and short-range intermolecular interaction effects in the polarizability of their building blocks. Although the strong absorption of light in some of the transition-metal crystals may sometimes hamper their applications as optical materials, such analyses are anyway worthwhile because the developed protocols can be applied to any class of molecules.

The computational strategy outlined in this chapter is a useful and effective tool for the rational design of optical molecular materials, because it enables reasoning in terms of the transferable functional groups. Further studies are being performed to check the suitability of the strategy for organometallic systems.²² Finally, this protocol may also foster the development of models for the treatment of induction effects in force field simulations.

References

1. Champagne, B.; Bishop, D. M. *Adv. Chem. Phys.* **2003**, *126*, 41-92.
2. Hammond, J. R.; Govind, N.; Kowalski, K.; Autschbach, J.; Xantheas, S. S. *J. Chem. Phys.* **2009**, *131*, 214103.
3. (a) Bader, R. F. W.; Larouche, A.; Gatti, C.; Carroll, M. T.; MacDougall, P. J.; Wiberg, K. B. *J. Chem. Phys.* **1987**, *87*, 1142-1152. (b) Laidig, K. E.; Bader, R. F. W. *J. Chem. Phys.* **1990**, *93*, 7213-7224. (c) Bader, R. F. W.; Keith, T. A.; Gough, K. M.; Laidig, K. E. *Mol. Phys.* **1992**, *75*, 1167-1189. (d) Bader, R. F. W.; Matta, C. F. *Int. J. Quantum Chem.* **2001**, *85*, 592-607.

4. (a) Keith, T. A. Atomic Response Properties. In *The Quantum Theory of Atoms in Molecules*; Matta, C. F.; Boyd, R. J. (Eds.); Wiley-VCH: Weinheim, **2007**, p 61-94. (b) Krawczuk, A.; Pérez, D.; Macchi, P. *J. Appl. Cryst.* **2014**, *47*, 1452-1458.
5. (a) Chimpri, A. S.; Gryl, M.; Dos Santos, L. H. R.; Krawczuk, A.; Macchi, P. *Cryst. Growth Des.* **2013**, *13*, 2995-3010. (b) Petrosyan, H. A.; Karapetyan, H. A.; Antipin, M. Y.; Petrosyan, A. M. *J. Cryst. Growth* **2005**, *275*, e1919-e1926. (c) Petrosyan, A. M.; Karapetyan, H. A.; Sukiasyan, R. P.; Aghajanyan, A. E.; Morgunov, V. G.; Kravchenko, E. A.; Bush, E. A. *J. Mol. Struct.* **2005**, *752*, 144-152. (d) Petrosyan, A. M.; Sukiasyan, R. P.; Karapetyan, H. A.; Terzyan, S. S.; Feigelson, R. S. *J. Cryst. Growth* **2000**, *213*, 103-111.
6. (a) Frisch, M. J.; Trucks, G. W.; Schlegel, H. B.; Scuseria, G. E.; Robb, M. A.; Cheeseman, J. R.; Montgomery, J. A., Jr.; Vreven, T.; Kudin, K. N.; Burant, J. C. et al. Gaussian 09; Gaussian, Inc.: Wallingford, CT, **2009**. (b) Keith, T. A. AIMAll, Version 14.04.17; TK Gristmill Software: Overland Park, KS, USA, **2014**, aim.tkgristmill.com.
7. (a) Krawczuk, A.; Pérez, D.; Stadnicka, K.; Macchi, P. *Trans. Am. Cryst. Assoc.* **2011**, *42*, 1-25. (b) Krawczuk, A.; Macchi, P. *Chem. Central J.* **2014**, *8*, 68. (c) Macchi, P.; Krawczuk, A. *Comput. Theor. Chem.* **2015**, *1053*, 165-172.
8. Bonin, K. D.; Kresin, V. *Electric-Dipole Polarizabilities of Atoms, Molecules and Clusters*; World Scientific: Singapore, **1956**.
9. Biegler-König, F. W.; Bader, R. F. W.; Tang, T. H. *J. Comput. Chem.* **1982**, *3*, 317-328.
10. (a) McMeekin, T. L.; Groves, M. L.; Hipp, N. J. Refractive Indices of Amino Acids, Proteins and Related Substances. In *Amino Acids and Serum Proteins*; Stekol, J. (Ed.); American Chemical Society: Washington, **1964**, p 54-66. (b) Khanarian, G.; Moore, W. J. *Aust. J. Chem.* **1980**, *33*, 1727-1741.
11. (a) Reis, H. *J. Chem. Phys.* **2006**, *125*, 014506. (b) Kassimi, N. E.-B.; Thakkar, A. J. *Chem. Phys. Lett.* **2009**, *472*, 232-236.
12. Ma, H.; Jen, A. K.-Y.; Dalton, L. R. *Adv. Mat.* **2002**, *14*, 1339-1365.
13. Medved, M.; Champagne, B.; Noga, J.; Perpète, E. A. Dipole Polarizability and Second Hyperpolarizability of Difluoroacetylene: Basis Set Dependence and Electron Correlation Effects. In *Computational Aspects of Electric Polarizability Calculations: Atoms, Molecules and Clusters*; Maroulis, G. IOS Press: Amsterdam, **2006**, p 17-31.
14. Helgaker, T.; Ruden, T. A.; Jørgensen, P.; Olsen, J.; Klopper, W. *J. Phys. Org. Chem.* **2004**, *17*, 913-933.
15. Papajak, E.; Zheng, J.; Xu, X.; Leverentz, H. R.; Truhlar, D. G. *J. Chem. Theory Comput.* **2011**, *7*, 3027-3034.
16. (a) Sousa, S. F.; Fernandes, P. A.; Ramos, M. J. *J. Phys. Chem. A*, **2007**, *111*, 10439-10452. (b) Yanai, T.; Tew, D. P.; Handy, N. C. *Chem. Phys. Lett.* **2004**, *393*, 51-57. (c) Iikura, H.; Tsuneda, T.; Yanai, T.; Hirao, K. *J. Chem. Phys.* **2001**, *115*, 3540-3544.
17. de Wergifosse, M.; Champagne, B. *J. Chem. Phys.* **2011**, *134*, 074113.
18. (a) Song, J.-W.; Watson, M. A.; Sekino, H.; Hirao, K. *J. Chem. Phys.* **2008**, *129*, 024117. (b) Sekino, H.; Maeda, Y.; Kamiya, M.; Hirao, K. *J. Chem. Phys.* **2007**, *126*, 014107. (c) Kamiya, M.; Sekino, H.; Tsuneda, T.; Hirao, K. *J. Chem. Phys.* **2005**, *122*, 234111. (d) Zhao, Y.; Truhlar, D. G. *Theor. Chem. Acc.* **2008**, *120*, 215-241.

19. (a) Chemla, D. S.; Oudar, J. L.; Jerphagnon, J. *Phys. Rev. B*, **1975**, *12*, 4534-4546. (b) Reis, H.; Raptis, S.; Papadopoulos, M. G.; Janssen, R. H. C.; Theodorou, D. N.; Munn, R. W. *Theor. Chem. Acc.* **1998**, *99*, 384-390. (c) Reis, H.; Papadopoulos, M. G.; Calaminici, P.; Jug, K.; Köster, A. M. *Chem. Phys.* **2000**, *261*, 359-371. (d) Munn, R. W. *Mol. Phys.* **1988**, *64*, 1-20. (e) Reis, H.; Papadopoulos, M. G.; Munn, R. W. *J. Chem. Phys.* **1998**, *109*, 6828-6838.
20. (a) Dunmur, D. A. *Mol. Phys.* **1972**, *23*, 109-115. (b) Cummins, P. G.; Dunmur, D. A.; Munn, R. W.; Newham, R. J. *Acta Cryst. Sect. A* **1976**, *32*, 847-853.
21. Ernst, M. *Master Thesis*; University of Bern, **2015**.
22. Macchi, P.; Krawczuk, A. *Comput. Theoret. Chem.* **2015**, *1053*, 165-172.

Chapter 3

Electron Density Distributions and Magnetic Properties in Copper Pyrazine Nitrate Quasi-Low-Dimensional Quantum Magnets*

In this chapter, electron density distributions and magnetic properties of two metal-organic polymeric magnets, the quasi-one-dimensional (1D) $\text{Cu}(\text{pyz})(\text{NO}_3)_2$ and the quasi-two-dimensional (2D) $[\text{Cu}(\text{pyz})_2(\text{NO}_3)]\text{NO}_3 \cdot \text{H}_2\text{O}$, have been investigated by high-resolution single-crystal X-ray diffraction and DFT calculations in the crystalline state as well as in the gas phase. QTAIM topological analyses enabled the characterization of possible magnetic exchange pathways and the establishment of relationships between the electron (charge and spin) densities and the exchange-coupling constants. In both compounds, the experimentally observed antiferromagnetic coupling can be quantitatively explained by the Cu–Cu superexchange pathway mediated by the pyrazine bridging ligands, through a σ -type mechanism. The materials can be regarded as low-dimensional magnets for most practical purposes, although very weak interchain and interlayer interactions may lead to three-dimensional long-range ordering, as detected in a previous experiment. We also employed molecular orbital analysis along with calculated spin density distributions to characterize the role of spin delocalization and spin polarization in determining the bulk magnetic behaviour of these coordination polymers.

3.1. Introduction, motivation and specific goals

Among magnetic metal-organic polymers, quasi-1D or -2D compounds are of particular interest because they are intermediate situations between high-nuclearity magnetic clusters and three-dimensional magnetic frameworks.¹ These compounds are characterized by ordered chains or layers consisting of metal ions bridged by polydentate ligands. The interchain or interlayer interactions are often, but not always, very weak. These architectures lead to predominantly low-dimensional ferromagnetic (FM) or antiferromagnetic (AFM) materials, even though weak interchain and interlayer couplings can also take place, giving rise to three-dimensional pathways and sometimes magnetic ordering, depending on the molecular structure and on the crystal packing.² Furthermore, 1D magnets have long been recognized as prototypical for the experimental studies of physics in reduced dimensions, with the linear chain Heisenberg antiferromagnet model (LCHAFM) being the subject of extensive investigations.¹ Quasi-1D Cu-compounds are widely studied,³ but copper(II) pyrazine dinitrate, $\text{Cu}(\text{pyz})(\text{NO}_3)_2$ (**1**), has been the most successful realization of the LCHAFM. This material has a relatively small exchange-coupling constant, $J = -7.26 \text{ cm}^{-1}$ (-10.4 K), as determined from magnetic susceptibility, high-field magnetization and specific heat measurements.^{4a} The ratio of interchain to intrachain exchange constants, J'/J , has been estimated to be negligible, thus showing that the chains are well isolated. However, evidence for three-dimensional long-range magnetic order has been recently detected based on zero-field muon-spin relaxation measurements. This technique

*All magnetic measurements discussed in this chapter were performed and provided by prof. Jamie L. Manson, Eastern Washington University, USA. A manuscript based on this chapter has been submitted to J. Am. Chem. Soc.

provided an estimate of J'/J significantly larger than previously thought, although $J' = +0.03 \text{ cm}^{-1}$ ($+0.046 \text{ K}$) is still very small.^{4b} On the other hand, the cationic three-dimensional net of copper(II) di(pyrazine) nitrate, $[\text{Cu}(\text{pyz})_2(\text{NO}_3)]^+$, is investigated in this thesis for the first time, as obtained in single-crystals of the hydrated salt $[\text{Cu}(\text{pyz})_2(\text{NO}_3)]\text{NO}_3 \cdot \text{H}_2\text{O}$ (**2**).

In this work, we correlate accurate electron density distributions in **1** and **2** with their magnetic properties. For **1**, both the experimental density (from X-ray diffraction) and theoretical density (from quantum mechanical calculations) are investigated. For **2**, only theoretical electron densities are discussed because single-crystals suitable for accurate high-resolution X-ray diffraction experiments could not be obtained. For both samples, crystals suitable for PND could not be grown, therefore the experimental spin density cannot be obtained. Nevertheless, calculated spin density distributions are also discussed.

Quantitative reasoning of the chemical bonding, in particular around the metallic center, is achieved using the real-space partitioning derived from quantum theory of atoms in molecules (QTAIM). This study is particularly devoted to establishing relationships between the electron charge and spin densities and the exchange-coupling constants, but our investigation is supplemented by molecular orbital analyses. From this work, we also reveal the cooperative nature of *spin delocalization* and *spin polarization* mechanisms and that they are not mutually exclusive. This finding may be representative for a larger class of copper(II) pyrazine quantum magnets.

3.2. Experimental and computational techniques

3.2.1. X-ray data collection and structure refinement

Single-crystals of **1** and **2** were mounted on an Agilent SuperNova diffractometer. The crystals were cooled to 100 K (**1**) and 173 K (**2**) with N_2 . The CRYCALIS PRO programs were used to perform data collection and reduction. A total of 24441 and 12729 intensities were harvested, respectively for **1** and **2**. While for the latter a standard measure up to resolution of $\sin\theta_{\text{max}}/\lambda = 0.7 \text{ \AA}^{-1}$ was undertaken, diffraction data for compound **1** was measured up to $\sin\theta_{\text{max}}/\lambda = 1.19 \text{ \AA}^{-1}$. A total of 2487 image frames were obtained from 23 oscillation runs, with four different sets of exposure times. These were 2.5 + 2.5, 20 + 20, 40 + 40 and 80 + 80 s per image, totalling 51 h of exposure time. The oscillation angle of 1° was used, with ω being the oscillation axis. Batch scaling factors for each oscillation run within each of the four sets showed no consistent variation in time, indicating no significant sample decay. The high-angle sets utilized the longer exposure times to improve the measurement statistics, while the shorter exposure times were used to accurately record the intense low-angle data, avoiding pixel overflow or integration failure. The scan sets with small θ offsets were measured first in the data collection strategy, in order to alleviate problems with ice rings which may gradually build up during the collection. The high-angle images showed no evidence of contamination from ice rings. The unit-cell dimensions used for refinement purposes were determined by post-refinement of 15085 reflections with $3 < \theta < 57^\circ$. The frame images were integrated using spot elongation for the high-angle data, in order to, at least partially, account for the $K\alpha_1$ - α_2 splitting.

Table 3.1. Crystallographic details and refinement results for Cu(pyraz)(NO₃)₂ (1) and [Cu(pyraz)₂(NO₃)]NO₃·H₂O (2).

Crystal data	Compound 1	Compound 2
Chemical formula	CuC ₄ H ₄ N ₄ O ₆	(CuC ₈ H ₈ N ₅ O ₃)NO ₃ ·H ₂ O
Crystal system, space group	Orthorhombic, <i>Pmna</i>	Orthorhombic, <i>Ima2</i>
Temperature (K)	100.0 (5)	173.0 (5)
<i>a</i> , <i>b</i> , <i>c</i> (Å)	6.70122 (7), 5.11854 (5), 11.6351 (1)	13.6081 (5), 9.9487 (4), 9.4287 (3)
<i>V</i> (Å ³)	399.089 (7)	1276.48 (8)
<i>Z</i>	2	4
θ range (°) for cell measurement	3.5–37.5	3.0–26.8
μ (mm ⁻¹)	2.757	1.762
Crystal size (mm)	0.22 × 0.12 × 0.08	0.07 × 0.07 × 0.03
Data collection		
Absorption correction	Numerical	Numerical
<i>T</i> _{min} , <i>T</i> _{max}	0.962, 0.985	0.897, 0.960
No. of measured, independent and observed [<i>F</i> > 3σ(<i>F</i>)] reflections	24441, 2933, 2737	12729, 1821, 1503
Redundancy	8.3	7.0
<i>R</i> _{int} ^a	0.018	0.083
θ values (°)	$\theta_{\max} = 57.6$, $\theta_{\min} = 1.7$	$\theta_{\max} = 29.7$, $\theta_{\min} = 4.1$
(sin θ/λ) _{max} (Å ⁻¹)	1.188	0.697
Range of <i>h</i> , <i>k</i> , <i>l</i>	<i>h</i> = -15 → 15, <i>k</i> = -12 → 12, <i>l</i> = -27 → 27	<i>h</i> = -18 → 18, <i>k</i> = -13 → 13, <i>l</i> = -12 → 12
Spherical, independent-atom model refinement		
Refinement on	<i>F</i> ² (for <i>F</i> > 0)	<i>F</i> ² (for <i>F</i> > 0)
<i>R</i> [<i>F</i> > 3σ(<i>F</i>)], <i>R</i> _{all} , <i>wR</i> , <i>S</i> ^b	1.68, 1.92, 2.67, 1.39	5.11, 7.95, 6.08, 1.14
No. of parameters	48	113
(Δ/σ) _{max}	0.001	0.001
Δρ _{max} , Δρ _{min} (e Å ⁻³)	0.53, -1.22	0.94, -0.92
Extinction coefficient	0.023 (2)	
Multipole refinement		
Refinement on	<i>F</i> ² (for <i>F</i> > 0)	
<i>R</i> [<i>F</i> > 3σ(<i>F</i>)], <i>R</i> _{all} , <i>wR</i> , <i>S</i> ^b	0.95, 1.18, 1.40, 0.83	
No. of parameters	175	
(Δ/σ) _{max}	0.002	
Δρ _{max} , Δρ _{min} (e Å ⁻³)	0.28, -0.22	
Extinction coefficient	0.045 (2)	

^a $R_{int} = \sum_{\mathbf{h}} |F_{\mathbf{h},obs}^2 - \langle F_{\mathbf{h},obs}^2 \rangle| / \sum_{\mathbf{h}} F_{\mathbf{h},obs}^2$ (summation is carried out only where more than one symmetry equivalent reflection is averaged). ^b $R(F) = 100 \cdot \sum_{\mathbf{h}} \left| |F_{\mathbf{h},obs}| - |F_{\mathbf{h},calc}| \right| / \sum_{\mathbf{h}} |F_{\mathbf{h},obs}|$, $wR(F) = 100 \cdot \left[\sum_{\mathbf{h}} w_{\mathbf{h}} (|F_{\mathbf{h},obs}| - |F_{\mathbf{h},calc}|)^2 / \sum_{\mathbf{h}} w_{\mathbf{h}} F_{\mathbf{h},obs}^2 \right]^{1/2}$, $S = \left[\sum_{\mathbf{h}} w_{\mathbf{h}} (F_{\mathbf{h},obs}^2 - F_{\mathbf{h},calc}^2)^2 / (N - P) \right]^{1/2}$ with $w_{\mathbf{h}} = 1/\sigma_{\mathbf{h},obs}^2$, *N* as the number of reflections and *P* as the number of parameters. Both in the spherical model and in the multipole model refinements the calculated structure-factor magnitudes are properly multiplied by a scale factor η and by an additional factor $Y_{\mathbf{h}}(\epsilon)$ that corrects for secondary extinctions. For the spherical model, $Y_{\mathbf{h}}(\epsilon) = [1 + 0.001 \epsilon F_{\mathbf{h},calc}^2 \lambda^3 / \sin(2\theta_{\mathbf{h}})]^{-1/4}$, while, for the multipole model, $Y_{\mathbf{h}}(\epsilon)$ has been chosen following the Becker and Coppens equations.⁹

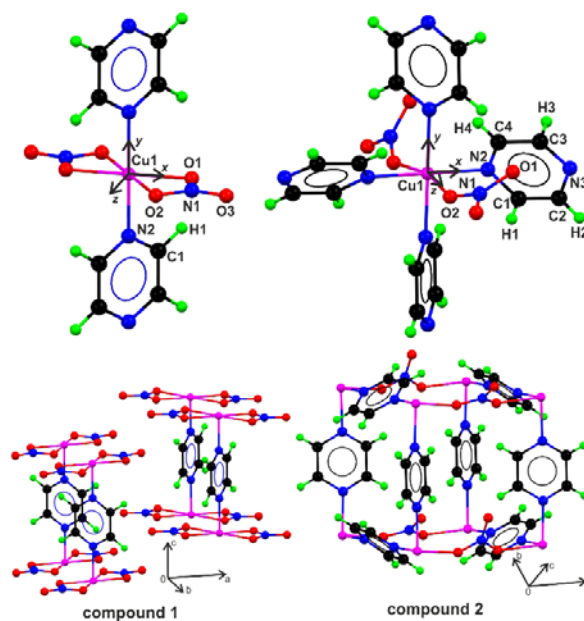


Figure 3.1. Experimental molecular structure of crystalline $\text{Cu}(\text{pyz})(\text{NO}_3)_2$ (**1**) and $[\text{Cu}(\text{pyz})_2(\text{NO}_3)]\text{NO}_3 \cdot \text{H}_2\text{O}$ (**2**). Only the asymmetric units are labelled. Local axes at the copper atoms are also shown. For **2**, counter-ions and solvent molecules are omitted.

Numerical absorption corrections were applied for both crystals. The resulting data for **1** was additionally sorted and merged in Laue group mmm using SORTAV,⁵ giving 2933 independent reflections with a mean redundancy of 8.3. Additional data are tabulated in Table 3.1. Coordinates and atomic displacement parameters (ADPs) were refined applying the independent-atom model (IAM) as implemented in SHELXL.⁶ The experimental geometries are shown in Fig. 3.1.

3.2.2. Multipole refinement

The IAM parameters were used as initial values for multipole modelling of **1**. This was performed using the XD2006 program⁷ and the Hansen-Coppens formalism. The core and spherical valence densities are composed of Slater-type atomic relativistic wavefunctions obtained at the PBE/QZ4P level of theory for neutral atoms in their ground-state configuration.⁷ For the Cu-atom, Hartree-Fock wavefunctions expanded in single- ζ orbitals with energy-optimized Slater exponents^{8a} are used for defining the radial part of the deformation terms as a combination of orbital products.⁷ The (4s4s) product was used to construct the radial portion of the deformation monopole while the (3d3d) product was applied in the construction of the quadrupole and the hexadecapole radial densities. By crystallographic symmetry restrictions, dipole and octupole functions are not allowed at the metallic center. For all the other atoms, single- ζ orbitals with energy-optimized Slater exponents are used for the radial part of the deformation terms.^{8b} A number of models were tested to optimize the fit to the experimental intensities. In the final model, the multipole expansion was truncated at the hexadecapole level for all the non-H atoms, while only a bond-directed dipole was applied to H1. The κ parameters were refined for each atomic type. For O, N and C atoms, a single κ' was refined for all the l values belonging to a defined set while κ' for Cu and H1 were constrained to the corresponding refined κ values. A high-order refinement with $\sin \theta/\lambda \geq 0.7 \text{ \AA}^{-1}$ was performed for the non-hydrogen atoms to obtain accurate positional and displacement parameters. Afterwards, the H-atom coordinates and isotropic ADP were freely refined. An isotropic extinction coefficient was also refined according to the Becker-Coppens equations.⁹

The ground-state electronic configuration of Cu corresponds to $[\text{Ar}]4s^13d^{10}$ and the $4s$ orbital is well known to contribute to the valence density. However, it is also established that transition metals present problems when refining the deformation density because of the significantly different radial extensions of the $(n-1)d$ and ns valence orbitals. This would require the treatment of two different valence deformation densities or, as it is often the case, that the ns density is constrained to its nominal value and formally associated with the frozen core density.¹⁰ In **1**, scattering from the copper $4s$ density is only significant for $\sin\theta/\lambda < \sim 0.18 \text{ \AA}^{-1}$ and only 14 reflections satisfy this criterion. In view of such a small number of reflections, their standard uncertainty and the fact that the monopole population P_{00} in Eqn. 1.50 is expected to be a rather small quantity, it is not surprising that attempts to refine the $4s$ population independently through the $l = 0$ deformation function gave physically unrealistic populations. Thus, a model based on the $[\text{Ar}]4s^03d^9$ electronic distribution for Cu(II) was also tested. This gave significantly better residuals and the final model was based on this configuration.

Anharmonic motion was modelled for the Cu atom by refining Gram-Charlier coefficients up to fourth-order.¹¹ It led to an improvement on the residual density distribution in the vicinity of the Cu nucleus. In the final refinement, the maximum and minimum residual density peaks were $+0.29$ and $-0.22 e \cdot \text{\AA}^{-3}$ using all data. Residual density maps show only few and small discrepancies that could not be removed by any deformation model. Topological properties and integrated atomic charges were calculated using the TOPXD module.⁷ Recent studies suggest an estimate of approximately $\pm 5\%$ for the accuracy of the integrated atomic properties.¹²

3.2.3. Theoretical calculations

As discussed in Chapter 1, the exchange-coupling constant J can be related to the energy difference between states with different spin multiplicities. For this purpose, accurate unrestricted wavefunctions for the high- and low-spin states are required. For our purposes, we assume that the low-spin state can be well approximated by a *broken-symmetry solution*. We have investigated the high-spin and the broken-symmetry states in the dinuclear models of compounds **1** and **2** represented in Fig. 3.2. Models 1-d1 and 2-d1 comprise dimeric versions of the infinite chain structures present in **1** and **2** respectively. They contain two Cu(II) centers bridged by a pyrazine ligand, while the other models account for interchain interactions or intrachain pathways mediated by the nitrate ligand. All systems have been investigated within unrestricted Kohn-Shan theory using the B3LYP/6-311G(2d,2p) level of theory, as implemented in the Gaussian 09 package.^{13a} The AIMAll software^{13b} has been used to partition the corresponding electron densities and to calculate integrated atomic properties.

CRYSTAL09^{14a} was used to perform periodic DFT calculations on ferro- and antiferromagnetic phases of **1** and **2** using the B3LYP hybrid functional. The basis set for the Cu atom is 86-411G(41d),^{15a} while for the non-metallic atoms, it is 6-31G(1d).^{15b} Topological analysis of the periodic electron densities and integrated atomic properties were calculated using the TOPOND09 software.^{14b}

Our periodic calculations on **1** considered the magnetic phases schematically represented in Fig. 3.3. The ferromagnetic phase (FM) corresponds to the high-spin structure, whereas the antiferromagnetic phases (AFM) correspond to low-spin ones. The unit cell of FM and sAFM contain two formula units whereas the simulations of the aAFM and the bAFM phases require double cells. Due to prohibitively high computational costs, only the phases FM and sAFM were investigated for compound **2**, see Fig. 3.3. The coupling constant can be estimated from the energy gap between the FM phase and the AFM phase according to well established protocols that are simply based on Eqn. 1.74.¹⁶ To obtain a fair comparison with experiment, the calculated structure factors of the FM and AFM phases of **1** were also fitted against the best multipolar model derived experimentally.

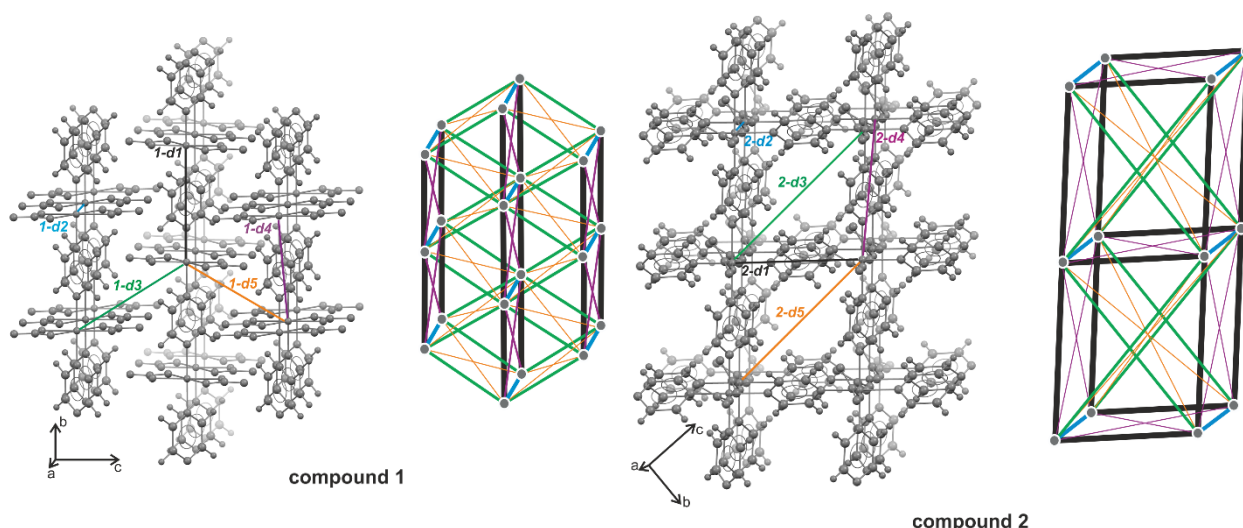


Figure 3.2. Disposition of the dinuclear models in $\text{Cu}(\text{pyz})(\text{NO}_3)_2$ (1) and $[\text{Cu}(\text{pyz})_2(\text{NO}_3)]\text{NO}_3 \cdot \text{H}_2\text{O}$ (2). Schematic views of the packing in terms of Cu positions and the network generated from the shortest $\text{Cu} \cdots \text{Cu}$ contacts are also shown with line thickness representing the relative magnitude of the coupling constants.

3.3. Results and discussion

Structural investigations carried out on molecular magnetic materials are often able to correlate the exchange-coupling constant to structural parameters, in particular for spin-only or dinuclear systems.¹⁷ Intermetallic distances or angles between metal centers and a bridging ligand are then considered within the context of orbital overlap in order to provide an intuitive understanding of the exchange mechanism.¹⁸ However, as discussed in Chapter 1, only a few studies have been carried out to correlate the magnetic behaviour of a material to its electron density distribution, as experimentally obtained from high-resolution X-ray diffraction. We begin by briefly describing the crystalline structure of 1 and 2, then we turn to the analysis of $\rho_1(\mathbf{r})$, either obtained experimentally or theoretically. Finally, we complement our study through molecular orbital analysis of the spin density distributions.

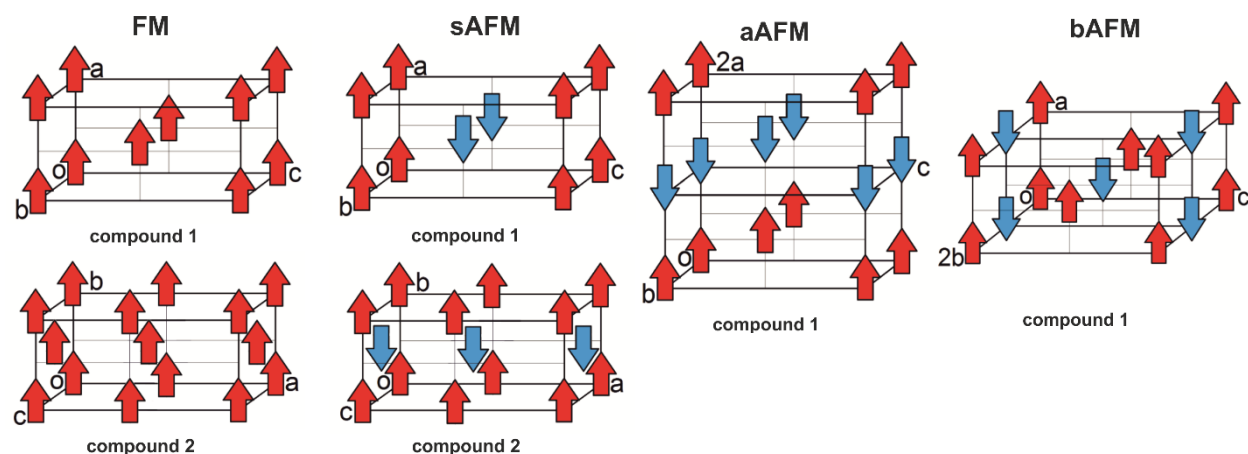


Figure 3.3. Orthorhombic unit cells for magnetic phases of $\text{Cu}(\text{pyz})(\text{NO}_3)_2$ (1) and $[\text{Cu}(\text{pyz})_2(\text{NO}_3)]\text{NO}_3 \cdot \text{H}_2\text{O}$ (2). The ferromagnetic (FM) and three possible antiferromagnetic (sAFM, aAFM and bAFM) structures are considered. Red and blue arrows indicate spin-up and spin-down $\text{Cu}(\text{II})$ moments, respectively.

3.3.1. Crystal structures

Our high-resolution X-ray diffraction data collection on the $\text{Cu}(\text{pyz})(\text{NO}_3)_2$ 1D coordination polymer implied also a re-determination of the already known^{4a} crystal structure (Fig. 3.1), without finding any major difference. Each Cu occupies a $2/m$ crystallographic site and lies at the center of a distorted octahedron formed by two of each Cu–O1 [2.0022 (2) Å], Cu–O2 [2.4796 (3) Å] and Cu–N2 [1.9765 (2) Å] chemical bonds. Adjacent metallic centers are linked by pyrazines along the crystallographic a direction, whereas the nitrates lie at the $0, y, z$ and $\frac{1}{2}, y, z$ mirror planes. Owing to the symmetry of Cu, all N2–Cu–O angles are 90° , whereas the O1–Cu–O2 angle of $56.74 (2)^\circ$ is far from the ideal octahedral angle, due to the inherent rigidity of the nitrate ligand. Along the Cu-pyrazine chain, the Cu atoms are separated by 6.701 (1) Å. Weak C–H \cdots O hydrogen bonds [C1 \cdots O2 = 3.447 (1) Å] and C \cdots O contacts [C1 \cdots O3 = 3.122 (1) Å] connect adjacent chains along the b direction. As discussed in the following, although these interactions may stabilize the three-dimensional lattice, our results confirm the weak nature of the superexchange pathways. Thus, the material would be classified as a 1D quantum magnet.

The crystal structure of the $[\text{Cu}(\text{pyz})_2(\text{NO}_3)]\text{NO}_3 \cdot \text{H}_2\text{O}$ 3D polymer was here determined for the first time (Fig. 3.1). The presence of two pyrazine ligands per Cu induces a 3D coordinative network, given that each ligand act as a bidentate bridge. The cavities formed by the $[\text{Cu}(\text{pyz})_2(\text{NO}_3)]^+$ network are filled by the non-coordinating nitrate and a water molecule. Cu lies on a 2-fold axis, at the center of a slightly distorted octahedron formed by two of each Cu–O2 [2.337 (4) Å], Cu–N2 [2.039 (9) Å] and Cu–N3 [2.038 (9) Å] bonds. The N2–Cu–N3 angle is almost right [$88.8 (1)^\circ$], whereas O2–Cu–N3 and O2–Cu–N2 are distorted [$83.8 (2)^\circ$ and $95.3 (2)^\circ$, respectively]. The pseudo-tetragonal Cu-pyrazine layers are perpendicular to direction a and the Cu-pyz-Cu edges elongate along the $\{011\}$ and $\{01\bar{1}\}$ directions, with Cu \cdots Cu distances of 6.853 (5) Å. The NO_3^- ligands connect the layers (Cu \cdots Cu distances of 6.804 (2) Å) along the pseudo Jahn-Teller distorted direction. The only relevant superexchange pathways are those formed by Cu atoms bridged by pyrazines, addressing the material as a 2D quantum magnet.

3.3.2. Electron density distributions and topological analyses

Formally, Cu has oxidation state +2 in both **1** and **2**. Being a d^9 metal, the observed stereochemistry can be explained by *pseudo-Jahn-Teller distortion*, i.e. stabilization of four coordination directions in a plane and destabilization of the two remaining out-of-plane directions. The analysis of the electron density distribution enables investigating in details these features, going beyond the mere bond lengths. The observed electron population of Cu reflects the bonding mechanism of the ligand-to-metal electron donation and the potential metal-to-ligand back donation. The electron distribution around Cu also informs on the specific bonding contribution, identifies the magnetic orbital and provides more details of the Jahn-Teller distortion.

The experimentally refined valence population of Cu in **1** is 9.89 (8) e . As already emphasized in Chapter 1, the multipolar expansion is itself an atomic partitioning, hence the valence electronic population determines the atomic charge, in this case +1.11 (8) e for **1**. However, because the multipolar parameters correlate, sometimes strongly, within a refinement (indeed, the largest

correlation coefficients among different atoms in the multipolar refinement of **1** are significant, 30-40%) and different combinations of multipolar coefficients may describe the same global electron density distribution, a better estimation of the atomic charges comes from the partitioning of the total density reconstructed with a multipolar model, because these methods offer more exportable methods of determining atomic charges. In Table 3.2, QTAIM charges are shown for the experimental multipolar fitted density of **1**, as well as for the periodically calculated FM and AFM densities, and the dinuclear model densities of **1** and **2**. Despite their inherent differences, both QTAIM and pseudo-atom schemes indicate that Cu(II) receives quite substantial donation, thus reducing its formal charge. Pyrazine is slightly positive, and the charge of the nitrate coordinated to the metallic center is largely negative, but less than -1. Furthermore, all atoms that directly binds Cu bears rather negative charges.

Table 3.2. Experimental and theoretical QTAIM charges on relevant atoms and ligands of compounds **1** and **2**.^a

	Cu(py ₂)(NO ₃) ₂ (1)				[Cu(py ₂) ₂ (NO ₃)]NO ₃ ·H ₂ O (2)	
	MM Exptl.	MM FM/AFM	FM/AFM	Dinuclear Models	FM/AFM	Dinuclear Models
Cu	+1.08	+1.44	+1.27	+1.19	+1.25	+1.22
O1	-0.47	-0.44	-0.61	-0.61	-0.61	-0.49
O2	-0.53	-0.52	-0.57	-0.54	-0.61	-0.49
N2	-1.20	-0.85	-1.33	-1.14	-1.29	-1.07
N3					-1.30	-0.93
pyrazine	+0.44	-0.06	+0.38	+0.24	+0.29	+0.20
nitrate	-0.72	-0.68	-0.82	-0.72	-0.91	-0.85

^aMM Exptl.: $\rho_1(\mathbf{r})$ from the multipole model fitted against the experimental structure factors; MM FM/AFM: $\rho_1(\mathbf{r})$ from the multipole model fitted against the periodic B3LYP structure factors; FM/AFM: $\rho_1(\mathbf{r})$ directly from the periodic B3LYP calculation; Dinuclear models: $\rho_1(\mathbf{r})$ from the gas-phase B3LYP calculation.

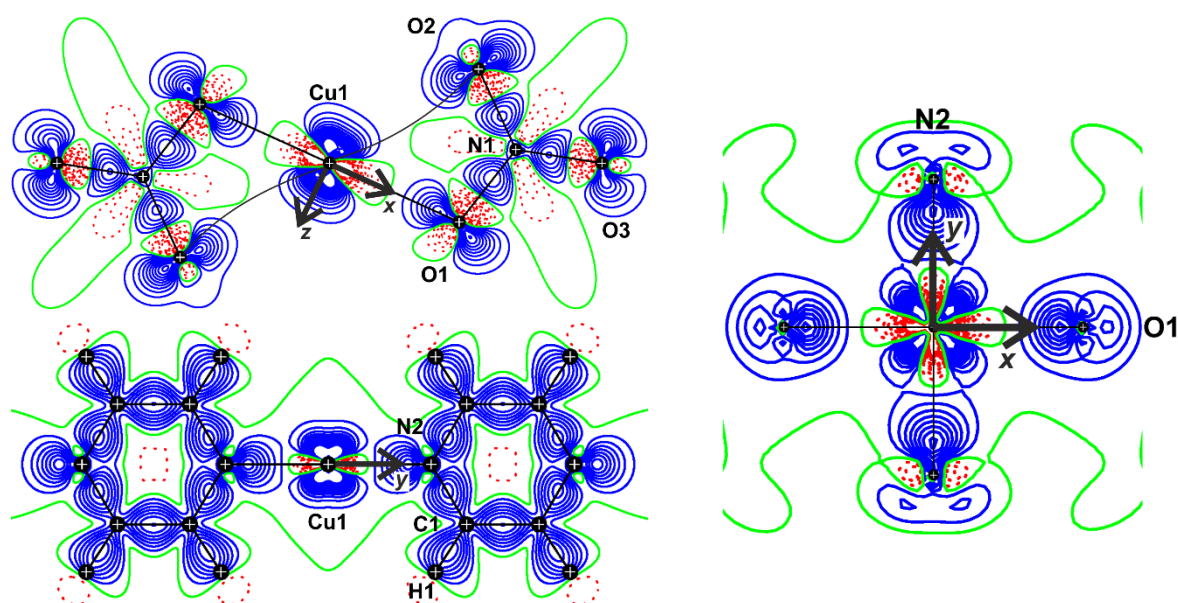


Figure 3.4. Experimental static deformation densities for Cu(py₂)(NO₃)₂ (**1**). Positive contours as solid blue lines, negative contours as dotted red lines and zero contours as solid green lines. The contour level is 0.015 au.

Beside the charges, the electron distribution around the atoms are useful to identify the features affecting the magnetism of the systems. Deformation density maps around Cu(II) (shown in Fig. 3.4 for **1**) address a significant electron density depletion in the copper valence shell towards the directions defining the $3d_{x^2-y^2}$ orbital. They correspond to the Cu–O1 and Cu–N2 bond directions for **1** and to the two Cu–pyrazine directions for **2**, in keeping with the expectations from bond distances. Complementarily, the electron density on the ligand-binding atoms is accumulated in these directions. More interesting is the electron density distribution along the Jahn-Teller distorted directions (Cu–O2, for both **1** and **2**). Of course, Cu presents a charge accumulation along its z axis (due to the $3d_{z^2}$ orbital) that would produce a repulsion with the O2 lone-pair lobe. However, in **1** (and somewhat in **2** as well), the deformation density on O2 in part interacts with the depletion produced by the $3d_{x^2-y^2}$ orbital in the xy plane, due to the distorted binding mode of the nitrate. The Laplacian maps (see below) and the distorted Cu–O2 bond-path (see Fig. 3.4) fully confirm this evidence.

The topological analysis of $\rho_1(\mathbf{r})$ (Table 3.3 for **1**) is also very useful to clarify the nature of the interactions. First we stress that there is no appreciable difference in $\rho_1(\mathbf{r})$ as a function of the spin coupling mechanisms (FM or AFM phases), therefore, results of the topological analysis of the periodic DFT calculations are collectively tabulated under the heading FM/AFM. The dinuclear models give slightly different values. Overall, there is a close agreement between the theoretical and the experimental results for **1**. As expected,¹⁹ the electron density at the bond critical points ρ_{bcp} closely correlates with the Cu–X distances. For both **1** and **2**, it is easy to differentiate the bonds along the pseudo Jahn-Teller distortion (z) from those in the xy plane: Cu–O2 is always associated with a smaller amount of electron density in a rather flat region. All the coordinative interactions at Cu are characterized by positive Laplacian at the bond critical points ($\nabla^2\rho_{bcp}$). This is not surprising and, at variance with what is often stated in the literature, it does not indicate any predominance of closed-shell character.^{19b} In fact, the delocalization index²⁰ (DI) of all Cu–X bonds is approximately one-half of an electron pair, except for Cu–O2 (DI ca. 0.1) in keeping with the smaller ρ_{bcp} and $\nabla^2\rho_{bcp}$. As anticipated, the Cu–O2 bond path in **1** is significantly bent (Fig. 3.4) towards the magnetic orbital $d_{x^2-y^2}$, indicating that the Cu–O2 interaction partially involves this orbital whereas no interaction with d_{z^2} occurs. Albeit much smaller, a similar bending characterizes the corresponding bond-path in **2**, where not stereochemical constraint forces O2 to deviate from z direction. As a consequence of this curvature, the ellipticity of Cu–O2 is considerably larger than for all other Cu–X bonds.

The atomic graph of Cu (obtained from the topology of $L(\mathbf{r}) = -\nabla^2\rho_1(\mathbf{r})$) is quite informative of its stereochemistry. For **1**, both the experimental (Fig. 3.5) and the periodic DFT calculations support a rather distorted octahedral coordination. The emerging graph is in keeping with the expectations of ligand field theory: the 3d electrons avoid the charge concentrations of the ligands. In the Cu VSCC region, critical points of $L(\mathbf{r})$ are located about 0.28–0.30 Å from the nucleus, being mainly determined by the 3d electronic shell. The six (3,+1) critical points (charge depletions) are along the 4-fold axes of the ideal octahedron, thus in direction of the ligand atoms; the four (3,–3) critical points represent charge concentrations in the xy plane whereas, out of this plane, eight (3,–1) critical points are found. In the region of valence shell charge depletion (VSCD), six (3,+3) critical points are found along the six bond paths emanating from the metallic center and approximately at 0.42 Å from the nucleus. This topology can be compared with that of a Cu^{2+} in a perfectly octahedral environment.

Table 3.3. Bond critical point properties for Cu(pyz)(NO₃)₂ (**1**)^a

	MM Exptl.	MM FM/AFM phases	FM/AFM phases	Dinuclear models
Cu–O1				
d_{bcp}	0.990	0.998	0.965	0.966
ρ_{bcp}	0.068	0.082	0.075	0.074
$\nabla^2\rho_{bcp}$	0.425	0.377	0.447	0.386
ϵ	0.24	0.31	0.10	0.09
DI				0.410
Cu–O2				
d_{bcp}	1.237	1.269	1.223	1.235
ρ_{bcp}	0.023	0.034	0.027	0.028
$\nabla^2\rho_{bcp}$	0.119	0.108	0.096	0.109
ϵ	1.07	0.75	0.84	0.54
DI				0.111
Cu–N2				
d_{bcp}	0.952	0.974	0.907	0.943
ρ_{bcp}	0.094	0.123	0.111	0.090
$\nabla^2\rho_{bcp}$	0.445	0.416	0.604	0.417
ϵ	0.13	0.10	0.05	0.05
DI				0.444
N1–O1				
d_{bcp}	0.656	0.639	0.624	0.622
ρ_{bcp}	0.436	0.411	0.427	0.426
$\nabla^2\rho_{bcp}$	–0.454	–0.432	–0.721	–0.722
ϵ	0.19	0.20	0.15	0.13
DI				1.290
N1–O2				
d_{bcp}	0.643	0.621	0.606	0.603
ρ_{bcp}	0.468	0.456	0.474	0.474
$\nabla^2\rho_{bcp}$	–0.557	–0.566	–0.686	–0.881
ϵ	0.17	0.15	0.13	0.12
DI				1.495
N1–O3				
d_{bcp}	0.619	0.616	0.592	0.592
ρ_{bcp}	0.495	0.479	0.499	0.499
$\nabla^2\rho_{bcp}$	–0.601	–0.691	–0.985	–0.976
ϵ	0.16	0.15	0.12	0.12
DI				1.628
N2–C1				
d_{bcp}	0.828	0.844	0.882	0.857
ρ_{bcp}	0.332	0.331	0.342	0.331
$\nabla^2\rho_{bcp}$	–1.123	–1.190	–0.587	–0.825
ϵ	0.07	0.03	0.05	0.09
DI				1.240
C1–C1				
d_{bcp}	0.695	0.693	0.664	0.682
ρ_{bcp}	0.319	0.320	0.365	0.317
$\nabla^2\rho_{bcp}$	–0.892	–0.982	–1.219	–0.910
ϵ	0.12	0.15	0.23	0.22
DI				1.304
C1–H1				
d_{bcp}	0.719	0.713	0.685	0.694
ρ_{bcp}	0.259	0.295	0.316	0.300
$\nabla^2\rho_{bcp}$	–0.901	–1.065	–1.342	–1.105
ϵ	0.05	0.01	0.02	0.02
DI				0.916

^a d_{bcp} represents the distance, in Å, of the atom A of the A–B bond to the bond critical point, ρ_{bcp} and $\nabla^2\rho_{bcp}$ are the electron density and its Laplacian, in au., at the bond critical point, ϵ is the bond ellipticity and DI is the delocalization index. MM Exptl.: $\rho_1(\mathbf{r})$ from multipole model fitted against experimental structure factors. MM FM/AFM: $\rho_1(\mathbf{r})$ from multipole model fitted against theoretical structure factors. FM/AFM: $\rho_1(\mathbf{r})$ directly from the periodic B3LYP calculation. Experimental standard uncertainties are omitted as they are usually smaller than 10^{-3} au.

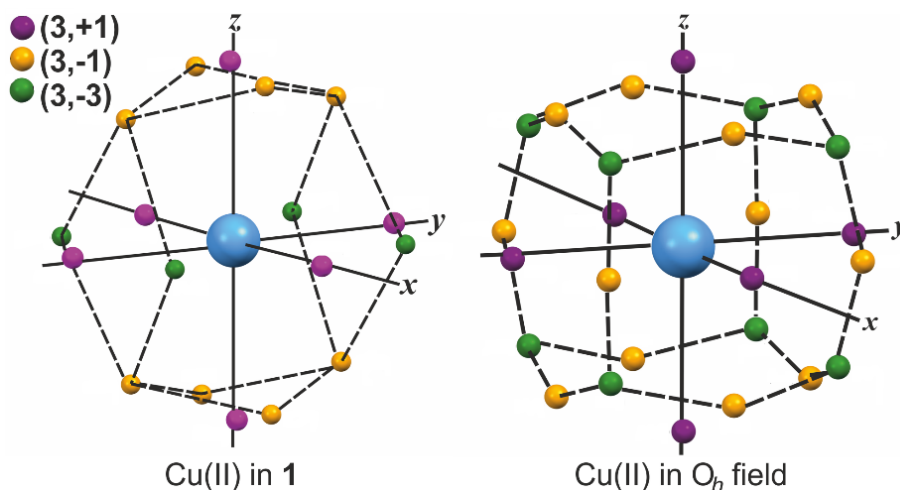


Figure 3.5. The atomic graph for Cu in $\text{Cu}(\text{pyz})(\text{NO}_3)_2$ (**1**) and in a hypothetical octahedral environment.

The graph of this Jahn-Teller unstable configuration would have the topology of a cube, see Fig. 3.5. Upon distortion along z , the $(3,-3)$ critical points lying on the vertexes of the cube collapse onto the xy plane defined by the d_{xy} orbital. Along z , the $(3,-1)$ charge accumulations remain, two of them would be in proximity of the VSCC of O2. Due to repulsion between the Cu $(3,-1)$ and O2 $(3,-3)$ charge concentrations, the former critical points assume a distorted topology respect to that observed in an O_h field: the $(3,-1)$ points in the xz plane are closer to the $(3,+1)$ in **1**, while the corresponding points in the yz plane are farther from the $(3,+1)$ points. However, the distance of the $(3,-1)$ critical points to the Cu remains constant (0.28 \AA). Moreover, the repulsion between the Cu $(3,-1)$ and O2 $(3,-3)$ charge concentrations also causes the observed bending of the Cu–O2 bond-path. This means that the residual weak Lewis acidity of the Cu(II) in z direction is not used by the second coordination of the nitrate, which prefers instead using the stronger Lewis acidity of the magnetic orbital. Although smaller, this effect also occurs in **2**, where the atomic graph of Cu is a cuboid elongated in the z direction, as a consequence of the pseudo-tetragonal symmetry of the $\text{Cu}(\text{pyz})_2$ layers.

3.3.3. d-Orbital populations and magnetic moment

The d orbital populations of Cu can be calculated from the multipolar parameters refined against structure-factor amplitudes, see Eqn. 1.81. Table 3.4 gathers the results obtained from the structure factors collected in the X-ray diffraction experiment of **1**, along with those obtained directly from population analysis of the theoretical electron densities. In both **1** and **2**, the choice of local axes (Fig. 3.1) makes $d_{x^2-y^2}$ the most energetically destabilized orbital, and therefore the least populated. As it is often the case, the multipolar model refined populations may exceed the limit of two electrons, because they are d-like density functions that are produced not only by the d-orbital of the metal.

Although the d occupancies have only a qualitative meaning, we can compute an *effective magnetic moment* μ_S (Table 3.4) as $g\mu_B\sqrt{nS(S+1)}$, in which n is the “fractional” number of unpaired electrons (defined as the excess population when the d orbital occupancy is larger than 2, and as the lacking population when the occupancy is less than 2), $S = 1/2$ for Cu(II), and the experimentally derived g-factors (2.18 and 2.11, respectively for **1** and **2**) are used. Those values agree quite well with experimental measurements of magnetic moments in other complexes of Cu(II) in distorted octahedral environments.²¹

Table 3.4. d Atomic orbital populations and spin-only magnetic moments for the Cu center in $\text{Cu}(\text{pyz})(\text{NO}_3)_2$ (**1**) and $[\text{Cu}(\text{pyz})_2(\text{NO}_3)]\text{NO}_3 \cdot \text{H}_2\text{O}$ (**2**), obtained after multipolar refinement of the experimental structure factors of (**1**), and from the periodic DFT calculations.

	$d_{x^2-y^2}$	d_{xz}	d_{xy}	d_{yz}	d_{z^2}	μ_S/μ_B
Compound 1						
Exptl.	1.34(2)	2.10(1)	2.22(1)	2.23(1)	2.00(2)	2.15
FM/AFM	1.55	1.99	1.98	1.98	1.76	1.55
Compound 2						
FM/AFM	1.43	1.98	1.98	1.98	1.99	1.38

Table 3.5. Exchange-coupling constants computed for the d1-d5 dinuclear models and for the crystal structures of **1** (using the aAFM phase) and **2** (using the sAFM phase). Experimental values are also shown for comparison.

Dinuclear model	$\text{Cu}(\text{pyz})(\text{NO}_3)_2$ (1)		$[\text{Cu}(\text{pyz})_2(\text{NO}_3)]\text{NO}_3 \cdot \text{H}_2\text{O}$ (2)	
	Cu...Cu / Å	J(di) / cm^{-1}	Cu...Cu / Å	J(di) / cm^{-1}
d1	6.70	-7.66	6.85	-5.54
d2	5.12	0.12	6.80	-0.12
d3	6.71	-0.08	9.43	-0.02
d4	8.43	0.04	9.66	0.00
d5	8.44	0.00	12.05	0.00
Periodic DFT		-7.44		-5.59
Exptl.		-7.26		-5.27

3.3.4. Magnetic exchange-coupling constants

Five possible interaction pathways between two Cu(II) centers have been identified in **1** and **2**, see Fig. 3.2. Interactions of type d1 form infinite one-dimensional chains (two of them are present in compound **2**, thus producing a bi-dimensional network) in that the metallic centers are connected by the linearly bridging pyrazine ligands. Instead, interactions of type d2 establish interchain contacts in **1** along the b crystallographic direction, whereas d2 in **2** corresponds to the direction of coordination Cu–nitrate. The remaining interactions d3-d5 are longer range contacts connecting two Cu–pyrazine chains. The DFT calculations of the exchange-coupling constants for these dinuclear models afforded the values shown in Table 4.5, in perfect agreement with a previous calculation.²² It follows that the experimentally observed magnetic behaviour in **1** and **2**, antiferromagnet with nearest-neighbour exchange constant J equals to -7.26 cm^{-1} and -5.27 cm^{-1} , respectively, can be almost exclusively attributed to interactions of type d1. Therefore, for practical purposes, material **1** can be regarded as a quasi-1D spin-1/2 quantum magnet, whereas **2** can be considered a quasi-2D magnet.

These findings are further confirmed by our periodic calculations on the FM and AFM phases. The unit cells corresponding to the aAFM phase of **1** and the sAFM phase of **2** (Fig. 3.3), thus considering the spin coupling among two Cu centers to be mediated by the pyrazine ligands, are the most stable among the considered systems. When these unit cells are used in conjunction with the corresponding FM cells for estimation of the low-spin-high-spin energy gap, a remarkably good agreement is observed with the experimental exchange-coupling constants (Table 3.5). Long-range magnetic ordering (LRO) has been already demonstrated for $\text{Cu}(\text{pyz})(\text{NO}_3)_2$,^{4b} whereas it was here verified for the first time in $[\text{Cu}(\text{pyz})_2(\text{NO}_3)]\text{NO}_3 \cdot \text{H}_2\text{O}$. However, in both cases, the interchain coupling constant estimated by zero-field muon-spin relaxation measurements, $J' = +0.03 \text{ cm}^{-1}$, is very small.

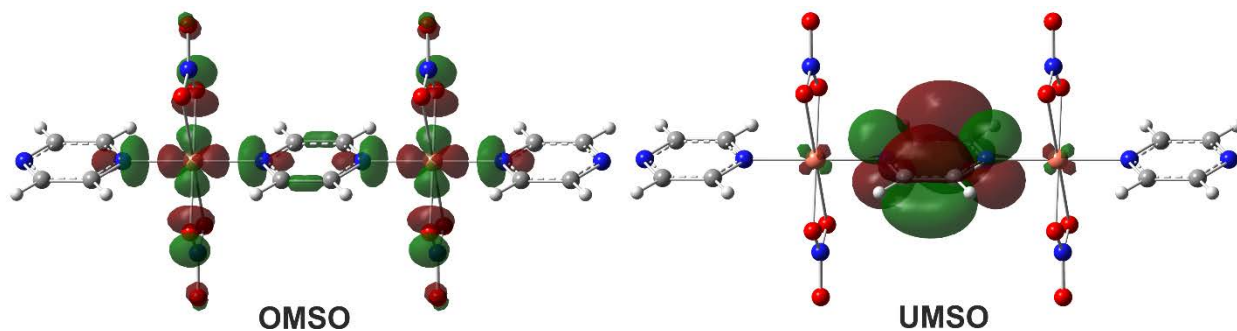


Figure 3.6. Two of the magnetic spin orbitals calculated for the triplet state of the dinuclear model 1-d1.

3.3.5. Molecular orbital analysis and magnetic-exchange mechanism

It is now convenient to look at the molecular orbitals relevant to describe the electronic states involved in the magnetic phenomena. Because the exchange-coupling constants are related to the energy difference between states with different spin multiplicities, one should focus on the orbitals bearing the unpaired electrons in the low- and high-spin states. We investigated the dinuclear model 1-d1 extracted from the infinite $\text{Cu}(\text{pyz})(\text{NO}_3)_2$ chain that is composed of two metallic centers, each one coordinated to two nitrates and two pyrazine ligands. In an unrestricted Kohn-Sham calculation, four molecular orbitals are required for describing the magnetism of this Cu(II) dinuclear model. We adopted the nomenclature proposed by Desplanches and co-workers:^{18b} the singly occupied spin-orbitals from the unrestricted calculation are called the occupied *magnetic spin-orbitals* (OMSOs). For the triplet state of the 1-d1 dinuclear complex, there are two OMSOs and two unoccupied magnetic spin-orbitals (UMSOs). Two of these orbitals are shown in Fig. 3.6. Noteworthy, the pyrazine ligand and the O1 atom of the nitrate contribute significantly to the OMSOs, which are of type $d_{x^2-y^2}$ at the metallic center, whereas O2, the oxygen atom weakly coordinated to the Cu, has a negligible contribution to these orbitals. On the other hand, the UMSOs are much more localized at the pyrazine ligands than on the nitrates. At the Cu, the UMSOs clearly present major contributions from the d_{xy} and d_{yz} atomic orbitals. The fact that both occupied and unoccupied magnetic orbitals show large contribution at the pyrazine ligands, and to a less extent at the O1 atom, confirms the role of this ligand as mediator of the Cu...Cu superexchange.

Exchange through heterocyclic diamines was first verified by Hatfield in a series of Cu(II) 1D polymers.^{17a} Since then, many studies have confirmed that the superexchange occurs mainly along the Cu–diamine–Cu chains.⁴ Hatfield proposed a π -heterocyclic exchange mechanism, according to which the spin coupling would result from the overlap between a π orbital at N and the $3d_{yz}$ or $3d_{xy}$ orbital of Cu. If the hypothesis was correct, the superexchange strength should be proportional to the tilting angle of the pyrazine ring relative to the plane defined by the $d_{x^2-y^2}$ magnetic orbital, with a maximum value at 45° . However, in light of new crystal structures and magnetic measurements, it became clear that the tilting angle is not correlated to the exchange-coupling constants. Conversely, if the spin coupling propagates through a sigma pathway only (thus characterizing a σ -mechanism), the tilting angle should have no influence on the coupling constant. Noteworthy, if the overlap between the Cu d_{yz} or d_{xy} orbital and the pyrazine π molecular orbital is significant, the tilting angle might be of relevance, in addition to the σ -exchange.²³

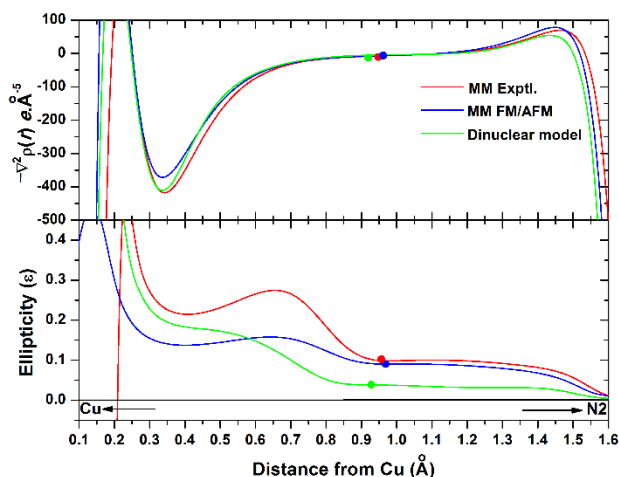


Figure 3.7. Laplacian and bond ellipticity profiles along the Cu–pyrazine bond path of $\text{Cu}(\text{pyz})(\text{NO}_3)_2$ (**1**). Filled circles represent the bond critical point positions.

The OMSOs of the 1-d1 dinuclear model show significant σ -overlap along the Cu–pyrazine bond direction (Fig. 3.6), which could be traced back as the superposition of the $d_{x^2-y^2}$ orbital of Cu with the sp^2 -hybridized orbitals at N. Conversely, the UMSOs are characterized by a π -overlap between both d_{yz} and d_{xy} orbitals of Cu and the p_z orbitals at the pyrazine atoms. Indeed, the tilting angle in **1** is 51° , very close to the 45° angle that maximizes the π -overlap. Similarly, in **2**, the tilting angle of the two pyrazine ligands with respect to the $d_{x^2-y^2}$ orbital plane is 53 and 56° .

In order to evaluate the role of N π density in the Cu–N2 bond, a useful parameter is the bond ellipticity (ϵ), which informs on asymmetric concentration of electron density in directions perpendicular to the bond paths. ϵ can be calculated at the bond critical point (see Table 3.3), but its evaluation along the bond paths provides more significant information.²⁴ Fig. 3.7 shows the ellipticity profiles of the Cu–N2 coordinative bond in the valence shell region of **1**. The ellipticity reaches a local maximum close to the bond critical point. In the direction BCP–Cu, it decreases only slightly before a large jump caused by the unbalanced d occupancy. In the direction BCP–pyrazine, instead, the ellipticity drops indicating low preferential accumulation of electronic charge perpendicularly to the bond path. While the theoretical results are biased by lack of a multi-configurational treatment, the experimental result also suggest negligible π bonding interaction between Cu and pyrazine. In view of these results, it seems that the exchange mechanism driven by the π -overlap between the d_{yz} and d_{xy} orbitals of Cu and the p_z orbitals at the pyrazine is much less relevant for the magnetic behaviour than it is the mechanism based on σ -exchange.

3.3.6. Spin density distributions

The most relevant calculated atomic spin populations are in Table 3.6 while the spin density distribution for the broken-symmetry singlet state of the dinuclear models 1-d1 and 2-d1 are shown in Fig. 3.8. The spin populations in both compounds are very similar. Although the largest part of the spin density is located at the copper atoms, there is an important delocalization of the unpaired electron, mostly to the N2 donor atoms of the pyrazine ligands, but also to the O1 atom of the nitrate ligand in compound **1**. The minute participation of the O2 atom in the OMSOs and UMSOs of 1-d1 is appreciated in its rather small negative spin population.

Table 3.6. Calculated spin populations for the dinuclear models 1-d1 and 2-d1, and for the most stable crystalline phase of **1** (aAFM) and **2** (sAFM).

	Cu(pyz)(NO ₃) ₂ (1)		[Cu(pyz) ₂ (NO ₃)]NO ₃ ·H ₂ O (2)	
	1-d1	aAFM	2-d1	sAFM
Cu	0.649	0.624	0.696	0.652
O1	0.101	0.095	0.001	0.001
O2	-0.003	-0.002	-0.001	0.000
O3	0.011	0.005		
N1	-0.003	-0.004	-0.002	0.000
nitrate	0.106	0.094	-0.003	0.001
C1	-0.003	-0.015	-0.004	0.000
C2			0.006	0.011
C3			0.006	0.014
C4			-0.006	-0.015
N2	0.071	0.102	0.082	0.093
N3			0.077	0.090
pyrazine	0.138	0.148	0.164	0.190

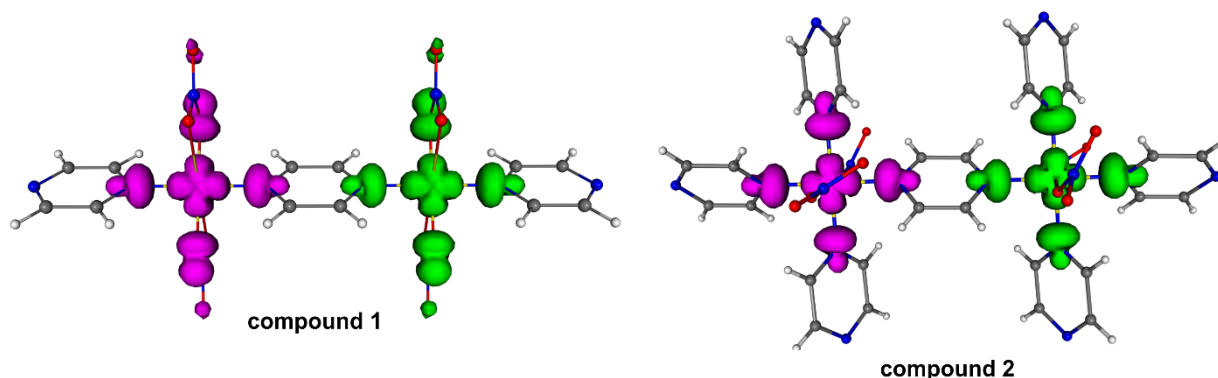


Figure 3. 8. Spin density distributions for the d1 models of **1** and **2**, in the broken-symmetry singlet state, represented at an isodensity value of 0.003 au.

The spin density distribution features observed in Table 3.6 and in Fig. 3.8 can be rationalized in terms of two mechanisms, which explain how the unpaired 3d electron of the Cu places some spin density at the other atoms of the molecule.²⁵ On the one hand, the molecular orbital that hosts the unpaired electron density, even with major contribution from the $d_{x^2-y^2}$ orbital of the copper center, presents expressive contributions from the ligands, mostly from the N2 donor atoms. If one adopts the convention that the unpaired electron has a positive spin, its delocalization results in a distribution of positive spin density throughout the whole system, as determined by the composition of the OMSOs. This behaviour characterizes the so-called *spin delocalization mechanism*. On the other hand, the positive spin at the paramagnetic center may induce some spin density of opposite sign at the atoms bonded to it, through a *spin polarization mechanism*. This results from the exchange term introduced by the Pauli principle, which disfavours the probability of finding two electrons of identical spin in the same region of space. Therefore, the spin of a bonding electron pair is polarized, in such a way that the positive spin is concentrated close to the paramagnetic center, whereas a concentration of negative spin is favoured around the atoms bonded to it. Because this effect also propagates through the system away from the metallic center, the net spin density at a particular atom, resulting from the combination of the two mechanisms, can be either positive or negative. Table 3.6 shows that the spin

delocalization mechanism dominates most of the atomic spin populations, remarkably in the xy plane defined by the Cu–O1 and Cu–N2 bonds, in **1**, and by only Cu–N2 bonds in **2**. However, spin polarization is predominant in the region of the atoms N1, O2 and C1 for compound **1**, and in the atoms N1, C1 and C4 for compound **2**.

3.4. Conclusions and perspectives

In this chapter, the electron density distribution in the low-dimensional quantum magnets Cu(pyz)(NO₃)₂ and [Cu(NO₃)(pyz)₂]NO₃·H₂O have been determined from a combination of high-resolution single-crystal X-ray diffraction and DFT calculations. The magnetic properties have been examined and correlated to the QTAIM topological and integrated properties of the electronic distributions. This has enabled the detailed rationalization of the experimental antiferromagnetic exchange-coupling constants in terms of the intrachain Cu···Cu superexchange interactions. Molecular orbitals and spin density analyses have been used to identify the atomic and group sources of the magnetism. In particular, pyrazine acts as a typical non-innocent ligand, with large part of the spin density developed on its atoms. Noteworthy in Cu(pyz)(NO₃)₂, the O1 and N2 atoms, which are directly coordinated to the transition-metal center towards the lobes of the magnetic orbital, have significant spin populations, due to spin delocalization, whereas O2, the weakest coordinated atom, has negligible spin population. In [Cu(NO₃)(pyz)₂]NO₃·H₂O, only N2 atoms are coordinated to the Cu through the magnetic orbital and they feature quite large spin densities.

From this study, it is clear that electron density analyses on magnetic transition-metal compounds could lead to a better understanding of the superexchange mechanisms. Firstly, QTAIM topological analyses are not only able to locate and characterize intra- and intermolecular contacts that can mediate magnetic couplings in the crystal, but also to relate the electron density distributions with the ligand field splitting of the orbitals at the metal centers, as discussed here for the topology of the negative Laplacian (atomic graph) of Cu(II) in compounds **1** and **2**. This kind of information is particularly valuable for the relevant cases where (pseudo)Jahn-Teller distortion takes place because the field splitting may not be particularly clear from the spatial disposition of the ligands around the metal. Secondly, the deformation density at the transition-metal site allows derivation of the d orbital occupancies, thus informing on the magnetic orbitals. Finally, if analysed in conjunction with the molecular orbitals bearing the unpaired electrons, $\rho_1(\mathbf{r})$ is also able to provide insight on the orbitals involved in the magnetic exchange. Even though the knowledge of the spin density distribution, that could be obtained from experimental techniques such as NMR spectroscopy or polarized neutron diffraction, but also from DFT calculations, is required to quantitatively predict the magnetic behaviour of a material, it is our believe that electron density-property relationships can be successfully established as the number of this kind of studies grow. We are presently investigating a larger series of transition-metal compounds in order to examine the influence of ligand type and metal nature on the magnetic properties, as well as to identify rigorous signature of magnetic interactions in the electron density distributions. In a long term view, we expect to develop electron density-based methodologies to rationally design magnetic transition-metal molecular materials.

References

1. (a) Kahn, O. *Molecular Magnetism*; Wiley-VCH: New York, **1993**. (b) Miller, J. S.; Drillon, M. (Eds.); *Magnetism: Molecules to Materials*; Wiley-VCH: Weinheim, **2001**.
2. (a) Manson, J. L.; Baldwin, A. G.; Scott, B. L.; Bendix, B. L.; Del Sesto, R. E.; Goddard, P. A.; Kohama, Y.; Tran, H. E.; Ghannadzadeh, S.; Singleton, J.; Lancaster, T.; Möller, J. S.; Blundell, S. J.; Pratt, F. L.; Zapf, V. S.; Kang, J.; Lee, C.; Whangbo, M.-H.; Baines, C. *Inorg. Chem.* **2012**, *51*, 7520-7528. (b) Amo-Ochoa, P.; Delgado, E.; Gómez-García, C. J.; Hernández, D.; Hernández, E.; Martin, A.; Zamora, F. *Inorg. Chem.* **2013**, *52*, 5943-5950.
3. (a) Amo-Ochoa, P.; Castillo, O.; Gómez-García, C. J.; Hassanein, K.; Verma, S.; Kumar, J.; Zamora, F. *Inorg. Chem.* **2013**, *52*, 11428-11437. (b) Herringer, S. N.; Deumal, M.; Ribas-Arino, J.; Novoa, J. J.; Landee, C. P.; Wikara, J. L.; Turnbull, M. M. *Chem. Eur. J.* **2014**, *20*, 8355-8362.
4. (a) Hammar, P. R.; Stone, M. B.; Reich, D. H.; Broholm, C.; Oshikawa, M. *Phys. Rev. B* **1999**, *59*, 1008-1015. (b) Lancaster, T.; Blundell, S. J.; Brooks, M. L.; Baker, P. J.; Pratt, F. L.; Manson, J. L.; Landee, C. P.; Baines, C. *Phys. Rev. B* **2006**, *73*, 020410.
5. Blessing, R. H. *Cryst. Rev.* **1987**, *1*, 3-58.
6. (a) Sheldrick, G. M. *Acta Cryst. Sect. A* **2008**, *64*, 112-122. (b) Farrugia, L. J. *J. Appl. Cryst.* **1999**, *32*, 837-838.
7. Volkov, A.; Macchi, P.; Farrugia, L. J.; Gatti, C.; Mallinson, P.; Richter, T.; Koritsanszky, T. *XD2006 - A Computer Program Package for Multipole Refinement, Topological Analysis of Charge Densities and Evaluation of Intermolecular Interaction Energies from Experimental and Theoretical Structure Factors*; University at Buffalo, State University of New York, NY, USA; University of Milano, Italy; University of Glasgow, UK; CNRISTM, Milano, Italy; Middle Tennessee State University, TN USA, **2006**.
8. (a) Clementi, E.; Roetti, C. *At. Nucl. Data Tables* **1974**, *14*, 177-478. (b) Clementi, E.; Raimondi, D. L. *J. Chem. Phys.* **1963**, *38*, 2686-2689.
9. Becker, P. J.; Coppens, P. *Acta Cryst. Sect. A* **1974**, *30*, 129-153.
10. Farrugia, L. J.; Mallinson, P. R.; Stewart, B. *Acta Cryst. Sect. B* **2003**, *59*, 234-247.
11. Herbst-Irmer, R.; Henn, J.; Holstein, J. J.; Hübschle, C. B.; Dittrich, B.; Stern, D.; Kratzert, D.; Stalke, D. *J. Phys. Chem. A* **2012**, *117*, 633-641.
12. Kamiński, R.; Domagała, S.; Jarzemska, K. N.; Hoser, A. A.; Sanjuan-Szklarz, F.; Gutmann, M. J.; Makal, A.; Malińska, M.; Bąk, J. M.; Woźniak, K. *Acta Cryst. Sect. A* **2014**, *70*, 72-91.
13. (a) Frisch, M. J.; Trucks, G. W.; Schlegel, H. B.; Scuseria, G. E.; Robb, M. A.; Cheeseman, J. R.; Montgomery, J. A., Jr.; Vreven, T.; Kudin, K. N.; Burant, J. C. et al. Gaussian 09; Gaussian, Inc.: Wallingford, CT, **2009**. (b) Keith, T. A. AIMAll, Version 14.04.17; TK Gristmill Software: Overland Park, KS, USA, **2014**, aim.tkgristmill.com.
14. (a) Dovesi, R.; Saunders, V. R.; Roetti, C.; Orlando, R.; Zicovich-Wilson, C. M.; Pascale, F.; Civalleri, B.; Doll, K.; Harrison, N. M.; Bush, I. J.; D'Arco, P.; Llunell, M. *CRYSTAL09 User's manual*; University of Torino, **2009**. (b) Gatti, C. *TOPOND* **2009**, CNR-CSR SRC, Milan, Italy.

15. (a) Doll, K.; Harrison, N. M. *Chem. Phys. Lett.* **2000**, *317*, 282-289. (b) Gatti, C.; Saunders, V. R.; Roetti, C. *J. Chem. Phys.* **1994**, *101*, 10686-10696.
16. (a) Towler, M. D.; Allan, N. L.; Harrison, N. M.; Saunders, V. R.; Mackrodt, W. C.; Aprà, E. *Phys. Rev. B* **1994**, *50*, 5041-5054. (b) Towler, M. D.; Dovesi, R.; Saunders, V. R. *Phys. Rev. B* **1995**, *52*, 10150-10159. (c) Dovesi, R.; Fava, F. F.; Roetti, C.; Saunders, V. R. *Faraday Discuss.* **1997**, *106*, 173-187. (d) Reinhardt, P.; Moreira, I. de P. R.; de Graaf, C.; Dovesi, R.; Illas, F. *Chem. Phys. Lett.* **2000**, *319*, 625-630. (e) Datta, S. N.; Hansda, S. *Chem. Phys. Lett.* **2015**, *621*, 102-108.
17. (a) Crawford, V. H.; Richardson, H. W.; Wasson, J. R.; Hodgson, D. J.; Hatfield, W. E. *Inorg. Chem.* **1976**, *15*, 2107-2110. (b) Laborda, S.; Clérac, R.; Anson, C. E.; Powell, A. K. *Inorg. Chem.* **2004**, *43*, 5931-5943. (c) Walsh, J. P. S.; Sproules, S.; Chilton, N. F.; Barra, A.-L.; Timco, G. A.; Collison, D.; McInnes, E. J. L.; Winpenney, R. E. P. *Inorg. Chem.* **2014**, *53*, 8464-8472.
18. (a) Cauchy, T.; Ruiz, E.; Jeannin, O.; Nomura, M.; Fourmigué, M. *Chem. Eur. J.* **2007**, *13*, 8858-8866. (b) Desplanches, C.; Ruiz, E.; Rodríguez-Fortea, A.; Alvarez, S. *J. Am. Chem. Soc.* **2002**, *124*, 5197-5205. (c) Manson, J. L.; Conner, M. M.; Schlueter, J. A.; McConnell, A. C.; Southerland, H. I.; Pratt, F. L.; Singleton, J.; McDonald, R. D.; Lee, C.; Whangbo, M.-H. *Chem. Mater.* **2008**, *20*, 7408-7416.
19. (a) Gibbs, G. V.; Downs, R. T.; Cox, D. F.; Rosso, K. M.; Ross, N. L.; Kirfel, A.; Lippmann, T.; Morgenroth, W.; Crawford, T. D. *J. Phys. Chem. A* **2008**, *112*, 8811-8823. (b) Macchi, P.; Sironi, A. *Coord. Chem. Rev.* **2003**, *238*, 383-412.
20. Mebs, S.; Kalinowski, R.; Grabowsky, S.; Förster, D.; Kickbusch, R.; Justus, E.; Morgenroth, W.; Paulmann, C.; Luger, P.; Gabel, D.; Lentz, D. *Inorg. Chem.* **2011**, *50*, 90-103.
21. Vulfson, S. G. *Molecular Magnetochemistry*; Overseas Publishers Association: Amsterdam, **1998**.
22. Jornet-Somoza, J.; Deumal, M.; Robb, M. A.; Landee, C. P.; Turnbull, M. M.; Feyerherm, R.; Novoa, J. *J. Inorg. Chem.* **2010**, *49*, 1750-1760.
23. Butcher, R. T. *PhD Thesis*; Worcester, **2008**.
24. Scherer, W.; Herz, V.; Hauf, C. *Struct. Bond.* **2012**, *146*, 159-204.
25. Ruiz, E.; Cirera, J.; Alvarez, S. *Coord. Chem. Rev.* **2005**, *249*, 2649-2660.

Chapter 4

Unconstrained and X-ray Constrained Extremely Localized Molecular Orbitals: Analysis of the Reconstructed Electron Density*

The recently developed X-ray constrained Extremely Localized Molecular Orbital (XC-ELMO) technique is a potentially useful tool for the determination and analysis of experimental electron densities. Molecular orbitals strictly localized on atoms, bonds or functional groups allow to combine the quantum-mechanical rigor of the wavefunction-based approaches with the easy chemical interpretability typical of the multipole models, with the additional advantage of being largely transferable among systems. In this chapter, using very high-quality X-ray diffraction data for the glycylglycine crystal, a detailed assessment of capabilities and limitations of this new method is given. In particular, the effects of constraining the ELMO wavefunctions to experimental X-ray structure-factor amplitudes and the ability of the method to reproduce benchmark electron distributions have been accurately investigated. Topological analysis of the XC-ELMO electron densities and of the QTAIM integrated charges and dipole moments show that the new strategy is already reliable, provided that sufficiently flexible basis sets are used. These analyses also open new questions and call for further improvements of the method towards applications in materials science.

The following abbreviations are frequently used in this chapter:

<i>General</i>	
ELMO	Extremely Localized Molecular Orbital
XC-ELMO	X-ray Constrained Extremely Localized Molecular Orbital
IAM	Independent Atom Model
MM	Multipole Model
$\{F_{h,obs}\}, \{F_{h,calc}\}$	Set of experimentally observed or calculated structure-factor amplitudes
$\sigma(F_{h,obs}), \sigma(F_{h,obs}^2)$	Standard uncertainty associated with the experimental amplitude $F_{h,obs}$ or with the corresponding intensity $F_{h,obs}^2$
η	Overall h -independent scale factor which multiplies the calculated structure-factor amplitudes
<i>One-electron densities</i>	
$\rho^{MM/XC}$	Multipole-fitted (X-ray constrained) electron density; refined against experimental structure factors
$\rho^{MM/P-B3LYP}$	Multipole-fitted periodic B3LYP electron density; refined against B3LYP/6-31G(2d,2p) crystal-phase calculated structure factors
$\rho^{MM/ELMO}$	Multipole-fitted ELMO electron density; refined against ELMO gas-phase calculated structure factors
$\rho^{MM/XC-ELMO}$	Multipole-fitted XC-ELMO electron density; refined against XC-ELMO calculated structure factors
$\rho^{P-B3LYP}$	Electron density calculated directly from the periodic B3LYP/6-31G(2d,2p) computation
ρ^{ELMO}	Electron density calculated directly from an ELMO gas-phase wavefunction
$\rho^{XC-ELMO}$	Electron density calculated directly from an XC-ELMO wavefunction
ρ^{HF}	Electron density calculated directly from a Hartree-Fock gas-phase wavefunction
ρ^{XC-HF}	Electron density calculated directly from an XC-Hartree-Fock wavefunction
ρ^{IAM}	Independent Atom Model density; sum of spherically averaged electron densities of isolated atoms

*This chapter was taken and modified from Dos Santos, L. H. R.; Genoni, A.; Macchi, P. *Acta Cryst. Sect. A* **2014**, *70*, 532-551.

4.1. Introduction, motivation and specific goals

As discussed in Chapter 1, even though the wavefunction is the fundamental entity that contains all the information of a system, Hohenberg and Kohn have shown that the ground-state electron density and the wavefunction of an electronic system can be used alternatively as full descriptors of the ground-state and, therefore, it would be possible to obtain all properties of a material from its electron density distribution, which is an observable and, unlike the wavefunction, is a simple three-dimensional function of the spatial coordinates.¹

The prominence conferred by the Hohenberg-Kohn theorems to the electron density together with the observation that the knowledge of the electron distribution and of its properties has profound consequences for the understanding of chemical bonding has significantly increased the importance of accurate determination of electron densities in crystals by means of high-resolution X-ray diffraction experiments.² Nevertheless, as also discussed in Chapter 1, the observed diffraction intensities do not directly provide the electron density because only a finite number of structure factors can be collected and, within the kinematic approximation, their phase cannot be measured. Consequently, the electron distribution in the unit cell can be accurately reconstructed only by fitting a model against the collected X-ray diffraction intensities. The parameters of this model electron density are usually obtained minimizing the difference between experimentally observed and calculated structure factors.

Within this context, the *multipole models* are by far the most widely adopted approaches.² Since the total electron distribution is the sum of the aspherical atom-centered density functions (also known as *pseudo-atoms*, see Eqn. 1.46), the resulting ground-state electron density of a molecule is simply approximated by the sum of atomic electron distributions deformed by the presence of chemical interactions. This is the main reason why these models offer an easy chemical interpretability. Notwithstanding this advantage, they also exhibit a non-negligible drawback: the number of properties directly available from the model electron density is limited because the exact functional relation between the ground-state electron distribution and the ground-state wavefunction is practically unknown. Furthermore, the parameters of a multipole expansion may strongly correlate with the atomic displacement parameters (ADPs).

A possible solution to overcome these drawbacks is offered by a work which dates back to 1969, thus even before the appearance of multipole models. Clinton *et al.*³ proposed to derive wavefunctions or one-electron density matrices constrained to experimental or theoretical X-ray diffraction data. Since then, many researchers drew inspiration from the Clinton's ideas.⁴ Within this framework, the most promising method is the *X-ray constrained wavefunction approach* developed by Jayatilaka and co-workers.⁵ As discussed in Chapter 1, the method exploits the Lagrange multiplier technique to provide a single-Slater determinant which, other than minimizing the corresponding energy, reproduces a set of experimentally collected X-ray structure-factor amplitudes within a predefined precision. In particular, the Lagrange multiplier is iteratively adjusted until the desired agreement level is achieved between the structure-factor amplitudes obtained from the diffraction experiment and those calculated from the single-Slater determinant *ansatz*. Therefore, the constrained wavefunction reproduces the experimental data within a given precision, and, as it possesses all the quantum-mechanical features of a wavefunction, it can be used to compute also those properties that are not directly related to the

experimental structure factors used to determine the wavefunction itself.⁶ Compared to the multipole models, the approach enables to obtain quantum-mechanically rigorous electron densities, but it is affected by a reduced chemical interpretability because the *canonical molecular orbitals* are usually completely delocalized over the whole system. Therefore, they are far from the traditional and intuitive picture of a molecule constituted by atoms, bonds and functional groups, typical of the pseudo-atom approaches.

Genoni has recently devised a new technique to extract from X-ray diffraction data a single-Slater determinant built-up with molecular orbitals strictly localized (without tails) on molecular fragments, such as atoms, bonds or functional groups.^{7a,b} This strategy can be considered as a combination of the experimentally constrained wavefunction approach proposed by Jayatilaka with the method developed by Stoll for the determination of *extremely localized molecular orbitals* (ELMOs).⁸ This synergy should be useful to solve the above-mentioned drawback associated with the X-ray constrained canonical molecular orbitals. Moreover, due to the complete absence of tails, the ELMOs are directly transferable, thus they can be computed on fragments of small model molecules and afterwards properly exported to subunits belonging to more complex systems.^{7c,d} The ELMOs *transferability* is analogous to the well-known pseudo-atoms transferability within the framework of the multipole models. In this view, new databases could be constructed from X-ray constrained ELMOs (XC-ELMOs) and used as complement to the existing experimental⁹ or theoretical¹⁰ libraries of pseudo-atoms, successfully used for the refinement of macromolecular crystallographic structures and for the evaluation of electrostatic properties in crystals.

In this chapter, we present a comprehensive assessment of the performances of XC-ELMO technique. In particular, we analyse the machinery of the constraint procedure, evaluating how much the unconstrained and the X-ray constrained wavefunctions differ and to what extent the XC-ELMO electron density is able to reproduce the “exact” crystal electron density. The latter is approximated with two well-established methods, namely the multipole model density fitted or, in analogy with the wavefunction approach, *constrained* to the experimental structure factors, hereinafter $\rho^{MM/XC}$, and the electron density directly obtained from a periodic DFT calculation with a standard hybrid functional, $\rho^{P-B3LYP}$. To accomplish this task we have investigated the α -glycylglycine crystal, already known from X-ray and neutron diffraction experiments.¹¹ Except for a qualitative deformation electron density study by Kvick^{11c} and a spherical κ -formalism refinement by Coppens,^{11d} to the best of our knowledge, no complete electron density refinement for this system has been reported in literature.

The chapter is structured as it follows. First, we summarize the theory of the X-ray constrained ELMO technique. Afterwards, we describe the experimental and computational methodologies and then we analyse the results. We initially focus on the effects of the fitting procedure, comparing the residual

*Here we adopt the terminology currently used in the literature: the wavefunction fitted to the X-ray structure factors is called *constrained*, and not *restrained* as it would have been more intuitive for crystallographers. The traditional multipolar fitting can also be considered as an “X-ray constrained density function”. Therefore, we will call the traditional multipolar model fitted to the X-ray structure factors as “X-ray constrained multipolar model” (MM/XC). Of course, this nomenclature does not imply an additional constraint equation to be satisfied, other than the least squares minimization functions and those already present in the multipolar fitting (e.g. electroneutrality condition). When discussing about local symmetry constraints on the multipolar model, which implies that some parameters are not refined, we will refer to them as *rigid constraints* to avoid ambiguity.

features and the topological properties computed from unconstrained or X-ray constrained ELMO electron densities (from now on, ρ^{ELMO} and $\rho^{XC-ELMO}$, respectively). In a second step, we compare ρ^{ELMO} and $\rho^{XC-ELMO}$ with the density from a periodic calculation ($\rho^{P-B3LYP}$). In a third step, we project ρ^{ELMO} and $\rho^{XC-ELMO}$ in terms of multipoles, thus obtaining $\rho^{MM/ELMO}$ and $\rho^{MM/XC-ELMO}$ respectively, and we compare these densities with multipole electron distributions fitted against the experimental intensities ($\rho^{MM/XC}$) or against theoretical structure factors obtained from the periodic calculation ($\rho^{MM/P-B3LYP}$). This procedure allows us to compare all the densities equally affected by the limitations of the multipolar model. Finally, we investigate how the choice of initial parameters (fractional coordinates and ADPs of the atoms in the unit cell) affects the XC-ELMO results and the convergence of the fitting process. In the last section, we draw some conclusions and discuss perspectives offered by this new strategy.

4.2. Extremely localized molecular orbitals

The extremely localized molecular orbitals (ELMOs) method proposed by Stoll⁸ can be considered one of the many theoretical approaches that have been developed to decompose the global electronic wavefunction into functions describing smaller subsets of electrons,¹² with the purpose of recovering concepts such as bonds, atoms and functional groups in molecules, which are inherently lost when canonical molecular orbitals are computed. ELMOs are *a priori* localized only on a selected set of atoms and are variationally determined under this constraint, at variance with the so-called *localized molecular orbitals* (LMOs), obtained from *a posteriori* transformation of the delocalized orbitals. Even though LMOs recover to a great extent the concepts of atoms, functional groups, bonds, etc., they are not directly transferable because they preserve *tails* on the entire molecule, thus their transferability to other systems requires the tail deletion. On the other hand, the complete absence of tails makes ELMOs the best orbitals consistent with a chosen localization scheme, besides being directly transferable among the same atoms or functional groups in different molecules.^{7c}

Let us consider an N -electron closed-shell molecule and introduce a localization scheme that subdivides the system into f fragments (e.g., atoms, bonds or functional groups) that can overlap. Due to this fragmentation, each subunit j is characterized by a local basis set $\{\phi_{\mu}^j(\mathbf{r})\}$, which is constituted by the only K^j atomic basis functions centred on the atoms belonging to the fragment, see Eqn. 1.13 for a direct analogy to canonical orbitals. Consequently, the ELMOs describing the subunit are expanded on ϕ_{μ}^j and, therefore, the generic i -th ELMO for the j -th fragment can be written as⁷

$$\varphi_i^j(\mathbf{r}) = \sum_{\mu=1}^{K^j} C_{\mu i}^j \phi_{\mu}^j(\mathbf{r}) \quad (4.1)$$

It should be observed that pre-defined subunits may overlap and, consequently, share atomic orbitals, which leads to a natural non-orthogonality between ELMOs associated with different fragments.

Following Stoll,⁸ the wavefunction describing the system is a normalized single-Slater determinant (see Eqns. 1.10 and 11) built-up with ELMOs:

$$\Psi_{ELMO}(\mathbf{x}_1, \mathbf{x}_2, \dots, \mathbf{x}_N) = \frac{1}{\sqrt{N!} \det[\mathbf{S}]} \begin{vmatrix} \chi_i^j(\mathbf{x}_1) & \chi_k^l(\mathbf{x}_1) & \dots & \chi_m^f(\mathbf{x}_1) \\ \chi_i^j(\mathbf{x}_2) & \chi_k^l(\mathbf{x}_2) & \dots & \chi_m^f(\mathbf{x}_2) \\ \vdots & \vdots & & \vdots \\ \chi_i^j(\mathbf{x}_N) & \chi_k^l(\mathbf{x}_N) & \dots & \chi_m^f(\mathbf{x}_N) \end{vmatrix} \quad (4.2)$$

where $\det[\mathbf{S}]$ is the determinant of the overlap matrix between the occupied ELMOs. The coefficients in (4.1) are obtained variationally minimizing the energy associated with the ELMO wavefunction, which is equivalent to solve self-consistently the following Hartree-Fock equations for each subunit:

$$\mathbf{f}_i^j \chi_i^j(\mathbf{x}) = \varepsilon_i^j \chi_i^j(\mathbf{x}) \quad (4.3)$$

with \mathbf{f}_i^j being the modified one-electron operator for the generic fragment j that can be seen as the sum of a *local contribution*, which depends only on the occupied ELMOs of the fragment, and a *global contribution*, which depends on all the occupied ELMOs of the system. Because of the latter term, Eqn. 4.3 couples all the modified Hartree-Fock equations associated with the different subunits, similarly to Eqn. 1.16. However, due to the non-orthogonality of the ELMOs, convergence problems and instabilities may arise when solving (4.3). To overcome these drawbacks, different strategies have been implemented.^{7c}

Of course, the localization scheme is rather arbitrary and dependent on the applications. Usual schemes can be obtained from the Lewis formula of the molecule and defining one ELMO for each bond or lone pair.^{7a,b}

Finally, we note that because the procedure of determination of ELMOs is based on a reduction in the number of variational coefficients used to describe them, the electronic energy of Ψ_{ELMO} is necessarily larger than the corresponding Hartree-Fock energy.

For the determination of *X-ray constrained extremely localized molecular orbitals* (XC-ELMOs), one simply searches for the ELMOs that minimize the functional (1.55). Similarly to the case of canonical orbitals, this is equivalent to solve self-consistently a new set of eigenvalue problems (4.3) for each fragment, modified according to the constraint (1.56) associated with the X-ray diffracted intensities. Noteworthy, previous application of this technique to amino acids and other materials have shown that the experimental constraint entails significant redistribution of the electronic charge.^{7b} This result has been discussed in light of the potential ability of XC-ELMOs to include electronic correlation and crystal field effects in gas-phase molecular ELMO calculations, but systematic investigation in this direction is still lacking. This possibility is also addressed in this chapter for the case of glycylglycine.

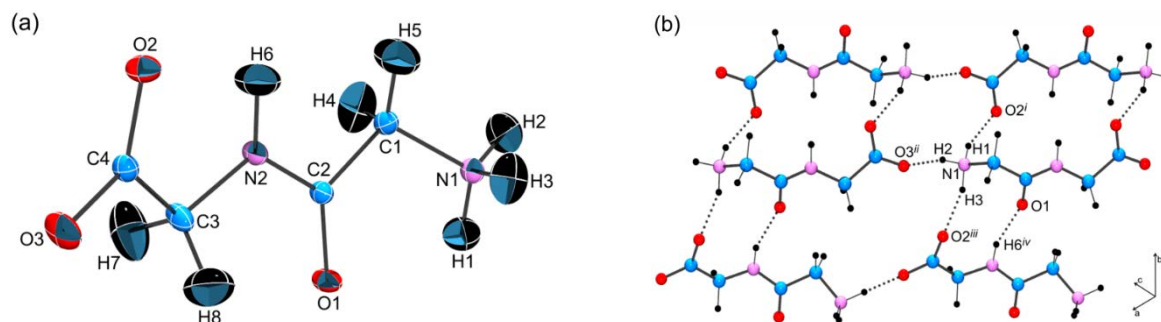


Figure 4.1. Experimental molecular structure of crystalline α -glycylglycine (a) and strongest hydrogen bond network (b). Thermal ellipsoids are drawn at 70% probability level. Symmetry codes: (i) $-x+1, y+1/2, -z+3/2$; (ii) $x+1, y, z+1$; (iii) $-x+1, -y, -z+1$; (iv) $-x+1, y+1/2, -z+3/2$.

4.3. Experimental and computational details

4.3.1. X-ray data collection and processing

α -Glycylglycine, Fig. 4.1(a), was recrystallized by slow evaporation of an *n*-propanol-water mixture. We have re-determined the crystal structure by single-crystal X-ray diffraction at 100 K. The temperature was stable within ± 0.5 K. Details of data collection and refinement procedures are given in Table 4.1. Measurements were carried out on an Agilent SuperNova diffractometer equipped with a MoK α Al-filtered micro-source¹³ and an Oxford Cryo-system 700 cryostream for low temperature. Data collection, reduction and cell refinement were performed using the CRYSTALIS PRO programs. A total of 2765 image frames were obtained from 33 ω scan sets (1.0° oscillation angle) using three different exposure times. The scan sets with low detector θ offsets were measured for 10 + 10 s, intermediate-angle images were collected for 30 + 30 s and the high-angle images were measured for 60 + 60 s. The unit-cell dimensions were determined by post-refinement of 18946 reflections ($2.7^\circ < \theta < 52.4^\circ$). An analytical absorption correction was applied using a multifaceted crystal model based on expressions derived by Clark and Reid¹⁴ as implemented in SCALE3 ABSPACK scaling algorithm. A total of 38933 reflections were collected with a mean redundancy of 5.9. The resulting data were merged using SORTAV¹⁵ giving 6597 independent reflections until resolution of $\sin \theta_{max}/\lambda = 1.12 \text{ \AA}^{-1}$ ($\theta_{max} = 52.6^\circ$ for MoK α radiation).

4.3.2. Spherical, independent atom refinement

Atomic coordinates and ADPs were taken from Ref. 11a and refined on F^2 applying the independent atom model (IAM) and using all data with full-matrix least-squares as implemented in SHELXL,^{16a} within the WINGX package.^{16b} The weighting scheme $w_h = [\sigma^2(F_{h,obs}^2) + (AP)^2 + BP]^{-1}$ was applied, where $P = F_{h,obs}^2/3 + 2F_{h,calc}^2/3$ and $A = 0.0606$, $B = 0.0360$. All non-hydrogen atoms were refined anisotropically. X–H distances and hydrogen ADPs were fixed according to experimental neutron diffraction data.^{11b} As recommended by Blessing,¹⁷ the H-atom ADPs were scaled against the ADPs obtained for the heavier atoms from the two experiments. An isotropic extinction parameter was also refined according to the empirical expression implemented in SHELXL, where $F_{h,calc}$ is multiplied by $\eta[1 + 0.001 \epsilon F_{h,calc}^2 \lambda^3/\sin(2\theta_h)]^{-1/4}$, with η as the overall scale factor and ϵ as the extinction parameter, which was refined to 0.007 (4).

Table 4.1. Crystallographic details and results of IAM and multipolar refinements for glycylglycine.

Crystal data	
Crystal system, space group	Monoclinic, $P2_1/c$
a, b, c (Å)	7.9798 (1), 9.5201 (1), 7.7643 (1)
β (°)	106.151 (1)
V (Å ³)	566.56 (1)
Z	4
θ range (°) for cell measurement	2.7–52.4
μ (mm ⁻¹)	0.13
Crystal size (mm)	0.20 × 0.17 × 0.07
Data collection	
Absorption correction	Analytical (Clark and Reid, 1995)
T_{\min}, T_{\max}	0.974, 0.991
No. of measured, independent and observed [$F > 3\sigma(F)$] reflections	38933, 6597, 5467
Redundancy	5.9
R_{int}^a	0.029
θ values (°)	$\theta_{\max} = 52.6, \theta_{\min} = 2.1$
$(\sin \theta/\lambda)_{\max}$ (Å ⁻¹)	1.118
Range of h, k, l	$h = -17 \rightarrow 17, k = -21 \rightarrow 21, l = -17 \rightarrow 17$
Spherical, independent atom refinement	
Refinement on	F^2 (for $F > 0$)
$R[F > 3\sigma(F)], R_{\text{all}}, wR, S, \chi^2{}^b$	2.82, 4.15, 4.16, 1.06, 2.60
No. of parameters	107
$(\Delta/\sigma)_{\max}$	0.001
$\Delta\rho_{\max}, \Delta\rho_{\min}$ (e Å ⁻³)	0.54, -0.37
Extinction coefficient	0.007 (4)
Multipole refinement	
Refinement on	F^2 (for $F > 3\sigma(F)$)
$R[F > 3\sigma(F)], R_{\text{all}}, wR, S, \chi^2{}^b$	1.97, 3.30, 2.14, 1.03, 0.91 (MM1) 1.72, 2.93, 1.71, 0.80, 0.57 (MM2) 1.70, 2.91, 1.68, 0.80, 0.55 (MM3)
No. of parameters ^c	271
$(\Delta/\sigma)_{\max}{}^c$	0.00001
$\Delta\rho_{\max}, \Delta\rho_{\min}$ (e Å ⁻³) ^c	0.14, -0.14
Extinction coefficient ^c	0.315 (15)

^a $R_{\text{int}} = \sum_{\mathbf{h}} |F_{\mathbf{h},\text{obs}}^2 - \langle F_{\mathbf{h},\text{obs}}^2 \rangle| / \sum_{\mathbf{h}} F_{\mathbf{h},\text{obs}}^2$ (summation is carried out only where more than one symmetry equivalent reflection is averaged). ^b $R(F) = 100 \cdot \sum_{\mathbf{h}} \left| |F_{\mathbf{h},\text{obs}}| - |F_{\mathbf{h},\text{calc}}| \right| / \sum_{\mathbf{h}} |F_{\mathbf{h},\text{obs}}|$, $wR(F) = 100 \cdot \left[\sum_{\mathbf{h}} w_{\mathbf{h}} (|F_{\mathbf{h},\text{obs}}| - |F_{\mathbf{h},\text{calc}}|)^2 / \sum_{\mathbf{h}} w_{\mathbf{h}} F_{\mathbf{h},\text{obs}}^2 \right]^{1/2}$, $S = \left[\sum_{\mathbf{h}} w_{\mathbf{h}} (F_{\mathbf{h},\text{obs}}^2 - F_{\mathbf{h},\text{calc}}^2)^2 / (N - P) \right]^{1/2}$ with $w_{\mathbf{h}} = 1/\sigma_{\mathbf{h},\text{obs}}^2$, N as the number of reflections and P as the number of parameters. χ^2 is given by Eqn. 1.56. Both in the spherical model and in the multipole model refinements the calculated structure-factor magnitudes are properly multiplied by a scale factor η and by an additional factor $Y_{\mathbf{h}}(\epsilon)$ that corrects for secondary extinctions. For the spherical model, $Y_{\mathbf{h}}(\epsilon) = \left[1 + 0.001 \epsilon F_{\mathbf{h},\text{calc}}^2 \lambda^3 / \sin(2\theta_{\mathbf{h}}) \right]^{-1/4}$, while, for the multipole model, $Y_{\mathbf{h}}(\epsilon)$ has been chosen following the Becker and Coppens equations.²⁰ ^c For MM2 model.

4.3.3. Multipole refinement

The multipole refinement was performed using the XD2006 program¹⁸ and the Hansen-Coppens formalism. The core and spherical valence density (ρ_1^{core} and ρ_1^{val} , respectively, see Eqn. 1.48) are composed of Hartree-Fock wavefunctions expanded in Slater-type orbitals.^{19a} The valence shell is either contractible or expandable by the use of the κ parameter. Single-zeta orbitals with energy-optimized Slater exponents are used for the radial part of the deformation terms.^{19b} Additional radial parameters κ' are defined for each angular momentum l in order to deal with the radial expansion or contraction of the deformation density. Several multipole models were tested, see Section 4.4.

The function minimized in the least-squares procedure was $\sum_{\mathbf{h}} w_{\mathbf{h}} (F_{\mathbf{h},obs}^2 - \eta Y_{\mathbf{h}}(\epsilon) F_{\mathbf{h},calc}^2)^2$ where the statistical weight $w_{\mathbf{h}} = 1/\sigma^2(F_{\mathbf{h},obs}^2)$ was applied and where only those reflections characterized by $F_{\mathbf{h},obs} > 3\sigma_{\mathbf{h},obs}(F_{\mathbf{h},obs})$ were included. Furthermore, η is the overall scale factor while $Y_{\mathbf{h}}(\epsilon)$ is the correction for secondary extinctions according to the model proposed by Becker and Coppens.²⁰ This model depends on the isotropic extinction parameter ϵ , which was refined to 0.315 (15), corresponding to a mosaicity spread of 10".

The multipole expansion was truncated at the hexadecapole level for all the non-H atoms, while bond-directed dipoles and quadrupoles were applied to all the H-atoms. The κ and κ' parameters were initially set to proper reference values²¹ and posteriorly refined. A single κ' was refined for all the l values belonging to a defined set while κ' for the H-atoms was not refined. The X–H distances were initially set to neutron diffraction averages but then freely refined. A high-order refinement with $\sin \theta/\lambda \geq 0.7 \text{ \AA}^{-1}$ was performed for the non-H atoms to obtain accurate positional and displacement parameters. In the next step, the H-atom ADPs were estimated by the SHADE routine²² and the obtained values were used as fixed parameters in the subsequent refinements.

4.3.4. Ab initio periodic calculation and multipole refinement of theoretical structure factors

In order to provide an additional and reliable benchmark for the XC-ELMO calculations, a single-point periodic calculation was performed on the final multipole model geometry without including thermal smearing, using the CRYSTAL09 package²³ at the density functional theory level using the B3LYP functional. The calculation was carried out using the standard 6-31G(2d,2p) basis-set.

In order to mimic the experimental refinement as much as possible, the calculation of theoretical structure factors was limited to the \mathbf{h} directions observed experimentally and, afterwards, a static multipole model refinement (i.e., ADPs set to zero) of the theoretical data was performed without optimizing atomic positions, thus eliminating an important source of correlation between parameters. As for the experimental refinement, the multipole expansion was truncated at the hexadecapole level for the non-H atoms and only bond-directed dipoles and quadrupoles were refined for the H-atoms. Both κ and κ' parameters were refined independently for each heavy atom, while only one κ was refined for all the H-atoms. The rigid local symmetry constraints and chemical equivalences were also consistent with the experimental refinement (see Section 4.4).

4.3.5. Unconstrained and X-ray constrained ELMO and Hartree-Fock calculations

The X-ray constrained ELMO strategy has been implemented by Dr. Alessandro Genoni (University of Lorraine, France) modifying the version 8 of the GAMESS-UK quantum chemistry package,²⁴ which has been used to perform all the unconstrained ($\lambda = 0$) and constrained ($\lambda \neq 0$) ELMO calculations that will be discussed.

In order to assess the fitting effects on the ELMO electron density of the glycylglycine molecule, ELMO and XC-ELMO calculations have been performed using the 6-31G, 6-31G(d,p) and cc-pVDZ basis sets and considering both the IAM and the MM experimental molecular geometries obtained from the X-ray diffraction experiment. Electron density-related properties derived from the constrained ELMO wavefunctions were afterwards compared to the ones corresponding to the unconstrained ELMO wavefunctions.

For all the ELMO calculations, the adopted localization scheme almost corresponds to the Lewis structure of the molecule, with atomic fragments, which describes the core electrons and the lone-pairs associated with each atom, and with bond subunits, which describe all the electron pairs between each couple of nuclei. The only exceptions are represented by two three-atom fragments: one for the σ and the π electrons of the amide group O1–C2–N2 (comprising also the electrons for the delocalized lone pair of the nitrogen atom) and another one for the σ and the π electrons of the carboxylic group O2–C4–O3. The same localization scheme has been used for all the XC-ELMO calculations for which the unit cell parameters and the ADPs associated with the different refinement models were also taken into account. Concerning the experimental structure-factors amplitudes used to constrain the ELMO wavefunctions, only those characterized by $F_{h,obs} > 3\sigma_{h,obs}(F_{h,obs})$ were selected (overall 5467 reflections). As anticipated, the set of amplitudes $\{F_{h,obs}\}$ was previously corrected for secondary extinctions. Furthermore, the scale factor η was properly optimized during the XC-ELMO computations.

For sake of comparison, using the Tonto package,²⁵ we have computed unconstrained and X-ray constrained Hartree-Fock electron densities (ρ^{HF} and ρ^{XC-HF} , respectively) for the three selected basis sets. These densities are to be compared with the corresponding ELMO and XC-ELMO densities.*

4.3.6. Topological analyses

QTAIM has been exploited to analyze all the obtained charge distributions. In particular, the TOPXD module²⁶ was used to partition and integrate the atomic basins of all the multipole-fitted electron densities. The TOPOND98 software²⁷ was used to perform the topological analysis of the periodic B3LYP/6-31G(2d,2p) electron density $\rho^{P-B3LYP}$, while the analyses of all the ρ^{ELMO} , $\rho^{XC-ELMO}$, ρ^{HF} and ρ^{XC-HF} electron distributions were performed with the AIMAll software.²⁸

*XC-HF wavefunctions were computed at the same λ_{max} values as the corresponding XC-ELMO wavefunctions, except for the 6-31G basis set, for which SCF convergence could not be achieved for $\lambda \geq 0.40$ (see Table 4.2).

Given the complexity associated with the definition of zero-flux surfaces in the electron density and with the subsequent integration,²⁹ the numerical integration error of the atomic basins, which is defined by

$$L(\Omega) = -\frac{1}{4} \int_{\Omega} \nabla^2 \rho(\mathbf{r}) d\mathbf{r} \quad (4.4)$$

and which should be zero for an ideal integration, was also carefully monitored. In this work, the values of $L(\Omega)$ approximately ranged from 3×10^{-6} to 2×10^{-3} au.

4.4. Fitting effects on the multipole model

In this section, we analyse the effects of fitting several Hansen-Coppens multipole models against the experimentally collected structure factors. In other words, we investigate step-by-step the relaxation of the local symmetries of atoms from spherical and neutral to aspherical and charged. After the spherical atom refinement (Section 4.3.2), an initial multipole model (MM1) was refined using several rigid constraints on the local symmetry of the atomic density functions (*mm2* for O1, O2, O3 and C4; *m* for C1, C2, C3 and N2; *3m* for N1; see Fig. 4.1(a) for atomic labels) and chemical equivalences (O2 = O3, C1 = C3). These constraints imply sp^2 hybridization for N2, C4 and for all the O atoms and sp^3 hybridization for N1, C1 and C3 (however, a “perfect” hybridization includes here an asymmetric polarization induced by chemical bonds to atoms of different electronegativity). The H-atoms were treated with cylindrical symmetry ($m\infty$) and those bonded to equivalent heavier atoms were also treated as equivalent.

The atomic symmetries were progressively reduced, using the statistical parameters R and wR and the residual density maps as guides to select the best refinement model. The chemical equivalences were then removed and the following local symmetries were used (MM2 model): *mm2* for C4, *3m* for N1 and *m* for all the other non-H atoms and $m\infty$ for all the H's. This implies sp^2 hybridization for C4, sp^3 for N1, C1 and C3 but a mixed character for all the O atoms and N2. In the last cycle, the coordinates and the ADPs for all the non-H atoms, the coordinates for the H-atoms, the κ and κ' parameters, the multipole populations, the extinction parameter ϵ and the overall scale factor η were refined together, for an overall optimization of 271 parameters. A satisfactory deconvolution of thermal motion from the deformation electron density distribution has been obtained, as shown by the Hirshfeld rigid-bond test.³⁰ In fact, the largest differences of mean-squares displacement amplitudes (DMSDA) was $5 \times 10^{-4} \text{ \AA}^2$, which is lower than the limit of 0.001 \AA^2 suggested by Hirshfeld. Additionally, the comparison between the final ADPs of the MM2 model with those previously published for the neutron diffraction on glycylglycine^{11b} shows a mean absolute difference of $0.0008(14) \text{ \AA}^2$, taking however into account that the temperatures of the two experiments are different (100 K of the current X-ray diffraction vs. 82 K for the neutron diffraction). The neutron and X-ray geometries are in good agreement, but, as expected, larger discrepancies occur for positions of H atoms: in fact, X–H distances are on average $0.04(2) \text{ \AA}$ shorter in the MM2 model with respect to the neutron diffraction geometry. The maximum and minimum residual peaks are $+0.14$ and $-0.14 e \cdot \text{\AA}^{-3}$, with the residual density maps showing only few and small discrepancies that could not be removed by any deformation model.

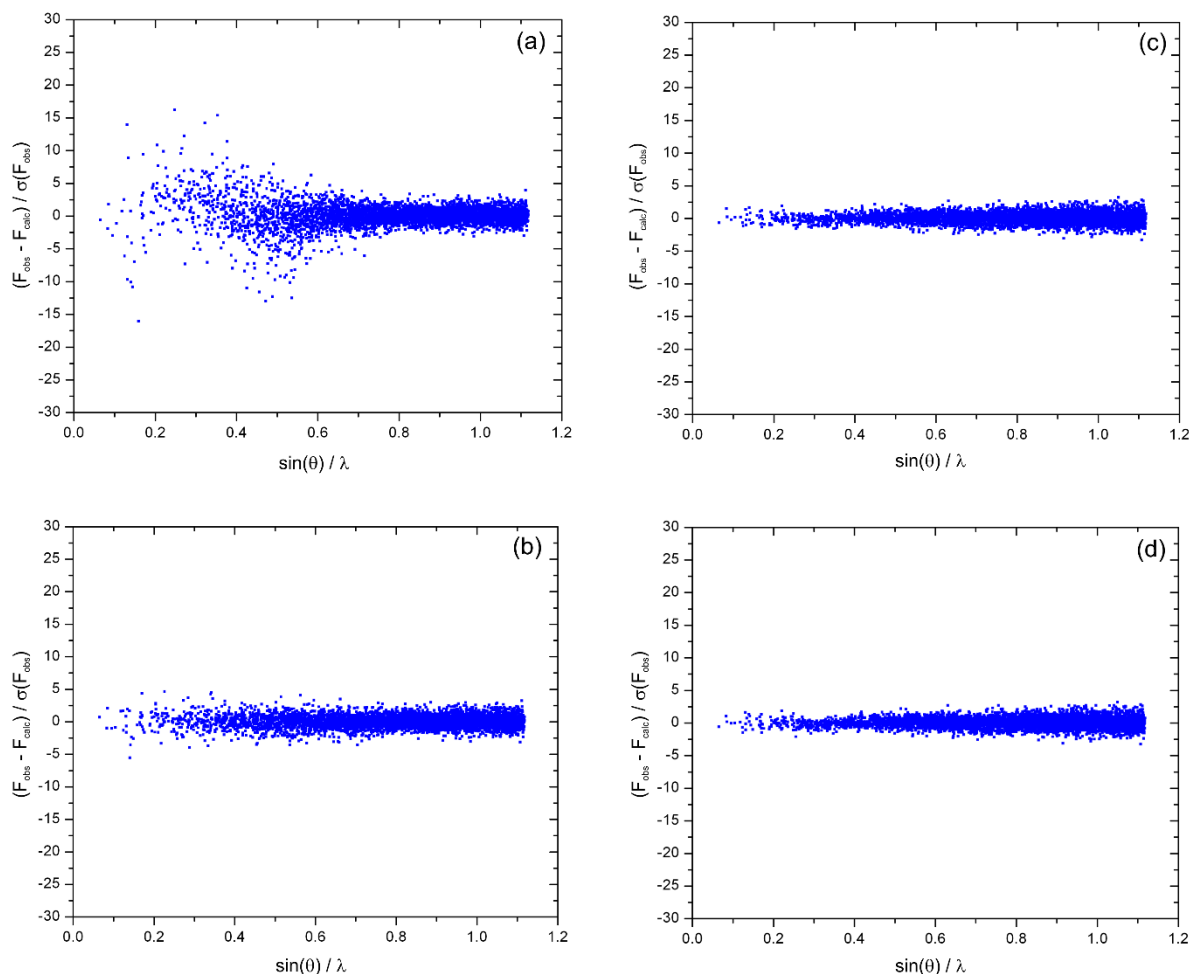


Figure 4.2. Normalized residuals of the structure-factor amplitudes vs. the scattering resolution for the (a) IAM and the different multipole models (b) MM1, (c) MM2 and (d) MM3 refined against the experimental set of structure factors.

For the sake of completeness, we have also performed a multipole refinement up to hexadecapole level for all non-H atoms and up to the quadrupole level for the H-atoms without imposing any local symmetry constraint (MM3), namely we have refined all the corresponding multipoles, accounting 423 parameters overall. The final statistical agreements (see Table 4.1) are very close to those obtained in the last refinement cycle of the symmetry constrained MM2 model described above.

Fig. 4.2 shows scatter plots of the difference between experimental and calculated structure-factor amplitudes normalized by the experimental standard deviations as a function of the $\sin \theta / \lambda$ resolution for the IAM and the three MM refinements. It is obvious that the multipolar refinement improves the agreement between measured and calculated structure factors compared to the IAM, Fig. 4.2(a), even when rigid local symmetry constraints are extensively applied, MM1 model, Fig. 4.2(b). The progressive reduction of the local symmetries and the removal of equivalences (MM2) further improve the agreement, Fig. 4.2(c), whereas a model without any local symmetry constraint (MM3) does not further reduce the normalized residuals, Fig. 4.2(d). In fact, the number of reflections computed within $\pm 1\sigma$ from the observed ones is 3336, 3888, 4236 and 4276, for IAM, MM1, MM2 and MM3, respectively. The Hamilton significance test³¹ also indicates that removing the local symmetry constraints from MM2 does not lead to a significant model improvement, despite using 152 additional parameters. Therefore, the models MM2 and MM3 are not statistically different and from now on,

we only refer to the results obtained using the local symmetry constrained multipole model MM2 just described. A similar conclusion can be reached refining the P-B3LYP structure factors with these two models, meaning that also the theoretical crystal density shows such a local symmetry for all the atoms.

Attempts to refine core deformations were not carried out, as this would be beyond the scope of this paper. Such a study would require even higher resolution and, at present, has been applied only on smaller and more symmetric crystals.³²

Based on the difference density maps, the residual density analysis^{33a} and the normal probability plots,^{33b} one can easily conclude that both the measured intensities and the refined multipole models are of extremely good quality and therefore could be a very good benchmark for the XC-ELMO calculations.

4.5. Fitting effects on the ELMO wavefunctions

4.5.1. Agreement statistics and energy

The agreement statistics and the energies for all the X-ray constrained computations on glycylglycine, using the geometry and the ADPs from MM2 refinement, are reported in Table 4.2. For each basis set, the XC-ELMO calculations are of course in better agreement with the measured intensities. For the 6-31G basis set, however, the desired agreement cannot be reached ($\chi^2 = 1.27$ for $\lambda_{max} = 0.40$, with an asymptote above 1.0), whereas it is quite smoothly obtained for the larger and more flexible basis sets 6-31G(d,p) and cc-pVDZ ($\chi^2 \leq 1$ for λ as large as 0.12), see Fig. 4.3. Here we point out that for the 6-31G basis set the second termination criterion in (1.58) is satisfied, while in the other two cases we have observed the fulfillment of the more traditional condition $\chi^2 < 1$.

χ^2 rapidly decreases as λ increases, showing that even a weak constraint to the X-ray data is sufficient to improve significantly the agreement. The asymptotic value of χ^2 is slightly above the limit obtained for the multipolar models (0.57 and 0.55 for MM2 and MM3, respectively) and smaller than for the

Table 4.2. Statistical agreements^a and energy values corresponding to all the unconstrained and constrained calculations performed on the glycylglycine considering the geometry and the ADPs resulting from the Multipole Model refinement.

Basis set	χ^2	%R(F)	%wR(F)	Energy (au)	λ_{max}	χ^2	%R(F)	%wR(F)	Energy (au)
ELMO Calculations ^b					XC-ELMO Calculations				
6-31G	2.56	2.62	3.44	-489.161	0.40	1.27	2.17	2.43	-489.060
6-31G(d,p)	1.74	2.38	2.84	-489.385	0.12	1.00	2.04	2.15	-489.357
cc-pVDZ	1.66	2.36	2.78	-489.394	0.12	0.98	2.03	2.13	-489.368
Hartree-Fock Calculations ^b					XC-Hartree-Fock Calculations				
6-31G	2.11	2.47	3.13	-489.310	0.38 ^c	1.15	2.05	2.17	-489.227
6-31G(d,p)	1.41	2.25	2.56	-489.549	0.12	0.85	1.93	1.98	-489.528
cc-pVDZ	1.31	2.20	2.47	-489.574	0.12	0.83	1.93	1.97	-489.556

^a $\chi^2 = (1/(N_r - N_p)) \sum_h w_h (\eta |F_{h,calc}| - |F_{h,obs}|)^2$, $\%R(F) = 100 \left[\frac{\sum_h |\eta |F_{h,calc}| - |F_{h,obs}||}{\sum_h |F_{h,obs}|} \right]$, $\%wR(F) = 100 \left[\chi^2 / \sum_h w_h F_{h,obs}^2 \right]^{1/2}$ with $w_h = 1/\sigma_{h,obs}^2(F_{h,obs})$. ^bThe scale factors η have been optimized using the density matrices obtained from the corresponding unconstrained calculations. ^c χ^2 reaches an asymptotic values above $\lambda = 0.3$ but no SCF convergence is found for $\lambda \geq 0.40$.

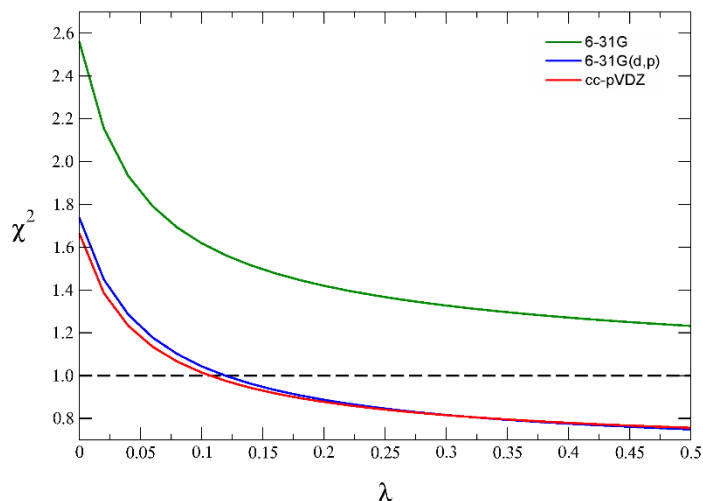


Figure 4.3. The variation of χ^2 agreement with the Lagrange multiplier λ for the XC-ELMO 6-31G (green), 6-31G(d,p) (blue) and cc-pVDZ (red) calculations, using geometry and ADPs from the Multipole Model MM2.

IAM (2.60). The agreement indexes R and wR shown in Table 4.2 mirror the behaviour of the χ^2 statistics, but they are much less sensitive to λ and, therefore, less useful to compare the quality of the different constrained wavefunctions. On the other hand, R and wR can be used for comparison against the multipole models (see Table 4.1), which of course give better agreements because they do not have to satisfy an energy minimization criterion and, above all, because they are not subject to the termination criterion $\chi^2 \leq 1$ imposed by Eqn. 1.58. Furthermore, R and wR confirm that XC-ELMO performs much better than an IAM refinement.

Fig. 4.4 shows the normalized differences between experimental and ELMO or XC-ELMO structure-factor amplitudes in function of the resolution. Almost all the structure-factor amplitudes computed from the 6-31G(d,p) and cc-pVDZ XC-ELMO wavefunctions, Fig. 4.4(e) and (f), are within $\pm 5\sigma$ from the experimental values without any obvious resolution dependence. The number of reflections within the $\pm 1\sigma$ range is 4149 and 4240 for the 6-31G(d,p) and the cc-pVDZ basis sets, respectively, contrasting with 3663 and 3764 reflections within $\pm 1\sigma$ for the unconstrained ELMO 6-31G(d,p) and cc-pVDZ wavefunctions, respectively. On the other hand, for the XC-ELMO/6-31G wavefunction, for which $\chi^2 = 1.27$, only the structure-factor amplitudes calculated at resolution $\sin \theta / \lambda > 0.5 \text{ \AA}^{-1}$ agree with the experimental values within $\pm 5\sigma$, while many low-angle structure factors significantly exceed the 5σ limit, Fig. 4.4(d). Moreover, the XC-ELMO/6-31G plot shows a distribution of normalized residuals quite similar to that associated with the unconstrained ELMO wavefunctions (respectively 3689 and 3954 reflections are within the $\pm 1\sigma$ range for the unconstrained and the X-ray constrained ELMO 6-31G wavefunctions, respectively), meaning that the X-ray constraining procedure was actually not particularly effective, despite the better agreement indexes. In this respect, the comparison between Fig. 4.4(d) with 4.4(b) and 4.4(c) is extremely elucidative because it shows that an X-ray constrained wavefunction is not better than an unconstrained one in the absence of polarization functions in the basis set. This demonstrates that the ELMO/6-31G wavefunction is definitely not flexible enough to fit the experimental data. On the contrary, if sufficient variational flexibility is present in the basis set, even unconstrained ELMO wavefunctions better reproduce the experimentally collected structure factors.

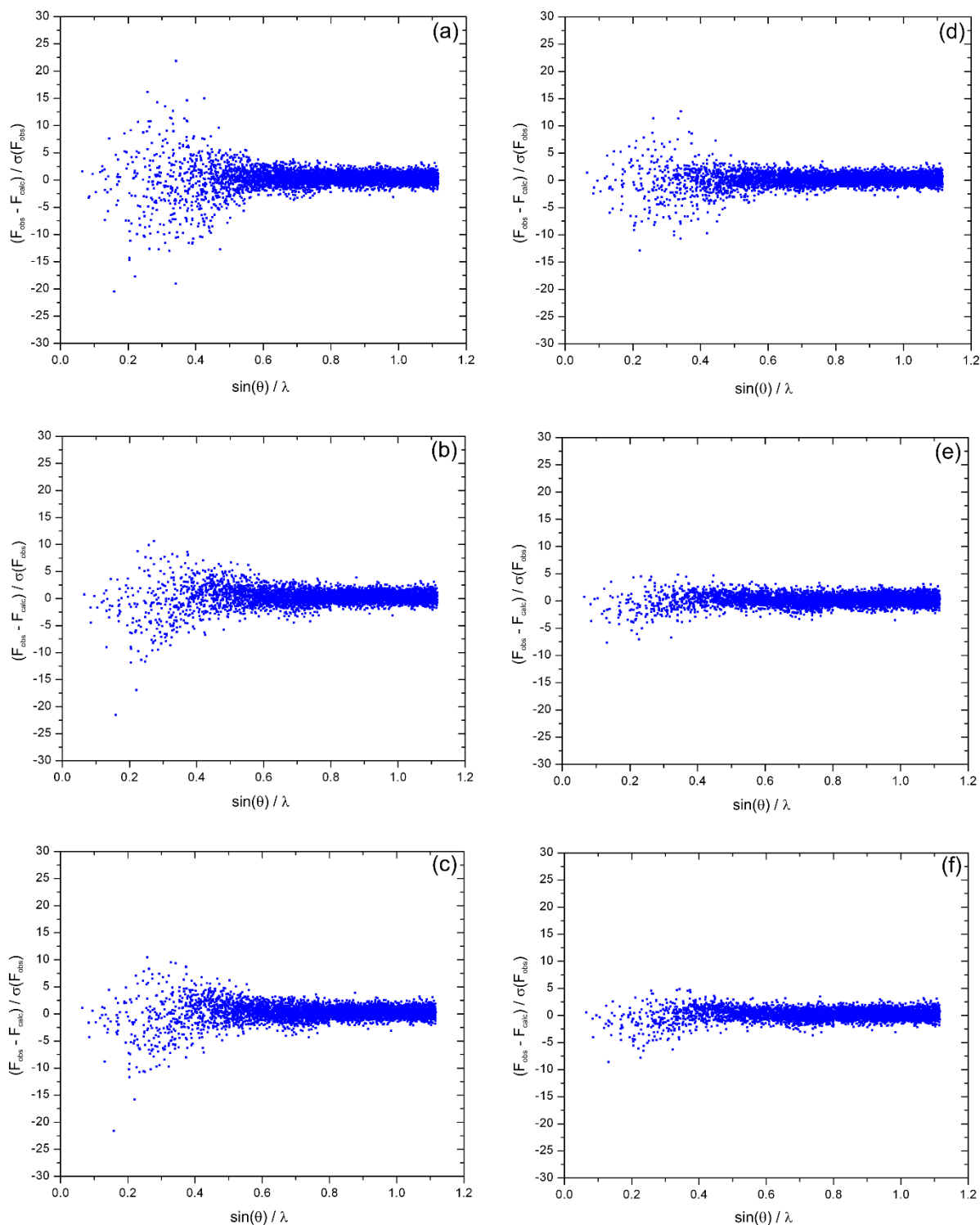


Figure 4.4. Normalized residuals of the structure-factor amplitudes vs. the scattering resolution for the unconstrained ELMO (a) 6-31G, (b) 6-31G(d,p) and (c) cc-pVDZ wavefunctions and for the XC-ELMO (d) 6-31G, (e) 6-31G(d,p) and (f) cc-pVDZ wavefunctions.

The constraint to strictly localize the molecular orbitals on molecular subunits introduces additional approximations over the usual Hartree-Fock method, which enables full delocalization of the canonical molecular orbitals. In order to quantify this effect, we have computed unconstrained and X-ray constrained Hartree-Fock electron densities (ρ^{HF} and ρ^{XC-HF} , respectively) for the three selected basis sets and compared them with the corresponding ELMO and XC-ELMO densities. Both

unconstrained and X-ray constrained Hartree-Fock electron densities produce better statistical agreements than the corresponding ELMO and XC-ELMO electron distributions. Moreover, the gap between ρ^{HF} and ρ^{ELMO} is roughly constant as a function of λ , see Table 4.2. These results suggest that ρ^{HF} and ρ^{ELMO} are equally able to incorporate the information from the experimental structure-factor amplitudes.

In Table 4.2 the energies associated with all the unconstrained and constrained wavefunctions are also reported. As already observed, the energies of constrained wavefunctions are always higher, in keeping with what is expected in a variational procedure when a constraint is added without introducing a new variational parameter.

4.5.2. Electron density distribution and its topology

Fig. 4.5 shows three-dimensional plots of $\rho^{XC-ELMO} - \rho^{ELMO}$ for the 6-31G and the 6-31G(d,p) basis sets, the distribution associated with the cc-pVDZ case is very similar to the 6-31G(d,p) one. While for the 6-31G(d,p) basis set the main consequences of the fitting consist in a large redistribution of the electron density around the nuclei and in only small rearrangements in the bonding regions, the 6-31G fitting procedure entails significant changes of the electron density both in the core and in the bonding domains. This is especially evident for the oxygen atoms, for which a depletion of electron density in the lone-pairs regions is noteworthy. Other important fitting effects are the reduction of electron density associated with the C–H bonds and the shifting of electronic charge from the H atoms to the N atoms. Shifts of electron density from C3 to C4 and, analogously, from C2 to N2 and from N1 to C1 are also observed.

Topological properties at the bond critical points of ρ^{ELMO} and $\rho^{XC-ELMO}$ are gathered in Table 4.3 and they are compared to the results obtained from the periodic B3LYP/6-31G(2d,2p) computation ($\rho^{P-B3LYP}$). The properties obtained from the XC-ELMO wavefunctions are in general similar to those obtained from the corresponding unconstrained ELMO calculations, especially the electron density at the bond critical points, $\rho(\mathbf{r}_b)$. Upon closer inspection, we see that the XC-ELMO $\rho(\mathbf{r}_b)$ generally approach the P-B3LYP limit for the more complete and polarized basis sets.

The analysis of the Laplacian at the bond critical points, $\nabla^2\rho(\mathbf{r}_b)$, show much larger discrepancies. As previously discussed,³⁴ this is a consequence of the intrinsic nature of the Laplacian, especially for polar bonds. Fig. 4.6 depicts the plots of $L = -\nabla^2\rho(\mathbf{r})$, which shows regions of electron density concentration ($L > 0$) and depletion ($L < 0$), in the plane of the glycylglycine carboxylate group. The constrained or unconstrained plots are qualitatively very similar, showing regions of electronic charge concentration along the C–C, and C–O bonds as well as in the lone-pairs regions of the oxygen atoms. The atomic graphs of C4, O2 and O3 have the expected trigonal arrangement of three charge concentration maxima in both constrained and unconstrained cases. Nevertheless, because polar bond critical points lie close to nodal surfaces of the Laplacian, small changes in the position of these bond critical points may lead to large changes of $\nabla^2\rho(\mathbf{r}_b)$. This explains the large differences between constrained and unconstrained $\nabla^2\rho(\mathbf{r}_b)$ values found in Table 4.3 and stress the importance of correctly locating the critical point along the corresponding bond path.^{34b}

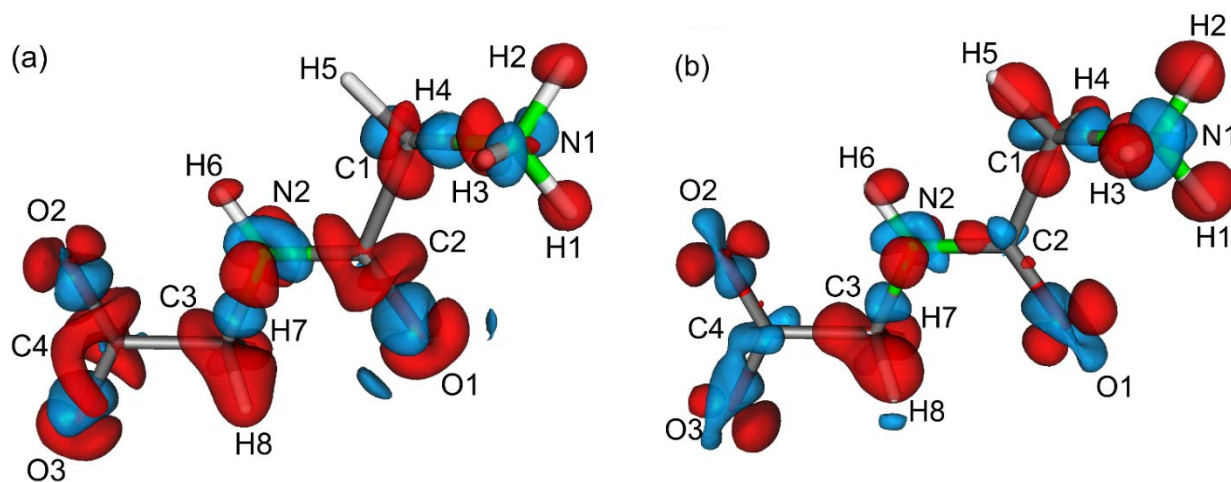


Figure 4.5. Three-dimensional plots of the electron density difference $\rho^{XC-ELMO} - \rho^{ELMO}$ for the (a) 6-31G and the (b) 6-31G(d,p) basis sets. The isosurface value is 0.005 au, with negative isosurfaces in red and positive isosurfaces in blue.

For sake of completeness, we have also computed the topological properties for both the ρ^{HF} and ρ^{XC-HF} electron densities. The comparison with the corresponding ELMO and XC-ELMO densities indicates that the ELMO approximation does not introduce significant changes in the electron distributions, in keeping with the small differences between the agreement indices reported in Table 4.2. For example, the difference in electron density at the bond critical points between ρ^{ELMO} and ρ^{HF} and between $\rho^{XC-ELMO}$ and ρ^{XC-HF} are usually less than 5% for the 6-31G basis set and even less for the larger 6-31G(d,p) and cc-pVDZ basis sets.

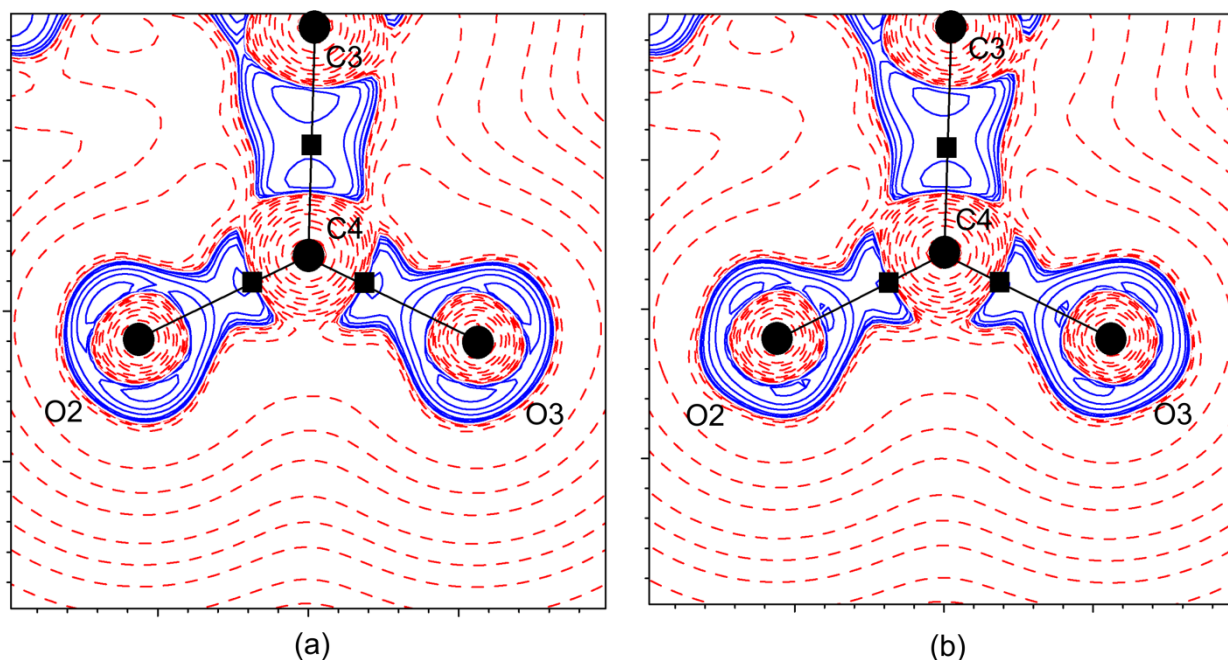


Figure 4.6. Plots of $L = -\nabla^2\rho(\mathbf{r})$ for the (a) ELMO/6-31G(d,p) and (b) XC-ELMO/6-31G(d,p) wavefunctions of glycylglycine in the carboxylate plane. Contours are drawn at intervals of $(\pm 2, \pm 4, \pm 8) \times 10^n e.\text{\AA}^{-5}$ ($n = -3$ to 3). Blue lines denote regions of charge concentration ($L > 0$) and red lines denote regions of charge depletion ($L < 0$).

Table 4.3. Bond critical point data^a for all glycyglycine electron densities resulting from unconstrained and constrained ELMO calculations. Data for the $\rho^{P-B3LYP}$ density are also shown.

	$\rho_{6-31G(2d,2p)}^{P-B3LYP}$	ρ_{6-31G}^{ELMO}	$\rho_{6-31G(d,p)}^{ELMO}$	$\rho_{cc-pVDZ}^{ELMO}$	$\rho_{6-31G}^{XC-ELMO}$	$\rho_{6-31G(d,p)}^{XC-ELMO}$	$\rho_{cc-pVDZ}^{XC-ELMO}$
O1-C2							
d_A	0.825	0.799	0.833	0.835	0.806	0.835	0.837
$\rho(\mathbf{r}_b)$	0.397	0.386	0.406	0.401	0.398	0.405	0.404
$-\nabla^2\rho(\mathbf{r}_b)$	0.409	0.922	0.346	0.243	0.917	0.158	0.123
O2-C4							
d_A	0.837	0.811	0.849	0.850	0.819	0.851	0.851
$\rho(\mathbf{r}_b)$	0.380	0.368	0.388	0.383	0.375	0.389	0.387
$-\nabla^2\rho(\mathbf{r}_b)$	0.532	0.908	0.387	0.330	0.842	0.217	0.229
O3-C4							
d_A	0.834	0.807	0.845	0.846	0.813	0.846	0.847
$\rho(\mathbf{r}_b)$	0.385	0.374	0.395	0.389	0.381	0.393	0.390
$-\nabla^2\rho(\mathbf{r}_b)$	0.519	0.952	0.413	0.342	0.888	0.223	0.194
N1-C1							
d_A	0.879	0.957	1.012	1.004	0.907	1.000	0.981
$\rho(\mathbf{r}_b)$	0.252	0.218	0.240	0.235	0.233	0.249	0.246
$-\nabla^2\rho(\mathbf{r}_b)$	0.642	0.326	0.271	0.307	0.521	0.502	0.575
N2-C2							
d_A	0.836	0.798	0.885	0.879	0.854	0.890	0.888
$\rho(\mathbf{r}_b)$	0.350	0.335	0.363	0.355	0.327	0.346	0.344
$-\nabla^2\rho(\mathbf{r}_b)$	1.282	1.110	1.153	1.213	0.959	0.846	0.927
N2-C3							
d_A	0.874	0.957	0.995	0.989	0.897	0.988	0.975
$\rho(\mathbf{r}_b)$	0.263	0.227	0.248	0.243	0.250	0.259	0.256
$-\nabla^2\rho(\mathbf{r}_b)$	0.712	0.259	0.203	0.253	0.629	0.429	0.528
C1-C2							
d_A	0.747	0.777	0.786	0.788	0.757	0.749	0.751
$\rho(\mathbf{r}_b)$	0.256	0.242	0.277	0.270	0.240	0.267	0.262
$-\nabla^2\rho(\mathbf{r}_b)$	0.560	0.509	0.862	0.772	0.505	0.770	0.703
C3-C4							
d_A	0.757	0.787	0.797	0.802	0.776	0.764	0.771
$\rho(\mathbf{r}_b)$	0.254	0.240	0.275	0.268	0.238	0.266	0.260
$-\nabla^2\rho(\mathbf{r}_b)$	0.551	0.503	0.867	0.778	0.505	0.771	0.705
N1-H1							
d_A	0.808	0.771	0.792	0.804	0.776	0.798	0.807
$\rho(\mathbf{r}_b)$	0.322	0.322	0.354	0.339	0.316	0.336	0.326
$-\nabla^2\rho(\mathbf{r}_b)$	1.849	-1.590	2.094	1.925	1.553	1.900	1.825
N1-H2							
d_A	0.785	0.741	0.763	0.774	0.741	0.768	0.776
$\rho(\mathbf{r}_b)$	0.352	0.346	0.378	0.364	0.342	0.353	0.346
$-\nabla^2\rho(\mathbf{r}_b)$	2.083	1.710	2.232	2.001	1.679	1.937	1.837
N1-H3							
d_A	0.804	0.763	0.784	0.797	0.768	0.793	0.803
$\rho(\mathbf{r}_b)$	0.325	0.324	0.356	0.342	0.324	0.338	0.330
$-\nabla^2\rho(\mathbf{r}_b)$	1.873	1.581	2.085	1.855	1.600	1.887	1.802
C1-H4							
d_A	0.708	0.696	0.692	0.697	0.695	0.709	0.723
$\rho(\mathbf{r}_b)$	0.269	0.268	0.297	0.290	0.267	0.287	0.284
$-\nabla^2\rho(\mathbf{r}_b)$	0.893	0.817	1.163	1.142	0.813	1.114	1.134
C1-H5							
d_A	0.692	0.680	0.674	0.684	0.676	0.690	0.703
$\rho(\mathbf{r}_b)$	0.287	0.282	0.312	0.304	0.276	0.298	0.294
$-\nabla^2\rho(\mathbf{r}_b)$	1.036	0.921	1.290	1.255	0.878	1.188	1.197
N2-H6							
d_A	0.789	0.750	0.768	0.779	0.759	0.779	0.788
$\rho(\mathbf{r}_b)$	0.331	0.332	0.363	0.348	0.332	0.349	0.339
$-\nabla^2\rho(\mathbf{r}_b)$	1.899	1.610	2.093	1.815	1.640	1.942	1.814
C3-H7							
d_A	0.678	0.641	0.629	0.639	0.647	0.655	0.667
$\rho(\mathbf{r}_b)$	0.289	0.298	0.327	0.318	0.285	0.300	0.297
$-\nabla^2\rho(\mathbf{r}_b)$	1.041	1.019	1.396	1.330	0.973	1.168	1.179
C3-H8							
d_A	0.646	0.631	0.619	0.638	0.620	0.630	0.642
$\rho(\mathbf{r}_b)$	0.317	0.316	0.345	0.335	0.289	0.303	0.301
$-\nabla^2\rho(\mathbf{r}_b)$	1.277	1.172	1.565	1.489	1.013	1.187	1.205

^aFor each bond critical point A-B, d_A is its distance from the nucleus A in Å, $\rho(\mathbf{r}_b)$ is its electron density value in au and $\nabla^2\rho(\mathbf{r}_b)$ is its Laplacian value in au.

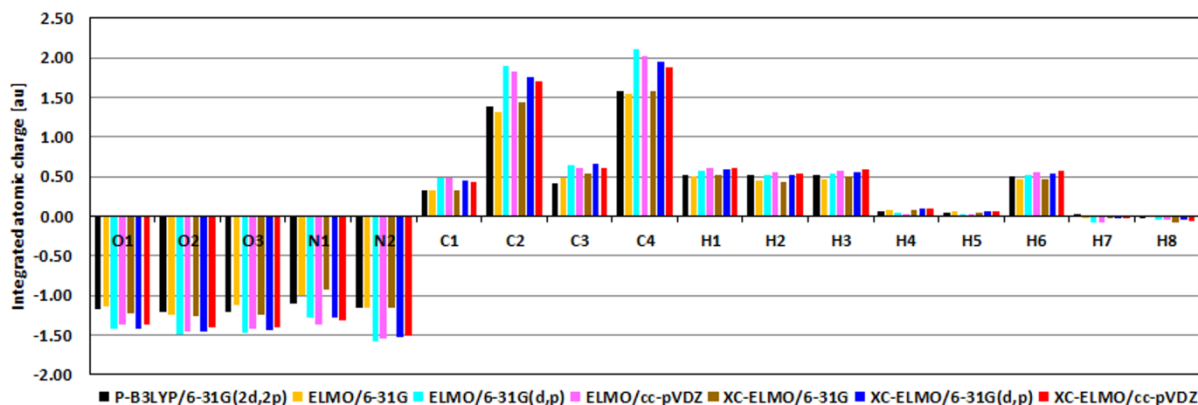


Figure 4.7. Integrated atomic charges (au) from unconstrained (ρ^{ELMO}) and constrained ($\rho^{XC-ELMO}$) ELMO densities and from the *ab initio* periodically calculated density ($\rho^{P-B3LYP}$).

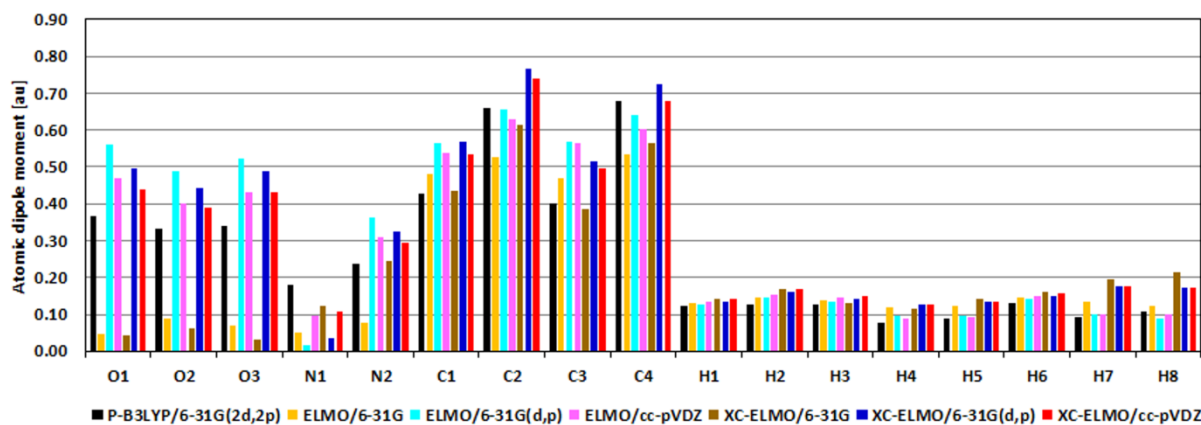


Figure 4.8. Atomic dipole moments (au) from unconstrained (ρ^{ELMO}) and constrained ($\rho^{XC-ELMO}$) ELMO densities and from the *ab initio* periodically calculated density ($\rho^{P-B3LYP}$).

4.5.3. QTAIM atomic charges and dipoles

Bar-graphs of the atomic charges are shown in Fig. 4.7. Overall, charges from ELMO and XC-ELMO wavefunctions are qualitatively similar, addressing negatively charged oxygen and nitrogen atoms, positively charged carbon and hydrogen atoms of the amino group and basically neutral methylenic hydrogens. For the O, N and C atoms, the XC-ELMO/6-31G charges are relatively close to the ELMO/6-31G results with the largest discrepancy around 0.13 au. The differences are even smaller for the polarized and more flexible basis sets. For the hydrogen atoms, the relative changes are larger, but these charges are very small, so the largest absolute differences are around 0.04 au. Furthermore, the results obtained from the $\rho^{XC-ELMO}$ and $\rho^{P-B3LYP}$ densities are similar for all the basis sets, with the XC-ELMO charges slightly larger in absolute values. Surprisingly, the best agreement with the $\rho^{P-B3LYP}$ results is found for the charges calculated using the smaller 6-31G basis set. However, the results previously discussed indicate that this better agreement must be just incidental.

Magnitudes of atomic dipole moments are given as bar-graphs in Fig. 4.8. For oxygen atoms, ELMO/6-31G and XC-ELMO/6-31G dipole moments are markedly underestimated compared to the more polarized basis sets and P-B3LYP. For these atoms, the extra d functions are therefore vital to describe the internal polarization. Using $\rho^{P-B3LYP}$ as benchmark, we see that the X-ray constraining

improves the dipole moments of oxygen atoms for the 6-31G(d,p) and the cc-pVDZ ELMO wavefunctions, although they remain considerably overestimated. The largest discrepancies between unconstrained and constrained calculations are always observed for the carbonylic oxygen O1, with decrements of 0.06 and 0.03 au for the 6-31G(d,p) and cc-pVDZ basis-sets, respectively.

On the contrary, for the nitrogen atoms, the XC-ELMO/6-31G wavefunction gives a dipole moment closer to the one associated with $\rho^{P-B3LYP}$. For N1 and N2, the X-ray constraining is helpful, whereas the polarization functions are not so necessary. The largest difference between ELMO and XC-ELMO dipole moments is 0.07 au for N1, the amino nitrogen involved as “donor” atom in some hydrogen bonds with neighboring molecules.

For carbon and hydrogen atoms, the polarized basis sets usually perform better and the dipole moment magnitude improves after the fitting procedure. The directions of the atomic dipole moments is substantially similar for all methods, with a maximum difference smaller than 2° .

Magnitudes of the molecular dipole moments for glycylglycine are given as bar-graphs in Fig. 4.9(a). As discussed in Chapter 1, Spackman *et al.*³⁵ have shown that typical enhancements of molecular dipole moments from gas-phase to crystals are within 10-40%, depending on the polarizability of the molecule and its specific packing in the solid state. The gas-phase B3LYP/6-31G(2d,2p) molecular dipole moment of glycylglycine is 9.445 au whereas the P-B3LYP molecular dipole moment, using the same basis set, is 11.337 au, corresponding to an enhancement of 20%. In our work, the difference between $\rho^{P-B3LYP}$ and $\rho^{XC-ELMO}$ dipole moments may inform us on the ability of XC-ELMO wavefunctions to account for intermolecular crystal field effects. In fact, from Fig. 4.9(a), we see that the X-ray constraining procedure makes the molecular dipole moment quite closer to the P-B3LYP value, but the increase is smaller than 10% for all the basis sets. The value obtained with the 6-31G basis set is closer to the P-B3LYP one, but this seems again a consequence of the fortuitous agreement on atomic charges described before. In reality, we learn from Fig. 4.9(a) that, as the basis sets become more complete and flexible, the dipole moments obtained through the X-ray constrained wavefunctions converges to a value that is ca. 5% smaller than the P-B3LYP one.

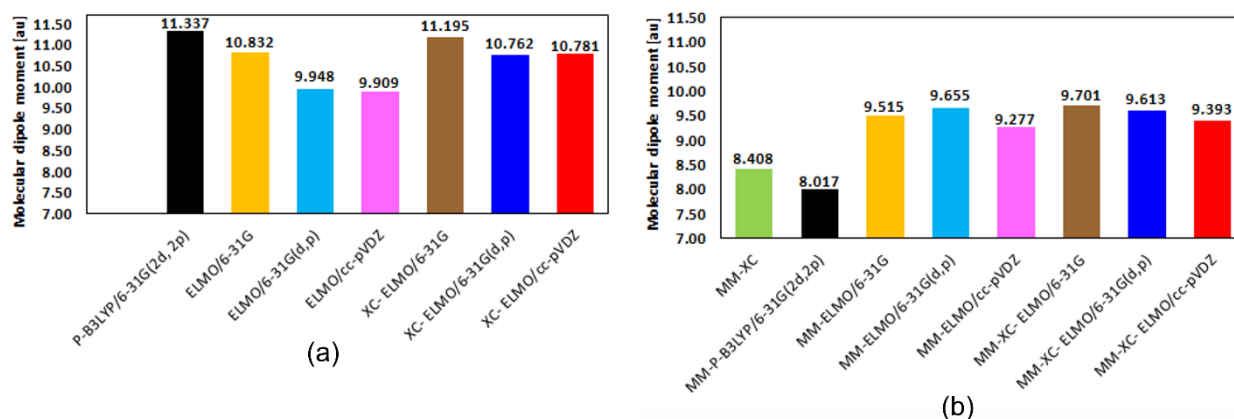


Figure 4.9. Molecular dipole moments (au) from unconstrained (ρ^{ELMO}) and constrained ($\rho^{XC-ELMO}$) ELMO densities and from the *ab initio* periodically calculated density ($\rho^{P-B3LYP}$). Dipole moments calculated from both (a) the primary densities and (b) the multipole-projected densities are shown.

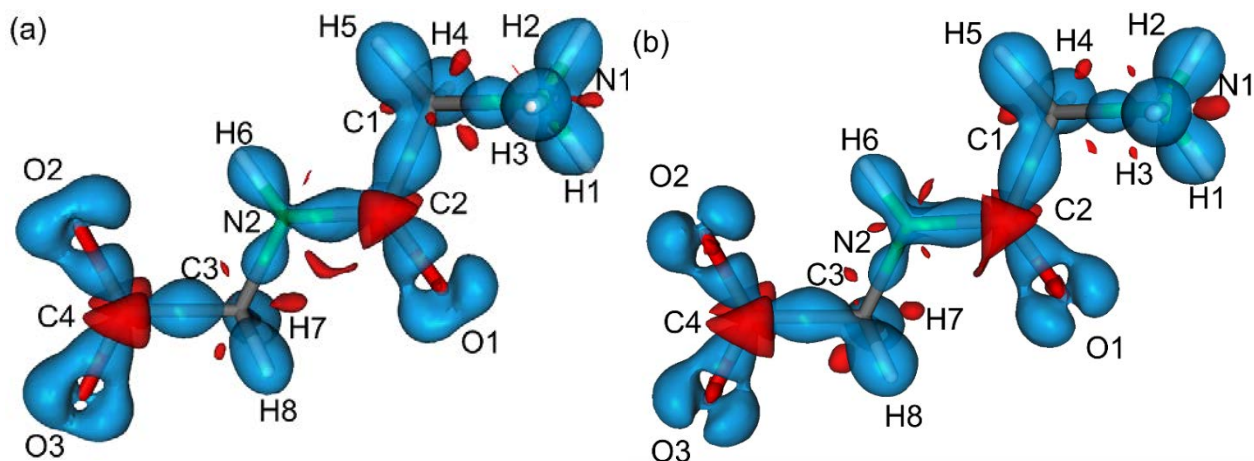


Figure 4.10. Three-dimensional plots of deformation electron densities (a) $\rho^{MM/XC} - \rho^{IAM}$ and (b) $\rho^{MM/P-B3LYP} - \rho^{IAM}$ for glycylglycine. The isosurface value is set to 0.02 au, with negative isosurfaces in red and positive isosurfaces in blue.

4.6. Fitting effects on the multipole model-projected ELMO electron densities

In order to avoid potential ambiguities due to the multipolar expansion used to model the benchmark experimental electron density, we have also projected the P-B3LYP, all the ELMO and XC-ELMO electron densities in terms of Hansen-Coppens multipoles, using the very same MM2 model discussed in Section 4.4. This will enable us to compare all the densities, affected in the same way by the inherent limitations of the multipolar expansion.³² Of course, all the atomic coordinates and ADPs (for XC-ELMO) were kept fixed to those from the MM2 refinement against experimental data.

4.6.1. Deformation density

Fig. 4.10 shows the deformation densities $\rho^{MM/XC} - \rho^{IAM}$ and $\rho^{MM/P-B3LYP} - \rho^{IAM}$ for glycylglycine. As expected, the plots clearly show an accumulation of electron density in all the covalent bonds and in the lone-pairs domains of the oxygen atoms. Electron density depletions are mainly concentrated around the nuclei.

In Fig. 4.11, we show the deformation density plots $\rho^{MM/ELMO} - \rho^{IAM}$ and $\rho^{MM/XC-ELMO} - \rho^{IAM}$ using the 6-31G and 6-31G(d,p) basis sets. At the ELMO/6-31G level, Fig. 4.11(a), the electron accumulation in the bonding regions is significantly smaller, especially for the N2–C3 and all the C–O bonds. The experimental constraint gives only a slight improvement, Fig. 4.11(b). This result confirms that constraining an ELMO wavefunction to experimental structure factors leads to a meaningful electron density distribution only if the basis set is sufficiently flexible. In fact, the deformation densities derived from the unconstrained and constrained ELMO/6-31G(d,p) wavefunctions, Figs. 4.11(c) and 4.11(d), are significantly closer to the $\rho^{MM/XC}$ and $\rho^{MM/P-B3LYP}$ deformation densities.

The $\rho^{MM/ELMO}$ deformation density calculated with the polarized 6-31G(d,p) basis set, Fig. 4.11(c), is already very similar to the $\rho^{MM/P-B3LYP}$ deformation density, Fig. 4.10(b), although only the latter takes into account crystalline environment effects through a fully periodic approach.

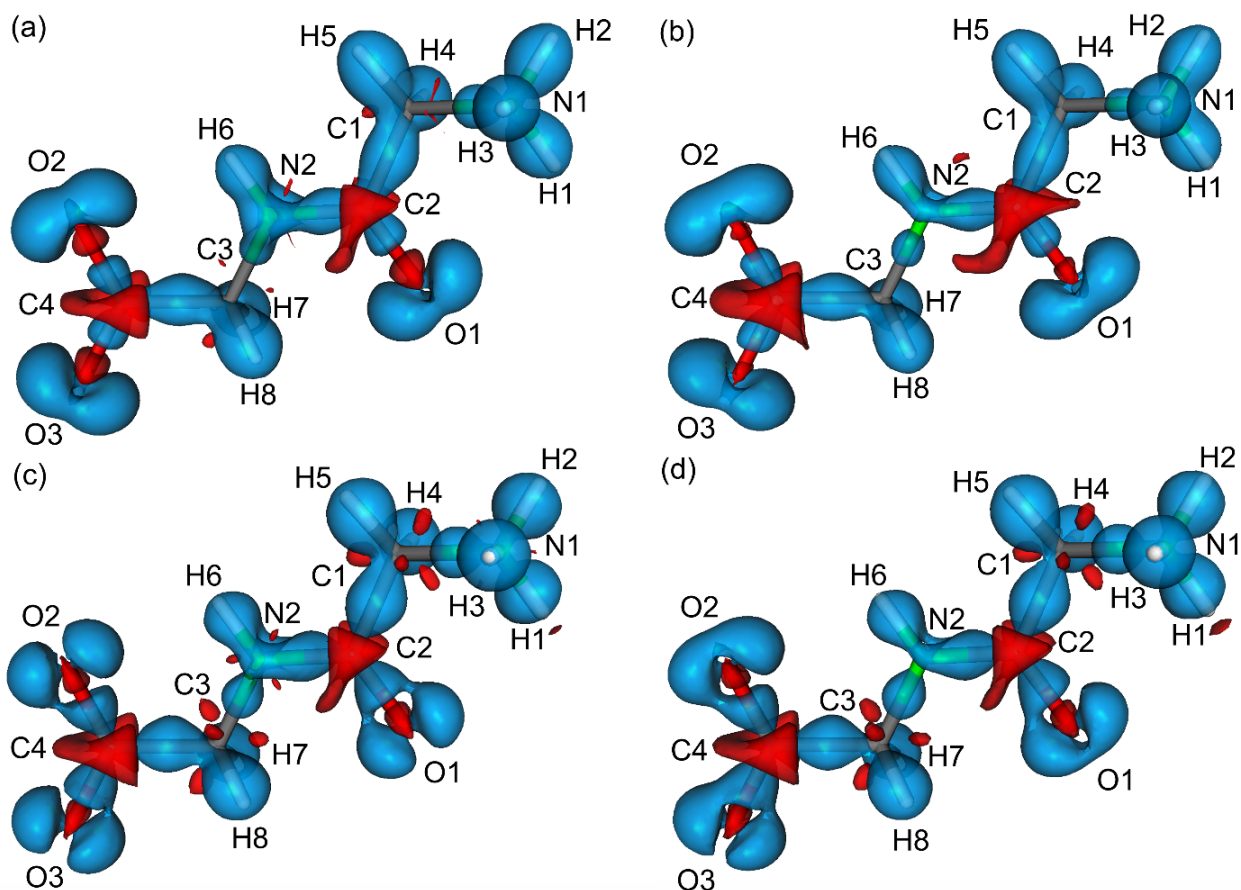


Figure 4.11. Deformation electron densities for glycylglycine obtained from unconstrained $\rho^{MM/ELMO} - \rho^{IAM}$ and constrained $\rho^{MM/XC-ELMO} - \rho^{IAM}$ ELMO wavefunctions. (a) ELMO/6-31G; (b) XC-ELMO/6-31G; (c) ELMO/6-31G(d,p); (d) XC-ELMO/6-31G(d,p). The isosurface value is set to 0.02 au, with negative isosurfaces in red and positive isosurfaces in blue.

A finer analysis shows that Fig. 4.11(d) (deformation density for $\rho^{MM/XC-ELMO}$ with 6-31G(d,p) basis set) is closer to Fig. 4.10(a) ($\rho^{MM/XC}$) than to Fig. 4.10(b) ($\rho^{MM/P-B3LYP}$), in particular for the lone pair domains of the O atoms. This means that some features of the deformation densities are genuinely due to the X-ray constraint rather than to a crystal field effect (at least if calculated at B3LYP level). This is particularly encouraging because it shows the ability of XC-ELMO to extract information from experimental intensities.

4.6.2. Topological properties, charges and dipoles

The results for the topological analysis of all the electron density distributions projected to the Hansen-Coppens MM2 multipole model are in good agreement with the topological features shown in Table 4.3, i.e. the multipole model projections are not significantly different from the corresponding non-projected electron distributions: $\rho(\mathbf{r}_b)$ differ by less than 5%, the positions of the bond critical points are on average within 0.08 au. As expected, $\nabla^2\rho(\mathbf{r}_b)$ change more significantly. In general, $\rho^{MM/XC-ELMO}$ are closer to the $\rho^{MM/XC}$ and $\rho^{MM/P-B3LYP}$ benchmark densities than $\rho^{MM/ELMO}$ and, more importantly, the agreement is better when the larger basis sets 6-31G(d,p) and cc-pVDZ are used.

Table 4.4. Bond critical point data^a corresponding to all the unconstrained and constrained multipole model-projected electron densities for the shortest hydrogen bonds in the crystal structure of glycylglycine. Data for the $\rho^{P-B3LYP}$ density are also shown.

	$\rho_{6-31G(2d,2p)}^{P-B3LYP}$	$\rho^{MM/XC}$	$\rho_{6-31G(2d,2p)}^{MM/P-B3LYP}$	$\rho_{6-31G}^{MM/ELMO}$	$\rho_{6-31G(d,p)}^{MM/ELMO}$	$\rho_{cc-pVDZ}^{MM/ELMO}$	$\rho_{6-31G}^{MM/XC-ELMO}$	$\rho_{6-31G(d,p)}^{MM/XC-ELMO}$	$\rho_{cc-pVDZ}^{MM/XC-ELMO}$
H1...O2ⁱ									
d_H	0.713	0.680	0.695	0.679	0.663	0.661	0.675	0.665	0.663
$\rho(\mathbf{r}_b)$	0.024	0.030(3)	0.033	0.032	0.029	0.029	0.031	0.030	0.030
$\nabla^2\rho(\mathbf{r}_b)$	0.081	0.109(1)	0.102	0.105	0.098	0.097	0.109	0.098	0.097
λ_3	0.14	0.20	0.20	0.20	0.18	0.18	0.20	0.19	0.18
H2...O3ⁱⁱ									
d_H	0.610	0.650	0.644	0.641	0.624	0.624	0.651	0.628	0.630
$\rho(\mathbf{r}_b)$	0.038	0.043(4)	0.041	0.041	0.037	0.038	0.042	0.039	0.040
$\nabla^2\rho(\mathbf{r}_b)$	0.130	0.115(1)	0.103	0.126	0.116	0.107	0.116	0.109	0.103
λ_3	0.24	0.26	0.24	0.26	0.24	0.23	0.25	0.24	0.23
H3...O2ⁱⁱⁱ									
d_H	0.627	0.666	0.679	0.652	0.647	0.644	0.641	0.646	0.642
$\rho(\mathbf{r}_b)$	0.038	0.036(4)	0.038	0.037	0.033	0.033	0.039	0.033	0.034
$\nabla^2\rho(\mathbf{r}_b)$	0.107	0.111(1)	0.110	0.134	0.129	0.126	0.116	0.119	0.117
λ_3	0.22	0.23	0.23	0.25	0.22	0.22	0.24	0.22	0.22
H6...O1^{iv}									
d_H	0.904	0.964	0.968	0.950	0.944	0.946	0.942	0.953	0.954
$\rho(\mathbf{r}_b)$	0.014	0.011(1)	0.011	0.011	0.010	0.011	0.012	0.011	0.011
$\nabla^2\rho(\mathbf{r}_b)$	0.046	0.047(1)	0.047	0.048	0.044	0.045	0.051	0.046	0.047
λ_3	0.07	0.07	0.07	0.07	0.06	0.07	0.08	0.07	0.07

^aFor each bond critical point H...O, d_H is its distance from the nucleus H in Å, $\rho(\mathbf{r}_b)$ is its electron density value in au, $\nabla^2\rho(\mathbf{r}_b)$ is its Laplacian value in au and λ_3 is its positive curvature in au. Symmetry codes: (i) $-x+1, y+1/2, -z+3/2$; (ii) $x+1, y, z+1$; (iii) $-x+1, -y, -z+1$; (iv) $-x+1, y-1/2, -z+3/2$.

Having multipolar projected electron densities, it is possible to thoroughly analyze the hydrogen bonds and comment on the performances of the XC-ELMO approach, in particular verifying if there is any improvement upon the fitting. Fig. 4.1 (b) shows the pattern of strongest hydrogen bonds in the crystal structure of glycylglycine and Table 4.4 collects their topological features. All these bonds are of N-H...O type, with H...O distance ranging from 1.77 (2) to 1.98 (2) Å.

Topological features of hydrogen bonds from experimental electron density analyses have been often used to classify various types of interactions.³⁶ However, Spackman observed that for many medium-weak hydrogen bonds, the electron density, its topology and the local energy densities can be well approximated even using the pro-molecule, that is the electron density distribution calculated from IAM model.³⁷ As a matter of facts, the topological properties of hydrogen bonds calculated from all the electron density models for glycylglycine are rather similar. Wavefunctions computed with the 6-31G basis set provide slightly larger electron densities than the 6-31G(d,p) and the cc-pVDZ ones. However, the effect of X-ray constraining is extremely small. This observation, along with the small dipole moment enhancements discussed in above, suggests that the long-range crystal interactions do not polarize the electron density in the bond critical point region of the H-bond. This is quite different from what happens in the electron lone-pairs and intramolecular bonding regions, where the effects due to the crystal field or the X-ray constraining are more evident. Jayatilaka briefly discussed the effects of long-range interactions on the electron density of oxalic acid dihydrate by means of a

relatively large molecular cluster calculation.^{5d} He concluded that, even when considering the electron distributions of intramolecular bonds and lone-pairs, the influence of the crystalline environment is not significant, at least when the long-range interactions are modeled at DFT level. However, in our opinion, much more work is needed before finding a more general understanding.

Integrated atomic charges calculated from the Hansen-Coppens multipole model-projected electron densities differ by 5-10% from those calculated from the respective primary densities, corresponding to an average absolute value of about 0.1 au. The largest differences are observed for the oxygen atoms at the 6-31G level. In this respect, the influence of the basis set on the integrated charges is much more pronounced than the influence of the multipole projection itself, see Fig. 4.7. For all the basis sets, the atomic charges obtained from X-ray constrained calculations are closer to the $\rho^{MM/XC}$ ones.

The atomic dipole moments from the multipole-projected ELMO and XC-ELMO electron densities are in reasonable agreement with those from the respective primary densities using the 6-31G(d,p) and cc-pVDZ basis sets (differences in the 10-20% range), whereas larger discrepancies (up to 80%) are observed for the 6-31G basis set. As for the non-projected densities, the multipole-projected atomic dipole moments calculated for oxygen atoms using the 6-31G basis set are markedly underestimated compared to the values determined using the larger basis sets or P-B3LYP. Again, the $\rho^{MM/XC-ELMO}$ electron distributions generally give more accurate atomic dipole moment magnitudes.

Molecular dipole moment magnitudes obtained from the multipole-projected electron densities are shown in Fig. 4.9(b). Both unconstrained and constrained ELMO dipole moments are larger than the $\rho^{MM/XC}$ and $\rho^{MM/P-B3LYP}$ values. Compared to the values obtained from the primary densities, Fig. 4.9(a), the multipole projection produces an underestimation of the molecular dipole moments of about 20%, corresponding to ca. 1.5 au. The underestimation due to multipolar projection is even larger for P-B3LYP.

4.7. Influence of fractional coordinates and ADPs on the X-ray constrained calculations

Since the current version of the X-ray constrained ELMO strategy does not allow to refine atomic positions and thermal parameters, all the XC-ELMO wavefunctions considered in the previous sections have been carried out using parameters refined from the multipole model MM2 (Section 4.4).

On the contrary, if XC-ELMO computations are performed using the IAM coordinates and ADPs, the statistical agreements and the energy values (Table 4.5) do not sensitively change, but the convergence toward $\chi^2 = 1$ is much slower, as it occurs for a larger λ_{max} . On the other hand, since the desired agreements is anyway reached (at least for the more flexible basis sets), the small biases in the initial coordinates and ADPs have been artificially “absorbed” into the wavefunction and this would affect the electron density and its topology: $\rho(\mathbf{r}_b)$ are not much affected (with changes smaller than 0.03 au); the distances of the bond critical points from the nuclei differ by less than 5%; $\nabla^2\rho(\mathbf{r}_b)$ change more significantly (up to 15%, corresponding to about 0.05 au). The same holds true for atomic dipole moment magnitudes, the largest differences being of the order of 3%, representing absolute differences around 0.04 au.

Table 4.5. Statistical agreements^a and energy values corresponding to all the unconstrained and constrained calculations performed on the glycyglycine considering the geometry and the ADPs resulting from the Independent Atom Model refinement.

Basis set	ELMO Calculations ^b				XC-ELMO Calculations				
	χ^2	%R(F)	%wR(F)	Energy (au)	λ_{max}	χ^2	%R(F)	%wR(F)	Energy (au)
6-31G	3.04	2.83	3.75	-489.158	0.42	1.45	2.29	2.59	-489.036
6-31G(d,p)	2.03	2.52	3.06	-489.384	0.18	0.98	2.04	2.14	-489.335
cc-pVDZ	2.01	2.51	3.05	-489.396	0.18	0.98	2.04	2.13	-489.350

^a $\chi^2 = (1/(N_r - N_p)) \sum_{\mathbf{h}} w_{\mathbf{h}} (\eta |F_{\mathbf{h},calc}| - |F_{\mathbf{h},obs}|)^2$, $\%R(F) = 100 \left[\sum_{\mathbf{h}} |\eta |F_{\mathbf{h},calc}| - |F_{\mathbf{h},obs}|| / \sum_{\mathbf{h}} |F_{\mathbf{h},obs}| \right]$, $\%wR(F) = 100 \left[\chi^2 / \sum_{\mathbf{h}} w_{\mathbf{h}} F_{\mathbf{h},obs}^2 \right]^{1/2}$ with $w_{\mathbf{h}} = 1/\sigma_{\mathbf{h},obs}^2(F_{\mathbf{h},obs})$. ^bThe scale factors η have been optimized using the density matrices obtained from the corresponding unconstrained calculations.

It is important to point out that the IAM was refined against a high-resolution dataset and therefore non-hydrogen atomic positions and ADPs are already quite accurate, certainly more than those of typical crystal structure determinations. Significantly different results are expected in case of an IAM refined against structure factors up to a lower resolution, for which a multipolar model would also not be reliable.

4.8. Conclusions and perspectives

We have demonstrated that XC-ELMO is a new and potentially useful tool for the determination and the analysis of experimental electron densities. All the X-ray constrained wavefunction methods use the X-ray data in order to capture, at least in part, the effects of electron correlation and crystal environment. XC-ELMO has the additional advantage to resume the atomistic interpretation typical of the pseudo-atom approaches, since the orbitals are one-electron functions accounting for the electron distributions of atoms, bonds or functional groups, depending on the localization scheme.

This work is part of a long project aiming at studying the efficiency of XC-ELMO wavefunctions in molecular crystals and testing the transferability of the ELMOs to larger systems in order to devise new strategies for refining crystallographic structures and electron densities of macromolecules, such as proteins or polymers. In this first step, we have performed a detailed comparison between unconstrained and X-ray constrained ELMO wavefunctions, using traditional multipolar electron density or periodic density functional as benchmarks. The main conclusions can be summarized as follows:

- 1) Sufficiently flexible basis sets are fundamental to obtain a meaningful fitting of the wavefunction. In fact, all calculations confirm that the desired agreements with the experimental data is reached only if polarized basis functions are used.
- 2) The fractional coordinates and ADPs used for XC-ELMO have a strong influence on the convergence: the more accurate the initial parameters are, the faster the convergence is. The inaccuracy of the initial set of coordinates and ADPs is absorbed into the molecular orbital coefficients, thus affecting the electron density. A strategy for the direct refinement of atomic coordinates and ADPs in the framework of the XC-ELMO strategy is currently in preparation.
- 3) When $\chi^2 = 1$ is reached, the constrained ELMO wavefunction is of course in much better agreement with the X-ray data than the unconstrained one, but in less good agreement than a standard

multipole model, for which there is not a strict “control” on the desired precision. In fact, while XC-ELMO only partially uses (through λ) the information contained in the X-ray intensities, the multipole models MM2 and MM3 fully exploit the experimental observations through global least square refinements of the available diffraction data, which leads to χ^2 values much lower than 1.0. Therefore, for a definitive and fair comparison with the traditional multipole models, we should push the X-ray constrained computations beyond the usual $\chi^2 = 1.0$ limit (namely, we should consider larger λ). Whitten *et al.*^{35b} have proposed to pursue the fitting until the weighted residual wR values approach that obtained in the multipole refinement of the same X-ray structure-factor magnitudes. This idea could be reformulated using χ^2 as a criterion, but, unfortunately, this is partially hampered by the problem of determining the optimal value for the Lagrange multiplier λ (see final discussion in Section 1.3.4). However, also in this case, theoretical approaches to overcome this last important drawback are under investigation.

4) The multipolar models seem to be much more sensitive to the valence electron density than the XC-ELMO strategy. Fig. 4.2 shows that the two most flexible multipolar models reproduce the low angle diffracted intensities much better than the high angle ones, whereas this is not true for the XC-ELMO technique that seems more “tempered”. This might be interpreted as an over-fitting of the low angle data by the multipolar models, which, in fact, converge to lower χ^2 , or otherwise as the evidence of a too restricted model that could be improved by a more flexible treatment of the core electrons, as suggested by Fischer.³² A model with strictly hybridized atoms, MM1, is instead closer to $\chi^2 = 1$, and shows a more uniform agreement with the observed structure factors, like the XC-ELMO calculations (Fig. 4.4). However, one would normally consider MM1 as too rigid (*i.e.*, insufficient to exhaust the present data quality) and many indicators address the more flexible MM2 (or the statistically equivalent MM3) as more reliable. Once more, this observation prompts a revision of the current recipes for the X-ray constrained wavefunction calculations that could be too much biased by the quantum-mechanical part of the functional in Eqn. 1.55, and not sufficiently influenced by the experimental data, the second part of the functional.

5) Many properties of the XC-ELMO reconstructed electron density suggests that the constrained wavefunction approaches the “exact” electron density in the crystal, using as benchmark the experimental multipole model or the periodic calculations at density functional level. However, some atomic charges and molecular dipole moments are not properly reproduced. In particular the XC-ELMO calculations generally underestimate the molecular dipole moment and this might be ascribed to the inability of XC-ELMO to include *all* the effects of the crystalline environment, in particular the polarization of the molecule. Interestingly, also the multipolar model underestimate the dipole moment in this case.

6) For the intermolecular interactions, here represented by medium strength N-H...O hydrogen bonds, there is limited perturbation by the crystal packing, therefore it is not possible to judge the efficiency of the X-ray constrained procedure.

Although X-ray constrained methods have been known and used for more than a decade, until now it has not been reported such an accurate comparison with respect to traditional multipolar expansions refined against X-ray intensities or theoretical calculations with periodic boundary conditions.

Therefore, we believe that our results could be important not only to appreciate the advantages of XC-ELMO, but more generally to understand the necessities and pitfalls of all kinds of X-ray constrained wavefunction calculations.

In view of these results, we plan to further investigate the XC-ELMO technique in order to better analyse the ability of the XC-ELMO wavefunctions to include electronic correlation and crystal field effects into the electron density. This may enable us to establish better criteria for the best Lagrange multiplier, which is a crucial parameter in the X-ray constrained wavefunction strategies. Moreover, we will analyse the performances of the XC-ELMO wavefunctions on a broad spectrum of molecules, including metal complexes and stronger hydrogen bond adducts.

References

1. Hohenberg, P.; Kohn, W. *Phys. Rev. B* **1964**, *136*, 864-871.
2. (a) Coppens, P. *X-Ray Charge Densities and Chemical Bonding*; Oxford University Press: New York, **1997**. (b) Gatti, C.; Macchi, P. (Eds.) *Modern Charge-Density Analysis*; Springer: Netherlands. **2012**.
3. (a) Clinton, W. L.; Nakhleh, J.; Wunderlich, F. *Phys. Rev.* **1969**, *177*, 1-6. (b) Clinton, W. L.; Galli, A. J.; Massa, L. J. *Phys. Rev.* **1969**, *177*, 7-13. (c) Clinton, W. L.; Henderson, G.A.; Prestia, J. V. *Phys. Rev.* **1969**, *177*, 13-18. (d) Clinton, W. L.; Lamers, G. B. *Phys. Rev.* **1969**, *177*, 19-27. (e) Clinton, W. L.; Galli, A. J.; Henderson, G. A.; Lamers, G. B.; Massa, L. J.; Zarur, J. *Phys. Rev.* **1969**, *177*, 27-33.
4. (a) Clinton, W. L.; Massa, L. J. *Phys. Rev. Lett.* **1972**, *29*, 1363-1366. (b) Frishberg, C.; Massa, L. J. *Phys. Rev. B* **1981**, *24*, 7018-7024. (d) Massa, L.; Goldberg M.; Frishberg, C.; Boehme, R. F.; Placa, S. J. L. *Phys. Rev. Lett.* **1985**, *55*, 622-625. (e) Tanaka, K. *Acta Cryst. Sect A* **1988**, *44*, 1002-1008. (f) Howard, S. T., Huke, J. P., Mallinson, P. R.; Frampton, C. S. *Phys. Rev. B* **1994**, *49*, 7124-7136. (g) Cassam-Chenaï, P. *Int. J. Quantum Chem.* **1995**, *54*, 201-210. (h) Snyder, J. A.; Stevens, E. D. *Chem. Phys. Lett.* **1999**, *313*, 293-298. (i) Gillet, J. M.; Becker, P.; Cortona, P. *Phys. Rev. B* **2001**, *63*, 235115. (j) Hibbs, D. E.; Howard, S. T.; Huke, J. P.; Waller, M. P. *Phys. Chem. Chem. Phys.* **2005**, *7*, 1772-1778. (k) Gillet, J. M. *Acta Cryst. Sect. A* **2007**, *63*, 234-238.
5. (a) Jayatilaka, D. *Phys. Rev. Lett.* **1998**, *80*, 798-801. (b) Jayatilaka, D.; Grimwood, D. J. *Acta Cryst. Sect. A* **2001**, *57*, 76-86. (c) Húdak, M.; Jayatilaka, D.; Peraínova, L.; Biskupic, S.; Kozísek, J.; Bucinsky, L. *Acta Cryst. Sect. A* **2010**, *66*, 78-92. (d) Grimwood, D. J.; Jayatilaka, D. *Acta Cryst. Sect. A* **2001**, *57*, 87-100.
6. (a) Grimwood, D. J.; Bytheway, I.; Jayatilaka, D. *J. Comput. Chem.* **2003**, *24*, 470-483. (b) Whitten, A. E.; Jayatilaka, D.; Spackman, M. A. *J. Chem. Phys.* **2006**, *125*, 174505. (c) Jayatilaka, D.; Munshi, P.; Turner, M. J.; Howard, J. A. K.; Spackman, M. A. *Phys. Chem. Chem. Phys.* **2009**, *11*, 7209-7218.
7. (a) Genoni, A. *J. Phys. Chem. Lett.* **2013**, *4*, 1093-1099. (b) Genoni, A. *J. Chem. Theory Comput.* **2013**, *9*, 3004-3019. (c) Genoni, A.; Ghitti, M.; Pieraccini, S.; Sironi, M. *Chem. Phys. Lett.* **2005**, *415*, 256-260. (d) Sironi, M.; Ghitti, M.; Genoni, A.; Saladino, G.; Pieraccini, S. *J. Mol. Struct. THEOCHEM* **2009**, *898*, 8-16. (e) Sironi, M.; Genoni, A.; Civera, M.; Pieraccini, S.; Ghitti, M. *Theor. Chem. Acc.* **2007**, *117*, 685-698.
8. Stoll, H.; Wagenblast, G.; Preuss, H. *Theor. Chim. Acta* **1980**, *57*, 169-178.
9. (a) Pichon-Pesme, V.; Jelsch, C.; Guillot, B.; Lecomte, C. *Acta Cryst. Sect. A* **2004**, *60*, 204-208. (b) Jelsch, C.; Pichon-Pesme, V.; Lecomte, C.; Aubry, A. *Acta Cryst. Sect. D* **1998**, *54*, 1306-1318. (c) Zarychta, B.; Pichon-Pesme, V.; Guillot, B.; Lecomte, C. *Acta Cryst. Sect. A* **2007**, *63*, 108-125.

10. (a) Koritsanszky, T.; Volkov, A.; Coppens, P. *Acta Cryst. Sect. A* **2002**, *58*, 464-472. (b) Volkov, A.; Li, X.; Koritsanszky, T.; Coppens, P. *J. Phys. Chem. A* **2004**, *108*, 4283-4300. (c) Dittrich, B.; Hubschle, C.B.; Luger, P.; Spackman, M. A. *Acta Cryst. Sect. D* **2006**, *62*, 1325-1335. (d) Dittrich, B.; Koritsanszky, T.; Luger, P. *Angew. Chem. Int. Ed. Engl.* **2004**, *43*, 2718-2721. (e) Dominiak, P. M.; Volkov, A.; Li, X.; Messerschmidt, M.; Coppens, P. *J. Chem. Theory Comput.* **2007**, *3*, 232-247.
11. (a) Biswas, A. B.; Hughes, E. W.; Sharma, B. D.; Wilson, J. N. *Acta Cryst. Sect. B* **1968**, *24*, 40-50. (b) Kwick, A.; Al-Karaghoul, A. R.; Koetzle, T. F. *Acta Cryst. Sect. B* **1977**, *33*, 3796-3801. (c) Kwick, A.; Koetzle, T. F.; Stevens, E. D. *J. Chem. Phys.* **1979**, *71*, 173-179. (d) Coppens, P.; Guru Row, T. N.; Leung, P.; Stevens, E. D.; Becker, P. J.; Yang, Y. W. *Acta Cryst. Sect. A* **1979**, *35*, 63-72.
12. (a) Adams, W. H. *J. Chem. Phys.* **1961**, *34*, 89-102. (b) Huzinaga, S.; Cantu, A. A. *J. Chem. Phys.* **1971**, *55*, 5543-5549. (c) Matsuoka, O. *J. Chem. Phys.* **1977**, *66*, 1245-1254. (d) Smits, G. F.; Altona, C. *Theor. Chim. Acta* **1985**, *67*, 461-475. (e) Francisco, E.; Pendás, A. M.; Adams, W. H. *J. Chem. Phys.* **1992**, *97*, 6504-6508. (f) Couty, M.; Bayse, C. A.; Hall, M. B. *Theor. Chem. Acc.* **1997**, *97*, 96-109. (g) Fornili, A.; Sironi, M.; Raimondi, M. *J. Mol. Struct. THEOCHEM* **2003**, *632*, 157-172. (h) Szekeres, Z.; Surján, P. R. *Chem. Phys. Lett.* **2003**, *369*, 125-130.
13. Macchi, P.; Buerger, H.-B.; Chimpri, A. S.; Hauser, J.; Gal, Z. *J. Appl. Cryst.* **2011**, *44*, 763-771.
14. Clark, R. C.; Reid, J. S. *Acta Cryst. Sect. A* **1995**, *51*, 887-897.
15. Blessing, R. H. *Cryst. Rev.* **1987**, *1*, 3-58.
16. (a) Sheldrick, G. M. *Acta Cryst. Sect. A* **2008**, *64*, 112-122. (b) Farrugia, L. J. *J. Appl. Cryst.* **1999**, *32*, 837-838.
17. Blessing, R. H. *Acta Cryst. Sect. B* **1995**, *51*, 816-823.
18. Volkov, A.; Macchi, P.; Farrugia, L. J.; Gatti, C.; Mallinson, P.; Richter, T.; Koritsanszky, T. *XD2006 - A Computer Program Package for Multipole Refinement, Topological Analysis of Charge Densities and Evaluation of Intermolecular Interaction Energies from Experimental and Theoretical Structure Factors*; University at Buffalo, State University of New York, NY, USA; University of Milano, Italy; University of Glasgow, UK; CNRISTM, Milano, Italy; Middle Tennessee State University, TN USA, **2006**.
19. (a) Clementi, E.; Roetti, C. *At. Nucl. Data Tables* **1974**, *14*, 177-478. (b) Clementi, E.; Raimondi, D. L. *J. Chem. Phys.* **1963**, *38*, 2686-2689.
20. Becker, P. J.; Coppens, P. *Acta Cryst. Sect. A* **1974**, *30*, 129-153.
21. Volkov, A.; Abramov, Y. A.; Coppens, P. *Acta Cryst. Sect. A*, **2001**, *57*, 272-282.
22. Madsen, A. O. *J. Appl. Cryst.* **2006**, *39*, 757-758.
23. Dovesi, R.; Saunders, V. R.; Roetti, C.; Orlando, R.; Zicovich-Wilson, C. M.; Pascale, F.; Civalleri, B.; Doll, K.; Harrison, N. M.; Bush, I. J.; D'Arco, P.; Llunell, M. *CRYSTAL09 User's manual*; University of Torino, **2009**.
24. Guest, M. F.; Bush, I. J.; van Dam, H. J. J.; Sherwood, P.; Thomas, J. M. H.; van Lenthe, J. H.; Havenith, R. W. A.; Kendrick, J. *Mol. Phys.* **2005**, *103*, 719-747.
25. Jayatilaka, D.; Grimwood, D. J. *Tonto: A Fortran Based Object-Oriented System for Quantum Chemistry and Crystallography*. Computational Science – ICCS **2003**, *4*, 142-151.
26. Volkov, A.; Abramov, Y.; Coppens, P.; Gatti, C. *Acta Cryst. Sect. A* **2000**, *56*, 332-339.

27. Gatti, C. *TOPOND* **1998**, CNR-CSRSRC, Milan, Italy.
28. Keith, T. A. AIMAll, Version 13.11.04; TK Gristmill Software: Overland Park, KS, USA, **2014**, aim.tkgristmill.com.
29. Popelier, P. L. A. *Comput. Phys. Commun.* **1998**, *108*, 180-190.
30. Hirshfeld, F. L. *Acta Cryst. Sect. A* **1976**, *32*, 239-244.
31. Hamilton, W. C. *Acta Cryst.* **1965**, *18*, 502-510.
32. Fischer, A.; Tiana, D.; Scherer, W.; Batke, K.; Eickerling, G.; Svendsen, H.; Bindzus, N.; Iversen, B. B. *J. Phys. Chem. A* **2011**, *115*, 13061-13071.
33. (a) Meindl, K.; Henn, J. *Acta Cryst. Sect. A* **2008**, *64*, 404-418. (b) Meindl, K.; Henn, J. *Struct. Bond.* **2012**, *147*, 143-192. (c) Abrahams, S. C.; Keve, E. T. *Acta Cryst. Sect. A* **1971**, *27*, 157-165.
34. (a) Macchi, P.; Proserpio, D. M.; Sironi, A. *J. Am. Chem. Soc.* **1998**, *120*, 13429-13435. (b) Bytheway, I.; Grimwood, D. J.; Jayatilaka, D. *Acta Cryst. Sect. A* **2002**, *58*, 232-243.
35. (a) Spackman, M. A.; Munshi, P.; Jayatilaka, D. *Chem. Phys. Lett.* **2007**, *443*, 87-91. (b) Whitten, A. E.; Turner, P.; Klooster, W. T.; Piltz, R. O.; Spackman, M. A. *J. Phys. Chem. A* **2006**, *110*, 8763-8776.
36. (a) Espinosa, E.; Souhassou, M.; Lachekar, H.; Lecomte, C. *Acta Cryst. Sect. B* **1999**, *55*, 563-572. (b) Rozas, I.; Alkorta, J.; Elguero, J. *J. Am. Chem. Soc.* **2000**, *122*, 11154-11161.
37. Spackman, M. A. *Chem. Phys. Lett.* **1999**, *301*, 425-429.

General conclusions and outlook

If one considers that the field of electron density analysis was born in middle 60's, when Phillip Coppens published the first accurate deformation density maps in simple organic compounds,¹ and when Hohenberg and Kohn demonstrated their theorems,² then it is fair saying that during the 20 years that followed, a few notable progresses occurred in this area, such as the development of many deformation density models, the quantum theory of atoms in molecules, and the Kohn-Sham reformulation of DFT. However, mainly due to the inherent limitations in hardware and software, electron density analysis was certainly far from being a routine technique. Nevertheless, an enormous amount of work was dedicated to establish the nature and strength of chemical bonding in crystals, mostly focused on organic compounds,^{3a} but a few concerned with chemical bonds in inorganic or metal-organic materials.^{3b} Such problems, seeking ever more accurate experimental data and theoretical models, were in part responsible for the technical developments seen during the 90's in the field of electron density analysis. In theoretical chemistry, one could cite the long-range corrections applied to DFT, which aimed at accurately treat large systems bound by weak intermolecular interactions. In X-ray crystallography, area detectors certainly stood apart. Due to these progresses, in 1998, Coppens described electron density analysis as a technique ready for application to a wide range of problems in chemistry, physics and biology.⁴

Indeed, the last 15 years have shown that electron density analysis has entered the stage of applications.⁵ For the chemists, this particularly means applying electron density distributions to understand the intricate mechanisms governing the phenomena of relevance for materials science and biochemistry, the two outstanding sub-fields of chemical science. Following this tendency, and motivated by the obvious importance of such studies, this thesis aimed at correlating observable properties of organic and metal-organic materials with their ground-state electron density distributions. In particular, we have focused on optical and magnetic properties of crystals, but the methodologies developed here can be applied to a wider range of properties. The studied compounds have been selected based on their recent applications as materials: amino acid molecules and derivatives have received some attention due to their linear and non-linear optical properties,^{6a} while copper(II) pyrazine nitrate coordination polymers are particularly useful realizations of low-dimensional quantum magnets.^{6b}

With the purpose of designing linear optical materials, we have calculated atomic and functional group polarizabilities of amino acids and their hydrogen bonded aggregates.⁷ Our study has enabled the identification of the most efficient functional groups, able to build-up the largest susceptibilities in the crystal, as well as the creation of a databank for distributed polarizabilities, thus allowing the prediction of most of the linear optical behaviour of a material prior to its synthesis. Furthermore, we have quantified the role played by intermolecular interactions on modifying the polarizability of the isolated building blocks, and identified the most relevant parameters that should be controlled or corrected when such perturbations are applied semi-empirically, thus allowing accurate prediction of "in-crystal" properties from the constituent molecules calculated in an infinitely diluted gas. Finally, the dependence of the distributed polarizabilities on the one-electron basis set and the many-electron Hamiltonian was carefully analysed for selecting the most efficient level of theory to estimate the susceptibilities in this kind of materials.

In future, the transferable polarizabilities calculated in this work could be further explored, for example to estimate the dispersive component of the interaction energy between molecules in aggregates, or to map the most reactive sites in a material. Moreover, the analyses carried out here should be extended for the relevant cases of non-linear optical materials, whose corresponding non-linear polarizabilities and susceptibilities are much more challenging to be estimated, either from first-principles or semi-empirically, because the effects of intermolecular interactions are typically much more pronounced.

Aiming at designing magnetic materials, relationships have been established between the electron density distribution and the magnetism of two copper(II) pyrazine nitrate metal-organic polymers.⁸ QTAIM was used to identify the possible magnetic exchange pathways, and DFT calculations of the corresponding pairwise exchange-coupling constants enabled us to recognize the most fundamental building blocks that determine the magnetism in these crystals. The occupancy of the d orbitals at the metallic center, which is a direct manifestation of the deformation density at that atom, was used to identify the magnetic orbital, and the fine structure of $\nabla^2\rho_1(\mathbf{r})$ has revealed in detail the consequences of the pseudo-Jahn-Teller distortion to the electron density distribution of the copper(II). The ellipticity profile, available after a QTAIM topological analysis of $\rho_1(\mathbf{r})$, was used, along with molecular orbital and spin density analyses, to shed light on the mechanism governing the exchange interaction in the family of copper(II) pyrazine magnetic materials. Even though a quantitative elucidation of the magnetism necessarily seeks the experimental spin density distribution, this finding is of relevance because it indicates that some aspects of the magnetic phenomena may be correlated to features of the position charge density, thus being in principle available from a multipolar electron density fitted against the set of experimentally collected structure factors.

Much more work in this area must be performed in the future. In particular, other copper(II) coordination polymers should be analysed to clarify the role played by the σ and the potential π mechanism on determining the magnetic properties of these materials. We note that some coordination compounds containing ligands closely related to pyrazine, such as 1,4-diazabicyclo-octane, may prevent a π mechanism. The Cu(II) congener has been already synthesized, but its magnetism has yet not been investigated properly. A few other materials are currently under investigation in our group, $\text{Cu}(\text{pyz})_2(\text{ClO}_4)_2$ and $[\text{Cu}(\text{pyz})_2\text{Cl}]\cdot\text{BF}_4$, but the lower quality of their crystals make the accurate electron density analyses more challenging.

In the last chapter of this thesis, we have investigated the recently proposed X-ray constrained extremely localized molecular orbitals (XC-ELMOs) technique.⁹ Although also useful for the determination and analysis of experimental electron densities, we plan to use this tool to derive transferable orbitals that, having no tails, are strictly localized on atoms or functional groups. Here, we have analysed in detail the effect of constraining the ELMO wavefunctions to high-quality experimental X-ray structure-factor amplitudes, and its ability to reproduce very accurate benchmark electron densities. Among our findings, we mention the need of sufficient flexible basis sets to obtain a meaningful fit of the wavefunction, and of an accurate set of atomic coordinates and ADPs to reliably predict the electron densities, as the inaccuracy of these initial parameters is easily absorbed into the orbital coefficients, thus affecting the resultant density. Analyses of χ^2 values obtained from the traditional multipolar fitting and from the XC-ELMO fitting reveal that, because the former fully exploit the experimental observations, while the latter is controlled by the desired agreement Δ , the

traditional multipole fittings typically achieve smaller χ^2 values. Therefore, a fair comparison among the electron densities can only be obtained when pushing the X-ray constrained computations beyond the usual $\chi^2 = 1.0$ limit. This finding is of relevance because it may help design more suitable termination criteria for the ELMO fitting against the experimental observations.

We plan to further investigate the XC-ELMO technique in order to quantify the ability of the constrained wavefunctions to include electronic correlation and crystal field effects into the electron density, and to test whether such effects could be reliably retrieved from the X-ray collected intensities. This would be highly desirable as a new approach to, for example, include intermolecular interactions effects on gas-phase molecular calculations.

We believe that this work furnishes, at least partially, the prerequisites for understanding materials properties from the electron density distribution of their building blocks. This could be particularly important to engineering new functional materials based on specific desired behaviours, or to predict the properties of materials already prepared. Our approach is expected to mainly contribute to the future research in supramolecular chemistry, crystal engineering and electron density analysis, but the synergy among experiment and theory stressed here is certainly of relevance for the broader fields of materials science and chemical crystallography.

References

1. Coppens, P. *Science*. **1967**, *158*, 1577-1579.
2. Hohenberg, P.; Kohn, W. *Phys. Rev. B*. **1964**, *136*, 864-871.
3. (a) Gilli, G.; Gilli, P. *The Nature of the Hydrogen Bond*; Oxford University Press: Oxford. **2009**. (b) Macchi, P.; Sironi, A. *Coord. Chem. Rev.* **2003**, *238*, 383-412.
4. Coppens, P.; *Acta Cryst. Sect. A* **1998**, *54*, 779-788.
5. Gatti, C.; Macchi, P. (Eds.) *Modern Charge-Density Analysis*; Springer: Netherlands. **2012**.
6. (a) Petrosyan, H. A.; Karapetyan, H. A.; Antipin, M. Y.; Petrosyan, A. M. *J. Cryst. Growth* **2005**, *275*, e1919-e1926. (b) Lancaster, T.; Blundell, S. J.; Brooks, M. L.; Baker, P. J.; Pratt, F. L.; Manson, J. L.; Landee, C. P.; Baines, C. *Phys. Rev. B* **2006**, *73*, 020410.
7. (a) Dos Santos, L. H. R.; Krawczuk, A.; Macchi, P.; *J. Phys. Chem. A* **2015**, *119*, 3285-3298. (b) Chimpri, A. S.; Gryl, M.; Dos Santos, L. H. R.; Krawczuk, A.; Macchi, P. *Cryst. Growth Des.* **2013**, *13*, 2995-3010.
8. Dos Santos, L. H. R.; Lanza, A.; Manson, J. L.; Macchi, P. *Submitted* **2015**.
9. Dos Santos, L. H. R.; Genoni, A.; Macchi, P. *Acta Cryst. Sect. A* **2014**, *70*, 532-551.

Declaration of consent

on the basis of Article 28 para. 2 of the RSL05 phil.-nat.

Name/First Name: Rezende dos Santos / Leonardo Humberto

Matriculation Number: 12-126-413

Study program: Chemistry and Molecular Sciences

Bachelor

Master

Dissertation

Title of the thesis: Materials Properties from Electron Density Distributions: Molecular Magnetism and Linear Optical Properties

Supervisor: PD Dr. P. Macchi

I declare herewith that this thesis is my own work and that I have not used any sources other than those stated. I have indicated the adoption of quotations as well as thoughts taken from other authors as such in the thesis. I am aware that the Senate pursuant to Article 36 para. 1 lit. r of the University Act of 5 September, 1996 is authorised to revoke the title awarded on the basis of this thesis. I allow herewith inspection in this thesis.

3027 Bern, January 12th 2016

Place/Date



Signature

Curriculum Vitae

Personal Details

Name Rezende dos Santos
First Name Leonardo Humberto
Date of Birth 24 March 1988
Place of Birth Juiz de Fora MG Brazil
Citizenship Brazilian

Higher Education

Jul. 2012 - Feb. 2016 Doctorate in Chemistry and Molecular Sciences
Department of Chemistry and Biochemistry, University of Bern, Bern, Switzerland
Thesis: *Materials Properties from Electron Density Distributions: Molecular Magnetism and Linear Optical Properties*
Supervisor: PD Dr. P. Macchi

Mar. 2010 - Feb. 2012 Master in Chemistry
Department of Chemistry, Federal University of Minas Gerais, Belo Horizonte, Brazil
Thesis: *Crystal Structure and Electron Density Refinement of Piromellitic-Acid Salts*
Supervisor: Prof. N. G. Fernandes

Mar. 2006 - Feb. 2010 Licentiate in Chemistry
Federal University of Juiz de Fora, Juiz de Fora, Brazil

Publications

- Dos Santos, Leonardo H. R.** & Macchi, Piero. 2015. *The role of hydrogen bond in designing molecular optical materials*. Crystals, submitted manuscript.
- Dos Santos, Leonardo H. R.**, Lanza, Arianna, Barton, Alyssa, Brambleby, Jamie, Blackmore, William, Goddard, Paul, Xiao, Fan, William, Robert, Lancaster, Tom, Pratt, Francis, Blundell, Stephen, Singleton, John, Manson, Jamie L. & Macchi, Piero. 2015. *Experimental and theoretical electron density analysis of copper pyrazine nitrate quasi-low-dimensional quantum magnets*. J. Am. Chem. Soc., submitted manuscript.
- Dos Santos, Leonardo H. R.**, Krawczuk, Anna & Macchi, Piero. 2015. *Distributed atomic polarizabilities of amino acids and their hydrogen-bonded aggregates*. J. Phys. Chem. A, v. 119, 3285-3298.
- Dos Santos, Leonardo H. R.**, Genoni, Alessandro & Macchi, Piero. 2014. *Unconstrained and X-ray constrained extremely localized molecular orbitals: analysis of the reconstructed electron density*. Acta Cryst. Sect. A, v. 70, 532-551.
- Chimpri, Abita S., Gryl, Marlena, **Dos Santos, Leonardo H. R.**, Krawczuk, Anna & Macchi, Piero. 2013. *Correlation between accurate Electron density and Linear Optical Properties in Amino acid derivatives: L-histidinium Hydrogen Oxalate*. Cryst. Growth & Des. v.13, 2995-3010.
- De Assis, Joao V., Couri, Maria Rubia C., Porto, Ricardo S., De Almeida, Wagner B., **Dos Santos, Leonardo H. R.**, Diniz, Renata & De Almeida, Mauro V. 2013. *Synthesis of Mercaptobenzothiazole and Mercaptobenzimidazole condensed with Inositol derivatives*. J. Heterocyclic Chem. v.50, E142-E147.
- Dos Santos, Leonardo H. R.**, Rodrigues, Bernardo L., Idemori, Ynara M. & Fernandes, Nelson G. 2012. *Short hydrogen bonds in a new salt of pyromellitic acid: An experimental charge density investigation*. J. Mol. Struct. v.1014, 102-109.
- Corrêa, Charlane C., Lopes, Lívia B., **Dos Santos, Leonardo H. R.**, Diniz, Renata, Yoshida, Maria I., de Oliveira, Luiz F.C. & Machado, Flávia C. 2011. *Four new coordination polymers involving transition metals with 1,2,4,5-benzenetetracarboxylate and pyridyl-donor ligand di(4-pyridyl) sulphide*. Inorg. Chim. Acta. v.367, 187-193.